Semiconductors, Vol. 36, No. 7, 2002, pp. 717–739. Translated from Fizika i Tekhnika Poluprovodnikov, Vol. 36, No. 7, 2002, pp. 769–793.

REVIEWS

Wannier–Stark Localization in the Natural Superlattice of Silicon Carbide Polytypes

V. I. Sankin

Ioffe Physicotechnical Institute, Russian Academy of Sciences,
Politekhnicheskaya ul. 26, St. Petersburg, 194021 Russia
e-mail: sankin@widegap.ioffe.rssi.ru

Received December 24, 2001; accepted for publication December 24, 2001

Abstract—Results of a study of silicon carbide polytypes under high electric fields are presented. The presence of a natural superlattice in silicon carbide polytypes is shown to introduce a miniband structure into the conduction band, which leads to a number of effects: negative differential conductivity in the Bloch oscillation mode, electron–phonon resonances, localization in the lower miniband, resonance tunneling between the first and second minibands, prevalence of holes in the impact ionization in a wide range of fields, anomalously high avalanche breakdown fields (with a negative temperature dependence of the breakdown field) and other unusual effects. Notice that all the phenomena mentioned above are parts of a single Wannier–Stark localization process, which sets in as the mean electric field increases from 100 to 2900 kV/cm (the maximal field magnitude achieved in an abrupt *p–n* junction is twice larger). © *2002 MAIK "Nauka/Interperiodica".*

1. INTRODUCTION

High hardness, chemical resistance to an aggressive environment, retention of semiconductor properties up to a temperature as high as 1000°C, high heat conductivity, high breakdown fields, and many other features of silicon carbide are well known. Notwithstanding the fact that such a unique property of silicon carbide as polytypism is now widely known, only limited interest in SiC polytypes (PTs), as prominent examples of semiconductors with a superstructure, has been shown so far. One can distinguish an additional periodicity (apart from the basic one) with the spacing of a few or tens of lattice constants in practically all PTs. Such superperiodicity was named the natural superlattice (NSL). The influence of this phenomenon on the electronic properties of the PTs and the possible alternative use of NSL instead of the widely used artificial superlattice (SL) GaAs–$Ga_xAl_{1-x}As$ are of interest along with the nature of these superstructures. This problem is undeniably fundamental, but it is also of large practical interest, since SiC crystal properties are of much practical interest. A natural SL can be defined easily enough from the point of view of crystallography. Silicon carbide is known to form a set of crystals (PTs) with distinct crystallographic structures. Cubic 3*C*-SiC and hexagonal 2*H*-SiC are the simplest of these. There are no purely cubic and hexagonal crystals among more complex PTs. Every one of them consists of specifically alternating layers with cubic and hexagonal surroundings. The best known PTs are 4*H*, 6*H*, 8*H*, 15*R*, 21*R*, and 27*R*. The numbers stand for the quantity of atomic layers in the crystal unit cell along the chosen crystal axis *C*, and the letters indicate the unit cell symmetry; *H* stands for hexagonal and *R* for rhombohedral. Evidently, the unit cell size along the *C* axis for most PTs exceeds that for the simplest PTs. The unit cell size of the hexagonal sequence 4*H*, 6*H*, 8*H* is respectively 2, 3, and 4 times larger than for 2*H*. The alternating layers in some PTs are as follows: $(hk)_2$ for 4*H*, $(hkk)_2$ for 6*H*, $(hkkk)_2$ for 8*H*, $(hkhkk)_3$ for 15*R*, $(hkkhkkk)_3$ for 21 *R*, for $(hkhkhkhkk)_3$ and 27*R*. The letters *h* and *k* designate atomic layers with hexagonal and cubic orientations; the subscripts after parentheses show how many times the sequence indicated in parentheses are repeated in the unit cell. The period of this sequence for the series mentioned above far exceeds by 2, 3, 4, 5, 7, and 9 times the basic lattice constant for a given PT. Therefore, it is reasonable to define it as a superperiod and the superperiodicity as NSL.

Bloch showed in 1928 [1] that an electron reaching the upper edge of the allowed band under the effect of an electric field undergoes the Bragg reflection and moves in a direction opposite to the electric field. Losing its energy, the electron returns into the initial position, and this process recurs. The Bloch oscillation (BO) frequency reads

$$\nu = eFa/h, \tag{1}$$

where *F* is the electric field, and *a* is the lattice constant. We note that one more condition must be satisfied for BO to be realized:

$$eFl = E_1, \tag{2}$$

where *l* is the electron (hole) mean free path, and E_1 is the allowed bandwidth (subscript 1 indicates a lower position of the band). Consequently, on average, fields higher than 1000 kV/cm are necessary for conventional semiconductors with wide allowed bands of about a few electronvolts. Therefore, narrow bands are neces-

sary for the realization of the effect at acceptable fields. Such narrow bands are possible in crystals with superperiodicity.

Systems with superperiodicity attracted increased interest in the middle of the 1960s after Keldysh's paper [2] was published, in which he suggested that an additional potential with the period greatly exceeding the lattice constant be created in the crystal, i.e., with a superperiod, which, in turn, could split the continuous and wide band into a set of narrow minibands. The application of a high electric field to such a system induces the Bragg reflection mode and the electron localization named the Wannier–Stark localization (WSL) [3], and, therefore, the onset of the negative differential conductivity (NDC). We may state that Keldysh's idea has stimulated the manufacturing of artificial superlattices (SL) [4] based on a sequence of heterojunctions, which were hitherto the objects of a large number of studies whose main objective was to observe NDC. Unfortunately, this problem has essentially remained unsolved until the present time. Recently, the WSL problem has been widely discussed in numerous publications. It is not difficult to unify the physical phenomena of the Wannier–Stark quantization and BOs.

Doubts about the correctness of the Wannier solution leading to WSL were put forward in some works (in [5], for instance), since the one-band approximation, which did not take into account the possibility of the electric-field-induced mixing of states belonging to different bands, was used in the Wannier model. It was shown in [6] that WSL exists under interband tunneling conditions, but this publication also induced active discussion [7]. This discussion continues even today [8], which indicates the complexity of solving this problem theoretically and the necessity of acquiring experimental data on the entire range of related problems. Note that the active practical interest in the experimental results in this field is due to the basic possibility of obtaining NDC, which is important for a great number of applications.

The actual observation of the WSL effects is possible only if SLs with an electronic spectrum consisting of narrow minibands are used. The observation of Wannier–Stark ladders at optical transitions is substantial proof of the existence of WSL in a crystal with SL [9, 10]. The Wannier–Stark ladder levels formed the following series in optical transitions:

$$E_n = E_0 + neFd, \quad n = 0, \pm 1, \pm 2, \pm 3, \ldots. \qquad (3)$$

Here, E_0 is the transition energy within one well with $n = 0$, and d is the SL period. Some time later, polarization waves of the BOs were observed [11, 12] using the four-wave mixing technique. It is worthy of note that optical experiments, in themselves, do not give grounds to state unambiguously that the aforementioned effects are feasible. The fact that they are observed using highly sensitive optical methods indicates that the magnitude of the effects is small. The direct observation of the NDC under proper conditions could become a serious argument for the existence of the above effects.

The basic possibility of obtaining NDC related to field-induced localization in an artificial SL was shown by Esaki and Tsu (ET) [4]. This effect occurs when electrons heated by an electric field reach the region of the band spectrum where the effective mass is negative. This region is usually located near the upper miniband edge, but does not contact it. The publication of [4] may be considered the starting point of the extensive study of the Wannier–Stark quantization in artificial SLs.

Only twenty years after the inception of the study, publications [13–15] appeared; the results, in the opinion of the authors of these works, indicated the observation of the NDC due to the mechanism proposed in [4]. In particular, a detailed proof was given in [13, 14] of the statement that the observed effects are not related to WSL. However, optical and transport experiments were carried out on similar SLs in [16] where it was stated that the WSL and NDC effects were physically identical. Unfortunately, there was no quantitative or qualitative agreement between the results of [13–15] and similar studies were not continued.

The problem of electron transport under high electric fields in the NSL system of silicon carbide polytypes was analyzed for the first time in the studies that will be discussed below. Thus, the topical problem, which was not solved with artificial SLs, should necessarily become a subject of the study of NSL in SiC polytypes owing to the indisputable advantage of their structure quality over the artificial SLs and, particularly, because of the absence of interfaces. The problem of producing experimental SiC structures basically amounts to the growing of high-quality epitaxial homolayers, rather than heterolayers; substantial experience in solving such a problem has been accumulated both in Russia and abroad. The results of this study had to answer fundamental physical questions: whether WSL exists in crystals; whether it is possible to experimentally observe the BR and ET modes or other phenomena predicted theoretically; and whether it is the NSL in SiC that is an important factor or is it a long-range unique phenomenon that exerts almost no effect on the electronic properties. New data which is important for designing electronic devices could naturally be an expected result. That is why the study of hot carrier transport in silicon carbide polytypes began with the impact ionization and breakdown, which have great practical importance. These studies were quite innovative from the fundamental point of view, since there were no theoretical or experimental data at that time concerning the effect of the WSL on the above processes in semiconductors with SLs. The impact ionization and breakdown in SiC polytypes were extremely interesting from the point of view of NSL presence in these materials. This line of study naturally involved maximal fields, since the WSL took place in a wide

range of fields. Admittedly, the discovery of such a profound influence of the WSL on the impact ionization and breakdown came as a surprise. This influence not only radically changed the character of these processes, which were considered standard ones in all known semiconductors, but also led to radically new effects, in particular, the multipinching of the avalanche current. It is interesting that the character of these processes in the same crystals, but in the direction perpendicular the NSL axis, does not differ from all other semiconductors.

2. IMPACT IONIZATION IN SILICON CABIDE POLYTYPES

Impact ionization (II) is one of the most important processes in a semiconductor material. Impact ionization in semiconductors, like in gases, is the physical basis of operation of many semiconductor devices. Data on II were extremely necessary with respect to devices based on silicon carbide, since their main advantage was a high breakdown field. Furthermore, the effect of NSL could reveal itself in new and unexpected features, in particular, those concerning the device design.

2.1. Measurement of Impact Ionization in Silicon Carbide Polytypes

A study of II was carried out using the photomuliplication technique [17]. A sample with a *p–n* junction was exposed to light with the photon energy of 3.2–4.0 eV; the light was incident perpendicularly to the *p–n*-junction plane. The *p–n*-junction structure was abrupt and asymmetric, i.e., P^+–N or P^+–N–N^+, where P^+ is the *p*-type region heavily doped up to $N_a - N_d \approx 10^{21}$ cm^{-3}, N^+ is the *n*-type region doped less heavily by 3–4 orders of magnitude, and N^+ is the heavily doped *n*-type region with $N_d - N_a \approx 10^{21}$ cm^{-3}. Al sputtered at $T = 850$ K and Ni fused at $T = 1300$ K were used as contacts. Experimental samples were prepared in the form of mesostructures of 200–400 μm in diameter.

Reverse bias was applied to the sample; the field at the *p–n* junction increased with it. In order to avoid breakdown along the mesostructure lateral surface, the latter was irradiated with 30–150-keV protons [18]. The induced photocurrent was multiplied in the *p–n*-junction field due to II. The multiplication coefficient M was determined in the course of the experiment as the ratio of the multiplied photocurrent to the photocurrent without multiplication. Since the diffusion length of electrons and holes did not exceed 0.3 μm [19] and the *p–n*-junction width was about the same, the separate measuring of the hole and electron multiplication coefficients M_p and M_n was not possible in such system. The ratio between the electron α and hole β ionization coefficients was not known; therefore, we used estimates for them which are valid in extreme cases [17]:

(1) $\alpha = \beta$,

$$\alpha(\beta) = \frac{F_m}{M^2 X_m}\frac{dM}{dF_m}; \quad (4)$$

(2) α or $\beta = 0$,

$$\alpha(\beta) = \frac{F_m}{M X_m}\frac{dM}{dF_m}, \quad (5)$$

where F_m is the maximum field at the *p–n* junction, and X_m is the *p–n*-junction width. The voltage dependence of the capacitance $C(V)$ was measured in order to determine F_m and X_m. The contact potential magnitude was $V_b = 2.7$–2.9 V.

Absence of *p–n*-junctions with a homogeneous avalanche breakdown was the main reason why studies of II were not known up to the beginning of this research, and, for some time, our attempts to carry out such a study were fruitless. However, due to the analysis that was performed, proper conditions for the manufacturing of perfect *p–n* junctions [20] were found, the origin of the low-voltage microplasma was explained, and the vacancy cluster model was formulated [21]. An increase of the voltage up to breakdown was not accompanied by the formation of microplasmas in perfect *p–n* junctions, and the breakdown region consisted of a few domains with some distinction in the light-emission intensity between them. The uniformity of the electric field distribution and, therefore, the correctness of measuring the field dependence of the ionization coefficients were ensured in such *p–n* junctions.

The experimental data obtained for 6*H*-SiC were processed using formulas (4) and (5). Interestingly, if we assume that $\alpha = \beta$, the curve $\alpha(F)$ [17] not only did not show a tendency towards exponential rise, but began to fall at a certain field (see Fig. 1, curves *1*, *2*). Such behavior was not observed when a similar procedure was applied, for example, to silicon. A meaningful exponential increase in the $\alpha(F)$ function was obtained only for the case of $\alpha \ll \beta$ (see Fig. 1, curve *3*). The experimental plot fit well enough with the theoretical one calculated in accordance with [22] with the following values of parameters: the electron (hole) mean free path equals 23 Å; and $\hbar\omega_0/E_i = 0.026$, where $\hbar\omega_0 = 120$ meV is the optical phonon energy and $E_i = 1.5E_g$ is the ionization threshold energy. Thus, we may conclude that II behavior in 6*H*-SiC is monopolar. The measuring of II in other SiC polytypes such as 4*H*-, 10*H*-, 15*R*- and 21*R*-SiC showed identical II behavior (Fig. 2) [23]. The II curves for 15*R* and 10*H* coincided with those for 6*H* and 21*R*, respectively. It must be emphasized that this phenomenon was observed in the arrangement where the electric field was parallel to the NSL axis. As a result, a model for the heating of electron gas in a miniband was proposed. It was assumed in [24] that large (about a few tenths of an electronvolt) gaps in the

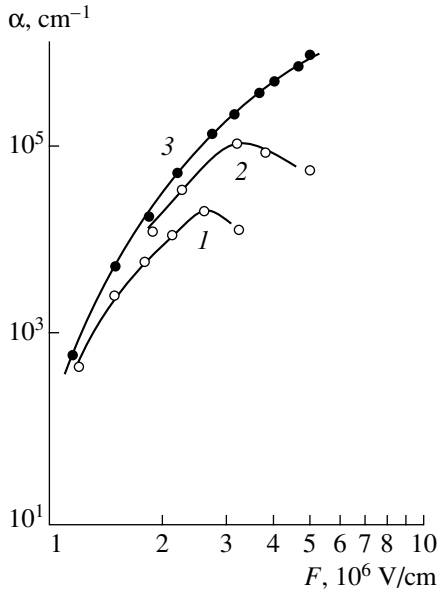

Fig. 1. Electric-field dependences of the ionization coefficient: (*1*, *2*) for $\alpha = \beta$ (*1* corresponds to sample *1* with $N_d - N_a = 3 \times 10^{17}$ cm^{-3}, and *2* corresponds to sample *2* with $N_d - N_a = 1.6 \times 10^{18}$ cm^{-3}); (*3*) for $\alpha \ll \beta$ for both samples. 6*H* polytype.

conduction band energy spectrum existed and the allowed band was narrowed to a few tenths of an electronvolt. At the same time, such gaps are absent in the valence band. The presence of large gaps in the conduction band, which prohibit interband tunneling, actually restricts electron heating to the first miniband width. Therefore, we can assume that holes ionize to a greater extent than electrons and the measured II coefficient is related to holes. In order to prove these assumptions, the following were necessary:

(1) to show the existence of the monopolar ionization effect using independent methods;

(2) to obtain convincing proof of the hole ionization;

(3) to show that the II monopolarity is associated inexorably with the direction of the field along the NSL axis.

2.2. Dependence of Impact Ionization on Electric Field Orientation

In order to elucidate the effect of the field orientation in reference to the NSL axis, it was necessary to fabricate a *p–n* junction in the plane parallel to this axis [25]. The *p–n* junctions had not been fabricated in this plane previously. The problem is associated with the fact that dislocations terminate in this plane and the structure quality of the latter is much worse than for the basal plane. That is why substrates having both satisfactory quality and this orientation are very rare. It is the selection of high quality substrates that presents the main difficulty in the fabrication of *p–n* junctions with the field $F \perp C$. The structures of *p–n* junctions with $F \parallel C$ and $F \perp C$ were identical.

Measurement of II in *p–n* junctions with $F \perp C$ [25] have shown that photomultiplication occurs in such junctions only in the immediate vicinity of the breakdown point; furthermore, the multiplication coefficient increases more rapidly with increasing field, and its peak value is smaller than for similar junctions with $F \parallel C$. Such features are characteristic of semiconductors with almost the same electron and hole ionization coefficients. The field dependence of II for $F \perp C$ is shown in Fig. 3. Analysis of the field dependence of the

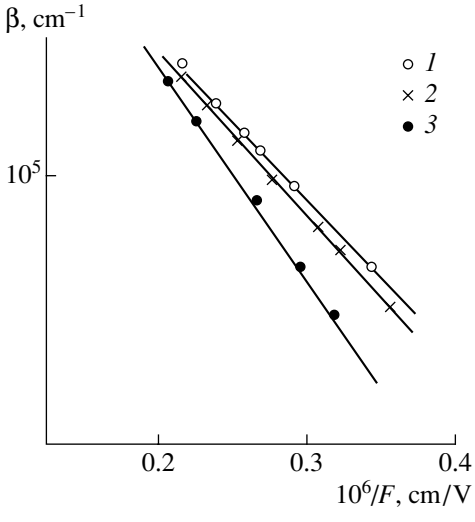

Fig. 2. Inverse field $1/F$ dependence of the hole impact-ionization coefficient for the (*1*) 6*H*, (*2*) 21*R*, and (*3*) 4*H* polytypes.

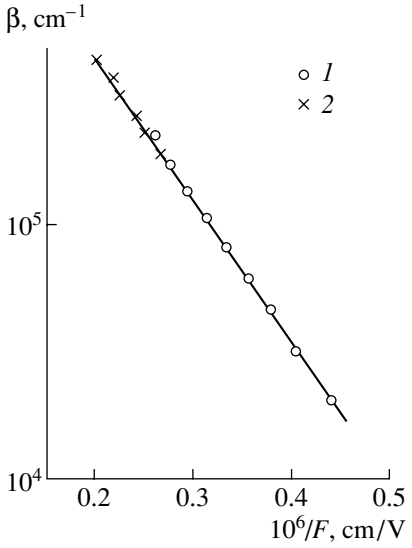

Fig. 3. Inverse field $1/F$ dependence of the hole impact-ionization coefficient for the field direction $F \perp C$. $(N_d - N_a) =$ (*1*) 1.4×10^{18} and (*2*) 3.0×10^{18} cm^{-3}.

multiplication coefficient showed that the electron and hole ionization coefficients actually differ by less than an order of magnitude. Their values of these coefficients were estimated from the expression [26]

$$\beta = M[1 + \kappa(M-1)]^{-1} dM/dw, \qquad (6)$$

where the ratio $\kappa = \beta/\alpha$ is assumed to be constant. While the exponential dependence $\beta(F^{-1})$ can be obtained for $F \parallel C$ only if $\alpha = 0$, it was obtained for $F \perp C$ at $\beta/\alpha = 2$–5; this means that II is bipolar, which is typical of a continuous band spectrum. These results point to the one-dimensional action of the NSL potential and the presence of a miniband spectrum in the conductance band only for the direction along the NSL axis. The ionization parameter F_0 is the same for both directions of the field in the dependence $\beta \propto \exp(-F_0/F)$, which is not surprising since holes ionize more efficiently for II at $F \perp C$ as well; therefore the parameter F_0 is determined by features of the valence band for both field directions.

2.3. A Study of the Avalanche Multiplication Noise

One of the most sensitive tools for determining II characteristics is the study of the avalanche multiplication noise. Experimental results are usually represented by a dependence of the noise spectral density i_s^2 on the multiplication coefficient M. According to [27], when α or β vanishes, $i_s^2 \propto M^2$ if strongly ionizing carriers are injected mainly into the multiplication region. In the case of combined injection, $i_s^2 \propto M^n$, where $n > 2$. If $\alpha = \beta$, then $i_s^2 \propto M^3$ irrespective of the ratio of initial currents. The same *p–n* structures were used for measuring the noise described in Subsections 2.1 and 2.2. The photocurrent in the sample was excited using a DRSh-500 lamp with or without a UFS-6 filter. All holes generated over the distance $W + L_p$ and all electrons generated over the distance of about $1/6W + L_e$ participated in multiplication. Here, W is the width of the *p–n*-junction space charge region, and L_p and L_e are the hole and electron diffusion lengths. $L_e \approx 0$ in the heavily doped P^+ region. Therefore, the ratio between the numbers of electrons and holes injected into the multiplication region was about 0.1. The dependence $i_s^2 = f(M)$ is presented in Fig. 4 for two samples with different breakdown voltages V_{br} (curves *1*, *2*) at $F \parallel C$ [28]. Two portions are clearly seen in curve *1*: the first one is described by the dependence $i_s^2 \propto M^{2.3 \pm 0.05}$; the second one is described by the dependence $i_s^2 \propto M^{2.6 \pm 0.05}$. Curve *2* is described mainly by the dependence $i_s^2 \propto M^{2.25 \pm 0.05}$. As was mentioned above, the ratio of the numbers of electrons and holes injected into the multiplication region was about 0.1. The unequivocal conclusion is that, in all aforementioned cases, the dependence $i_s^2 = f(M)$ characterizes the multiplication, where holes ionize more strongly than electrons; i.e., $\beta > \alpha$. Some excess over the quadratic dependence in $i_s^2 = f(M)$ stems from the small electron contribution, about 0.12, to the injection current. Estimates show that in the case of the opposite relation, i. e., $\alpha > \beta$, the power law exponent would be $n = 4$–5. $\beta > \alpha$ in the entire range of electric fields up to 4500 kV/cm for the sample with $V_{br} = 190$ V, while for the sample with $V_{br} = 70$ V, the relation between α and β changes, which is indicated by the inflection in curve *1*. The expression for the excess noise [29] at $M_p \gg M_e$ can be written as

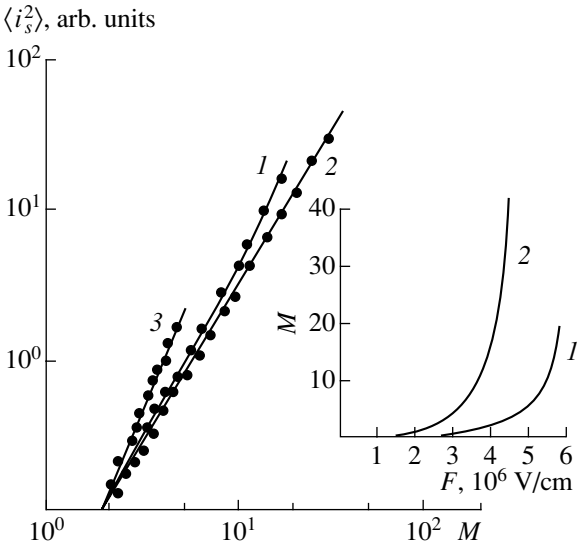

Fig. 4. Dependence of the noise spectral density $\langle i_s^2 \rangle$ on the multiplication coefficient M. (*1*, *2*) $F \parallel C$; (*3*) $F \perp C$. V_{br} = (*1*) 70, (*2*) 190, and (*3*) 41 V. In the inset: $M = f(F)$ for samples *1* and *2*.

$$Q_{\text{eff}} = \frac{M_p}{1-f}[1 - (1 - 1/\kappa)\{(M_p - 1)/M_p\}^2], \qquad (7)$$

where $f = J_{n_0}/J_t$, $J_t = J_{n_0} + J_{p_0}$, $\kappa = \beta/\alpha$, and $f \cong 0.1$. $Q_{\text{eff}} = 2.5$ for curve *2* at $M_p = 40$, and $Q_{\text{eff}} = 2.1$ in the first portion of curve *1* at $M_p = 10$. We obtain from (7) $1/\kappa \cong 0$–0.02, which actually means that $\beta \gg \alpha$ in the entire effective multiplication region up to $F_m \cong 5300$ kV/cm. We emphasize that the scatter of $1/\kappa$ values presented is a result of the insensitivity of the theoretical method to changes in $1/\kappa$ within this range.

Portion *2* in curve *1*, where $n \cong 2.6$, indicates that the electron contribution to II appears at $F_m \cong 5500$ kV/cm, but it remains smaller than the hole contribution. An estimation with the use of (7) at $M_p = 20$ yields $\kappa = 6$, which shows a tendency towards equalization of both contributions at $F_m \cong 5800$ kV/cm. This is no surprise

since the occurrence of the avalanche breakdown in these *p*–*n* junctions requires such an equalization: avalanche breakdown is fundamentally impossible if β or α vanishes. Data on the origin of the electron contribution in the case of the miniband spectrum will be obtained after a detailed study of electron transport under conditions of WSL in the pure form if the hole contribution is completely excluded. A new structure must be designed instead of the P^+–N–N^+ junction used previously. Hole ionization must dominate in the new structure, but injection of holes into the multiplication region must be excluded. That is why the inverted diode structure N^+–N–P^+ does not give the necessary effect.

The necessary structure for the study of the electron II [30] was designed, and the direct measurement of the electron contribution to II was carried out (see Subsection 4.3). It has been established [31] that, in the miniband spectrum case, electron II is not observed up to $0.9F_b$. Here, F_b is the avalanche breakdown field. Effects of the WSL clearly manifest themselves in this case, which excludes the possibility of II. However, tunneling of electrons into the upper miniband is observed at the field $>0.9F_b$, which radically changes the situation and creates conditions for the effective heating of electrons. One of the most convincing proofs of the decisive influence of the conduction miniband structure on II for $F \parallel C$ is the absence of such an influence for the direction $F \perp C$, for which there is no superstructure. The study of the avalanche noise showed (Fig. 4, curve *3*) that, for $F \perp C$, II is bipolar; this can also be deduced from the dependence $i_s^2 \propto M^{2.9 \pm 0.05}$. The obtained ratio β/α was equal to about 1–2 everywhere within the measured field range.

Thus, the results of this study showed the following:

(1) the monopolarity of II for the field direction along the NSL axis ($F \parallel C$) over a wide range of electric fields, which has no analogues in the known semiconductors;

(2) the dominant hole contribution to II for $F \parallel C$;

(3) the bipolarity of II for $F \perp C$; and

(4) the determining influence of the conductance miniband structure and WSL on the II features for $F \parallel C$.

2.4. Hole Ionization in Silicon Carbide Polytypes

The thoroughly studied II in the 6*H*-SiC-polytype could act as a kind of model for the comparative analysis of II in other SiC polytypes. This allowed us to ascertain the character of II carrying out a minimal number of experiments. Precisely in such a manner [23] were results for four more SiC polytypes (4*H*, 10*H*, 15*H*, 21*R*) for the electric field direction $F \parallel C$ (Fig. 2) obtained. Similarly to the case of 6*H*-SiC, the formula for the bipolar ionization did not yield meaningful results and the processing of the obtained experimental data on photomultiplication was conducted using formula (22) for the monopolar ionization. The curves $\beta = f(1/F)$ (Fig. 2) are similar to one another. Therefore, II for all polytypes mentioned above is predominantly monopolar and is effected by holes within the indicated field range F_m = 1000–5000 kV/cm.

The experimental data are described by the exponential function $\beta \propto \exp(-F_0/F)$, where F_0 is a characteristic field. We can give the following theoretical interpretation of the dependence obtained [25]. Notice that the coefficient β is proportional to the integral

$$\beta(F) \propto \int_{\varepsilon_i}^{\infty} W_i(\varepsilon) f(p, F) d^3p/(2\pi\hbar)^3, \qquad (8)$$

where ε_i is the II threshold energy, $W_i(\varepsilon)$ is the II probability, and $f(p, F)$ is the momentum distribution function (DF) for holes. Since the DF falls exponentially with increasing energy, the integral (8) is proportional to the DF value at the II threshold; i.e., $\beta(F) = f_0(\varepsilon_i, F)$ (f_0 is the symmetric part of DF).

Similarly to [32], we used the calculation method for the DF asymptotic behavior in the system of two heavy- and light-hole subbands. The mean free path is large in the latter subband; therefore, heating of the hole gas occurs in the light-hole subband. The heating is ballistic; i.e., the holes, which avoid collisions with phonons, acquire higher energies. The number of such holes, i.e., the asymptotic value of the DF, is determined by the ballistic transit probability, which equals $\exp\left[-\frac{1}{e}\lambda_i^{-1}(\varepsilon')d\varepsilon'\right]$. Then, we obtain the following expression for the II coefficient:

$$\beta(F) = \alpha_\infty \exp(-F_0/F), \qquad (9)$$

where

$$F_0 = \frac{1}{e}\int_0^{\varepsilon_i} \frac{d\varepsilon'}{\lambda_i(\varepsilon')}.$$

The mean free path λ_i is determined by scattering from the light-hole subband into the heavy-hole subband (scattering within the light-hole subband is significantly weaker because of the small density of states in this subband). The role of the light-hole subband in SiC polytypes is played by the subband Γ_i split off by the crystal field. The valence band splitting by the crystal field equals Δ = 53 and 83 meV for 6*H* and 4*H* [33, 34], which is much less than E_g. We calculated $\lambda_i(\varepsilon)$ assuming scattering by optical phonons with energy $\hbar\omega$ and the deformational potential interaction. We neglect the distinction between frequencies of transverse and longitudinal optical phonons. Notice that the valence band edge structure in SiC is rather complex: we have spin–orbit and crystal-field splitting of the energy levels, and pronounced anisotropy of the spectrum near the edge. However, the influence of all of the aforementioned factors on the light-hole band is appreciably weakened at large energies $E > E_g$, which are the most interesting.

This allows us to restrict ourselves to the spherically symmetric Hamiltonian and neglect the terms accounting for the valence-band splitting by the spin–orbit coupling and the crystal field. The three Bloch amplitudes $v_1 = X$, $v_2 = Y$, and $v_3 = Z$ are related to the point $p = 0$; they are transformed as the corresponding coordinates. Omitting the details of calculations, we present the final results. The mean free path is given by

$$\lambda_i^{-1} = \frac{d_0^2 m_l^{1/2} m_h^{3/2}}{2a^2\hbar^2\rho\hbar\omega}, \quad (10)$$

where ρ is the crystal mass density, a is the lattice constant, d_0 is the deformation potential, and m_l and m_h are the light- and heavy-hole masses. Only spontaneous emission of optical phonons was taken into account in the derivation of (10); i.e., it was assumed that $kT \ll \hbar\omega$. The following expression was obtained for F_0:

$$F_0 = \frac{d_0^2 m_h^{3/2} m_l^{1/2} E_g}{2a^2 e\hbar^2\rho\hbar\omega}. \quad (11)$$

Comparison of F_0 with experimental data is made difficult by a lack of data on m_l. Therefore, we can use our knowledge of $F_0 = 12000$ kV/cm and obtain for the m_l magnitude $\sim 0.15m_0$, which is in good agreement with the usually observed ratio m_l/m_h in other semiconductors. This comparison is quite appropriate since there is no miniband splitting in the valence band. The following values of SiC parameters were used in the calculations: $\rho = 3.2$ g/cm^3, $m_h = 1.6m_0$, $E_g = 3.065$ eV [33], $\hbar\omega = 110$ meV [33], and $d_0 = 69.3$ eV.

Thus, this theory satisfactorily describes the hole II in SiC and additionally confirms the validity of the above interpretation of the experimental data for SiC polytypes. Suppression of the electron contribution to II occurs according to this interpretation due to the miniband structure of the conductance band of the SiC polytypes.

The obtained dependence of the hole II is satisfactorily described by the theoretical model used previously for the valence band of other semiconductors, in particular, the III–V ones. This additionally confirms the statement that the valence band in SiC polytypes, in contrast to the conduction one, is free from pronounced miniband-structure features.

3. AVALANCHE BREAKDOWN IN SILICON CARBIDE POLYTYPES

Avalanche breakdown (AB) is one the most important processes in semiconductors. It differs from other kinds of electric breakdown in that it occurs due to electron and hole II with approximately equal efficiency, $\alpha \approx \beta$. Then, starting from the single ionization event, the process becomes self-sustained. The current–voltage (I–V) characteristic of the p–n structure will actually be a vertical line showing a sharp increase in the current. If α or β vanishes, the II process will not be self-sustained, and the current increase with the voltage will have a monotone, perhaps exponential, character. The AB voltage and field magnitudes determine the limiting parameters of various low- and high-power, low- and ultra high-frequency devices. The AB in silicon carbide was studied before this study was initiated [35, 36]. The authors of those studies pointed to two features: (i) the breakdown had a microplasma character; (ii) the dependence of the breakdown voltage on the donor-impurity concentration was less steep than in most semiconductors; and (iii) the breakdown voltage was anomalously high: it exceeded the voltages estimated from the dependence $V_b = f(E_g, N_d - N_a)$ by more than twofold, but did not reach the maximum values due to the microplasma breakdown.

The authors of [35, 36] could not explain the second and third features. Undoubtedly, for this, they needed the data on II that would become the physical grounds for the interpretation of the results of investigating the AB in this study. The specificity of the electron-gas heating under miniband-spectrum conditions is the main cause for numerous anomalies of AB, which will be discussed below. The main constituents of this work are the comparative studies of AB in the 4*H*, 6*H*, 8*H*, 10*H*, 15*R*, 21*R*, and 27*R* polytypes, which serve as objects possessing different NSL parameters, and in one polytype but with the perpendicular electric field direction.

3.1. Avalanche Breakdown in the Silicon Carbide Polytypes at Different Temperatures of the Lattice

The AB is a process occurring at limiting (for a given sample) voltages and sufficiently strong currents; therefore, a noticeable heat generation and temperature rise are inevitable. Whether the temperature arbitrarily rises or whether there will be a tendency to stabilization is determined mainly by the temperature dependence of the AB voltage. Most semiconductors have a so-called positive temperature coefficient for the AB voltage (TCABV), which means that the breakdown voltage increases with temperature; this is a factor stabilizing the AB. The mechanism of this effect implies that the scattering intensity increases with temperature and, hence, the charge-carrier mean free path decreases, which leads to the field increase and, accordingly, to an increase in AB voltage. Intense interest in the study of AB in silicon carbide was stimulated by the presence of large breakdown fields and the prospect of designing power avalanche transit-time diodes. Therefore, knowledge of the temperature features of AB was also absolutely necessary for applications. The results of the study of AB temperature dependence in 4*H*, 6*H*, 10*H*, 15*R*, and 21R silicon carbide polytypes [17, 23] using no less than 30 samples with a varying donor impurity content are indicative of a negative value of TCABV (Fig. 5 and Table 1.). The negative TCABV is obviously due to the specificity of the electron-gas heating. As

Table 1

SiC polytype	Band gap, eV $T = 300$ K	Avalanche-breakdown field F_m, $F \parallel C$, 10^6 V/cm	Avalanche-breakdown field F_m, $F \perp C$, 10^6 V/cm	TCBV, $F \parallel C$, 10^4 K^{-1}	TCBV, $F \perp C$, 10^4 K^{-1}
4*H*	3.25	5.9 (V_b = 90 V)		–4.6	
6*H*	3.065	5.5 (V_b = 78 V)	3.7 (V_b = 41.7 V)	–3.25	1.5
10*H*	3.095	4.6 (V_b = 55 V)		–1.4	
15*R*	2.995	5.4 (V_b = 76 V)		–1.93	
21*R*	2.865	4.7 (V_b = 57 V)		–1.2	

was shown above in Subsection 2.2, the electron II coefficient $\alpha \approx 0$ up to a certain value of the field; a further increase in the field causes α to increase until the magnitude of about β is reached. The mechanism of electron heating under conditions of the miniband spectrum implies that the energy of the motion perpendicular to the field $E(k_\perp)$ can increase owing to the energy of the motion along the field $E(k_\parallel)$. The electron gains the energy moving along the field within the first miniband and then pumps this energy into $E(k_\parallel)$ due to phonon scattering; the $E(k_\perp)$ spectrum is continuous. Monte Carlo simulation has shown [37] that the energy $E(k_\perp)$ reaches a maximum value approximately equal to the first miniband width E_1 and does not change with a further increase in the field. Then, $E(k_\perp)$ reaches a magnitude of (3–4)E_1 and also stops depending on the field. The same problem was solved [38] analytically and an expression for the electron temperature was obtained as $T_e = T[1 + (E_1/\hbar\omega)^2]$, where T is the lattice temperature and $\hbar\omega$ is the optical-phonon energy. This expression implies that the efficiency of heating in the miniband increases with increasing lattice temperature. However, estimation of the electron temperature yields a value which is much less than that necessary for ionization. Therefore, this channel of heating can be considered as the first phase of the process. The proper conditions for heating leading to II are attained after electron tunneling into the upper miniband whose width is much larger than that for the lowest miniband; this, in fact, removes an obstacle for effective electron-gas heating up to the level necessary for II. Thus, consideration of the possible model for the electron-gas heating shows that the intensity of the electron heating in the superlattice for the field directed along its axis increases with temperature. Therefore, the negative TCABV observed in SiC polytypes at $F \parallel C$ is quite natural and corroborates the miniband character of the electron spectrum in SiC polytypes. In order to make the above interpretation more convincing, it was necessary to show that TCABV was positive in samples with $F \perp C$. Otherwise, this interpretation could be ambiguous. Notice that the samples for the $F \parallel C$ and $F \perp C$ cases were cut from the same crystal to exclude the influence of differences in the impurity content in the samples. It is known that negative TCABV is observed in semiconductors doped with deep-level impurities. TCABV in the samples with $F \perp C$ proved to be positive (Fig. 5 and Table 1). This simple and unequivocal result is a rather convincing argument in favor of the proposed electron-heating mechanism in an NSL of silicon carbide polytypes.

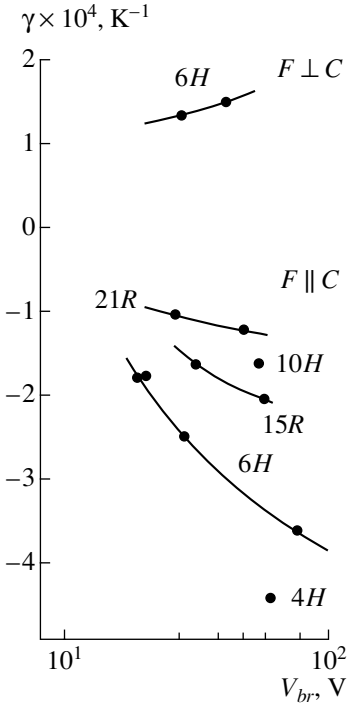

Fig. 5. Dependences of the breakdown-voltage temperature coefficient $\gamma = (dV_{br}/dT)/(1/V_{br})$ on V_{br} in samples of various polytypes at two field orientations: $F \parallel C$ and $F \perp C$.

3.2. Dependences of the Breakdown Voltage on the Donor Impurity Concentration, Electric-Field Orientation, and the Band Gap

According to a universal but empirical formula [39] which is valid for most semiconductors, the breakdown voltage (BV) of an abrupt asymmetric *p*–*n* junction is given by the following function:

$$V_b \cong 60(E_g/1.1)^{3/2}[(N_d - N_a)/10^{16}]^{-3/4}, \qquad (12)$$

where E_g is measured in electronvolts; $N_d - N_a$ is measured in cm^{-3}; and V_b, in volts. It was mentioned above that in [35] the dependence $V_b = f(N_d - N_a)$ is flatter in comparison with other semiconductors. The results obtained in this study indicate the following.

1. The dependence $V_b = f(N_d - N_a)$ for $F \parallel C$ almost coincides with (12) (Fig. 6) [23].

2. The dependence $V_b = f(N_d - N_a)$ for $F \perp C$ is somewhat flatter than in [23], but is also rather close to (12) (Fig. 6). The coincidence with (12) observed for $F \parallel C$ does not contradict the offered model of AB. The physical causes leading to the dependence $V_b = f(N_d - N_a)$ are valid in the conditions of the semiconductor with NSL. With respect to the flatter dependence for $F \perp C$, additional scattering centers due to a higher density of dislocations in the (1120), plane mentioned in Section 2.2, may be the reason for this.

The BV for $F \parallel C$ is five-to-seven times higher than the estimate made using (12) and higher than in [35, 36] by 15–30% (Fig. 7). The latter is due to the homogeneity of AB in our *p–n* structures. The anomalously high BV in SiC polytypes for $F \parallel C$ is qualitatively explained in terms of the proposed model of AB. The BV for a semiconductor with a miniband structure of the electron (hole) spectrum depends not only on E_g, but also on parameters of the miniband spectrum E_1 and E_2. It has been shown in Section 2.3 that there exists a wide range of fields where $\alpha \approx 0$, and the latter very rapidly increases only near the breakdown. The activation mechanism of the electron contribution to II was considered in Section 2.2. The excess increase in the AB electric field and voltage appears due to the interval between the electric-field values where $\alpha \approx 0$ and $\alpha \neq 0$.

The AB voltage for the *p–n* structure at $F \parallel C$ is two-to-three times lower than at $F \perp C$ (Fig. 7). Notice, however, that even in this case this voltage exceeds the AB voltage magnitude estimated using (12) by more than twofold.

Certain features of the electron heating in NSL lead to the nontrivial dependence of the BV on the band gap. According to the above, electron heating depends on the width of the first miniband, the minigap between the first and second minibands, or on the entire miniband structure. Therefore, BV is not only a function of the band gap, but also of the miniband structure. Since there is no direct correlation between these factors, the anomalies presented in Fig. 8, where BV in the 10*H* polytype with a wider band gap than in 15*R* and 6*H*, are determined by two independent factors: first, the wider band gap must give larger V_{br}; second, the miniband structure in 10*H* is favorable for the effective heating decrease V_{br}. The latter factor is more important in the case of 10*H*; as a result, V_{br} surprisingly falls.

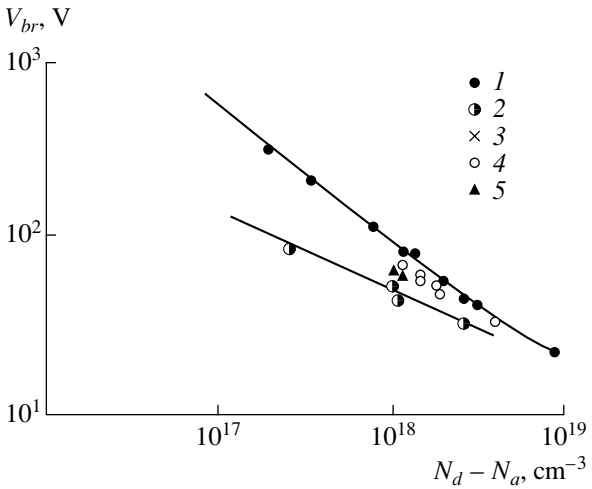

Fig. 6. Dependence of the breakdown voltage for (*1*, *2*) 6*H*, (*3*) 4*H*, (*4*) 21*R*, and (*5*) 10*H* on the concentration in the base $N_d - N_a$. (*1*, *3–5*) correspond to $F \parallel C$, and (*2*) corresponds to $F \perp C$.

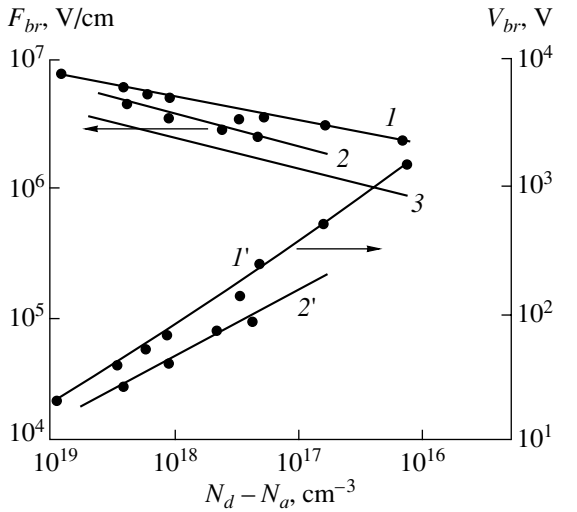

Fig. 7. Dependences of the (*1–3*) field F_{br} and (*1'*, *2'*) voltage V_{br} on the concentration in the base $N_d - N_a$ for the 6*H*-SiC polytype. (*1*, *1'*) represent F_{br} and V_{br} for $F \parallel C$; (*2*, *2'*) represent F_{br} and V_{br} for $F \perp C$; and (*3*) represents F_{br} using formula (12).

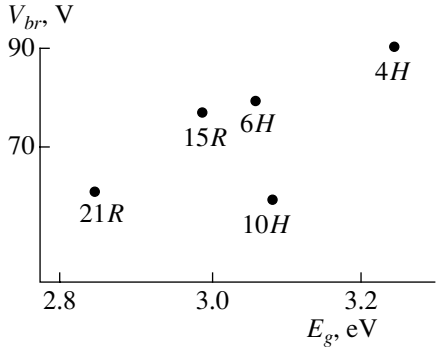

Fig. 8. Breakdown voltage in SiC polytypes with different band gaps.

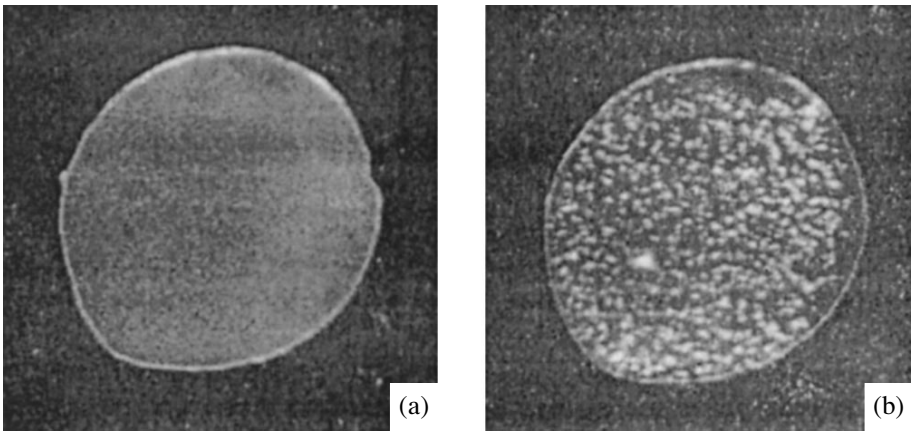

Fig. 9. Light emission at the avalanche breakdown in a 6*H*-SiC abrupt *p–n* junction: (a) uniform emission, and (b) with segregation of the electron–hole plasma.

3.3. Forming of Dissipative Structures and Pinching of the Current under Avalanche Breakdown

The distribution of the electron–hole plasma (EHP) in the *p–n*-junction plane can be visually examined using the EHP emission in the visible range of the spectrum (light-blue glow). The experimental study of EHP created in the reverse-biased *p–n* junction shows that EHP segregates in the *p–n*-junction plane in the case of $F \parallel C$ beginning with the current density $J > J_c \approx$ (10–20) A/cm^2 [40–42]. Segregation manifests itself in the replacement (as the current increases) of a uniform distribution of breakdown across the area (Fig. 9a) by a nonuniform one (Fig. 9b). The glow brightness of EHP increases at some spots and decreases at others with increasing current; at $J \geq 100$ A/cm^2, the pattern of the breakdown is a large array of bright spots against a dark background. The size of the spots and the distance between them are about 1–4 μm. Under the pulsed mode, the character of the pattern does not depend on the pulse duration within the range $\tau_p = 10^{-5}$–10^{-7} s and is determined only by the magnitude of current density. The differential resistance of samples within the range of currents where segregation of the EHP occurs is positive. An increase in the lattice temperature T_1 from 300 to 600 K causes an approximately twofold rise in J_c. In contrast, cooling of the sample causes a decrease in J_c, but at $T_1 < 230$ K, segregation of the EHP is not observed until $J = 500$ A/cm^2. With a deviation of the *p–n*-junction electric-field direction from the NSL axis by more than 10°, segregation is not observed and EHP remains homogeneous up to $J = 500$ A/cm^2.

Notice that the observed effect of EHP segregation occurs only in sufficiently homogeneous samples, where the breakdown is not related to the character of the microplasma but occurs homogeneously over the entire *p–n*-junction plane at small currents. In samples with a small quantity of microplasma, the segregation of EHP occurs only in homogeneous domains of the structure (outside of the microplasma).

As shown in Section 2.1, heating under conditions of the miniband spectrum occurs due to phonon scattering. However, the electron density n increases with increasing current density and the electron–electron collision rate increases. During such collisions, as is the case for electron–phonon ones, the energy of transverse motion increases; i.e., the density of hot electrons increases and, therefore, the II rate ν_i increases with n. The observed segregation is likely related to the appearance of an increasing ν_i dependence on n at high current densities. We will show below that, notwithstanding the insignificant number of electron–electron collisions in comparison with electron–phonon collisions in the electron heating process, the contribution of the former collisions to the instability of the EHP spatial distribution is dominant. This case is a prominent example of the role of the small (in absolute value) but nonlinear factor in the determination of the synergetic evolution scenario of a process.

Distributions of the electron density and the voltage drop $\tilde{V}$ over the *p–n*-junction plane (x and y axes) are approximately described by the continuity equation

$$\frac{dn}{dt} = D\Delta_\perp n + n\nu_i(n, \hat{V}) - \frac{n}{\tau_r(n, \tilde{V})} - \frac{n}{\tau_n} \qquad (13)$$

and the current density balance equation for the number of particles

$$c\frac{d\tilde{V}}{dt} = \sigma\tilde{W}\Delta_\perp\tilde{V} - en\nu_n + (V - \tilde{V})/\rho, \qquad (14)$$

where D is the bipolar diffusion coefficient; $\tau_n = w|\nu_n|$; w is the space charge region (SCR) width in the *p–n*-junction; ν_n is the electron drift velocity; $\rho = W/\sigma$; W and σ are the thickness and conductivity of the semiconductor base (quasi-neutral region of the structure); $\tilde{W}$ is the effective thickness that is characteristic of the

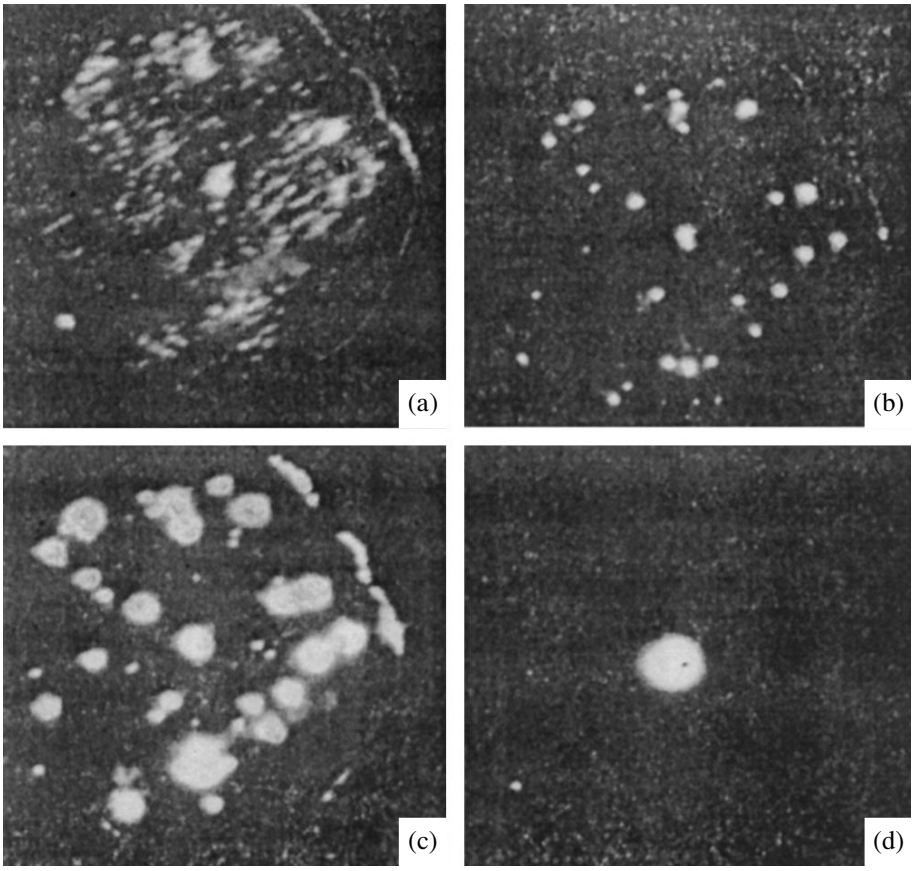

Fig. 10. Kinetics of avalanche-current filaments for the pulse durations of (a) 0.2, (b) 1.2, (c) 7, and (d) 100 μs.

transverse current spreading in the base ($\tilde{W} \le W$); τ_r is the carrier recombination time in the SCR; V is the total voltage at the structure; c is the reduced capacitance of the p–n junction; and $\Delta_\perp = d^2/dx^2 + d^2/dy^2$ (the Z-axis is chosen in the direction of the NSL axis). Linearizing (13) and (14) with respect to small fluctuations $\delta\tilde{V}$, $\delta n \propto \exp(ik_\perp \mathbf{r}_\perp - \gamma t)$ near the initial homogeneous state $\tilde{V} = \tilde{V}_h$ and $n = n_h$, we obtain the dispersion equation. An analysis of this equation shows that the EHP density and current density over the p–n-junction plane are unstable ($\mathrm{Re}\gamma < 0$) under the positive differential conductance of the structure, i.e., at

$$\xi < \Gamma\rho J_h/\tilde{V}_h, \tag{15}$$

with respect to homogeneous fluctuations with the frequency

$$\mathrm{Im}\gamma = \omega_0 = (c\tilde{V}_h\tau_h/J_h)^{-1/2}(\Gamma - V_h\xi/\rho J_h)^{1/2}, \tag{16}$$

when

$$\xi > \xi_w = \tau_n, \tag{17}$$

where $\xi = d\ln v_i/d\ln n$, $\Gamma = d\ln v_i/d\ln\tilde{V}$, and we take into account that usually $\tau_r \gg \tau_n$.

If the condition (17) is not satisfied, the aperiodic instability ($\mathrm{Im}\gamma = 0$) of EHP towards fluctuations with wave numbers near

$$k_\perp = k_0 = (l_\perp L)^{-1/2}\Gamma^{1/2}, \tag{18}$$

when

$$\xi > \xi_c, \tag{19}$$

where ξ_c is determined from the equation

$$\xi_c = (l_\perp^2/\tilde{W}W) + (2l_\perp/L)(\Gamma - \xi_c\tilde{V}_h/J_h)^{1/2}, \tag{20}$$

$J_h = en_h|v_n|$, $l_\perp = (D\tau_n)^{1/2}$ is the characteristic bipolar diffusion length for carriers in the x and y directions of the p–n-junction SCR, and $L = (\sigma\tilde{W}\tilde{V}_h/J_h)^{1/2}$ is the characteristic length for a change in the voltage drop across the p–n-junction (for inhomogeneous perturbations of $\tilde{V}$ near $\tilde{V} = \tilde{V}_h$). Using the characteristic values $\sigma = 20\ \Omega^{-1}\ \mathrm{cm}^{-1}$, $W = 3\times10^{-2}$ cm, $\tilde{V}_h = 50$ V, $J_h = 20$ A/cm^2, $w = 2\times10^{-5}$ cm, $v_n = 10^6$ cm/s, $c = 2\times10^4$ pF/cm^2, and $D \approx 1$ cm^2/s, as well as assuming that $\tilde{W} \approx 2\times10^{-3}$ cm and $\Gamma \approx 100$, we obtain $\xi_c = 2\times10^{-4}$, $\xi_w \approx 1$; i.e., EHP segregation condition (19) is significantly milder than the condition for oscillation onset (17). Thus, EHP seg-

regates at small $\xi > \xi_c = 10^{-4}$. These values correspond to small n and J. According to (18), the critical fluctuation period $L_0 = \pi/k_0 \approx 3 \times 10^{-4}$ cm, which is consistent with the experimentally observed distance between the bright spots of the segregated EHP. Segregation of the avalanche current is related to the fact that at a small local increase in the avalanche current in the region of size $d \approx k_0^{-1}$ ($l \ll d \ll L$), the II rate increases in this region, which, in turn, leads to an increase in the avalanche current density.

Such avalanche-like increase in the avalanche current in the region with the size $d \ll L$ is not quite suppressed by the voltage drop across the quasi-neutral regions of the structure due to pronounced current spreading over these quasi-neutral regions. This is precisely the cause of the avalanche current segregation observed under positive differential resistance of the p–n structure: the uniform avalanche current increase is completely suppressed by the proper uniform decrease in the voltage drop across quasi-neutral regions.

In the above consideration, the Joule heating of the p–n structure due to supplied power $P = IV$ was not taken into account. This is valid for the static conditions with small currents and a good heat sink. At larger currents, the pulsed mode was used.

If the Joule heating cannot be neglected, the evolution of the avalanche current filaments in the static mode and the kinetics of the avalanche current segregation will radically differ from those considered above. This stems from the fact that BV decreases and the ionization rate increases with temperature. It was ascertained using computer simulation [42] that this decrease in the avalanche BV leads to the situation where the size or diameter of current filaments increase and where the filament number decreases with increasing current and, therefore, temperature. Ultimately, beginning with some rather large current $I = I_f > I_c$, all current filaments merge into a single filament forming a single current pinch and a small-magnitude negative differential conductance appears in the system [43].

However, many qualitative features of this pinch are radically distinct from thermal pinches forming in different distributed systems under the conditions of thermal instability [44]. Thus, this ionization pinch does not contract, but expands with increasing total current, and the current density in the pinch center decreases [43]. These qualitative distinctions of the ionization pinch under consideration from the thermal one are related to the fact that the existence of the ionization pinch and the multiple filaments in the absence of marked Joule heating are due to the dependence of v_i on n. As a result of the incidental local overheating of one of the filaments, the current in this filament begins to increase due to the redistribution of current from the nearest filaments and, thus, their number decreases. Here, the Joule heating of the lattice plays a secondary role inducing the transformation of numerous current filaments into a single filament, i.e., the current pinch. These qualitative conclusions concerning the effect of Joule heating of the lattice on the properties of the current filaments are confirmed by the experimental (Figs. 10a–10d) and numerical study of the current segregation kinetics [42].

The system considered belongs to the class of active systems with diffusion; a nonlinear theory of the dissipative structures in these structures was developed in [45, 46]. The possibility of forming complex stable 2D static structures that were observed in this work was noted in [46]. However, the mechanism of EHP segregation and formation of dissipative structures considered in this study is being proposed for the first time.

4. QUANTUM-MECHANICAL TRANSPORT IN THE NATURAL SUPERLATTICE OF SILICON CARBIDE POLYTYPES

Two principal conclusions were drawn after the study of the II and AB in eight SiC polytypes.

1. The electron spectrum of the uniaxial SiC polytypes in the NSL axis direction has a pronounced miniband structure. Quasi-free electron transport in the range of medium electric fields from 1000 to 2500 kV/cm is, in fact, suppressed by the WSL processes.

2. No features related to the effect of WSL were detected in the hole spectrum. The hole transport within the mentioned field range is quasi-free.

However, II and AB are present in the final stage of the WSL process. This process begins at much lower fields, where, according to theoretical predictions, many interesting effects should be observed.

A result of development of the WSL problem in crystals is widely known as transformation (due to action of the electric field) of the continuous band spectrum into the spatially localized states with discrete levels known as the Wannier–Stark ladder [3]. The distance between the levels is given by

$$\Delta E = eFd. \tag{21}$$

Here e, F, and d are the electron charge, the electric field, and the SL period, respectively.

The experimental observation of the WSL effects is possible using only a superlattice (SL) in which the charge carrier spectrum consists of narrow subbands known as minibands. A family of WSL effects related to the appearance of the negative differential conductivity (NDC) in such objects was theoretically predicted.

The basic possibility of obtaining NDC related to the field-induced localization in an artificial SL was shown in [4]. The threshold field for the onset of NDC was determined as

$$eF_t d > \hbar/\tau, \tag{22}$$

for the Esaki-Tsu (E-T) criterion, and

$$eF_t d > 2\pi\hbar/\tau, \tag{23}$$

for the Bloch oscillation (BO) criterion. Here, $\hbar$ and τ are Planck's constant and the electron scattering time, respectively; and d is the SL period. Criteria (22) and (23) imply that the NDC related to these effects appears when the oscillation frequency $eF_t d/\hbar$ or $eF_t d/2\pi\hbar$ exceeds the scattering rate. Notice that it is difficult to attribute the experimentally observed NDC characterized by a threshold field F_t to one of the mentioned effects without a knowledge of the scattering time τ magnitude at high fields. In order to estimate it, we studied the electron drift velocities using a special technique. The drift velocity is an important transport characteristic and is related to scattering time by known analytic expressions.

The Stark energy eFd is so small in the effect considered above that the quasi-continuity of the first band is preserved; i.e., many Stark levels can reside within the band width. The size of the electron localization $L \approx E_1/eF$ decreases with a further increase in the field. Here, E_1 is the first-miniband width. The miniband in this case is destroyed and the spectrum takes the form of a series of discrete energy levels. The electron transport in such a system is described theoretically in [47, 48]. Conduction is possible in this range of fields due to phonon-assisted jumps between the discrete Stark levels. NDC related to resonance phonon transitions was predicted. Resonance fields are defined as

$$eFdn = \hbar\omega. \tag{24}$$

Here, $\hbar\omega$ is the relevant phonon energy and n takes values 1, 2, 3….

At higher electric fields, the Stark energy attains such a magnitude that only a single level exists within the miniband width. This case was considered theoretically in [49]. The NDC effect was predicted with the threshold field

$$F = E_1/2ed. \tag{25}$$

One more possible conduction mechanism in the WSL mode is the resonance interminiband tunneling considered in [50]. This occurs if the Wannier–Stark ladder spacing eFd equals the energy gap between the first and second minibands E_{12}:

$$eFd = E_{12}. \tag{26}$$

In this work, we proposed an object which is radically distinct from those used previously for the study of the WSL: NSL that is contained in most of SiC polytypes. The next natural step in developing these studies consisted in trying to observe the WSL effects directly in the electron transport by studying the high-field I–V characteristics of crystals containing NSL. The above results imply that success here depends on the possibility of obtaining a pure electron current since the hole contribution, which is not influenced by the WSL, obscures the features of I–V characteristics and prevents the observation of the sought-for effects. An attempt to solve this problem in the simplest way, i.e., using SiC with the n-type conduction, failed. Difficulties were due to an intolerably high current density at fields $F > 10^5$ V/cm, the influence of contacts, and nonuniform field distribution in the sample. As a result, an ingenious experimental structure satisfying all basic requirements was designed.

4.1. Experimental

The n^+–p^-–n^+ triode structure, which was developed for the study of electron transport in silicon carbide at high fields, has some important features that distinguish it from a conventional transistor; these features must be discussed separately [30, 51].

The main element is a base doped with a deep-level acceptor impurity (scandium) with an ionization energy $E > 0.5$ eV. This allows us to attain the hole concentration $p \approx 10^{10}$ cm^{-3} at room temperature, and, therefore, the real formula of the structure is n^+–π–n^+. The characteristic deionization time for such an impurity in the SCR at $p \approx 10^{10}$ cm^{-3} exceeds 10^{-2} s. This means that the forward-biased n^+–π junction can be turned on only with the dc voltage or with pulses of duration $t > 10^{-2}$ s. However, injection, which is really an inertialess process, can be induced with short pulses of duration $t < 10^{-6}$ s after lowering of the potential barrier.

Let us now consider the collector π–n^+ junction. Under reverse bias, the establishment of an electric field in the base is determined by the process of deep acceptor-impurity ionization, the duration of which is also long enough. Therefore, if the reverse bias is applied using fairly short pulses, the acceptor levels in the base remain neutral, and the hole density, as was mentioned above, does not exceed 10^{10} cm^{-3}, which corresponds to screening of the electric field at a length larger than 10^{-1} cm. Thus, for a base width of about 5–10 μm, the field screening is only slight and the field in the base can be considered as uniform. The field is defined as $F = V/w$, where V is the voltage pulse amplitude across the base and w is the base region width.

The principle behind the operation of the described structure is as follows. The reverse pulse bias V_p with a pulse repetition time $t_p \approx 10^{-7}$ s is applied across the collector and emitter. The direct dc bias V_B is applied to the emitter–base junction. The related emitter–base current hardly influences the injection level because of large p-region resistance (10^7–10^8 Ω). This bias is used to lower the contact-barrier height. The pulsed voltage applied across the collector and emitter provides a uniform electric field, which, upon spreading through the base, reaches the forward-biased emitter junction and induces a controlled injection. The injection current increases with V_p, but it can be limited by V_B. The base-region resistance decreases by 10^3–10^4 times due to the pulse-current effect, because the electrons injected into the base are pulled by the field, flow through the base, and reach the collector. In this way, barrier-injection transit-time current transport is accomplished in the

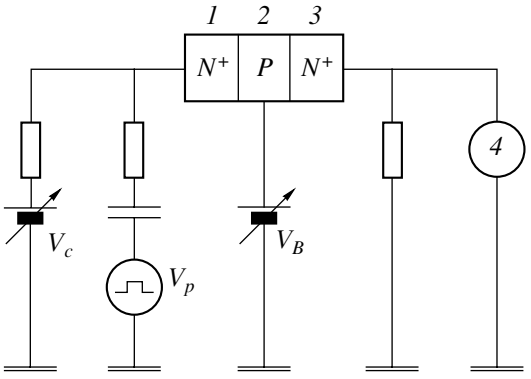

Fig. 11. The circuit used in measurements. (*1–3*) Represents the structure, and (*4*) oscilloscope.

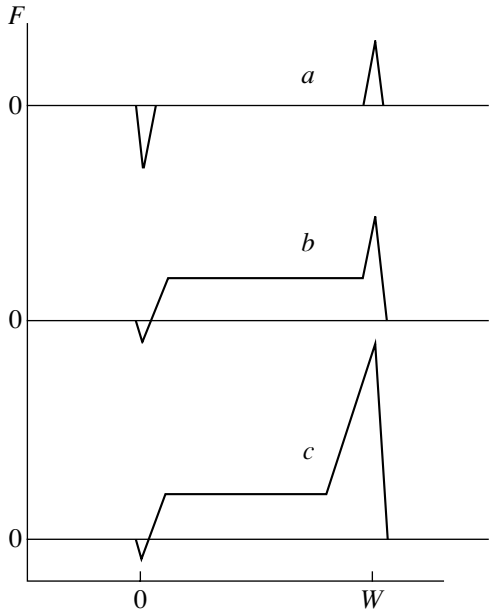

Fig. 12. Field *F* distribution in the active region of the bipolar triode structure: (*a*) $V_p = 0$, $V_B = 0$, and $V_c = 0$; (*b*) $V_p \neq 0$, $V_B \neq 0$, and $V_c = 0$; and (*c*) $V_p \neq 0$, $V_B \neq 0$, and $V_c \neq 0$.

experimental structure. The electric circuit described corresponds to a common-emitter transistor (Fig. 11). The electric field distribution in the structure for the initial state without a bias and for two operating modes is shown in Fig. 12. Thus, purely electron current, controlled by the dc bias, which does not influence the field in the base, flows through the base, i.e., the operative volume of the structure. The field is almost uniform along the whole width of the base.

All the aforementioned prerequisites, necessary for the study of electron transport in high fields under WSL conditions, are realized in the proposed experimental structure:

(1) the measured current is purely electronic;

(2) the electric field in the sample is uniform;

(3) the current through the sample can be controlled independently of the field;

(4) the field in the operating region is parallel to the NSL axis for all studied polytypes, $F \parallel C$; and

(5) the charge transport mechanism is of the barrier-injection transit-time type.

Notice that it is the properties of such a structure that ensure a current density less than 100 A/cm^2 at fields far exceeding 100 kV/cm. This, along with the perfection of the NSL crystal structure, allowed us to observe NDC in the static mode.

This experimental structure was described by us for the first time in [30]. Although the triode structure is more complex than the diode one, later on, because of the same circumstances and requirements, the triode structure was used in a study [14] by an American team of scientists.

Films of the 4*H*-, 6*H*-, 8*H*-, 15*R*- and 21*R*-SiC polytypes doped with scandium were grown for the fabrication of the described experimental structure on the *n*-type substrate by the sublimation sandwich method. Notice that the problem of controlled growth for one or another polytype has not been practically solved and the search for the necessary object requires choosing from a large number of samples. An n^+-type layer of thickness 1–2 μm was then grown on the *p*-type film. The base layer thickness was determined by the direct measurement of the width of the luminescence zone; radiation was emitted from the side plane of the manufactured three-layer structure. The base layer thickness was usually about 5–10 μm. The experimental structure was than manufactured using the photolithography technique. The collector, base electrode, and emitter diameter were equal to 420, 400, and 200 μm, respectively.

The emitter circuit current was fixed during the process. The base bias was kept constant when the pulse voltage changed. In addition, the dc currents in the emitter and base circuits were monitored in order to observe the state of the experimental structure.

4.2. Wannier–Stark Localization in the SiC Polytypes

The connection in this case is as shown in Fig. 12b. The results obtained from measuring the N-shaped *I–V* characteristics for 4*H*-, 6*H*-, and 8*H*- SiC polytypes are presented in Fig. 13 [52–58]. Threshold fields of the onset of the *I–V* dropping characteristic, i.e., where the NDC begins, were contained in various samples: 8*H* $F_t \approx 1.1 \times 10^5$ V/cm, 6*H* $F_t \approx 1.5 \times 10^5$ V/cm, and 4*H* $F_t \approx 2.9 \times 10^5$ V/cm. F_t was determined with an error of about 10% due mainly to error in measuring the base-layer width. It can be seen from Fig. 13 that the obtained *I–V* characteristics are similar, but the threshold fields are radically different. Note that the structures with the most pronounced *N*-shaped *I–V* characteristics are presented in Fig. 13. In some samples, the current drop did not exceed 20%. In addition, uncontrollable

current leakage and microplasma breakdown prevented observation of the above effect in many cases. The *I–V* characteristics of 30% of the samples remained monotonic up to the breakdown fields [55].

The scattering time τ near the threshold is necessary for numerical estimations using (22) and (23). Results of measuring the saturation electron-drift velocity v_s for $F \parallel C$ are used for such estimations, which will be discussed in detail in Section 4.5. The electric fields F_s such that the drift velocity levels off are equal to 135, 140, and 155 kV/cm, while the saturation velocities v_s are equal to 1.0×10^6, 2.0×10^6, and 3.3×10^6 cm/s for 8*H*, 6*H*, and 4*H* polytypes, respectively. According to [4], the drift velocity at the miniband transport can be expressed as

$$v_d = \frac{AF}{B(1 + (F/B)^2)}, \qquad (27)$$

where $A = dE_1/(2\hbar)$, $B = \hbar/ed\tau$, d is the NSL period, E_1 is the first miniband width, and τ is the scattering time. The first miniband width is determined experimentally for 6*H*-SiC (E_1 = 256 meV [59]), where the NSL period is d = 7.5 Å. The value for the scattering time $\tau = 5 \times 10^{-13}$ s obtained from (27) is in agreement with a similar value obtained from the criterion for the BO threshold field in (23), rather than from (22). Therefore, the observed NDC effects in the three polytypes most likely show a correlation with the Bloch oscillation mechanism.

The observed NDC can perhaps be explained by other mechanisms. It is known that the *N*-shaped *I–V* characteristic can also appear due to recombination instability when the charge carriers are captured by repelling centers [60]. However, electron transit times through the base layer $t < 10^{-10}$ s are much shorter than the recombination time, which reduces the probability of this process. Furthermore, in the case of recombination instability, the threshold fields for the 4*H*, 6*H*, and 8*H* polytypes would be almost equal.

Thus, the interpretation of the observed effects within the context of the WSL theory is apparently justified. The characteristic parameters of the effects meet the conditions for WSL, and the distinction between the threshold fields for the three polytypes corresponds to the difference between the NSL parameters of these polytypes. The ascending portion of the *I–V* characteristic to the right of the threshold point can be explained by the injection increase with field and by the transverse heating of electrons. In addition, not all electrons participating in the charge transport are influenced by the Wannier–Stark quantization. In view of the geometric characteristics of the experimental structure, current flow is possible not only in the NSL axis direction, but in other directions as well. The NDC observed for these polytypes in the BO mode may be considered as the initial phase of the WSL process, owing to the sequence of the process development of the WSL mentioned above.

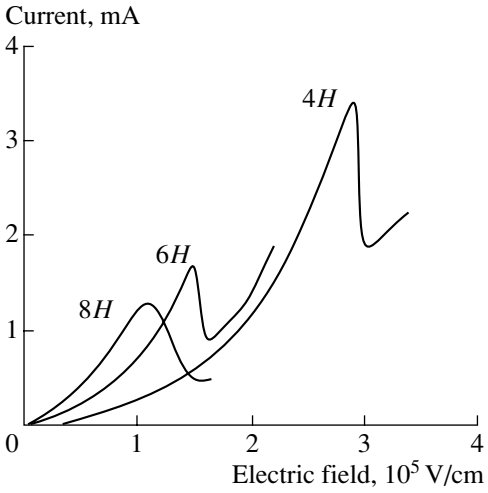

Fig. 13. The *I–F* characteristic of the experimental structure. See Figs. 11 and 12b.

4.3. Study of the WSL under a Superhigh Electric Field

So far we have discussed the WSL effects under a high field where the distance between the Stark ladder levels was, however, so small that the miniband could be considered as quasi-continuous; i.e., $E_1 \gg eFd$. Upon further increase in the electric field, the continuity of the electron spectrum is upset and the size of the region where the electron is localized decreases. Fields in which this size is much smaller than the mean free path l,

$$F \gg E_1/el, \qquad (28)$$

will be referred to as superhigh.

The experimental technique was slightly modified [61, 62] and the measuring circuit corresponded to the case (*c*) in Fig. 12 in order to study the further development of WSL under such fields. This was related to the fact that, because of local breakdown, the above-described technique was unsuitable for attaining fields above 5×10^5 V/cm. The main modification of the experimental conditions involved supplying a dc reverse bias voltage to the collector along with the pulse voltage. This resulted in the appearance of a significantly stronger dc voltage in the collector junction SCR, in addition to a pulse voltage, which was uniform in the base region (Fig. 12c). Since this junction is formed by the heavily doped n^+-region with $N_d - N_a = (3–5) \times 10^{18}$ cm^{-3} and the π-region with $N_a - N_d < 2 \times 10^{17}$ cm^{-3}, it can be considered abrupt and asymmetric, with the electric field changing linearly with the coordinate. The maximum field at the interface between the π- and n^+-regions [39] is given by

$$F_m = 2V(eN)^{1/2}/(2\varepsilon V)^{1/2}, \qquad (29)$$

where ε is the permittivity, and $N = N_a - N_d$. The mean field, which will mainly be used below, is equal to half of the maximum value. The pulse field in this circuit

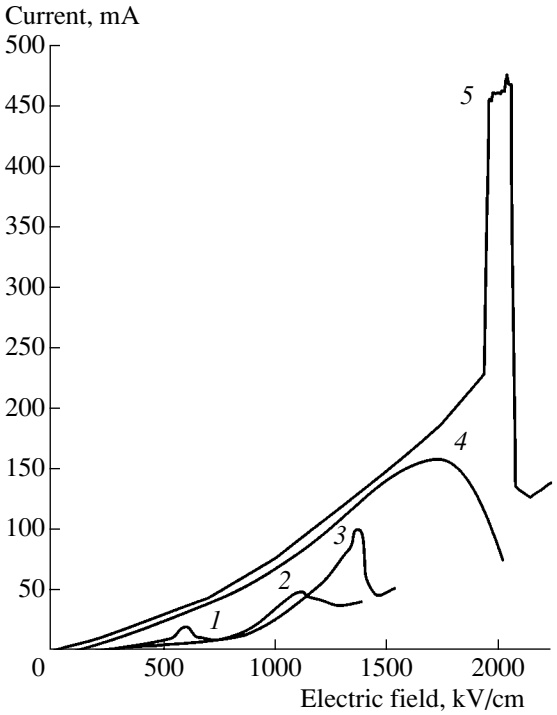

Fig. 14. The *I–F* characteristic of experimental structures for the 6*H*-SiC polytype. See Figs. 11 and 12c.

provided transport of electrons from the emitter to the high-field region of the collector.

The *I–F* characteristics of the 6*H* polytype, shown in Fig. 14, have five characteristic features marked by numbers *1*, *2*, *3*, *4*, and *5*. Region *1* is characterized by the threshold field of 600 kV/cm. It is unlikely that this effect is induced by the electron BO, i. e., by the initial stage of the WSL process. The BO threshold field was shown above to be about 150 kV/cm. It is not possible to attain such a weak field with the given experimental arrangement, since, even in the absence of an external field, the contact barrier of the *p–n* junction is 2.7 V high, which corresponds to the mean field in the space charge region exceeding 150 kV/cm. The external voltage across the collector junction must be inverted for the further reduction of the field, but then the three-electrode structure becomes inoperative.

The threshold field of 600 kV /cm for the 6*H* polytype is related to a Stark energy of 45 meV, which implies the possibility of strong localization leading to the upset of the quasi-continuity of the electron spectrum of the first miniband. Then, conduction can be effected via phonon-assisted electron hops between quasi-discrete levels. A theoretical consideration of this conduction mechanism was carried out in [47–49]. Calculations were based on different physical models; consequently, the results also differed. The conclusion that the *I–V* characteristic must have a series of resonances with threshold fields for the onset of NDC determined by relations (24) and (25) was common in the above studies. The phonon energy was used as the constant in [47, 48]; the first miniband width E_1 was the constant in [49]. Indices $n = 1, 2, 3,\ldots$ stand for the numbers of the superlattice layers jumped by an electron.

Features *1*, *2*, and *3* in the *I–V* characteristic of the 6*H* polytype are characterized by the Stark energies of 45, 80, and 103 meV, which are close to the energies of the transverse (46 meV) and longitudinal (77 meV) acoustic phonons, and the longitudinal optical phonon (103–112 meV) at the conduction band minimum [34]. Thus, the NDC observed in regions *1*, *2*, and *3* can be interpreted as the electron–phonon resonance between neighboring Stark ladder levels. The onset of NDC fields satisfy (24) for $n = 1$, i.e., for transitions between neighboring SL sites. Transitions between sites with $n > 1$ are not observed, since they occur at much lower fields which are not attainable in this experiment, as was mentioned above. Furthermore, low fields may violate the strong localization condition (28), which will make observation impossible. Note that transitions with $n > 1$ are finer effects and the observation of these may be difficult because of various drains in the bulk and on the surface, since the problem of crystal quality is very critical in studies at high fields. Thus, a basic possibility of observing the multiplicative series with $n > 1$ is unlikely in the case under consideration.

The Stark energy related to the threshold field in region *4* is about 125–130 meV, which is noticeably higher than the energies of all known phonons in the conduction band minimum. Therefore, there is reason to attribute these results to the electron plasma avalanche mechanism (EPAM) [49], by which the first miniband width E_1 must be a multiple of the Stark energy. According to [49], the threshold Stark energy equals $(1/2)E_1$. Therefore, it is easy to obtain $E_1 = 250$–260 meV. Thus, a direct estimate of the width E_1 is obtained for the first time; it does not contradict the interpretation presented above (Section 4.2) for the BO mode. A distinction between region *5* and the four preceding ones indicates that a sharp rise of the current comes before the NDC region. A sharp rise of the current itself is a common occurrence accompanying breakdown phenomena at high fields. A special feature of the case under consideration is that after a rise of the current its drop follows. Both the pulse current related to the electron flow from the emitter and the constant current induced by the local breakdown and uncontrolled leakage in the collector junction region were measured in the course of observation. The current drop was observed only in the pulse current *I–V* characteristic. In addition, the radiation accompanying the sharp rise of the current was suppressed at the NDC threshold.

The observed phenomena can be explained in the following way. The region of the sharp rise of the electron current is related to the miniband–miniband resonance tunneling (MMRT) of electrons from the states of the discrete spectrum of the first miniband into the second miniband, which preserves its quasi-continuity.

The subsequent drop of current can be due to BO in the second miniband. Using the simplest law for the increase of the miniband width with its number, we may conclude that the second miniband is four times wider than the first one and the quasi-continuity of the electron spectrum is not upset in the former miniband at actual field magnitude; therefore, the BO mechanism is possible for electrons in these conditions. Inter-miniband resonance tunneling is known to be possible if condition (26) is satisfied. It seems to be correct to characterize the resonance tunneling process by the highest field in the SCR (29), rather than by the mean field. Therefore, the Stark energy related to the inter-miniband tunneling is about 303 meV, which equals the sum $E_1/2 + E_{12}$ and, consequently, $E_{12} \approx 175$ meV. Then, we have $E_1 + E_{12} + E_2 \approx 1.46$ eV, which is in good agreement with the spectral position of the inter-miniband absorption band induced by transitions between the first and second minibands [24].

The experimental technique employed completely satisfies the requirements imposed on the study of the electron component of impact ionization. As follows from the above and from Fig. 14, the electron WSL processes, excluding the possibility of electron II, prevail at all fields up to $0.9F_b$. Delocalization of an electron occurs after its transition to the second miniband. Therefore, the electron contribution to II is possible at fields $F > 0.9F_b$, which is consistent with the data in Section 2.3.

Similar measurements were carried out for the 4*H* polytype. The *I–V* characteristics obtained are presented in Fig. 15. Only two specific regions were found in this case. They involve NDCs, which set in at the threshold fields of $(1.6–1.7) \times 10^6$ V/cm and $(1.9–2) \times 10^6$ V/cm; they correspond to the Stark energies of 80–85 and 96–100 meV. These values are close to the energies of the longitudinal acoustic (LA) and optical (LO) phonons [33]. Other features related to the resonance interaction of phonons with the Wannier–Stark ladder states in 4*H* were not detected. This can be explained by the fact that the strong localization condition is satisfied at higher fields in the 4*H* polytype, whose first miniband is much wider than that of 6*H* (the width is approximately proportional to $1/d^2$; i. e. the miniband width in 4*H* is more than twice as large). In particular, this condition cannot be satisfied with the Stark energy related to the transverse acoustic phonon.

The absence of a specific feature related to the complete localization in the first miniband and the miniband–miniband tunneling can be explained by the fact that conditions (25) and (26) are satisfied only under a very high electric field that exceeds the limit related to the avalanche breakdown, because the first miniband in 4*H* is wider.

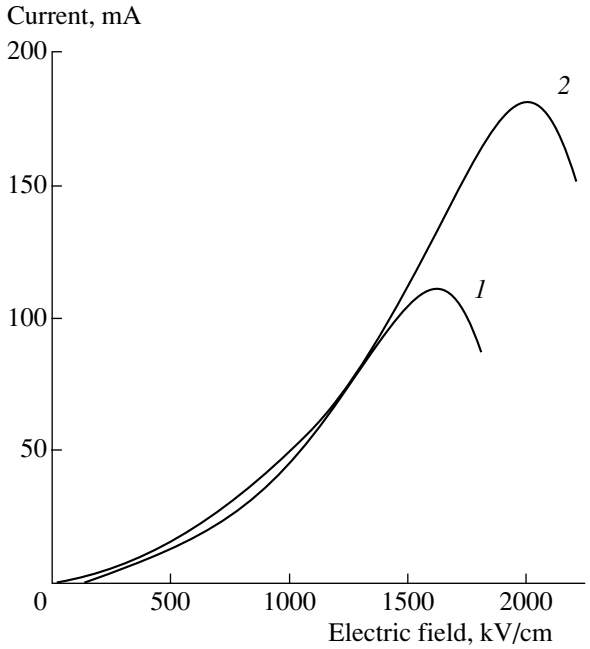

Fig. 15. The *I–F* characteristic of experimental structures for 4*H*-SiC. See Figs. 11 and 12c.

4.4. Saturation Drift Velocities of Electrons in the Silicon Carbide Polytypes

The saturation drift velocity is a very important parameter in a semiconductor crystal. It determines the upper frequency limit of semiconductor devices and, therefore, the range of their most effective operation. All of this is completely applicable to crystals based on silicon carbide. At the present time, saturation drift velocities are experimentally determined for two SiC polytypes, 4*H* and 6*H*, in the direction perpendicular to the NSL axis [34, 63]. In accordance with the presented data, the magnitudes of velocity coincide in both polytypes, which is not surprising if one takes into consideration the crystallographic identity of all polytypes in this direction. However, the crystallographic properties of dissimilar polytypes in the NSL axis direction differ considerably. The presence of a miniband structure in the electron spectrum of polytypes should influence the saturation velocities; in other words, a correlation between miniband spectrum parameters and the velocity value should be observed. Such a dependence of the drift velocity on the width of the first miniband was obtained analytically [4] and was observed in various systems with artificial SL.

Until now, such data for SiC were absent in the literature. Apparently, experimental difficulties of manufacturing the microstructures for charge transport along the NSL axis prevented the solving of this problem. However, many devices, including high-power high-frequency transistors, are designed precisely for such a configuration; therefore, the solution to this problem is of practical importance.

4.4.1. Experimental technique

Our technique is based on the following idea. If the mode of currents limited by the space charge and the drift current mode is realized in the experimental structure, this will allow us to determine the saturation velocity from the analysis of the *I–V* characteristic. Such a mode in the 1D case is described by the following equations:

$$d^2V/dX^2 = \rho/\varepsilon_S, \quad (30)$$

$$J = \rho v, \quad (31)$$

where V, X, J, ρ, ε_S, and v are the voltage across the structure, the coordinate along the direction of current, the current density, the space charge density, the dielectric constant of the semiconductor, and the drift velocity, respectively. After simple algebraic transformations, we obtain the following expression for the *I–V* characteristic of such a structure:

$$J = 2\varepsilon_S vV/w^2. \quad (32)$$

One can show that the *I–V* characteristic obtained consists of two portions: one where the drift velocity depends on the field and one where the drift velocity is saturated and does not depend on the field. If we assume that the velocity changes in the first portion as

$$v = \mu V/w, \quad (33)$$

then the *I–V* characteristic in this region will be given by the following expression:

$$J = 2\varepsilon_S \mu V^2/w^3. \quad (34)$$

Here, μ and w are the charge carrier mobility and the active region width of the structure, respectively. By keeping in mind that the mobility can be a function of the field, the actual *I–V* characteristic will then have a form distinct from (34).

The *I–V* characteristic in the second region, where v = const, will be described by the expression

$$J = 2\varepsilon_S v_S V/w^2, \quad (35)$$

where v_S is the saturation velocity. Thus, when the drift velocity is saturated, we should observe a linear portion of the characteristic.

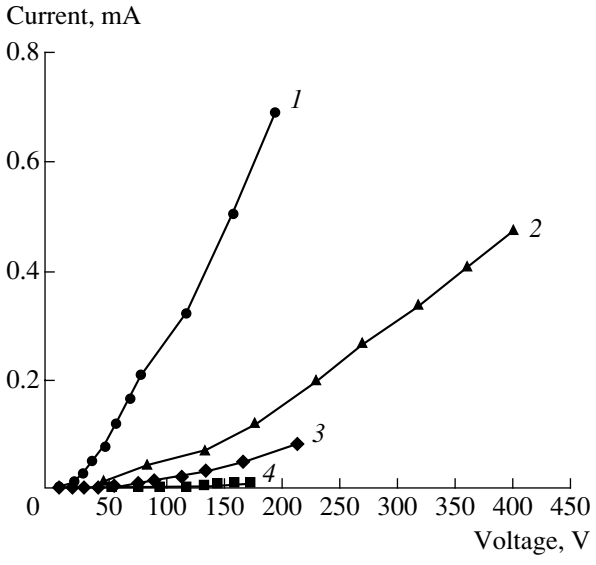

Fig. 16. The *I–F*-characteristics of the experimental structure for SiC (*1*) 6*H*, (*2*) 4*H*, (*3*) 8*H*, (*4*) 21*R* polytypes. See Figs. 11 and 12b.

4.4.2. Experimental structure

The n^+–p–n^+ structure, similar to the one used for measuring the WSL and described in Section 4.1, was used in this study. Because of a low free-hole density in the base, the density of electrons injected into the base exceeds the hole density at all currents, which ensures the mode of currents limited by the space charge in the base. In this case, there is drift electron motion and drift current in the base. This creates conditions for the validity equations (31) and (32).

This technique [64] essentially differs from the traditionally used method for the saturation of currents, where measurements are carried out at very high current densities. The latter requires precautionary measures for improving the heat sink and quality of contacts. We circumvent these difficulties in the technique proposed since the current density does not exceed 10^2 A/cm^2. Another distinction in this case is that electrons are in a *p*-type rather than in an *n*-type material, though the impurity concentration (about 10^{17} cm^{-3}) is approximately the same as in the *p*-type material used in [34, 63]. The latter is not very important since the saturation velocity, being the fundamental quantity, is determined by scattering by optical phonons, rather than by impurities. The operating conditions of the structure were similar to those used in Section 4.2. For measurements in such polytypes as 8*H*, 21*R* and 15*R*, where the BO critical field was less than the drift velocity saturation field, the structures were chosen where NDC was not observed, which was mentioned in Section 4.2. In the case of 4*H*- and 6*H*-SiC, where the BO threshold field was higher than the drift velocity saturation field, structures of both types were used but no noticeable differences in *I–V* were observed.

4.4.3. Experimental results and discussion

The results reported below were presented in [65, 66]. The *I–V* characteristics of structures based on several SiC polytypes are shown in Fig. 16. Three *I–V* characteristics for 4*H*, 6*H*, and 8*H* are very similar and include the nonlinear initial and the subsequent linear portions. The *I–V* characteristic for 21*R*-SiC does not include a nonlinear initial portion. In accordance with the expression presented above (35), the nonlinear portion must correspond to the quadratic voltage depen-

dence of the current $J \propto V^2$. However, in reality, the current varies following the power law with an exponent of about 1.6, i.e., $J \propto V^{1.6}$. Above, we assumed that the quadratic law would be invalid when the charge carrier mobility depends on the field. In our case, this dependence is probably expressed by the law $\mu \propto V^{-0.4}$, which leads to the departure of the initial portion in the *I–V* characteristic from the quadratic dependence. The absence of the nonlinear initial portion in the *I*–V characteristic of 21*R*-SiC is not induced by physical reasons. The very high internal resistance of these structures, due to the low electron mobility, prevented observation of the nonlinear initial portion in the *I–V* characteristic because of low currents. Therefore, the obtained *I–V* characteristic is represented by only a linear portion measured at sufficiently high fields ensuring the minimal level of currents necessary for observations. Analysis of the *I–V* characteristics allowed us to determine the saturation drift velocity of electrons in the 21*R*-SiC NSL. Its value appeared to be very low and was equal to 4×10^3 cm/s, which is indicative of the high degree of localization as a result of a very narrow miniband. The 21*R*-SiC polytype has the most complex and long-period superlattice. The latter gives rise to narrow minibands.

The SL period increases proportionally to the number of the polytype—from 5 to 10 Å in the series of 4*H*, 6*H*, and 8*H*. We estimated the first miniband width E_1 in 6*H*-SiC on the basis of the experimental study of the WSL (Section 4.3). The width of the first miniband for 4H and 8*H* polytypes with similar SL can be estimated from the relation $E_1 \approx k_d^2 = \pi^2/d^2$. In accordance with the above-mentioned values of the SL period, the E_1 value for 4*H* is larger by a factor of 2.25 and smaller in 8*H* than in 6*H* by a factor of 1.9. The obtained values for the electron saturation drift velocities are 10^6 for 8*H*, 2×10^6 for 6*H*, and 3.3×10^6 cm/s for 4*H*, which qualitatively confirms the dependence $v_s \propto 1/d$ [4]. Quantitative agreement is unlikely for the following reasons.

1. The simplicity of the theoretical concepts based on the quadratic dispersion law.

2. Experimental errors, first of all due to inaccuracy in measuring the base width *W*, which can be as large as ±(10–20)%, lead to ±(20–40)% errors in determining the velocity. The velocity saturation threshold fields for the polytype series 4*H*, 6*H*, and 8*H* were 1.55×10^5, 1.4×10^5, and 1.35×10^5 V/cm, respectively. The small discrepancy between these values may be due to differences in polytype characteristics and to errors discussed above. In accordance with [4], the drift velocity under the miniband transport conditions is given by the expression

$$v_d = \frac{AF}{B(1 + (F/B)^2)}, \qquad (36)$$

where $A = dE_1/(2\hbar)$ and $B = \hbar/ed\tau$. $E_1 = 256$ meV for 6*H*-SiC (Table 2). The scattering time $\tau = 5 \times 10^{-13}$ obtained from (36) is in agreement with the data in Section 4.2.

The field corresponding to the transition from nonlinear to linear *I–V* portions for 21*R* is not possible to observe for methodological reasons; therefore, it can be estimated as less than 1.6×10^5 V/cm. The 21*R*-SiC polytype is characterized by an extremely low electron saturation drift velocity, which is almost three orders of magnitude lower than for other polytypes. This cannot be explained on the basis of a single electron transport mechanism. According to the above, velocities for 4*H*, 6*H*, and 8*H* can be satisfactorily explained by the miniband transport, whereas the velocity in 21*R*-SiC is two orders of magnitude lower than that characteristic for the miniband transport. According to the WSL concept (Section 4.3), the electron spectrum of 21*R*-SiC becomes discrete even at rather weak fields of about $(1–2) \times 10^5$ V/cm. Notice that these fields are no lower than 6×10^5 V/cm for 6*H*, 4×10^5 V/cm for 8*H*, and about 10^6 V/cm for 4*H*. That is why the miniband transport is impossible at such fields in 21*R*; most likely, it is hopping electron transport that takes place in 21*R*, which explains such a low drift velocity in this polytype.

Summing up the obtained data, we can state that the drift velocity dependence on the NSL parameters observed in 4*H*, 6*H*, and 8*H* is in good qualitative and quantitative agreement with the simple theory by Esaki and Tsu [4]. This result is also an independent confirmation of the miniband transport at fields of about $(1–2) \times 10^5$ V/cm in these polytypes, which is consistent with concepts presented in Sections 4.2 and 4.3.

The anomalously low drift velocity in 21*R*-SiC indicates that the drift mechanism changes as a result of the essential modification of the miniband-spectrum parameters. In particular, narrowing of the miniband leads to fulfillment of the strong localization conditions at weaker fields, consequent suppression of the miniband transport, and a probable transition to hopping transport between cells of NSL. The *I*–F characteristic for the 15*R*-SiC polytype, which has been studied in a limited range of voltages because of the high leakage level, is not shown in Fig. 14. However, the saturation drift velocities were determined for the 15*R*-SiC as well. Values of the most important parameters characterizing the quantum transport in the silicon carbide NSL under the WSL conditions are presented in Table 2.

4.5. A Study of the Bloch oscillations in 6H-SiC diode n^+–n^-–n^+ Structures

The aforementioned special structure that formed as a bipolar transistor with a specifically designed base is, unfortunately, unsuitable for use in the microwave range. Unipolar n^+–n^-–n^+ diode structures, designed for this purpose, became possible after recent achievements in the growth of epitaxial layers with a low content of donor impurities. The base of such structures n^- has electron conduction with the electron concentration

Table 2

SiC polytype	F_t for the electron BO, 10^5 V/cm	F_t for electron–phonon resonance, 10^6 V/cm	F_t for EPAB of the first electron miniband, 10^6 V/cm	F_t for MMRT of electrons between the first and second minibands, 10^6 V/cm	E_1, meV	$E_{1,2}$, meV	V_s of electrons in the first miniband, $F \parallel C$, cm/s
4*H*	2.9	1.6; 2.0			≈500		3.3×10^6
6*H*	1.5	0.6; 1.1; 1.37	1.8	1.9	260	176	2.0×10^6
8*H*	1.1				≈140		1.0×10^6
15*R*							1.2×10^6
21*R*							4.4×10^3

10^{15} cm^{-3} < $N_d - N_a$ < 10^{17} cm^{-3}, while one of the two n^+-regions is the starting substrate with $N_d - N_a \approx (2–3) \times 10^{18}$ cm^{-3}, and another is the heavily doped epitaxial or implanted layer with $N_d - N_a \approx 10^{20}$ cm^{-3}. The structure is formed as a mesa with a cross section of about 25–40 μm and a base thickness of about 3–5 μm. The *I–V* characteristic of such a structure is shown in Fig. 17. This characteristic of the structure has no special features and is almost linear up to a certain voltage. A sharp increase in the current at a certain voltage across the structure is accompanied by the emission of light. The spectrum of this radiation coincides with that characteristic for the breakdown of *p–n* junctions. However, the uniform field does not exceed 150 kV/cm, which is at least an order of magnitude lower than the smallest known breakdown fields in 6*H*-SiC. Perhaps, such a field deficit could be overcome by the formation of a high-field domain in the base. This is possible, as is known, when NDC appears in the crystal. According to the aforesaid, NDC is observed in 6*H*-SiC at fields of about 150 kV/cm as a result of BO (Fig. 13).

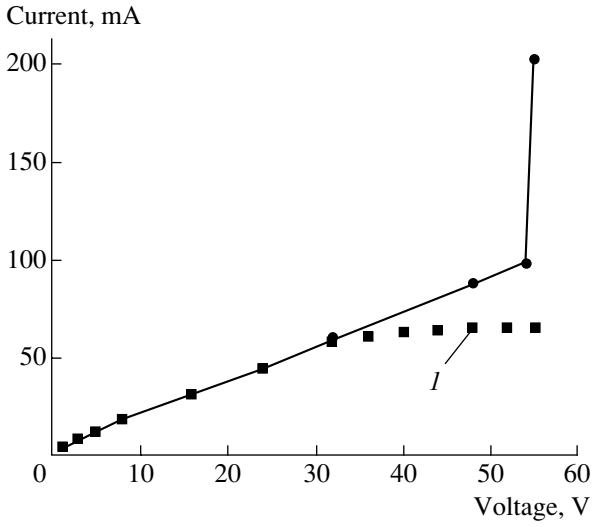

Fig. 17. The *I–V* characteristic of the n^+–n^-–n^+-diode structure for the 6*H*-SiC polytype. (*1*) Corresponds to a static domain.

If it is a domain, then is it static or drifting? Analysis of the *I–V* characteristic in Fig. 17 favors the latter. Actually, in our case, the localized domain should have the width $d = U/F_b$. At U = 50 V and F_b = 2000 kV/cm, $d \leq$ 0.25 μm. In the case of the static domain, the *I–V* characteristic would contain a flat portion with a differential conductance $R = L^2/\varepsilon v S$, which would be equal to 3×10^3 Ω for L = 3–5 μm, $\varepsilon = 10^{-12}$ F/cm, $v = 2 \times 10^6$ cm/s, L = 4 μm, and $S = 1.3 \times 10^{-5}$ cm^2 (Fig. 17, broken line), while the differential resistance in the breakdown region would be about 10–20 Ω. In the case of a mobile domain, the generation rate of electron–hole pairs in the breakdown region (assuming uniformity of generation and neglecting recombination because of the small transit time) is $G = I/SeL$, which yields $G = 1.2 \times 10^{26}$ cm^{-3}/s at I = 100 mA. We can estimate the generation rate using expression (12c) from [67] for propagating Gunn domains. Using the values $\alpha_\infty = 1 \times 10^6$ cm^{-1} [23, 28] and $n_r = 10^{16}$ cm^{-3}, we obtain $G = 2 \times 10^{26}$ cm^{-3}/s, which may be considered a good fit that confirms the assumption of the presence of mobile domains.

4.6. Study of the Bloch Oscillations in 6H-SiC Triode n^+–n^-–n^+ Structures

An additional experiment was carried out in order to obtain convincing proof of the stated assumption concerning the formation of an electric-field domain. For this purpose, we used a special technique to fabricate a new SiC-based unipolar triode n^+–n^-–n^+ structure, which is a static-induction transistor (SIT) with the *p–n* junction as the gate and has a shortened circumference (length of 200 μm). The schematic diagram of the SIT is shown in Fig. 18. The conducting channel with dimensions 40 × 2 × 3 μm^3, which is similar to the diode structure n^+–n^-–n^+ considered above, but, unlike the latter, is located between two *p–n* junctions with fields having a component perpendicular to the drain–source direction. Experiments showed that the *I–V* characteristic of such channels (Fig. 19a) at the gate voltage V_g = 0 is similar to that of the diode structure (Fig. 17).

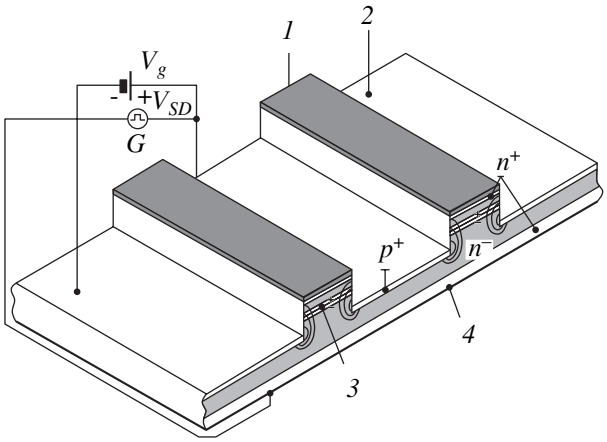

Fig. 18. A SIT structure based on the 6*H*-SiC polytype: (*1*) source, (*2*) gate, (*3*) domain, and (*4*) drain.

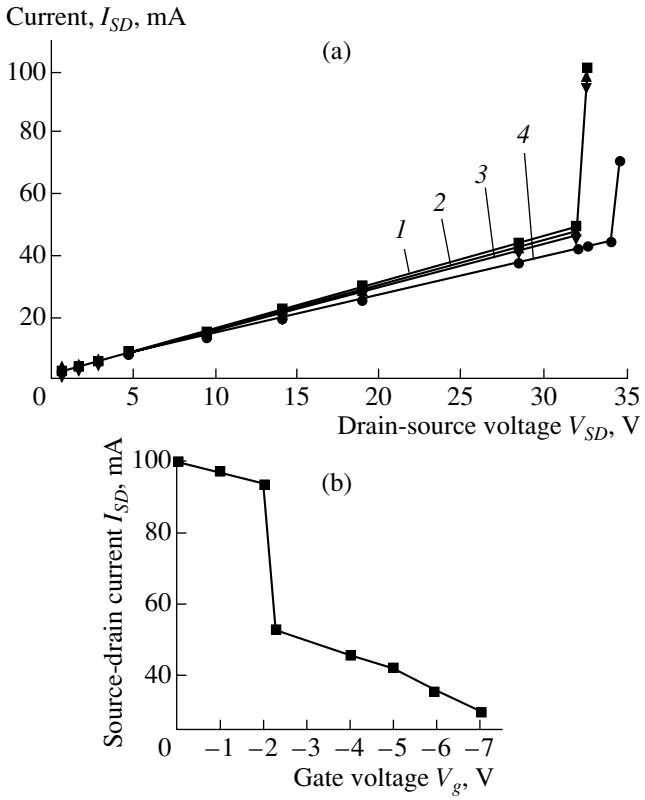

Fig. 19. (a) The I_{SD}–V_{SD} characteristics for a SIT structure of the 6*H*-SiC polytype at V_g = (*1*) 0, (*2*) 1, (*3*) 2, and (*4*) 3 V; (b) I_{SD}–V_g characteristic for a SIT structure of the 6*H*-SiC polytype.

It was ascertained experimentally that the run of the *I*–*V* characteristic are radically different in the linear and breakdown regions at $V_g \neq 0$. The behavior typical of SIT is observed in the linear portion: the current decreases with the slope S = 2–4 mA/V, and the gate field increases, which is consistent with the channel parameters. The slope can be increased by a factor of 30–50 if one designs a device whose SIT layout has parameters similar to those of a silicon SIT. However, the current falls with the slope S = 40–60 mA/V (Figs. 19a and 19b) in the breakdown region at a certain gate field magnitude. Thus, a large and sharp current fall can be caused by the destruction of the domain by the transverse electric field. Naturally, just after the destruction of the domain, the breakdown is suppressed and the current falls. This experimental fact is a convincing argument in favor of domain formation in the channel with NSL. At the same time, the obtained data conclusively prove the propagating nature of the domain, since, according to the SIT layout (Fig. 18), the gate field operates in the channel region, which is at a distance of 2.0 μm from the source and cannot affect the static domain, which is usually localized near the source (cathode). Unfortunately, these conditions are unsuitable for observation of the microwave signal, since we failed to stabilize the through current and the system rapidly degrades. At the same time, a new effect is obtained and its prospects for applications are possibly no less attractive than the generation of microwaves. A large and sharp current fall with high amplitude is a basis for the manufacturing of power devices with fast switching. Unfortunately, the degradation of the structure is an obstacle to the immediate practical implementation of this effect. However, this situation does not look hopeless but holds promise because of the inhomogeneity of the n^--layer based on silicon carbide. This problem of material research can usually be solved by carrying out directed studies for improving the quality of the material. It could be that this adverse phenomenon is a special feature of a material grown under conditions of a specific technological system. It is possible to use materials manufactured by an alternative process. It seems likely that the latter is not too complex if one takes into account the expanding range of studies in the field of silicon carbide growing processes.

5. CONCLUSION

The results obtained in this work indicate the decisive influence of the silicon carbide polytype NSL on the electronic transport along the special axis of SiC (the NSL axis) under a high electric field. This influence is expressed in the form of a series of pronounced effects under electronic transport in the quantizing electric field; these effects were observed directly using the *I*–*V* characteristics instead of through indirect observation using supersensitive optical detection. Most of the results obtained are the first substantial proofs of the pronounced effect of the Wannier–Stark localization on the electron spectra in crystals. Note that this was not done until now in artificial superlattices; this may have been due to their inadequate crystalline quality. The results presented, starting with the monopolarity of impact ionization and the discovery of a mobile electric-field domain, may act as the basis for the very inter-

esting and prospective practical development of unique devices using silicon carbide. According to the data obtained, the discovered propagating domain is similar to the Gunn domain in the known Gunn effect, and this most likely indicates the presence of microwave oscillations in the crystal; these oscillations can be considered as the transformed Bloch oscillations of electrons. Their direct observation is the subject of future study. The observation of electric domain destruction accompanied by sharp high-amplitude current switching also provides attractive prospects for practical applications.

REFERENCES

1. F. Bloch, Z. Phys. **52**, 555 (1928).
2. L. V. Keldysh, Fiz. Tverd. Tela (Leningrad) **4**, 2265 (1962).
3. G. N. Wannier, Phys. Rev. **11**, 432 (1960).
4. L. Esaki and R. Tsu, IBM J. Res. Dev. **14**, 61 (1970).
5. A. Rabinovitch and J. Zak, Phys. Rev. B **4**, 2358 (1971).
6. D. Emin and C. F. Hart, Phys. Rev. B **36**, 7353 (1987).
7. L. Kleinman, Phys. Rev. B **41**, 3857 (1990).
8. N. L. Chupricov, J. Phys.: Condens. Matter **11**, 1069 (1999).
9. E. E. Mendez, F. Agullo-Rueda, and J. M. Hong, Phys. Rev. Lett. **160**, 2426 (1988).
10. P. Voisin, J. Bleuse, C. Bouche, *et al.*, Phys. Rev. Lett. **61**, 1639 (1988).
11. J. Feldman, K. Leo, D. A. B. Miller, *et al.*, Phys. Rev. B **46**, 7252 (1992).
12. K. Leo, P. Haring Boilvar, E. Bruggeman, *et al.*, Solid State Commun. **84**, 943 (1992).
13. A. Sibille, J. F. Palmier, H. Wang, and F. Mollot, Phys. Rev. Lett. **64**, 52 (1990).
14. F. Bettram, F. Capasso, D. L. Sivco, *et al.*, Phys. Rev. Lett. **64**, 3167 (1990).
15. J. Grenzer, A. A. Ignatov, E. Schomburg, *et al.*, Ann. Phys. (Leipzig) **4**, 1 (1995).
16. A. Sibille, J. F. Palmier, and F. Mollot, Appl. Phys. Lett. **60**, 457 (1992).
17. Yu. A. Vodakov, A. O. Konstantinov, D. P. Litvin, and V. I. Sankin, Pis'ma Zh. Tekh. Fiz. **7** (7), 705 (1981) [Sov. Tech. Phys. Lett. **7**, 301 (1981)].
18. A. O. Konstantinov, A. P. Kuz'min, M. I. Lebedev, *et al.*, Zh. Tekh. Fiz. **54**, 1622 (1984) [Sov. Phys. Tech. Phys. **29**, 949 (1984)].
19. V. I. Sankin, R. G. Verenchikova, Yu. A. Vodakov, *et al.*, Fiz. Tekh. Poluprovodn. (Leningrad) **16**, 1325 (1982) [Sov. Phys. Semicond. **16**, 850 (1982)].
20. A. O. Konstantinov, D. P. Litvin, and V. I. Sankin, Pis'ma Zh. Tekh. Fiz. **7**, 1335 (1981) [Sov. Tech. Phys. Lett. **7**, 572 (1981)].
21. R. G. Verenchikova, Yu. A. Vodakov, D. P. Litvin, *et al.*, Fiz. Tekh. Poluprovodn. (Leningrad) **16**, 2029 (1982) [Sov. Phys. Semicond. **16**, 1309 (1982)].
22. G. A. Baraff, Phys. Rev. **128**, 2507 (1962).
23. Yu. A. Vodakov, D. P. Litvin, V. I. Sankin, *et al.*, Fiz. Tekh. Poluprovodn. (Leningrad) **19**, 814 (1985) [Sov. Phys. Semicond. **19**, 502 (1985)].
24. G. B. Dubrovskii, A. A. Lepneva, and E. I. Radovanova, Phys. Status Solidi **57**, 423 (1973).
25. A. P. Dmitriev, A. O. Konstantinov, D. P. Litvin, and V. I. Sankin, Fiz. Tekh. Poluprovodn. (Leningrad) **17**, 1093 (1983) [Sov. Phys. Semicond. **17**, 686 (1983)].
26. H. Ando and H. Kanbe, Solid-State Electron. **24**, 629 (1981).
27. A. S. Tager, Fiz. Tverd. Tela (Leningrad) **6**, 1093 (1964) [Sov. Phys. Solid State **6**, 1919 (1965)].
28. V. I. Sankin, Yu. A. Vodakov, and D. P. Litvin, Fiz. Tekh. Poluprovodn. (Leningrad) **18**, 2146 (1984) [Sov. Phys. Semicond. **18**, 1339 (1984)].
29. P. P. Webb, R. Y. McIntyre, and Y. Conradi, RCA Rev. **35**, 234 (1974).
30. V. I. Sankin, A. V. Naumov, M. G. Ramm, *et al.*, Pis'ma Zh. Tekh. Fiz. **15** (24), 43 (1989) [Sov. Tech. Phys. Lett. **15**, 970 (1989)].
31. V. I. Sankin and A. A. Lepneva, in *Proceedings of the International Symposium on Nanostructures: Physics and Technology, St. Petersburg, Russia, 1997.*
32. Z. S. Gribnikov, Zh. Éksp. Teor. Fiz. **74**, 2112 (1978) [Sov. Phys. JETP **47**, 1099 (1978)].
33. G. B. Dubrovskiĭ and V. I. Sankin, Fiz. Tverd. Tela (Leningrad) **14**, 1200 (1972) [Sov. Phys. Solid State **14**, 1024 (1972)].
34. G. B. Dubrovskiĭ and V. I. Sankin, Fiz. Tverd. Tela (Leningrad) **17**, 2776 (1975) [Sov. Phys. Solid State **17**, 1847 (1975)].
35. C. van Opdorp and J. Vrakking, J. Appl. Phys. **40**, 2320 (1969).
36. W. V. Muench and I. P. Pfaffeneder, J. Appl. Phys. **48**, 4831 (1977).
37. P. J. Price, IBM J. Res. Dev. **17**, 39 (1973).
38. R. A. Suris and B. S. Shchamkhalova, Fiz. Tekh. Poluprovodn. (Leningrad) **18**, 178 (1984) [Sov. Phys. Semicond. **18**, 111 (1984)].
39. S. Sze, *Physics of Semiconductor Devices* (Wiley, New York, 1981; Mir, Moscow, 1984).
40. B. S. Kerner, D. P. Litvin, and V. I. Sankin, Pis'ma Zh. Tekh. Fiz. **13** (8), 819 (1987) [Sov. Tech. Phys. Lett. **13**, 342 (1987)].
41. B. S. Kerner, D. P. Litvin, A. D. Roenkov, and V. I. Sankin, Springer Proc. Phys. **43**, 243 (1991).
42. V. A. Vashchenko, Yu. A. Vodakov, V. V. Gafiĭchuk, *et al.*, Fiz. Tekh. Poluprovodn. (Leningrad) **25**, 1209 (1991) [Sov. Phys. Semicond. **25**, 730 (1991)].
43. Yu. A. Vodakov, D. P. Litvin, E. N. Mokhov, *et al.*, Pis'ma Zh. Tekh. Fiz. **10** (3), 3 (1984) [Sov. Tech. Phys. Lett. **10**, 128 (1984)].
44. A. I. Baranenkov and V. V. Osipov, Mikroélektronika **1**, 63 (1972).
45. B. S. Kerner and V. V. Osipov, Zh. Éksp. Teor. Fiz. **74**, 1675 (1978) [Sov. Phys. JETP **47**, 874 (1978)].
46. B. S. Kerner and V. V. Osipov, Zh. Éksp. Teor. Fiz. **79**, 2218 (1980) [Sov. Phys. JETP **52**, 1122 (1980)].
47. V. V. Bryksin, Yu. A. Firsov, and S. A. Ktitorov, Solid State Commun. **39**, 385 (1981).
48. D. Emin and C. F. Hart, Phys. Rev. B **36**, 2530 (1987).
49. R. Tsu and G. Dohler, Phys. Rev. B **12**, 680 (1975).

50. R. F. Kazarinov and R. A. Suris, Fiz. Tekh. Poluprovodn. (Leningrad) **6**, 148 (1972) [Sov. Phys. Semicond. **6**, 120 (1972)].
51. D. P. Litvin, A. A. Mal'tsev, A. V. Naumov, *et al.*, Pis'ma Zh. Tekh. Fiz. **13** (12), 47 (1987) [Sov. Tech. Phys. Lett. **13**, 523 (1987)].
52. V. I. Sankin and A. V. Naumov, Pis'ma Zh. Tekh. Fiz. **16** (7), 91 (1990) [Sov. Tech. Phys. Lett. **16**, 281 (1990)].
53. V. I. Sankin and A. V. Naumov, Springer Proc. Phys. **43**, 221 (1991).
54. V. I. Sankin and A. V. Naumov, Superlattices Microstruct. **10**, 353 (1991).
55. V. I. Sankin, A. V. Naumov, and I. A. Stolichnov, Pis'ma Zh. Tekh. Fiz. **17** (12), 38 (1991) [Sov. Phys. Tech. Phys. **17**, 838 (1991)].
56. V. I. Sankin and I. A. Stolichnov, in *Proceedings of the International Symposium on Nanostructures: Physics and Technology, St. Petersburg, Russia, 1994.*
57. V. I. Sankin and I. A. Stolichnov, Superlattices Microstruct. **23**, 999 (1998).
58. V. I. Sankin and A. A. Lepneva, Fiz. Tekh. Poluprovodn. (St. Petersburg) **34**, 831 (2000) [Semiconductors **34**, 803 (2000)].
59. V. I. Sankin and I. A. Stolichnov, Pis'ma Zh. Éksp. Teor. Fiz. **64**, 105 (1996) [JETP Lett. **64**, 114 (1996)].
60. A. F. Volkov and Sh. M. Kogan, Usp. Fiz. Nauk **96**, 633 (1968) [Sov. Phys. Usp. **11**, 881 (1968)].
61. V. I. Sankin and I. A. Stolichnov, Pis'ma Zh. Éksp. Teor. Fiz. **59**, 703 (1994) [JETP Lett. **59**, 744 (1994)].
62. V. I. Sankin and I. A. Stolichnov, in *Proceedings of the International Symposium on Nanostructures: Physics and Technology, St. Petersburg, Russia, 1995.*
63. W. V. Muench and E. Petterpaul, J. Appl. Phys. **48**, 482 (1977).
64. I. A. Khan and J. A. Cooper, Jr., in *Proceedings of ICSCIII-N'97, Stockholm, 1997*, p. 57.
65. V. I. Sankin and A. A. Lepneva, in *Proceedings of the International Symposium on Nanostructures: Physics and Technology, St. Petersburg, Russia, 1998.*
66. V. I. Sankin and A. A. Lepneva, Fiz. Tekh. Poluprovodn. (St. Petersburg) **33**, 586 (1999) [Semiconductors **33**, 547 (1999)].
67. B. L. Gel'mont and M. S. Shur, Fiz. Tekh. Poluprovodn. (Leningrad) **7**, 453 (1973) [Sov. Phys. Semicond. **7**, 326 (1973)].

Translated by S. Ktitorov

Semiconductors, Vol. 36, No. 7, 2002, pp. 740–742. Translated from Fizika i Tekhnika Poluprovodnikov, Vol. 36, No. 7, 2002, pp. 794–796.

ATOMIC STRUCTURE AND NONELECTRONIC PROPERTIES OF SEMICONDUCTORS

Effect of Long-Term Annealing on Accumulation of Impurities

Yu. A. Bykovskiĭ*†, G. M. Voronkova*, V. V. Grigor'ev*, V. V. Zuev*, A. V. Zuev*, A. D. Kiryukhin*, V. I. Chmyrev, and S. A. Shcherbakov*****

** Moscow State Institute of Engineering Physics (Technical University), Kashirskoe sh. 31, Moscow, 115409 Russia*

e-mail: Solid@server25.mephi.ru

*** Kurnakov Institute of General and Inorganic Chemistry, Russian Academy of Sciences, Leninskiĭ pr. 31, Moscow, 117907 Russia*

**** Institute of Microprocessor Computer Systems, Russian Academy of Sciences, Moscow, 117872 Russia*

Submitted November 21, 2001; accepted for publication December 18, 2001

Abstract—The occurrence of changes in impurity accumulation after a long-term annealing preceding the in-diffusion of impurities is shown experimentally. Atoms of Au as acceptors affecting the resistivity and photoconductivity decay time were used as indicators in studies of these changes. © *2002 MAIK "Nauka/Interperiodica".*

1. The distribution of force (elastic) fields in an actual crystal due to the presence of various defects should appreciably affect the migration of impurity atoms at various heat treatments and at in-diffusion. These fields are responsible, among other processes, for internal gettering, i. e., the accumulation of contaminating impurities in corresponding segregates, such as oxygen precipitates at specially chosen heat treatments [1]. Specific fields occur also under external gettering when the surface of a material contains some imperfections, for example, micropores. It is clear that the force fields can be both static and dynamic (i.e., be time-dependent because of the time dependence of the distribution of defects, such as vacancies, interstitial atoms, their concentrations and fluxes).

In this study, we show experimentally that the internal state of an actual (imperfect) crystal can be affected profoundly by long-term cyclic heat treatment, which precedes the in-diffusion of Au. The observations were made using the well pronounced effect of the incorporation of Au atoms into Si due to the binding of free electrons to a deep acceptor state, which results in the increase in resistivity ρ and decrease in decay time τ of photoconductivity.

2. A Czochralski-grown crystal of Si having $\rho \cong 6$–$7\ \Omega$ cm and $\tau \approx 110$–$120\ \mu$s was used as the sample. The decay time was determined using a noncontact method for measuring the time dependence of reflected microwave power, which traced the time-dependent change of nonequilibrium photoconductivity excited in the sample by pulsed laser radiation ($\lambda = 1.06\ \mu$m). The oxygen content was about 10^{18} cm^{-3}. Prior to and after the heat treatments, the sample was mechanically and chemically treated according to a commonly used technique. The samples used were in the form of platelets about 0.15 cm in thickness. High-temperature treatments were performed in a quartz tube under uninterrupted pumping in a vacuum with a residual pressure of 0.1 Pa. The tube was preliminarily annealed at 1100°C for several hours.

The samples with a thermally deposited W layer were preliminarily cyclically annealed for 50 h at 950°C. The duration of each cycle was about 5 h daily. Each cycle ended with the slow cooling of the sample with a furnace.

After preliminary heat treatment (PHT), the resistivity ρ, measured by the four-point probe method, remained virtually the same as it was in the initial state of a sample, while the value of τ decreased by two orders of magnitude and became equal to about 1 μs. Thus, PHT results in the formation of additional (to the initially existing) recombination channels related to deep levels of defects with various concentrations. The oxygen precipitates, having a system of energy levels distributed in the Si band gap [1], may act as these defects.

A further step was the thermal deposition of Au, which was performed until a visible film was formed [4]. Afterwards, Au was diffused at 950°C for 1–7 h. Using layer-by-layer etching, the region with a constant value of resistivity was reached; the thickness of the etched-off layer could be as large as 100–150 μm. In order to reveal the differences in the internal states of the sample prior to and after PHT, two cooling modes were used after the diffusion of Au: quenching in oil and slow cooling (1 K/min or cooling in a furnace).

3. Figures 1 and 2 show the main experimental results. The most important result is the distinction between the values of ρ observed in the samples with and without PHT. The value of ρ in the PHT-subjected

† Deceased.

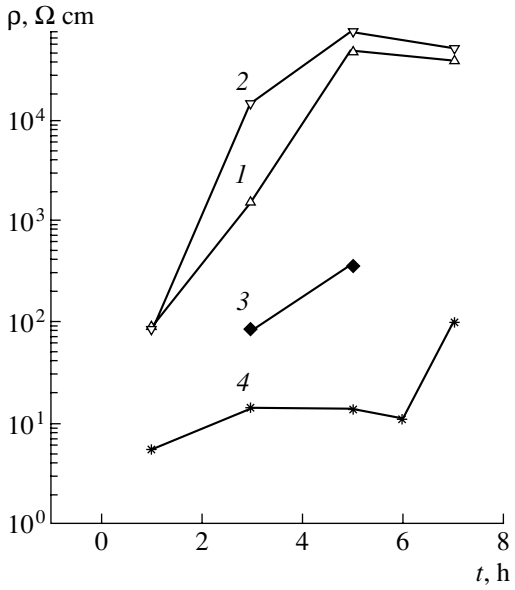

Fig. 1. Dependence of resistivity ρ on the duration *t* of the two-sided diffusion of Au at 950°C. (*1*) PHT 50 h, slow cooling (SC); (*2*) PHT 950°C, 50 h, quenching after Au diffusion; (*3*) diffusion into initial (reference) sample, SC; (*4*) diffusion into initial (reference) sample with oil quenching. The value of resistivity after PHT prior to Au diffusion (PHT at 950° for 50 h) ρ ≅ 5.6 Ω cm, initial sample, ρ ≅ 6–7 Ω cm.

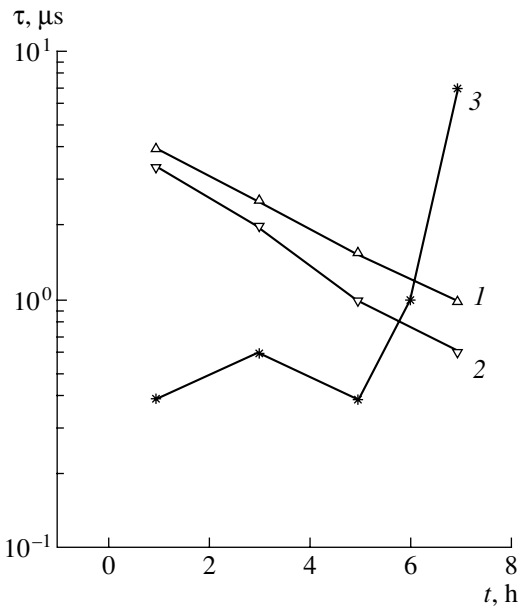

Fig. 2. Dependence of decay time of photoconductivity τ on the time *t* of the two-side diffusion of Au at 950°C. (*1*) PTH 950°C, 50 h, SC; (*2*) PTH 950°C, 50 h, quenching after Au diffusion; (*3*) diffusion into initial (reference) sample, SC. The value of τ after PHT prior to Au diffusion (PHT at 950° for 50 h, ρ ≅ 5.6 Ω cm) τ ≅ 0.6 μs.

samples increased equally both after quenching and slow cooling. The value of ρ in the samples without PHT after quenching was appreciably higher than after slow cooling. It is important that the increase in ρ in the samples with PHT preceding Au diffusion was larger after slow cooling than in quenched samples after Au diffusion into the initial sample; i. e., the concentration of Au in the acceptor state in the former case is higher than in the latter case.

The values of the decay time of photoconductivity in the samples subjected to PHT with the subsequent diffusion of Au after various modes of cooling are also found to be close to each other (Fig. 2). The decay time in the samples after PHT was always shorter than in the samples with the subsequent diffusion of Au.

4. The most logical conclusion that follows from the experimental data is that the force fields responsible for the migration of impurities (Au probes in our case) after PHT become more uniform. Indeed, at slow cooling, under the influence of the internal fields (static, dynamic, or the fluxes of defects), Au atoms in the initial sample are displaced towards the sites where they become electrically inactive. During quenching, Au atoms have no time to move to these sites. After PHT of a duration (50 h) exceeding the duration of the subsequent Au diffusion by approximately an order of magnitude, the processes involving various defects in the system at 950°C are almost completed; i.e., the succeeding Au diffusion proceeds, on average, in more uniform force fields of a crystal. This means that Au atoms remain at the same sites they occupied at a high temperature. In other words, even a prolonged cooling after PHT, judging from the value of ρ, cannot force the atoms of acceptor Au to be directionally moved either by static or by dynamic fields in a crystal towards electrically inactive positions. Almost identical values of the decay time of photoconductivity and their equal reduction with the diffusion time (i.e., with increasing content of acceptor Au, see Fig. 2) also confirm the above conclusion. The larger value of ρ for the samples after PHT and the subsequent diffusion of Au after quenching than that for the initial samples corresponds to a larger Au content in the acceptor state. The increase in Au concentration can be caused by the influence of various systems of defects on the Au solubility and diffusion coefficient. These defects can vary in form, composition, concentration, and they depend on the surrounding fields in the initial sample and in the sample after PHT [5].

The larger value of τ after the diffusion of Au in a sample with PHT, in comparison with the sample subjected only to PHT, points to the partial neutralization by Au of the recombination channels formed due to PHT. This seems quite probable because these channels can be donors [1] with the electron bound to a deep acceptor level of Au, thus ensuring the Coulomb attraction of impurities with the alteration of the process of recombination. The value of τ in Si after Au diffusion is smaller if the sample was subjected to PHT; this also indicates that the recombination mechanism in Si

depends heavily on the crystal state prior to Au diffusion. All this occurs, judging by the value of ρ, despite the fact that the concentration of Au in the acceptor state in Si subjected to PHT is higher than in Si without PHT. However, this can be observed only at the diffusion times of 1, 3, and 5 h (see Fig. 2). If the diffusion times are longer (6, 7 h), the decay times become equal to each other and even exceed the values in initial Si at the diffusion time of 7 h. Correspondingly, the value of resistivity at these diffusion times slightly increases (Fig. 1). Notably, the values of ρ and τ obtained after Au diffusion into the initial sample with slow cooling indicate that the concentration of acceptor Au is high enough to reduce τ from hundreds of microseconds to several, and even to fractions of microseconds, although the concentration of acceptor Au is lower or slightly higher than the concentration of free carriers in the conduction band of an initial sample, which can be judged from a small increase in ρ.

5. Thus, the experiments with high-temperature diffusion of Au as a probe for the effects of rapid and slow cooling revealed essential changes in the internal states of Si single crystals associated with the distribution of force fields (dynamic and static) induced by defects as a result of long-term PHT at the same temperatures as were used in the succeeding diffusion of Au. We believe that this is the first study in which a wide set of various experimental conditions, such as temperature and the duration of heat treatments and diffusion, have been used. Apart from information about internal fields, the results of our study may be helpful for the realization of specific states of diffusion-induced impurities that interact with a local field of other impurities or defects and affect the macroscopic characteristics [6, 7].

ACKNOWLEDGMENTS

This study was supported in part by the Russian Foundation for Basic Research, project no. 99-01-00854.

REFERENCES

1. J. M. Hwang and D. K. Schroder, J. Appl. Phys. **59**, 2476 (1986).
2. V. Raineri, P. G. Fallica, G. Percolla, *et al.*, J. Appl. Phys. **78**, 3727 (1995).
3. Yu. A. Bykovskiĭ, V. V. Zuev, A. D. Kiryukhin, *et al.*, Zh. Tekh. Fiz. **69** (4), 54 (1999) [Tech. Phys. **44**, 399 (1999)].
4. W. Lerch and N. A. Stolwijk, J. Appl. Phys. **83**, 1312 (1998).
5. J. S. Kang and D. K. Schroder, J. Appl. Phys. **65**, 2974 (1989).
6. Yu. A. Bykovskiĭ, V. V. Zuev, A. D. Kiryukhin, and É. A. Manykin, Pis'ma Zh. Tekh. Fiz. **9** (6), 9 (1983) [Sov. Tech. Phys. Lett. **9**, 422 (1983)].
7. A. G. Nikitin and V. V. Zuev, Fiz. Tekh. Poluprovodn. (St. Petersburg) **27**, 1211 (1993) [Semiconductors **27**, 668 (1993)].

Translated by A. Zalesskiĭ

Semiconductors, Vol. 36, No. 7, 2002, pp. 743–746. Translated from Fizika i Tekhnika Poluprovodnikov, Vol. 36, No. 7, 2002, pp. 797–800.

ATOMIC STRUCTURE AND NONELECTRONIC PROPERTIES OF SEMICONDUCTORS

Analysis of the Size-Distribution Function of Metallic Nanoclusters in a Hydrogenated Amorphous Carbon Host

V. I. Ivanov-Omskiĭ, A. B. Lodygin, and S. G. Yastrebov

Ioffe Physicotechnical Institute, Russian Academy of Sciences, Politekhnicheskaya ul. 26, St. Petersburg, 194021 Russia

e-mail: ivanov.ivom@ioffe.rssi.ru

Submitted December 19, 2001; accepted for publication December 20, 2001

Abstract—A method for mathematical processing of TEM images of nanocomposites with a pronounced noise background is proposed. This method is based on the spline filtering of an image by using the values of average background intensity and is applied to TEM images of amorphous Cu-doped carbon. A size distribution function obtained for copper clusters is in good agreement with previous data. The dependence of the cluster-to-cluster distance on cluster size is determined. This dependence validates the hypothesis of the fluctuation nature of cluster generation at a lower metal content and of the coalescence of clusters at higher metal contents. © *2002 MAIK "Nauka/Interperiodica".*

INTRODUCTION

Hydrogenated amorphous carbon (*a*-C:H) is commonly known as a universal coating due to the similarity of some of its chemical and physical properties to the properties of diamond. One of the structural modifications of *a*-C:H is even called a "diamond-like carbon" (DLC). Some other *a*-C:H properties related to the unique ability of carbon atoms to form various configurations of chemical bonds with transformations of one sp^3-hybridization state into another have been less studied. These properties of *a*-C:H may turn out to be useful for solving the problem of the encapsulation of metal nanoclusters in a solid-state media. The importance of this problem is illustrated by the nanostructures based on magnetic metals [1], since the encapsulation in this case can play a dual role: to prevent the aggressive effect of the environment and to reduce the exchange interaction between neighboring particles, thus offering a bright outlook for using such nanocomposites as devices for high-density magnetic recording. The ability of *a*-C:H to effectively protect the surface of a metal from degradation in aggressive media can be illustrated by the example of Ag, which is very susceptible to corrosion [2].

The films of hydrogenated amorphous C grown by magnetron cosputtering of C and a metal contain nanometer-sized metal clusters [3]. These clusters are formed by self-organization in the course of film growth. In this context, the problem of their size distribution arises. The problem of the determination of correlation in their mutual arrangement is no less important. Electron microscopy, which allows individual clusters to be observed, seems to be a suitable method for solving these problems. However, the images of C films obtained by transmission electron microscopy (TEM) are, as a rule, highly contaminated with noise. This is caused by the fact that amorphous C usually contains two phases: a diamond-like phase (sp^3 hybridization, a wide band gap) and a graphite-like phase (sp^2 hybridization, metallic conduction through the fragments of graphene planes). The phases are mixed in the form of nanocomposites with sizes close to the sizes of metal clusters. The concentration of each phase varies from point to point in a film, so that the intensity of the background in a micrograph also considerably varies, exceeding at some points the intensity of the signal from a metallic cluster. All these circumstances often make it impossible to obtain satisfactory results by conventional Fourier analysis of the image of amorphous C with metal dopants.

In this study, we analyze the TEM images of *a*-C:(H, Cu) films. Our analysis is based on the filtering of the image in direct space with a straightforward construction of the size distribution function of clusters.

SPLINE FILTERING OF IMAGE

A fragment of a typical dark-field microimage of amorphous Cu-doped C film is shown in Fig. 1 (the width of the area shown is 0.3 μm). An intense nonuniform background can be seen in this microimage; the absolute intensity of this background in some regions exceeds the intensity of metallic-cluster images. The profile of intensity distribution across the horizontal cross section is shown schematically in Fig. 2a. In order to obtain an image which permits making a count of the clusters and the determination of their sizes, one has to subtract the background from the image and normalize the intensity of the image of clusters to a constant value.

1063-7826/02/3607-0743$22.00

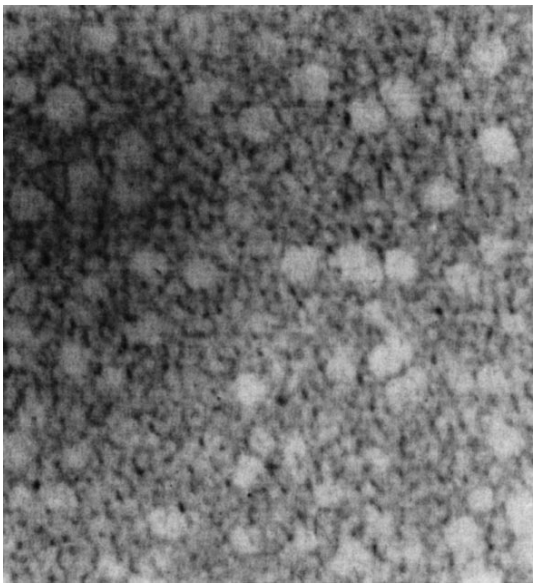

Fig. 1. A TEM micrograph of Cu-doped C film. The cross section dimension is 300 nm.

In order to filter the image, one can make use of the fact that the variation in the background intensity across the image is weaker than the variation of intensity from the clusters. The background intensity is determined in the following way. First of all, it is necessary to suppress high frequency noise, i.e., the intensity of jumps occurring over distances shorter than the resolution of an electron microscope. Such jumps have a comparatively low amplitude. The average amplitude of high frequency noise over a typical size of clusters is close to zero. Therefore, in order to suppress the high frequency noise, one can use Gaussian spreading. The image is divided into isolated dots (square fragments with sizes on the order of a wavelength with a high frequency). Then, each dot is substituted by a spot of intensity

$$I = I_0 \frac{1}{\pi} \exp\left(-\frac{|\mathbf{r} - \mathbf{r}_0|^2}{R^2} \right),$$

where R is the parameter of spreading, and I_0 is the initial intensity at the point r_0. Since R is chosen to be several times smaller than the characteristic size of a cluster, this broadening does not erase the image of cluster distribution. The spots are superimposed on each other, with the average intensity of the resulting image being equal to the average intensity of the initial image. The result of smoothing is illustrated in Fig 2b.

Next, the image is divided into square fragments with sizes exceeding the visible size of clusters, but being smaller than the characteristic size of variation in the background intensity. Then, the distribution in intensity of the image in each square is calculated. The upper part of the distribution is excluded from the consideration (60–90% of points, the parameter is selected to obtain the best reproducibility of results). The mean intensity over the remaining points (having the lowest intensity) is taken to describe the lower envelope of intensity in a given square. Elimination of the most intense points in the calculations of the mean intensity allows one to retain the shape of positive intensity

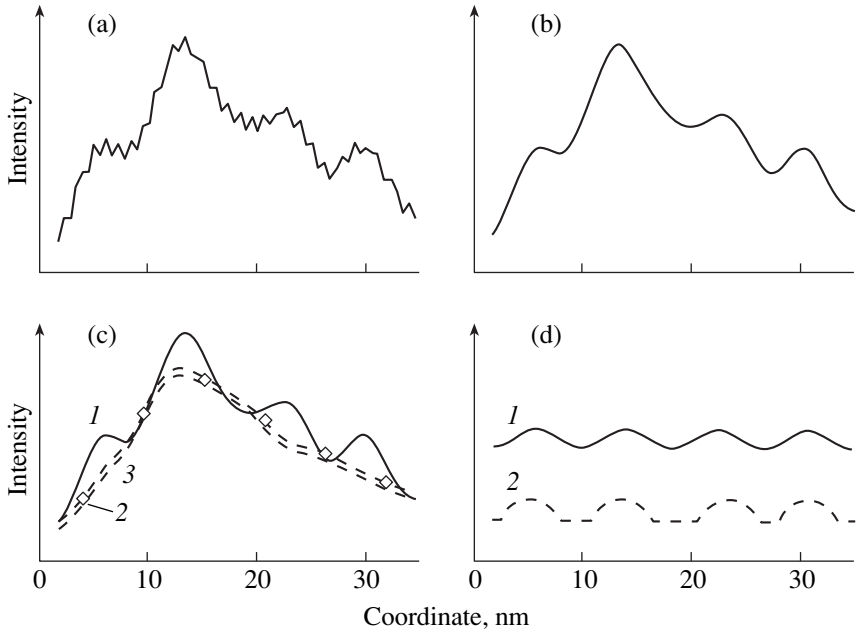

Fig. 2. (a) Profile of the image section; (b) profile after the Gaussian spreading; (c) (*1*) profile of the section, (*2*) the mean value of background intensity, and (*3*) interpolated background intensity; and (d) (*1*) profile after filtering, (*2*) the true intensity shape of cluster images.

peaks corresponding to the clusters. To construct a two-dimensional (2D) lower envelope, it is necessary to interpolate the mean values of the background intensity to the entire area of an image.

A two-dimensional bicubic spline is used for such interpolation. The 2D bicubic spline is a function consisting of each of the square fragments of a third-degree polynomial with respect to each coordinate; the function is equal to the mean value of intensity at the center of a given square, is joined at the boundaries of squares, and thus satisfies the condition for continuity of a spline (the equality of the first and second derivatives with respect to coordinates at the boundaries). By writing these conditions in terms of polynomial coefficients and solving the corresponding system of equations, one can obtain the polynomial coefficients and, thus, the values of the interpolated function (the background intensity) at each point of an image. The advantage of using a spline compared to other methods of extrapolations is the fact that spline interpolation allows stability to be maintained independently of the type of interpolated function. The mean values of background intensity are shown in Fig. 2c by diamonds; the spline is shown by a double dashed line (the spacing between lines corresponds to the interval of rejection of the most intense points in the calculation of the mean value).

The intensity of the background is subtracted from the intensity of the image, then the intensities of the peaks are normalized to unity. The result of such subtraction is illustrated in Fig. 2d (the upper curve). For comparison, the lower curve shows the profile of the image intensity for clusters used in constructing the model image in Fig. 2a.

The result of filtering an actual image of an *a*-C:(H, Cu) film shown in Fig. 1 is given in Fig. 3. The image of such quality can be analyzed in the direct space. In analysis, the connected regions with intensities higher than threshold values can be singled out as clusters.

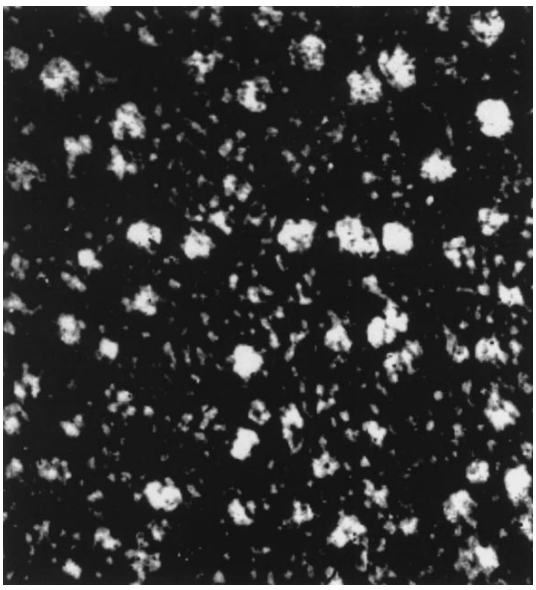

Fig. 3. Micrograph of the film after the image filtering.

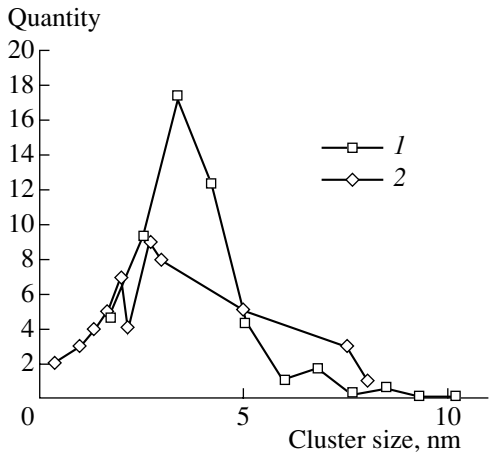

Fig. 4. Size distribution functions of Cu clusters for the films with (*1*) 9 and (*2*) 20 at. % of Cu.

ANALYSIS OF IMAGES OF AMORPHOUS Cu-DOPED CARBON

The spline filtering and direct counting of clusters were executed as a computer program and applied to the analysis of the electron microscope images of amorphous Cu-doped C with various Cu content. The resulting cluster size distribution functions for the films with Cu atomic concentrations of 9 and 20% are shown in Fig. 4. It can be seen that the distribution function for a film with 9% Cu has a peak at about 4 nm. As was previously shown [4], this cluster size, indeed, is characteristic of *a*-C:(H, Cu) films with Cu concentrations of 9–14%. In this case, the shape of the distribution function near the peak approaches the Gaussian one, which is indicative of the fluctuation mechanism of cluster formation.

The situation changes with the introduction of 20% of Cu. The size distribution function of clusters remains almost the same for small-sized clusters, but it is considerably extended towards large clusters (7–8 nm) and can no longer be described by the Gaussian distribution. This points to a new mechanism of cluster formation, namely, to the coalescence of smaller nuclei. The process of coalescence occurs in parallel with the fluctuation nucleation; its influence is greater the higher the concentration of Cu.

For the identification of the correlation in cluster arrangement, the dependence of cluster spacing on cluster size was also analyzed. For this purpose, the dependence of the directly measured mean distance from one cluster to its neighbor on the cluster size was plotted. The data obtained for the films containing 9 and 20 at. % of Cu are shown in Fig. 5. In both cases, it can be seen that the space near the large clusters is

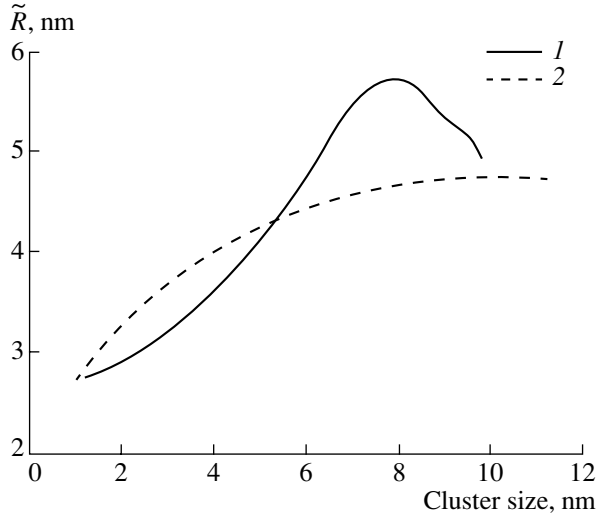

Fig. 5. Distribution function of intercluster spacing for the films with (*1*) 9 and (*2*) 20 at. % of Cu: dependence of the mean distance $\tilde{R}$ between neighboring cluster on cluster size.

larger than around smaller clusters. At comparatively low Cu contents and cluster sizes larger than 8 nm, this trend is violated, which can be understood assuming that the seemingly large clusters at low Cu concentrations most likely arise through the accidental superposition of the images from smaller clusters.

CONCLUSION

The spline filtering of electron microscope images of *a*-C:(H, Cu) films with high background noise made it possible to analyze, in direct space, the cluster size distribution function. We showed the following:

(1) At a Cu content of 9%, the film contains Cu clusters whose sizes obey the Gaussian distribution around a mean size of 4 nm. They arise due to the fluctuation mechanism of self-nucleation.

(2) The film also contains clusters with characteristic sizes of 7–8 nm; their fraction at 9% of Cu is insignificant, but it considerably increases at 20% of Cu. The nucleation of these clusters is probably a consequence of the coalescence of smaller clusters.

(3) The arrangement of clusters in a film is correlated. The larger clusters are surrounded by a space with a low density of Cu. The spacing of small clusters is about 3–4 nm.

The new software for spline filtering of images with a high-noise background can be applied not only to nanocomposites but also to any of the cases where the search and determination of the parameters of objects against the background of an intense low-frequency and a less intense high-frequency noise are required.

ACKNOWLEDGMENTS

This study was supported by the Russian Foundation for Basic Research, project nos. 01-02-06456 and 00-02-17004.

REFERENCES

1. T. Hayashi, S. Hirono, M. Tomito, and S. Umemura, Nature **381**, 772 (1996).
2. G. A. Dyuzev, V. I. Ivanov-Omskiĭ, E. K. Kuznetsova, *et al.*, Mol. Mater. **8**, 103 (1996).
3. T. N. Vasilevskaya, S. G. Yastrebov, N. S. Andreev, *et al.*, Fiz. Tverd. Tela (St. Petersburg) **41**, 2088 (1999) [Phys. Solid State **41**, 1918 (1999)].
4. V. I. Ivanov-Omskiĭ, A. B. Lodygin, A. A. Sitnikova, *et al.*, J. Chem. Vap. Deposition **5**, 198 (1997).

Translated by A. Zalesskiĭ

Semiconductors, Vol. 36, No. 7, 2002, pp. 747–750. Translated from Fizika i Tekhnika Poluprovodnikov, Vol. 36, No. 7, 2002, pp. 801–804.

ELECTRONIC AND OPTICAL PROPERTIES OF SEMICONDUCTORS

Modification of the Electrical and Photoelectric Properties of $Mg_{0.15}Cd_{0.85}Te$ Solid Solutions as a Result of Pulsed Laser Irradiation within the Transparency Range

A. Baĭdullaeva, E. F. Venger, A. I. Vlasenko, A. V. Lomovtsev, and P. E. Mozol'

Institute of Semiconductor Physics, National Academy of Sciences of Ukraine, Kiev, 03028 Ukraine

e-mail: baidulla@class.semicond.kiev.ua

Submitted September 18, 2001; accepted for publication October 30, 2001

Abstract—Changes in the equilibrium conductivity and photoconductivity of $Mg_{0.15}Cd_{0.85}Te$ solid solutions exposed to pulsed laser radiation at a frequency from the transparency range of the crystal are studied as a function of the laser fluence. An increase in the photoconductivity and a shift of the photoconductivity long-wavelength limit to higher energies are found. A change in the electrical properties of the crystals is attributed to an increase in the concentration of donors with ionization energies $E_1 = 0.015$ eV and $E_2 = 0.035$ eV in the surface region. Possible causes and mechanisms of the changes in the photoelectric properties of the II–VI crystals exposed to laser radiation are analyzed. © *2002 MAIK "Nauka/Interperiodica".*

$Mg_xCd_{1-x}Te$ solid solutions have been studied little, but they can be rated among the II–VI compounds which hold much promise for the design of light-emitting diodes (LEDs) [1, 2]. The possibility of having control over the electrical and photoelectric properties of the initial material is of particular interest, because these properties are mainly responsible for the operating characteristics of the LEDs.

According to our previous studies, the electrical properties of a material can be effectively modified by pulsed laser radiation with a nanosecond pulse duration and frequency from the fundamental absorption band [3, 4]. This is due to the fact that the properties of II–VI compounds are affected by the laser-induced intrinsic defects to a degree comparable to that provided by the dopants.

For example, a change in the electrical properties of $Mg_{0.20}Cd_{0.80}Te$ single crystals under ruby laser irradiation with the photon energy corresponding to the fundamental absorption range was attributed to both the formation of a Te film at the crystal surface and an increase in the concentration of shallow-level hydrogen-like donors with an ionization energy $E_1 = 0.015$ eV and the formation of deeper donors with an ionization energy $E_2 = 0.035$ eV. The formation of a layer with a wider band gap, which appeared in the surface region of the crystal, was related to the cadmium depletion of the solid solutions due to the low bonding energy of Cd compared to that of Mg in the metal sublattice of the of $Mg_{0.20}Cd_{0.80}Te$ solid solution.

In this study, we considered $Mg_{0.15}Cd_{0.85}Te$ single crystals with a band gap $E_g \approx 1.7$ eV. High-resistivity bulk single crystals with a sphalerite-type lattice were obtained by crystallization from a melt prepared by alloying Cd, Mg, and Te components in the proper atomic ratio in quartz cells evacuated down to a residual pressure of $\sim 10^{-5}$ Torr. The molar concentration was determined by X-ray phase analysis.

For dark conductivity and photoconductivity (PC) measurements, we prepared $2 \times 2 \times 1$ mm^3-size samples with contacts deposited on their ends. In order to obtain a profile of defects, the samples were subjected to layer-by-layer etching in the polishing etchant.

The samples were exposed at room temperature to neodymium laser pulses with the photon energy $h\nu = 1.17$ eV (within the transparency range of the crystal), pulse duration $\tau = 1.5 \times 10^{-8}$ s, and the laser fluence below the damage threshold, which resulted in only the slight heating of the samples up to 40°C [5].

After irradiation of the $Mg_{0.15}Cd_{0.85}Te$ crystals, their dark conductivity σ_d and photoconductivity σ_{ph} increased by a factor of 10–10^3 (the photoconductivity was measured under exposure to the visible light of an incandescent lamp with a luminosity of 500 lx) (Fig. 1). It is evident that, at the fluence $I = 5$ MW/cm^2 (below the threshold), both σ_d and σ_{ph} remain constant with an increase in the number of pulses N (curves *1*, *3*). At higher fluence I (above the threshold), σ_d and σ_{ph} first grow with N and then level off (curves *2*, *4*).

The spectral dependences of the photoresponse I_{pc} (Fig. 2) of the initial $Mg_{0.15}Cd_{0.85}Te$ sample (curves *1*, *4* at temperature $T = 300$ and 77 K, respectively) and the sample irradiated by neodymium laser pulses (curves *2*, *3* at 300 K and curve *5* at 77 K, irradiation dose $D = I\tau N$, corresponded to the ascending portion of the σ_d and σ_{ph}

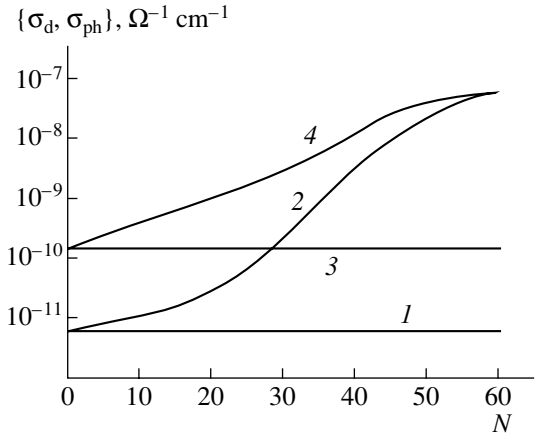

Fig. 1. (*1*, *2*) Dark conductivity σ_d and (*3*, *4*) photoconductivity σ_{ph} of $Mg_{0.15}Cd_{0.85}Te$ sample versus the number of laser pulses *N* at different fluences: (*1*, *3*) 5 and (*2*, *4*) 20 MW/cm^2.

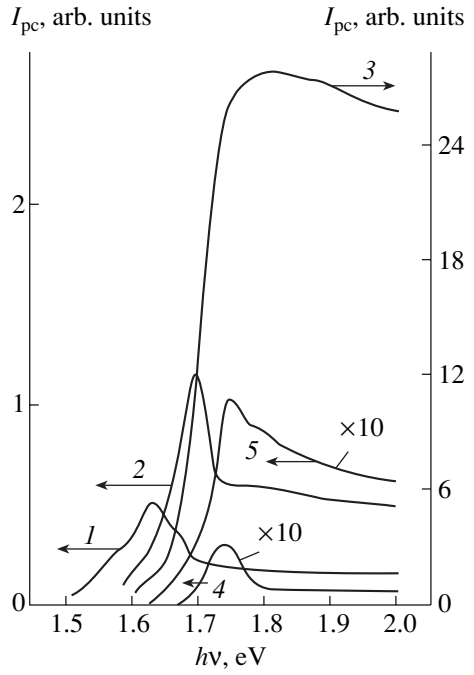

Fig. 2. Photoconductivity spectra of (*1*, *4*) as-prepared and (*2*, *3*, *5*) irradiated $Mg_{0.15}Cd_{0.85}Te$ samples at T = (*1*–*3*) 300 and (*4*, *5*) 77 K. Laser fluence $I_2 < I_3$ for curves *2* and *3*, respectively.

curves) indicate that laser irradiation leads to an increase in the photoconductivity amplitude and shifts the long-wavelength limit to higher energies but does not give rise to new photoconductivity bands. It should be noted that the initial crystals were highly inhomogeneous. For both the initial and the irradiated crystals, the broadening of the photoconductivity long-wavelength limit was ~0.11 eV.

In order to establish the cause of the shift of the photoconductivity peak, we performed a comparative analysis of the photoconductivity spectra at 300 and 77 K of the as-prepared and irradiated samples. It was found that, at low (below threshold) doses, the sample-to-sample difference of the shift for the crystals of the same composition ranged from 0.0035 and 0.023 eV at 77 K. A shift of the photoconductivity peak at 300 K amounted to ~0.1 eV, which is larger than the shift value at 77 K. This fact can be related to the origin of the photoconductivity peak: at 300 K, it has an impurity nature, while, at 77 K, intrinsic photoconductivity is observed. After irradiation, the photoconductivity spectrum at 300 K indicates a considerable growth of the intrinsic photoconductivity and the impurity peak is only slightly noticeable against the background of the band-to-band peak. The impurity nature of the photoconductivity peak in an as-prepared crystal is indicated by the fact that the special feature at this energy is retained after the low-dose irradiation, despite a pronounced increase in the photocurrent in the intrinsic range (the short-wavelength wing).

The photoconductivity spectra of the initial crystal at T = 77 K (Fig. 2, curve *4*) shows an abrupt short-wavelength falloff, which can be attributed to intense surface recombination. After laser treatment, the short-wavelength slope becomes less steep (Fig. 2, curve *5*), which is connected with a decrease in the surface recombination velocity from 10^5 cm/s in as-prepared to 10^3 cm/s in the irradiated samples due to the laser-induced cleaning of the crystal surface.

The layer-by-layer etching of the samples revealed that the shift of the photoconductivity cutoff, as well as the σ_d and σ_{ph} increase after the neodymium laser irradiation, is not uniform through the crystal bulk: being maximal at the sample surface, both effects become less profound with the distance from the surface and remain nearly constant in the depth of a sample. The increase in σ_d in the crystal bulk is considerable, while that of σ_{ph} is only moderate. The sensitized layer thickness is ~5 μm (Fig. 3). After etching to a depth of ~3 μm, the photoconductivity decreases without a change in the spectrum shape (Fig. 4, curves *3*, *4*). After further etching, the shape and the edge position of the spectrum are restored; however, the photoconductivity value remains elevated compared to that in the as-prepared sample (Fig. 4, curve *5*).

In the samples exposed to the surface-absorbed light (ruby laser radiation), the photoconductivity spectral dependences are similar to those shown in Fig. 2 (curves *2*–*4*) with the only difference being in the sensitized layer thickness of ~0.1 μm, which correlates with the absorption depth ~1/*K*, where *K* is the absorption coefficient at the ruby laser frequency.

It was demonstrated in [3] that ruby laser pulses with $h\nu$ = 1.78 eV give rise to a *p*-type conducting film of Te at the crystal surface. In our study, after irradiation the samples were etched in a methanol solution of 1N KOH, which dissolved the Te without etching the $Mg_{0.15}Cd_{0.85}Te$.

After rinsing the irradiated samples, their dark conductivity exceeded the initial *n*-type conductivity of as-prepared samples and the residual conductivity was also observed. The increased conductivity after the etching of the Te film indicates the formation of shallow (with an activation energy of 0.015 eV) donor levels. Then, the residual conductivity may also be explained by the presence of a low-resistivity layer on the high-resistivity crystal surface [6].

Etching CdTe in a bromine-containing polishing etchant lowers the equilibrium conductivity and gives rise to a slope of the conductivity temperature dependence corresponding to the 0.035 eV level.

The 0.015-eV level may be associated with either the interstitial defect Cd_i or the impurities of In and Cl [7]. This would point to Cd_i formation or to Cl and In release from the clusters. The appearance of a deeper 0.035-eV level may be associated, for example, with the formation of V_{Te} vacancies [8].

Thus, a change in the electrical properties of the crystals is caused by an increase in the donor concentration in the surface region.

In order to explain the changes in the electrical and photoelectric properties, we compared the results of laser irradiation and thermal annealing for different binary II–VI compounds [9]. The comparison revealed a number of certain common features for the laser-induced formation of defects in various II–VI semiconductors.

(1) For any relationship between the wavelength and the band gap ($h\nu > E_g$ or $h\nu < E_g$), the region of the most intense formation of defects is the crystal surface.

(2) Since the interstitial atoms tend to evaporate, the majority of the defects that are formed in the surface region are the vacancies of a metal (V_m) and the vacancies of a chalcogen (V_{ch}); therefore, it is often the difference between their concentrations or between the concentrations of the vacancies and impurities that controls the conductivity of a crystal. This is possible in view of the considerable concentration of vacancies that are formed in the surface region ($\sim 10^{18}$ cm^{-3}).

(3) The results of laser irradiation are similar to those of thermal annealing: the relationship between the evaporation rates of the metal and chalcogen is nearly the same for both actions (for example, the maximal concentration of electrons $n = V_m - V_{ch} \approx 10^{18}$ cm^{-3} in the surface region of CdS subjected either to laser irradiation or thermal annealing).

(4) Irradiation in a low-absorption spectral range produces both vacancies and interstitial atoms in the crystal bulk; however, the characteristics of the crystal are still controlled mainly by the surface region.

Let us take a closer look at the evolution of σ_d and σ_{ph} after the laser irradiation of crystals with different types of conductivity and at the different relationships between the rates of the removal of metal and chalcogen atoms. In accordance with the aforementioned, we will restrict our consideration to the surface region and take into account intrinsic defects only. The formation of complexes, including clusters, depends mostly on the interstitial atoms because of their high mobility and can be justifiably disregarded in the surface region where there are no interstitial atoms.

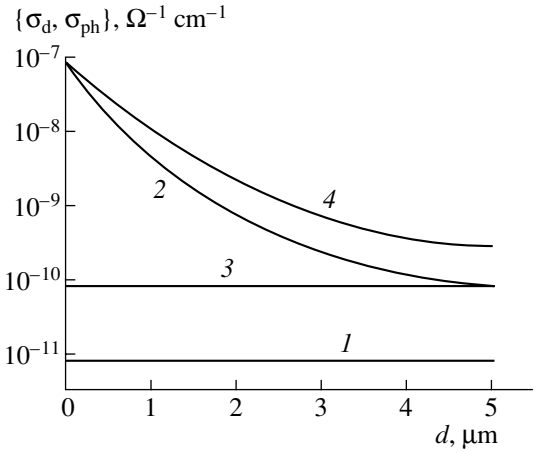

Fig. 3. (*1*, *2*) Dark conductivity σ_d and (*3*, *4*) photoconductivity σ_{ph} versus the etched layer thickness *d* for (*1*, *3*) as-prepared and (*2*, *4*) irradiated samples.

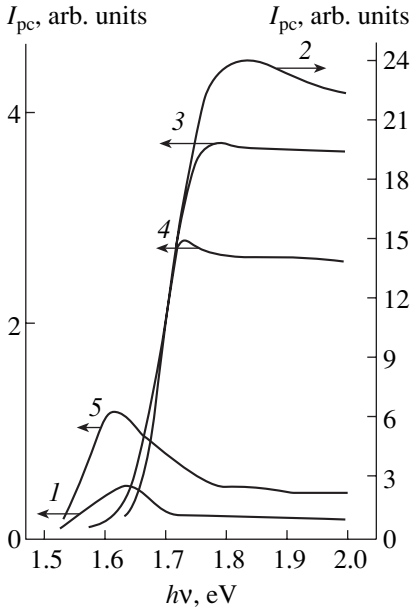

Fig. 4. Photoconductivity spectra of (*1*) as-prepared, (*2*) irradiated, and (*3*–*5*) etched $Mg_{0.15}Cd_{0.85}Te$ samples with the etched layer thickness of (*3*) 2, (*4*) 3, and (*5*) 5 μm at $T = 300$ K.

Two different cases will be considered.

(i) The rate of removal of the chalcogen is higher than that of the metal; i.e., the concentration of V_{ch} donors is higher than that of V_m acceptors. In an *n*-type crystal, an increase in the equilibrium conductivity and

photosensitivity of the surface region should be expected. The latter is due to the laser-induced formation of photosensitive centers compensated by donors (V_{ch}). In the opposite case of a *p*-type crystal, a decrease in the equilibrium conductivity and even a conversion of the conductivity type are possible. The photoconductivity may become lower (for the *n*-type conductivity), remain as it is, or increase (for the *p*-type conductivity).

(ii) The rate of removal of the chalcogen is lower than that of the metal; i.e., the region is enriched with acceptors V_m. In the *n*-type crystals, the equilibrium conductivity is expected to decrease (or even change its sign) and the same is true for the *n*-type photoconductivity, because the concentration of laser-induced donors turns out to be lower than the concentration of sensitivity centers; this leads to an increase in the concentration of nonequilibrium holes at these centers and reduces the electron lifetime.

In a crystal with the *p*-type equilibrium conductivity and photoconductivity, both σ_d and σ_{ph} are likely to increase.

These conclusions are supported in experimental studies on the effect of laser radiation on the electrical and photoelectric properties of CdS, CdSe, CdTe, and $Zn_xCd_{1-x}Se$ crystals [2, 4, 9].

In addition to the simple cases considered above, more complicated situations may be encountered, in which the influence of impurities and the formation of clusters should be taken into account. In particular, an increase in the vacancy concentration may force the impurity from the interstice into the lattice site, from one sublattice into another (for example, the transition of Ge from the Te sublattice to the Cd sublattice in CdTe), and from clusters into lattice sites [10, 11].

In summary, we can conclude the following.

(I) The changes induced in the electrical and photoelectric properties of $Mg_{0.15}Cd_{0.85}Te$ solid solutions by laser pulses with a photon energy in the transparency range are not uniform within the crystal bulk: the most important changes occur in the surface region.

(II) An increase in σ_d and σ_{ph} can be attributed to the laser-induced increase in the concentration of donors with activation energies $E_1 = 0.015$ eV and $E_2 = 0.035$ eV in the surface region.

(III) A comparison between the result of the laser irradiation with that of the thermal annealing of $Mg_{0.15}Cd_{0.85}Te$ solid solutions and II–VI semiconductor compounds suggests that it is the rate of removal of the components which accounts for the majority of laser-induced changes in the characteristics of these materials.

REFERENCES

1. R. Yaniomoto, M. Inoue, K. Hob, and T. Shitaya, Jpn. J. Appl. Phys. **6** (5), 537 (1967).
2. R. Yamomoto and K. Itoh, Jpn. J. Appl. Phys. **8** (3), 341 (1969).
3. A. P. Akhayan, A. Baĭdullaeva, N. E. Korsunskaya, and P. E. Mozol', Poverkhnost, No. 12, 106 (1987).
4. A. Baĭdullaeva, P. E. Mozol', E. A. Sal'kov, and N. I. Vitryakhovskiĭ, Fiz. Tverd. Tela (Leningrad) **28** (11), 3561 (1986) [Sov. Phys. Solid State **28**, 2009 (1986)].
5. P. E. Mozol', M. L. Lisitsa, V. S. Koval', *et al.*, Kvantovaya Élektron. (Kiev), No. 10, 31 (1976).
6. I. V. Markevich, V. A. Khvostov, and M. K. Sheĭnkman, Fiz. Tekh. Poluprovodn. (Leningrad) **5** (10), 1904 (1971) [Sov. Phys. Semicond. **5**, 1654 (1971)].
7. N. V. Agrinskaya, N. N. Zinov'eva, O. A. Matveev, and I. D. Yaroshetskiĭ, Fiz. Tekh. Poluprovodn. (Leningrad) **14** (1), 172 (1980) [Sov. Phys. Semicond. **14**, 100 (1980)].
8. M. Nagabhuoshanum, R. G. Ramchandar, and B. Hari Babu, J. Less-Common Met. **102**, 97 (1984).
9. P. E. Mozol', A. Baĭdullaeva, N. E. Korsunskaya, and E. A. Sal'kov, Kvantovaya Élektron. (Kiev) **35**, 41 (1988).
10. V. V. Matlakh, M. I. Ilashchuk, and O. S. Popenko, Izv. Akad. Nauk SSSR, Neorg. Mater. **19** (11), 1935 (1983).
11. A. Baĭdullaeva, B. Dzhumaev, N. E. Korsunskaya, and P. E. Mozol', Ukr. Fiz. Zh. **34** (8), 1265 (1989).

Translated by A. Sidorova-Biryukova

Semiconductors, Vol. 36, No. 7, 2002, pp. 751–754. Translated from Fizika i Tekhnika Poluprovodnikov, Vol. 36, No. 7, 2002, pp. 805–808.

ELECTRONIC AND OPTICAL PROPERTIES OF SEMICONDUCTORS

Titanium, Vanadium, and Nickel Impurities in 3*C*-SiC: Electronic Structure and Lattice Relaxation Effects

N. I. Medvedeva*, É. I. Yuryeva, and A. L. Ivanovskiĭ

Institute of Solid State Chemistry, Ural Branch, Russian Academy of Sciences, Yekaterinburg, 620219 Russia

**e-mail: medvedeva@ihim.uran.ru*

Submitted October 25, 2001; accepted for publication November 23, 2001

Abstract—Variations of chemical bonding and lattice relaxation in cubic silicon carbide in the presence of 3*d*-series impurity atoms (*M* = Ti, V, and Ni) were studied within the total-potential version of the method of linear muffin-tin orbitals. Substitution of the silicon atom with *M* causes a displacement of the closest carbon atoms outward from the impurity atom; the greatest effect is observed for the Ti atom. The conducting properties in doped compounds vary from semiconductor for the titanium atom (electron conduction) and nickel (hole conduction) to metallic in the case of vanadium. Features of chemical bonding were analyzed on the basis of the cohesion energy and charge densities. © *2002 MAIK "Nauka/Interperiodica".*

Silicon carbide is widely used in the search for new materials for active components of extreme semiconductor electronics. Functional properties of SiC single crystals, epitaxial layers, and films can be affected by various impurities, whose purposeful introduction allows for the control of the dielectric characteristics of a material [1, 2]. In recent years, 3*d*-series metals have been considered as efficient dopants for the modification of the SiC host properties [3, 4]. Energy states of single 3*d* impurities in 3*C*-SiC:*M* (*M* = Ti, V … Ni, and Cu) were studied in the context of the method of linear muffin-tin orbitals (LMTO) and Green's functions in [5]. It was concluded that a stable SiC:Ti system can be formed, while doping of the host with other 3*d* atoms is unfavorable in terms of energy. Calculations of the SiC:*M* system (*M* = Ti, V [6] and Cr, Fe, Co, Mn [7]) were carried out by the LMTO method using the tight-binding approximation and the supercell model. According to [7], the C sites are most probably occupied by Cr, Fe, and Co atoms, whereas Mn atoms predominantly reside at Si sites (Mn ⟶ Si).

In this study, the electronic structure of cubic (3*C*) SiC with substitutional impurities (3*C*-SiC:*M*, Mn ⟶ SiC) was calculated using the total-potential LMTO method. Metal atoms of the origin (Ti, V) and the end (Ni) of the 3*d* series were considered. The subject of the analysis was the effects of (i) structural changes (local lattice relaxation near the impurity center), (ii) band structure modification, and (iii) SiC energy state (cohesion energy) variations depending on the type of doping center.

The systems 3*C*-SiC:*M* (*M* = Ti, V, and Ni) were simulated using $MSi_7C_8E_8$ supercells (in the SiC fcc structure, a = 4.358 Å) with eight "empty" spheres (*E*) incorporated to meet the close packing condition. The impurity atom (*M*) has 4 carbon and 12 silicon atoms in the nearest neighborhood. In the nonrelaxed host, the distances M–C and M–Si are 1.89 and 3.08 Å, respectively. When optimizing the configuration of SiC:*M* systems, the coordinates of these atoms were varied (with retention of the total crystal symmetry); their equilibrium values were determined from the condition for the total-energy E_{tot} minimum. Calculations were carried out using the self-consistent spin-unlimited total-potential method of muffin-tin orbitals (TPMTO) [8] taking into account scalar-relativistic effects and using the exchange-correlation potential suggested in [9]. We calculated the energy bands, total and partial densities of states (DoS), and atomic magnetic moments (MM). To analyze the effect of impurities on the system of bonds in the host, the cohesion energies E_{coh} were calculated as the difference between the total phase energy and the sum of energies of phase-free atoms. To illustrate separate atomic interactions, we used charge density maps (CDM).

The results of calculations for defect-free 3*C*-SiC are shown in Fig. 1. The electron spectrum of the DoS contains two bands (from –15 to –10 eV and from –8 to 0 eV) separated by a gap of about 2 eV. The low-energy band includes contributions of C-2*s* and Si-3*s* states; its top region also includes a contribution of Si-3*p* states. The upper occupied band contains hybridized Si-3*s*, Si-3*p*, and C-2*p* states. The peak near the bottom of this band is mainly composed of Si-3*s*–C-2*p* states; the top of this band is caused by Si-3*p* and C-2*p* states. The conduction band is composed of Si-3*s*, -3*p*, -3*d*, and antibonding C-2*p* states. The band gap (an indirect transition is observed toward the Γ–*X* Brillouin zone) is about 2.4 eV wide. The above results are consistent with previous calculations [10–12] and the data of X-ray emission and photoelectron spectroscopy [13]. According to [13], the band gap is about 2.39 eV wide. The 3*C*-SiC crystal cohesion energy is 7.39 eV/atom,

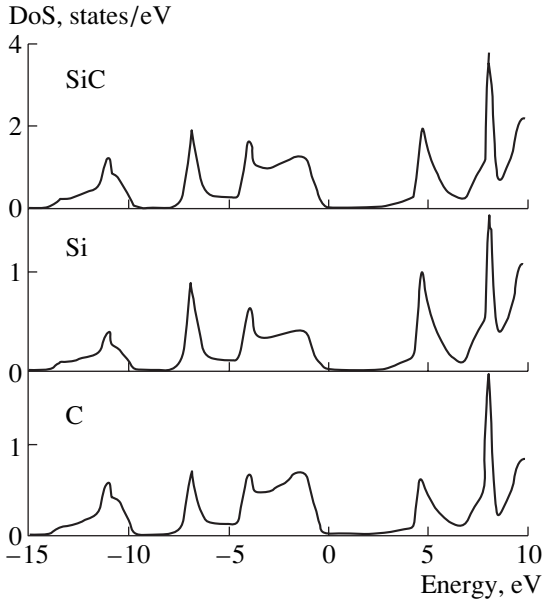

Fig. 1. Total (top) and partial densities of 3*C*-SiC states.

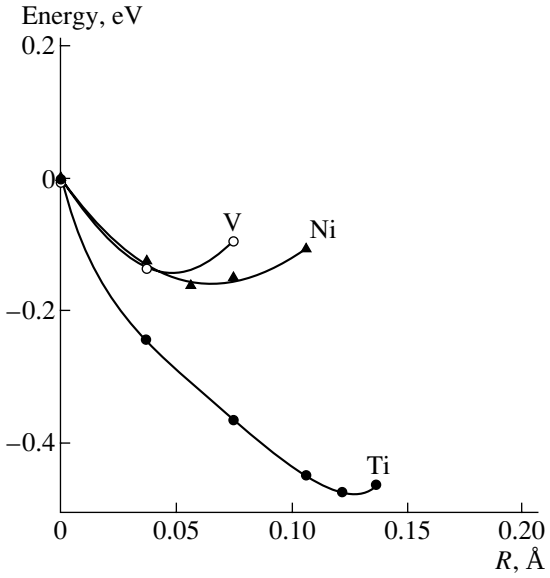

Fig. 2. Dependence of the total energy of SiC:*M* systems on the carbon atom displacement *R* from the *M* centers with respect to the equilibrium distance $R_{Si–C}$.

which also conforms to the experimental value of 6.50 eV/atom [14]. Estimations of E_{coh} within the Hartree–Fock pseudopotential method yield 4.51 and, taking into account the correlation correction, 6.40 eV/atom [12].

To analyze local distortions of the 3*C*-SiC:*M* lattice, we consider the dependence of the total energy E_{tot} on the positions of carbon atoms closest to impurity *M* (on the distance *M*–C ($R_{M–C}$)) (Fig. 2). One can see that doping of SiC with V and Ni atoms leads to rather weak relaxation effects: carbon atoms are displaced (with respect to the equilibrium value $R_{Si–C}$ = 1.89 Å) by 0.04 and 0.05 Å, respectively. In this case, the system energy changes by less than 0.2 eV. For SiC:Ti, the carbon atom displacement (about 0.12 Å) is much larger and is accompanied by a more significant decrease in the system energy (about 0.5 eV). The calculated atomic displacements in the Ti ⟶ V impurity series correlate with the ratio of atomic radii, $R_{at}(M) > R_{at}$(Si) [15]. For Ni, on the basis of the relation between atomic radii R_{at}(Ni) ≤ R_{at}(Si) [15], we may expect that the nearest atoms are displaced toward the impurity, which contradicts the results of numerical calculations. In contrast, the tendency found (radial displacements of carbon atoms from *M* centers) correlates with the covalent radii of Si and *M* ions [15]. This is indicative of the significant role of electronic interaction in the local relaxation effects.

To analyze the changes in the electron structure in the 3*C*-SiC:*M* systems, we consider their total and partial DoS (see Figs. 3–5). One can see that an additional intense peak (Fig. 3) arises in the region of the high-energy edge of the valence band bottom due to hybridization of *M*4*s*, 3*d*, Si-3*p*, and C-2*p* states. For Ti and V impurities, their 3*d* states control the structure of the conduction band edge, forming an almost localized subband separated from the silicon and carbon states by a pseudogap in SiC:Ti and a narrow (about 0.1 eV) band gap for SiC:V. The conduction types of systems with these dopants should differ. Isoelectronic substitutions of Ti ⟶ Si do not change the semiconductor properties of the host: all the bonding states are populated, while the conduction band is empty; in this case, the band gap is widened to 2.45 eV. With V at the Si site, the Fermi level is in the vicinity of the conduction band bottom (see Fig. 4); i.e., a metallic conduction type can be expected. The band gap between the valence and conduction bands narrows down to 1.42 eV. In contrast to Ti and Ni, the V impurity is magnetic: the MM of the vanadium atom is about $0.9\mu_B$ (μ_B is the Bohr magneton). For SiC:V, the Fermi level is at the slope of the sharp peak of V-3*d* states with an upward spin; the DoS at the Fermi level is $N(E_F)$ = 4.17 states/eV. The peak of V-3*d* states with a downward spin is higher than E_F by about 0.5 eV and does not contribute to $N(E_F)$. The valence band top for SiC:Ti (SiC:V) is mainly caused by Si-3*p* and C-2*p* states with an admixture of the 3*d* state of titanium (vanadium).

Radical differences are observed for the DoS of SiC:Ni (see Fig. 5). Impurity states are mostly localized below E_F, while the impurity-band width is close to that of the upper occupied band of the host. The semimetal properties of SiC:Ni are caused by the peak of the density of Ni-3*d*–C-2*p*–Si-3*p* states above E_F, $N(E_F)$ = 4.42 states/eV. Hole conduction may be expected for this system, which is caused by electron transitions from the valence band to the empty subband (Fig. 5). In contrast to SiC:(Ti, V), the conduction-

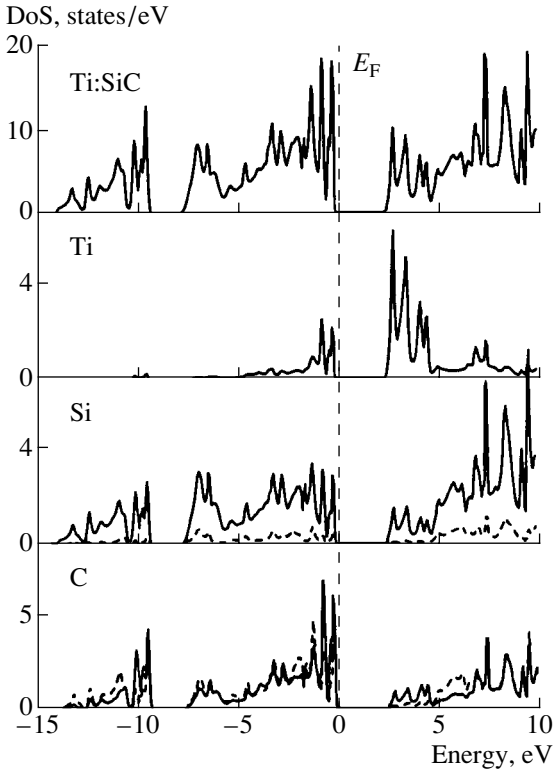

Fig. 3. Total (top) and partial densities of SiC:Ti states.

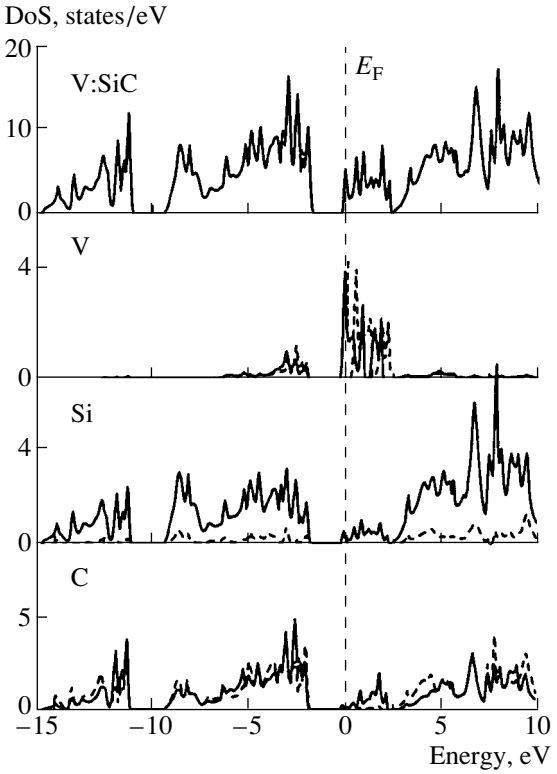

Fig. 4. Total (top) and partial densities of SiC:V states.

band bottom of SiC:Ni is strictly controlled by Si-3*p* and C-2*p* states, with the band gap being 1.67 eV wide.

Variation in the interatomic interaction in the 3*C*-SiC:*M* systems was analyzed by comparison of their cohesion energies E_{coh}. We found that E_{coh} = 7.34 (7.31, neglecting relaxation), 7.25, and 7.04 eV/atom for the systems with Ti, V, and Ni, respectively. Since E_{coh} accounts for the chemical bond force, it may be concluded that the *M*–C bonding in the SiC:*M* systems decreases in the series Ti > V > Ni. This tendency is evident when comparing the charge densities of the above system (Fig. 6), as well as when correlating these to the known laws of E_{coh} changes in binary carbides of the considered metals: 7.17 (TiC) > 6.95 (VC) > 5.65 (NiC) eV/atom [16].

The energy E_{sub} of silicon atom substitution may be estimated as the difference between E_{coh} of impurity systems and 3*C*-SiC, which yields E_{sub} = –0.05 (Ti), –0.14 (V), and –0.35 eV (Ni). It is evident that the titanium impurity is characterized by the lowest absolute value of E_{sub}, which is comparable to the energy kT (0.02 eV at room temperature). These calculations allow the following conclusions.

(i) Substitution of the silicon atom with titanium, vanadium, and nickel atoms is accompanied by radial displacements of the closest carbon atoms away from the impurity center; this effect is most pronounced for titanium.

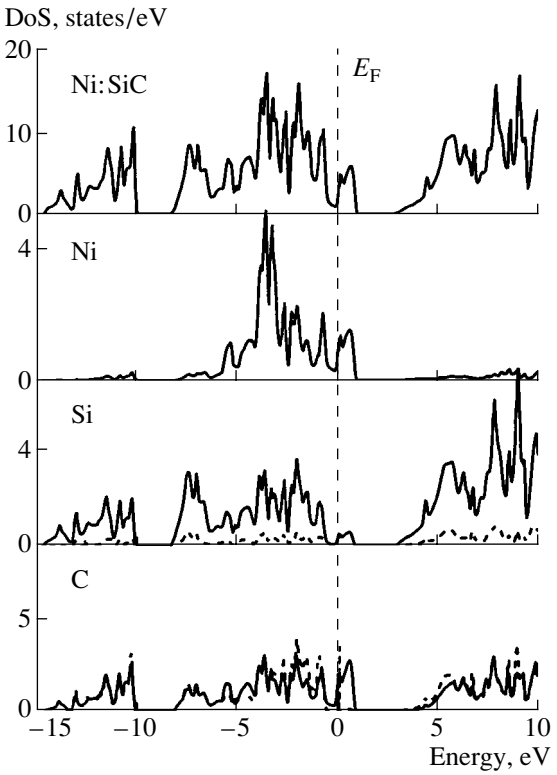

Fig. 5. Total and partial density of SiC:Ni states.

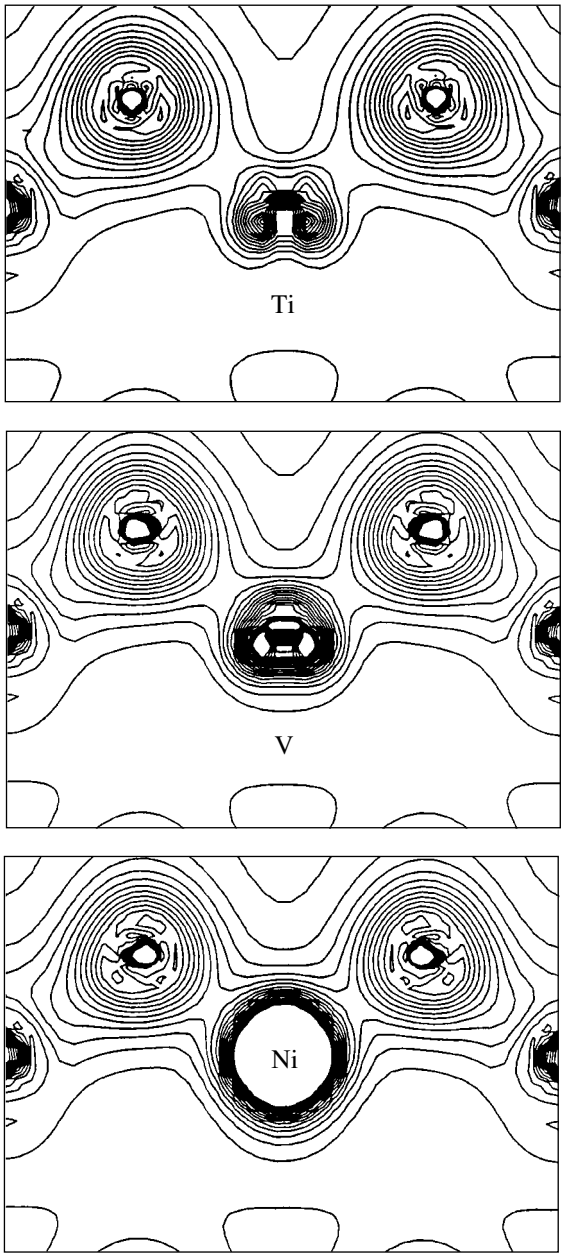

Fig. 6. Maps of the charge densities of valence states (at the section along the *M*–C bond lines) in SiC:(Ti, V, Ni).

(ii) The conducting properties of a doped material vary from those of a semiconductor for SiC:Ti (electron conduction) and SiC:Ni (hole conduction) to those of a metal in SiC:V.

(iii) The energy of silicon atom replacement with titanium, vanadium, and nickel atoms is negative; it is lowest for the titanium atom and grows (in absolute value) in the series of the considered substitutional impurities.

ACKNOWLEDGMENTS

This study was supported by the Russian Foundation for Basic Research, project no. 01-03-33175.

REFERENCES

1. A. A. Lebedev, Fiz. Tekh. Poluprovodn. (St. Petersburg) **33**, 129 (1999) [Semiconductors **33**, 107 (1999)].
2. T. P. Chow, V. Klemka, J. Fedison, *et al.*, Solid-State Electron. **44**, 277 (2000).
3. S. A. Reshanov, Author's Abstract of Candidate's Dissertation (St. Petersburg, 2000).
4. V. V. Ilyasov, T. P. Zhdanova, I. Ya. Nikiforov, and A. V. Ilyasov, Zh. Strukt. Khim. **42**, 120 (2001).
5. R. F. Sibiryanov, A. L. Ivanovskiĭ, and G. P. Shveĭkin, Zh. Neorg. Khim. **38**, 1572 (1993).
6. N. I. Medvedeva, Zh. I. Gertner, V. V. Kraskovskaya, *et al.*, Neorg. Mater. **31**, 55 (1995).
7. V. A. Gubanov, C. Boekema, and C. Y. Fong, Appl. Phys. Lett. **78**, 216 (2001).
8. M. Methfessel and M. Scheffler, Physica B (Amsterdam) **172**, 175 (1991).
9. S. H. Vosko, L. Wilk, and M. Nusair, Can. J. Phys. **58**, 1200 (1980).
10. A. R. Lubinsky, D. E. Ellis, and G. S. Painter, Phys. Rev. B **11**, 1537 (1975).
11. K. J. Chang and M. L. Cohen, Phys. Rev. B **35**, 8196 (1987).
12. M. Causa, R. Dovesi, and C. Roetti, Phys. Rev. B **43**, 937 (1991).
13. G. Weich, in *Soft X-ray Band Spectra and Electron Structures of Metallic Materials*, Ed. by D. J. Fabian (Academic, London, 1968), p. 59.
14. I. N. Gnesin, G. G. Frantsevich, and G. G. Gnesin, *Silicon Carbide* (Naukova Dumka, Kiev, 1975).
15. I. I. Kornilov, N. M. Matveeva, A. I. Pryakhina, and R. S. Polyakova, *Metal-Chemical Properties of Elements from the Periodic Table* (Nauka, Moscow, 1966).
16. J. Haglund, G. Grimvall, T. Jarlborg, and A. F. Guillermet, Phys. Rev. B **43**, 14400 (1991).

Translated by A. Kazantsev

Semiconductors, Vol. 36, No. 7, 2002, pp. 755–757. Translated from Fizika i Tekhnika Poluprovodnikov, Vol. 36, No. 7, 2002, pp. 809–811.

ELECTRONIC AND OPTICAL PROPERTIES OF SEMICONDUCTORS

Parameters of Excitons in Monoclinic Zinc Diarsenide

A. I. Kozlov*, S. G. Kozlova*, A. V. Matveev*, and V. V. Sobolev**

** International Laboratory of High-Temperature Superconductivity and Solid-State Electronics, Academy of Sciences of Republic Moldova, Chisinau, MD2028 Republic of Moldova*

e-mail: kozlov@lises.asm.md

*** Udmurt State University, Izhevsk, 426034 Russia*

Submitted December 4, 2001; accepted for publication December 5, 2001

Abstract—Optical functions of $ZnAs_2$ single crystal were calculated using the Kramers–Kronig relations on the basis of measured reflectance spectra. Absorption spectra were analyzed near the band gap taking into account the contributions of both the exciton ground state and continuum. The free exciton parameters were determined. © *2002 MAIK "Nauka/Interperiodica".*

Zinc diarsenide single crystals belong to the monoclinic system (the space group is $P2_1/C = C_{2h}^5$) with eight formula units in the unit cell and the lattice parameters a = 8.85 Å, b = 7.21 Å, c = 7.56 Å, and β = 102.3°. Zinc diarsenide exhibits high anisotropy of optical properties [1].

The shape of the edge absorption spectra [2] suggested that $ZnAs_2$ is a direct-gap semiconductor. Composite structures of, presumably, an exciton nature were detected [3] in the reflectance and photoeffect spectra of $ZnAs_2$ cleaved surfaces; however, imperfections of samples and the measuring technique did not allow for unambiguous interpretation. Later on, precision reflectance spectra of $ZnAs_2$ single crystals were studied in a wide energy range ($h\nu$ = 1–5 eV) in polarized light at room and liquid nitrogen temperatures [4], as well as near the absorption edge [5–8] at 4.2, 80, and 293 K. The measurements were carried out with samples grown from the gas phase, with a natural specular surface and with the principal crystallographic axis c in the surface plane. Direct exciton transitions take place in $ZnAs_2$. As in isomorphic β-ZnP_2 (black modification) [9], only one exciton series (n = 1, 2, …) is observed in the polarization $\mathbf{E} \parallel \mathbf{c}$ of the electric vector of a light wave. However, the leading-line intensity in $ZnAs_2$ is much lower; the peak with n = 2 at 80 K is broadened. Free exciton states with n = 1, 2 are observed at the helium temperature. The band gap E_g was estimated as 1.050 eV from the positions E_n of spectrum peaks, which should be described within the hydrogen-like model as $E_n = E_g - R_0/n^2$ (R_0 is the exciton Rydberg). We note that the calculation based on the first two peaks can yield a somewhat underestimated value. As the temperature increases from 80 to 293 K, the reflection variation amplitude decreases 20–25 times [5], while the average temperature coefficient of the shift is -3.3×10^{-4} eV K^{-1}.

Transmission spectra of melt-grown $ZnAs_2$ (plates were cut out in various crystallographic directions) were studied in [10]. The values of E_g at 80 K and the temperature coefficient of the shift were found to be 1.032 eV and -3.13×10^{-4} eV K^{-1}.

As for zinc diphosphide [9], the Kislovskiĭ method [11] can be used to estimate the energy E_i of the absorption peak, the absorptivity μ_i at the peak, and the oscillator strength f_i related to the crystal unit cell from $ZnAs_2$ reflectance spectra. At 80 K, for the exciton band with the reflectance R peak at 1.0297 eV, we have $\mu_1 = 1.8 \times 10^5$ cm^{-1} and $f_1 \approx 0.004$. In some samples, bands of exciton-impurity complexes with a pronounced dispersion contour were observed at photon energies $h\nu <$ 1.025 eV. Since these bands were much narrower than the fundamental exciton band, the corresponding oscillator strengths were significantly (by an order of magnitude) lower.

The exciton parameters can be determined more accurately from the known optical-function dispersions in the region $h\nu \approx E_g$. An analysis according to the

Positions of the optical function maxima of $ZnAs_2$ crystal at 80 K

Function	Energy of maximum, eV
ε_1	1.0283
n	1.0284
R	1.02970
ε_2	1.02980
$\varepsilon_2 E^2$	1.02983
μ	1.03021
k	1.03025
$-\mathrm{Im}(\varepsilon + 1)^{-1}$	1.03094
$-\mathrm{Im}(\varepsilon^{-1})$	1.03102
β	1.03127

1063-7826/02/3607-0755$22.00 © 2002 MAIK "Nauka/Interperiodica"

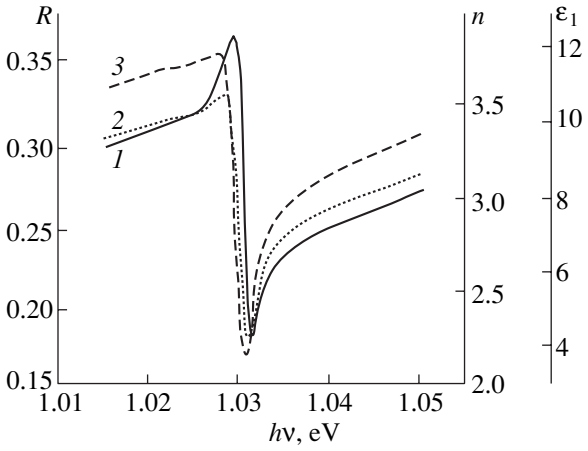

Fig. 1. Optical functions (*1*) *R*, (*2*) *n*, and (*3*) ε_1 of $ZnAs_2$ at 80 K and **E** || **c**.

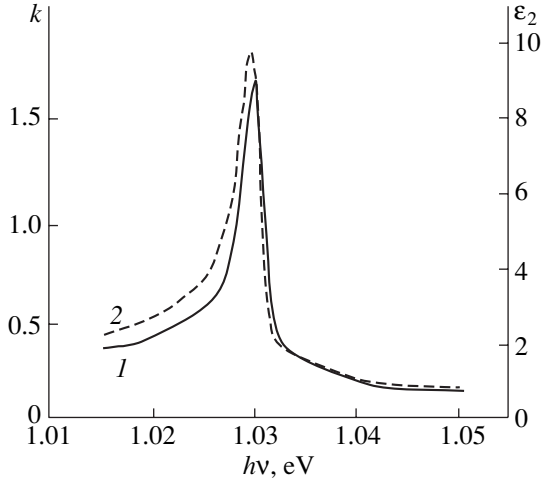

Fig. 2. Optical functions (*1*) *k* and (*2*) ε_2 of $ZnAs_2$ at 80 K and **E** || **c**.

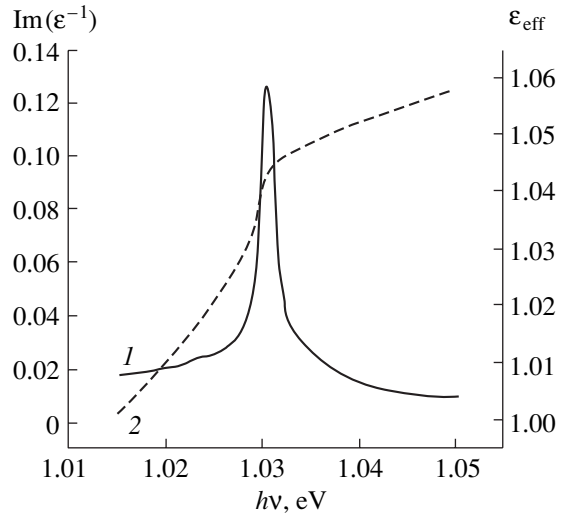

Fig. 3. Optical functions (*1*) $-\mathrm{Im}(\varepsilon^{-1})$ and (*2*) ε_{eff} of $ZnAs_2$ at 80 K and **E** || **c**.

Kramers–Kronig method [12] was carried out as applied to reflectance *R* spectra in the wide range including the exciton region. The data for 4.2 K were not used because of the probability of polaritonic effects. For 80 and 293 K, we measured the absorptivity (μ), absorption (*k*) and refractive (*n*) indices, imaginary (ε_2) and real (ε_1) parts of the dielectric constant ε, effective number n_{eff} of valence electrons, effective dielectric constant ε_{eff}, function $\varepsilon_2 E^2$ characterizing the reduced density of states, differential (electrooptical) functions α and β, reflected light phase θ, as well as functions of characteristic electron loss $-\mathrm{Im}(\varepsilon^{-1})$ and $-\mathrm{Im}(1 + \varepsilon)^{-1}$. The results of calculations for some functions are shown in Figs. 1–4. We note that the dispersion property of functions *R*, *n*, and ε_1 disappears at room temperature. Therefore, we dwell only on the results for 80 K. In the studied range, the functions *R*, *n*, and ε_1 are close in shape, while ε_2 and $\varepsilon_2 E^2$, as well as μ and *k*, virtually coincide. This is also valid for n_{eff} and ε_{eff}, and $-\mathrm{Im}(\varepsilon^{-1})$ and $-\mathrm{Im}(1 + \varepsilon)^{-1}$. The *R* dispersion curve span is about 18% with $n > k$ and $\varepsilon_1 > \varepsilon_2$; *n* and ε_1 are more slightly varied in magnitude than *k* and μ. Thus, the *R* spectra shape is completely governed by *n*, and ε_2 is controlled by *k*.

Table 1 lists the energies of the basic function maxima. It is obvious that the μ maximum at 80 K is close to the *R* inflection point (between the dispersion curve maximum and minimum). This corresponds to the case of ZnP_2 at 293 K. The maxima of functions μ, *k*, and ε_2 are very close, which was also observed in III–V and II–VI crystals, for which the dispersion curve *R* span is smaller than 10%.

The curves n_{eff} and ε_{eff} have a slight kink near the peak $n = 1$ of a free exciton, which indicates the onset of light absorption. In the considered region, n_{eff} attains the value of 0.003. The functions of characteristic loss exhibit longitudinal components of transitions, while transverse excitons manifest themselves in *k* and μ.

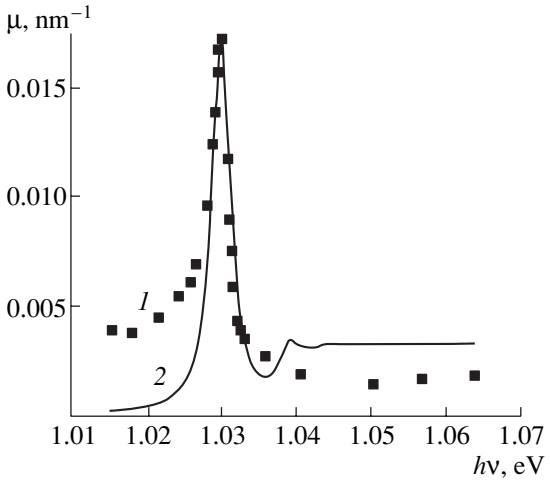

Fig. 4. Experimental (*1*) and calculated (*2*) spectra of the $ZnAs_2$ crystal absorptivity μ at 80 K and **E** || **c**.

Thus, we can estimate the longitudinal–transverse splitting: $\Delta E_{lt} \approx 0.7$–$0.8$ meV. In the exciton range, the phase θ ranges from 0.1 to 0.4. The function β reproduces the shape of ε_2, k, and μ; its maximum is shifted with respect to the R maximum by 3.5 meV to higher energies. The function α is antisymmetric to R; its minimum is shifted by 1 meV with respect to the R maximum to higher energies, while its maximum almost coincides with the R minimum.

To determine the exciton parameters, we can also use the known formula [13], which describes the absorption edge taking into account the exciton band and can be written as the Lorentzian

$$\mu(h\nu) = \mu_0\left\{\sum_n \frac{1}{n^3}\frac{(\Gamma_n/2)^2}{(h\nu - E_g - R_0/n^2)^2 + (\Gamma_n/2)^2} + \frac{\Gamma_c}{4R_0}\left[\frac{\pi}{2} + \arctan\left(\frac{h\nu - E}{\Gamma_c/2}\right)\right]\right\},$$

where E_g is the band gap, R_0 is the exciton Rydberg, n is the exciton excitation order, Γ_n is the oscillator half-width, Γ_c is the exciton continuum width, μ_0 is the coefficient proportional to the oscillator intensity f_{cv}, and $\Gamma_n = \Gamma_c - (\Gamma_c - \Gamma_1)/n^2$.

The parameters μ_0, Γ_1, Γ_c, R_0, and E_g were selected to achieve the best fit to the experimental data [14]. Summation was carried out only up to $n = 7$. The experimental data and the calculated curve of $ZnAs_2$ exciton absorption are displayed in Fig. 4. It turns out that E_g = 1.042 eV, R_0 = 0.012 eV, Γ_1 = 0.003 eV, Γ_c = 0.003 eV, and $\mu = 0.017$ nm^{-1}.

The value of R_0 was assumed in [5–8] to vary only slightly as the temperature increased from 4.2 to 80 K. Then, extrapolation of E_g to higher temperatures yielded the values E_g = 1.041 eV and R_0 = 12 meV, which virtually coincided with the results of this study. We also note good agreement between the maximum absorption estimated with the Kislovskiĭ method (requiring the known dispersion curve of R) and the data calculated using the Kramers–Kronig method. Finally, we call attention to the fact that the oscillator strength of the exciton ground state appreciably decreases as phosphorus is replaced by a heavier element (arsenic); i.e., this parameter in $ZnAs_2$ is smaller than in isomorphic β-ZnP_2 [15], although it remains larger than in III–V and II–VI crystals.

A separate oscillator with a symmetric Lorentzian absorption band in the Argand diagram $\varepsilon_2 = f(\varepsilon_1)$ or $n = f(k)$ is represented by a circle, from which the oscillator parameters can be readily determined [12]. The contour of all the known allowed excitons is a symmetric Lorentzian; i.e., the Argand diagram should represent a circle in the range of $n = 1$ with a high accuracy. In the case under consideration, deviations take place in the long-wave length region, which are most likely caused by overestimated reflectance because of the effect of the rear surface of the crystal. This can also explain the discrepancy between the calculated and experimental curves in Fig. 4. The former exhibits a pronounced state with $n = 2$, while this structure is indiscernible in the experimental curve. The intensity of the terms of the exciton series probably does not obey the Elliot law, as in the case of monoclinic zinc diphosphide [15].

Thus, for the first time, the spectral dependences of the optical functions R, n, ε_1, ε_2, k, μ, ε_{eff}, $-\text{Im}(\varepsilon^{-1})$, and others were studied for monoclinic $ZnAs_2$ in the absorption edge region. Knowledge of their features is of basic theoretical and practical importance. The shape of the exciton absorption band of $ZnAs_2$ was analyzed at 80 K.

The most important parameters of a free exciton—E_g, R_0, Γ_1, E_1, f_1, and others—were estimated.

REFERENCES

1. V. B. Lazarev, V. Ya. Shevchenko, Ya. Kh. Grinberg, and V. V. Sobolev, *II–V Semiconductor Compounds* (Nauka, Moscow, 1978).
2. W. J. Turner, A. S. Fishler, and W. E. Reese, Phys. Rev. **121** (3), 759 (1961).
3. V. V. Sobolev and N. N. Syrbu, Phys. Status Solidi **51** (2), 863 (1972).
4. V. V. Sobolev, A. I. Kozlov, S. G. Kroitoru, *et al.*, Fiz. Tekh. Poluprovodn. (Leningrad) **15** (7), 1428 (1981) [Sov. Phys. Semicond. **15**, 826 (1981)].
5. V. V. Sobolev and A. I. Kozlov, Zh. Prikl. Spektrosk. **41** (6), 1035 (1984).
6. V. V. Sobolev and A. I. Kozlov, Phys. Status Solidi B **126** (1), K59 (1984).
7. V. V. Sobolev and A. I. Kozlov, in *Proceedings of the International Conference "Excitons-84", Gustrow, 1984*, Part I, p. 41.
8. V. V. Sobolev, A. I. Kozlov, S. F. Marenkin, and K. A. Sokolovskiĭ, Izv. Akad. Nauk SSSR, Neorg. Mater. **21** (8), 1276 (1985).
9. V. V. Sobolev, A. I. Kozlov, and S. G. Kozlova, Opt. Spektrosk. **77** (5), 787 (1994) [Opt. Spectrosc. **77**, 706 (1994)].
10. V. A. Morozova, D. I. Pishchikov, S. M. Loseva, *et al.*, Fiz. Tekh. Poluprovodn. (Leningrad) **25** (9), 1664 (1991) [Sov. Phys. Semicond. **25**, 1005 (1991)].
11. L. D. Kislovskiĭ, Opt. Spektrosk. **7** (3), 311 (1959).
12. V. V. Sobolev and V. V. Nemoshkalenko, *The Methods of Computational Physics in the Theory of Solid State. Electronic Structure of Semiconductors* (Naukova Dumka, Kiev, 1988).
13. L. Roa, C. Rincon, J. Gonzalez, and M. Quintero, J. Phys. Chem. Solids **51** (6), 551 (1990).
14. A. V. Matveev, A. I. Kozlov, and V. V. Sobolev, in *Abstracts of the 3rd General Conference of Balkan Physical Union, Cluj-Napoca, 1997*, p. 198.
15. V. V. Sobolev, A. I. Kozlov, I. I. Tychina, *et al.*, Pis'ma Zh. Éksp. Teor. Fiz. **34** (3), 115 (1981) [JETP Lett. **34**, 108 (1981)].

Translated by A. Kazantsev

Semiconductors, Vol. 36, No. 7, 2002, pp. 758–762. Translated from Fizika i Tekhnika Poluprovodnikov, Vol. 36, No. 7, 2002, pp. 812–816.

ELECTRONIC AND OPTICAL PROPERTIES OF SEMICONDUCTORS

Structure and Properties of Silicon Carbide Grown on Porous Substrate by Vacuum Sublimation Epitaxy

N. S. Savkina*, V. V. Ratnikov, A. Yu. Rogachev, V. B. Shuman, A. S. Tregubova, and A. A. Volkova

Ioffe Physicotechnical Institute, Russian Academy of Sciences, Politekhnicheskaya ul. 26, St. Petersburg, 194021 Russia

**e-mail: nata.sav@pop.ioffe.rssi.ru*

Submitted December 17, 2001; accepted for publication December 18, 2001

Abstract—A SiC layer was grown by vacuum sublimation epitaxy on porous silicon carbide. A porous SiC layer about 10 μm thick was fabricated by electrochemical etching of an off-axis 6*H*-SiC substrate. The epitaxial layer was ~10 μm thick. Structural and optical properties of the initial substrate and the porous and epitaxial layers were investigated by X-ray, IR-reflection and photoluminescence methods. An epitaxial SiC layer grown on porous SiC exhibits improved characteristics when compared to a SiC layer on a conventional substrate. © *2002 MAIK "Nauka/Interperiodica".*

1. INTRODUCTION

In spite of considerable progress in the fabrication of silicon carbide substrates, substrate structural defects penetrating into an epitaxial layer during subsequent homoepitaxial growth can drastically affect the device properties. One of the ways to reduce this effect is through the fabrication of a porous interlayer between the substrate and the epitaxial layer (epilayer). As was shown recently [1], the number of defects in the layers grown by vacuum sublimation epitaxy (VSE) on porous SiC (*por*-SiC) substrates is reduced compared to the layers grown on conventional substrates. However, the most popular method for obtaining the SiC epilayers is vapor-phase epitaxy (VPE). Therefore, further reports referred mainly to studies of epilayers grown on *por*-SiC by precisely this method [2]. The essential difference between the two methods is the medium where the sample resides during epitaxial growth. For VSE it is a vacuum, while for VPE it is most frequently the silane–propane mixture $SiH_4 + C_3H_8$ and, which is very important, hydrogen. The presence of hydrogen inhibits the formation of excess carbon on the sample surface. We have observed the color of a porous layer changing from brown to black when heating *por*-SiC in vacuum, even at relatively low temperatures. Auger spectroscopy and IR-reflection studies confirmed the assumption that excess graphite is formed in *por*-SiC. Further, the cross-sectional X-ray microscopy of a system ⟨epitaxial SiC⟩–*por*-SiC –⟨SiC substrate⟩ [3] has revealed excess carbon not only in *por*-SiC, but also in the region of the epilayer adjacent to the ⟨epitaxial SiC⟩–*por*-SiC interface. Therefore, it seems of interest to apply different methods (X-ray, IR-reflection, photoluminescence) to investigate an epitaxial SiC layer formed on *por*-SiC by VSE.

2. SAMPLE

This report presents the results obtained in the study of a homoepitaxial layer grown by VSE on a commercial 6*H*-SiC substrate (CREE, the uncompensated donor density $N_d - N_a = 4.5 \times 10^{18}$ cm^{-3}) after the formation of an intermediate porous layer. The initial substrate with polished opposite faces (Si and C) was misoriented by 3.5° with respect to the **c** axis.

After a preliminary X-ray topography study, a fragment 12 × 12 mm^2 in size was selected for further experiments. Figure 1 shows the X-ray topogram of the substrate. Regions with different structures are clearly discernible in the topogram. The distribution of dislocations is uniform in area *A*, while strong local distortions are observed in area *B*.

The porous layer was produced on an Si face of the initial substrate by electrochemical anodization of the sample in an $HF : H_2O : C_2H_5OH = 1 : 1 : 2$ electrolyte at the current density of 20 mA/cm^2 and under UV illumination of the surface. The thickness of the obtained *por*-SiC layer was ~ 10 μm.

A 10-μm-thick epitaxial SiC (*epi*-SiC) layer was grown by VSE in a vertical water-cooled quartz reactor at the substrate temperature of ~1800°C. The concentration difference $N_d - N_a$ in the epilayer, determined from the capacitance–voltage characteristics, was 2×10^{16} cm^{-3}.

3. RESULTS AND DISCUSSION

3.1. X-ray Studies

X-ray studies of the initial substrate, porous layer, and epilayer were performed using double- and triple-crystal diffractometry (DCD and TCD) with Cu$K_{\alpha 1}$

Experimental values of the curvature radii R, stresses σ_a, and FWHM of double- and triple-crystal diffraction curves

Sample	R, m/σ_a, GPa	FWHM (DCD)		FWHM (TCD)			
		(0006)	(00012)	(0006)		(00012)	
				θ	θ–2θ	θ	θ–2θ
Substrate	+70/0	22	25	10	11	11	9
Porous layer	+13/–0.06	30	Two peaks	13	13	18	Two peaks
Epitaxial layer	–72/+0.028	23	42	15	12	15	14

Note: The FWHM values are in seconds of arc.

radiation. Macrostresses were evaluated from the bending radii R of the sample, which were defined by DCD. R was measured by recording the angular shift of the reflection peak from a sample during its linear X-ray scanning [4]. The structural quality of the layers was assessed from the angular full width at half-maximum (FWHM) of a diffraction curve for the symmetric Bragg (0006) and (00012) reflections. In TCD measurements, θ- and (θ–2θ)-scanning modes were used.

The table presents the bending radii R and the radii biaxial stresses σ_a calculated from these in the initial substrate, *por*-SiC, and in the *epi*-SiC grown on it. The initial sample bending arises from the difference of stresses produced on opposite faces during their mechanical polishing. The evaluated difference between the stresses at the SiC faces is $\Delta\sigma_a = 0.14 \times 10^{-6}$ GPa (see, *e.g*, [5]). In the calculation of stresses, the anisotropy of the SiC elastic properties was considered, with the elastic constants being taken from [6]. In the sample under study, the stresses in the surface layer on the Si face are compressive and increase after the formation of the porous layer, which is shown by a decrease in the bending radius. The biaxial compressive stresses in *por*-SiC calculated from R by the Stoney relation [7] are σ_a = –0.06 GPa. We believe that the source of the stresses is the electrostatic repulsive forces stemming from the incomplete removal of electrolyte from the pores. To verify this assumption, the curvature of *por*-SiC was measured immediately after its fabrication (R = + 13 m) and then after vacuum annealing for 1h at 700°C. This thermal treatment eliminated *por*-SiC bending (the pore size remained unchanged). Further immersion of the sample in electrolyte resulted in sample bending of R = + 59 m, which confirms the assumption about the effect of the in-pore electrolyte on sample bending.

High-temperature growth of the epilayer reverses the sign of bending. The epilayer on *por*-SiC is concave, but the tensile stresses in it are small (σ_a = + 0.027 GPa). In the evaluation of stresses, the *por*-SiC layer between the epilayer and substrate was disregarded. A decrease in sample curvature was observed in [8] for thin (2 μm) epilayers grown on *por*-SiC (the samples were straightened out, remaining convex). In this study, the *epi*-SiC on *por*-SiC was five times thicker, which led to the reversal of the bending sign. It is necessary to note that the evolution and relaxation of stresses during the cooling of a sample to room temperature are complicated processes and that the elastic properties and the thermal expansion coefficient of *por*-SiC are unknown. Therefore, the quantitative estimation of macrostresses arising during the growth of *epi*-SiC on *por*-SiC is difficult.

The table also presents the FWHM values obtained by taking into account the sample curvature and nonzero dispersion in the X-ray diffractometer optical system. The initial SiC sample had a high density of nonuniformly distributed dislocations, with the resulting angular misorientations of the crystal lattice in the area irradiated with an X-ray beam. This fact creates severe problems for the X-ray diffraction analysis of these samples, owing to permanent variation in the reflection curve during X-ray scanning over the sample. Therefore, the symmetric form of the TCD (θ–2θ) curve obtained with (0006) and (00012) reflections from the initial sample (which indicates that the angular misorientaion of the crystal lattice is negligible) served as the

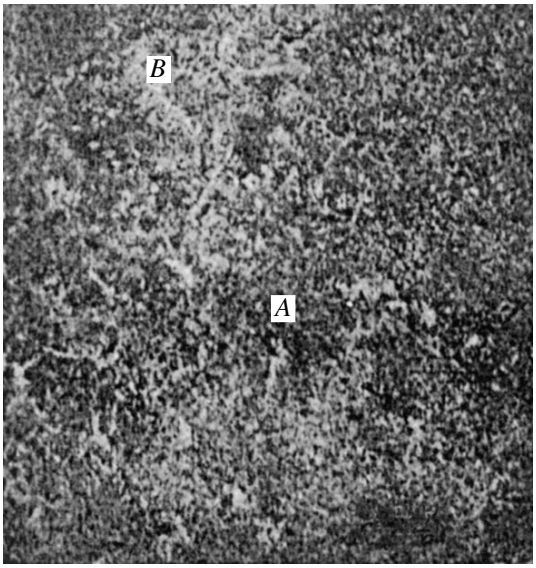

Fig. 1. X-ray topogram of the initial sample, 12×12 mm^2 in size. Cu$K_{\alpha 1}$ radiation, $(11\bar{2}.12)$ reflection. The areas with uniform distribution of basal dislocations (*A*) and strong local distortions (*B*) are seen.

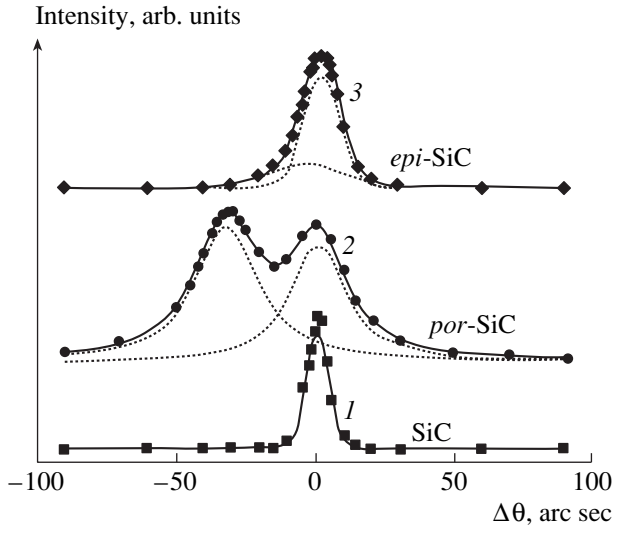

Fig. 2. TCD (θ–2θ) (00012) reflection from (*1*) initial SiC substrate, (*2*) porous SiC layer, and (*3*) epitaxial layer. A three-crystal diffractometer was used.

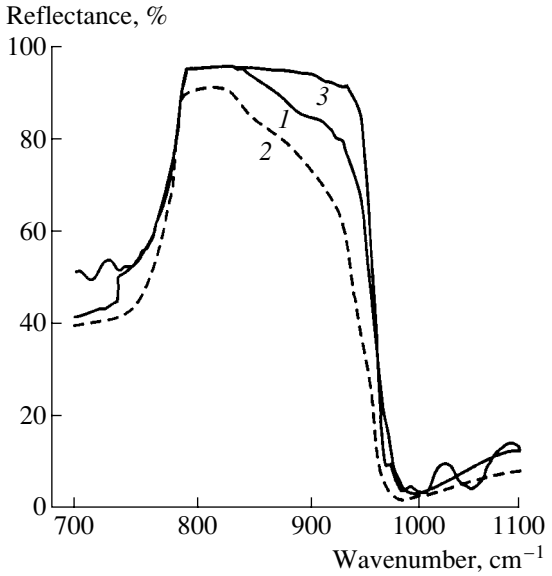

Fig. 3. IR reflection from (*1*) the initial substrate in area *A*, (*2*) porous layer in area *B*, and (*3*) epitaxial layer in area *A*.

criterion for selecting the area to be dealt with in further studies.

For the porous layer, the width of the diffraction curves (FWHM) increased significantly, and their shape was markedly modified. Intense diffuse scattering is observed in the (0006) DCD reflection curve near the pedestal of the narrow dynamical peak. Two peaks with an angular distance $\Delta\theta = 32''$ are observed in the (θ–2θ)-curve of (00012) TCD reflections (Fig. 2, curve *2*). Since this reflection provides information about an ~17 μm-thick surface layer and the thickness of the *por*-SiC layer in this sample is ~10 μm, the diffraction peak is attributed to the reflection from *por*-SiC at small θ and from the substrate at higher angles. The maximal FWHM of the peak from *por*-SiC is 1/3 higher than that from the underlying substrate. The lattice strain along the main crystal axis **c** was estimated as $\varepsilon_c = (d_{por} - d_{SiC})/d_{SiC} = \Delta\theta \cot\theta = +2 \times 10^{-4}$, where d_{por} and d_{SiC} are the interplanar spacings for *por*-SiC and SiC, and θ is the Bragg angle. The diffraction curves of *epi*-SiC on *por*-SiC are again unimodal, and the (θ–2θ)-curve is asymmetric (Fig. 2, curve *3*). In the latter case, the additional intensity may be ascribed to inhomogeneous deformation near the *por*-SiC–*epi*-SiC interface. The average strain in the epitaxial layer $\varepsilon_c = -0.08 \times 10^{-4}$ was calculated from the measured biaxial stresses during the bending of the *epi*-SiC–*por*-SiC–substrate system using the relation between the stress σ_a in the basic plane of a crystal of a hexagonal system and the strain ε_c (see, e.g, [9]).

An analysis of the data obtained leads to the following conclusion: in spite of the fact that the FWHM values for all the reflection peaks are slightly larger than those in the initial sample, the observed uniformity of the curves over the epilayer area and the small biaxial stresses in this layer indicate that the latter has an advantage over the initial SiC substrate.

3.2. Infrared Spectroscopy

The IR reflection spectra were recorded using an IKS-29 spectrophotometer eqipped with a IPO-22 unit, which allowed the recording of the spectra from local areas of 2.5×2.5 mm^2. Figure 3 presents the reflection spectra near the band of lattice resonance, with its edges corresponding to the energies of transverse and longitudinal optical phonons (TO and LO phonons, 788 and 970 cm^{-1}, respectively). Curve *1* shows the spectrum of the initial sample in the area with a low defect concentration (point *A* in the topogram). In the heavily distorted area *B*, the peak of the spectrum was lower by ~2%. Curve *2* presents the reflection spectrum of the porous layer in the area *B*. The spectrum of the porous layer in area *A* (not shown) lies slightly higher than curve *2*; the difference between the spectra recorded in points *A* and *B* is larger for the porous layer than for the initial sample. Curve *3* shows the spectrum of the *epi*-SiC layer on *por*-SiC.

The reflection spectrum of *por*-SiC features a specific falloff near the LO phonon frequency, which was first reported in [10]. The authors explain this variation in the spectrum by the fact that the TO phonon band is defined mainly by the short-range order, while the LO band depends on mid- and long-range orders which are more heavily distorted during the formation of a porous structure. As can be seen in Fig. 3 (curve *3*), the reflectance in the LO-phonon band in the spectrum of an epilayer on *por*-SiC is significantly larger than that of the initial sample, which is indicative of the higher struc-

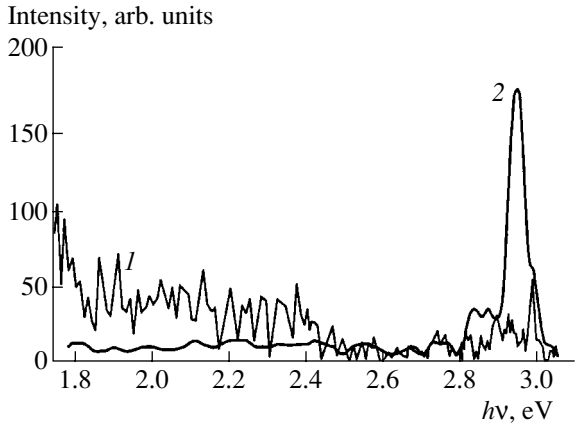

Fig. 4. Time-resolved PL spectra at the peak of the recorded pulse; the excitation energy is 3.68 eV, temperature 90 K. (*1*) Initial substrate; (*2*) *epi*-SiC on *por*-SiC, area *B*.

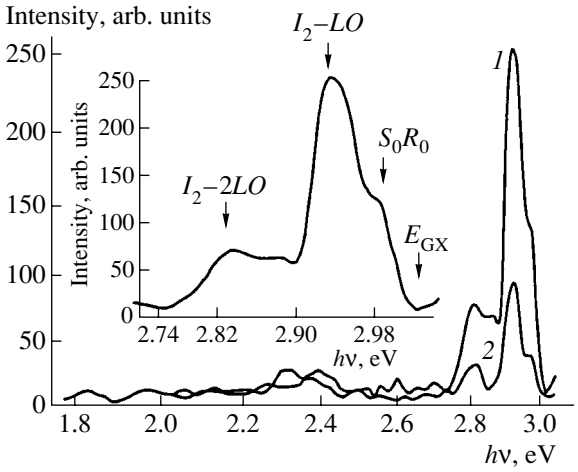

Fig. 5. The same as in Fig. 4. (*1*) *epi*-SiC on *por*-SiC, area *A*; (*2*) reference epilayer grown directly on the substrate. The inset: the excitonic portion of curve *1*, scale enlarged.

tural quality. It is worth noting that, although in the spectrum of the epilayer grown on a reference substrate (not presented) the reflectance in the major band is higher than for the initial sample, the band peak is not as flat as presented in Fig. 3. Further, a clearly pronounced interference pattern was observed at 4000–1000 cm^{-1} in the reflection spectrum of *epi*-SiC on *por*-SiC (its fragment is shown in Fig. 3), which indicates that the epitaxial layer is plane-parallel, and allows the determination of its thickness by nondestructive methods. In this case, the epilayer thickness was 10 μm. Interference was barely perceptible in the spectrum of the epitaxial layer on the reference sample.

We conclude that the IR spectroscopy data confirm the high structural perfection of the epitaxial layer grown on porous SiC.

3.3. Photoluminescence

Time-resolved photoluminescence (PL) was measured at 90 K at the peak of the recorded pulse from the initial substrate, and then from the epilayer grown after the formation of the intermediate porous layer, at points *A* and *B* marked on the topogram (Fig. 1). The PL was excited with a pulsed nitrogen laser (photon energy $h\nu$ = 3.68 eV, the spot diameter ~0.2 mm^2). The PL spectra were recorded in the range of energies $h\nu$ = 3.10–1.75 eV using a DFS-12 spectrometer and a FEU-79 photomultiplier. Figure 4 shows the PL spectra of the initial substrate and epilayer on *por*-SiC (curves *1*, *2*), which were recorded from the highly damaged area *B* of the initial substrate. Figure 5 presents the PL spectrum of *epi*-SiC on *por*-SiC in the area with low defect concentration *A* (curve *1*) and a portion of the spectrum in the exciton range in more detail (the inset). The PL spectrum of the initial substrate (not shown) was similar to that in Fig. 4, but its intensity in the range $h\nu$ = 1.8–2.4 eV was lower. For comparison, curve *2* presents the PL spectrum of the reference epilayer grown on the initial substrate without an intermediate porous layer.

PL bands at energies 2.99, 2.94, 2.83, and 2.4 eV are observed in all the obtained spectra. The classification and notation of lines were presented in [11, 12]. The band at 2.99 eV was assigned to zero-phonon recombination of an exciton bound by a neutral donor, i.e., nitrogen in cubic surroundings (S_oR_o band at 2.992 eV). The band at 2.94 eV is formed by the lines of a free exciton annihilating with the involvement of phonons: TA (2.982 eV), LA (2.954 eV), TO (2.933 eV), and LO (2.924 eV). The band at 2.83 eV is also always observed; we assign it to the 2LO satellite of the free exciton line. The band at $h\nu \approx 2.4$ eV is associated with the luminescence from defects.

Comparing the PL spectra obtained from epilayers grown either on porous SiC (*epi*-SiC on *por*-SiC) or on the initial substrate, we made the following conclusions: (i) the intensity of the "defect" band is nearly the same in both spectra, but it is lower than in the spectrum of the initial substrate; (ii) the intensity of the excitonic peak from *epi*-SiC on *por*-SiC exceeds that from the initial substrate by more than a factor of 5, and from *epi*-SiC on the substrate by a factor of 2.5; and (iii) the intensity of excitonic peaks in the (*epi*-SiC on *por*-SiC) spectrum depends only slightly on defects in the substrate (areas *A* and *B*).

4. CONCLUSION

The presence of a porous interlayer between the substrate and the epilayer does not hinder the fabrication of high-quality epilayers. X-ray and IR spectroscopy data clearly indicate the higher structural perfection of the epilayer grown on *por*-SiC compared with that grown directly on the substrate. X-ray topograms recorded from *epi*-SiC on *por*-SiC (not presented in this

paper) also demonstrate the improvement of the layer structure. The existence of larger pores near the *epi*-SiC–*por*-SiC interface [3] does not inhibit a clear interference pattern in the reflection spectrum, which indicates that the epitaxial layer on *por*-SiC is plane-parallel, and its thickness can be determined by nondestructive methods. The comparison of PL spectra of *epi*-SiC on *por*-SiC with those of the reference epilayer has shown that the "defect" band is observed in both spectra with nearly the same intensity, but this intensity is lower than in the spectrum of the initial substrate. The principal difference between the spectra is that the intensity of the exciton peak from *epi*-SiC on *por*-SiC is 5 times higher than that from the initial substrate, and 2.5 times higher than that from the reference epilayer. We conclude that further studies are necessary to optimize the parameters of porous SiC, as well as the vacuum sublimation epitaxy process for porous layers.

ACKNOWLEDGMENTS

We are grateful to Prof. R. Madar for providing us with the substrate and to A.M. Danishevskiĭ for his helpful participation in discussions.

This study was supported by the Russian Foundation for Basic Research (project nos. 01-02-17907 and 00-02-16760).

REFERENCES

1. M. Mynbaeva, N. Savkina, A. Zubrilov, *et al.*, Mater. Res. Soc. Symp. Proc. **587**, 08.6.1 (2000).
2. M. Mynbaeva, S. E. Saddow, G. Melnychuk, *et al.*, Appl. Phys. Lett. **78** (1), 117 (2001).
3. L. M. Sorokin, J. L. Hutchison, J. Sloan, *et al.*, in *Technical Digest of 1st Conference on SiC and Related Materials, ICSCRM2001, Tsukuba, Japan, 2001*, p. 408.
4. G. Rozgoniy, P. Petroff, and M. Panish, J. Cryst. Growth **27**, 106 (1974).
5. A.-J. Schell-Sorokin and R. M. Tromp, Phys. Rev. Lett. **64** (9), 1039 (1990).
6. *Properties of Advanced Semiconductor Materials: GaN, AlN, InN, BN, SiC, SiGe*, Ed. by M. E. Levinshtein, S. L. Rumyantsev, and M. S. Shur (Wiley, New York, 2001).
7. G. Stoney, Proc. R. Soc. London, Ser. A **82**, 172 (1925).
8. N. S. Savkina, V. V. Ratnikov, and V. B. Shuman, Fiz. Tekh. Poluprovodn. (St. Petersburg) **35** (2), 159 (2001) [Semiconductors **35**, 153 (2001)].
9. C. Kisielowski, J. Kruger, S. Ruvimov, *et al.*, Phys. Rev. B **54** (24), 17745 (1996).
10. A. M. Danishevskiĭ, V. B. Shuman, A. Yu. Rogachev, and P. A. Ivanov, Fiz. Tekh. Poluprovodn. (St. Petersburg) **29** (12), 2122 (1995) [Semiconductors **29**, 1106 (1995)].
11. M. Ikeda, T. Hayakawa, S. Yamagiva, *et al.*, J. Appl. Phys. **50**, 8215 (1979).
12. A. M. Danishevskiĭ and A. Yu. Rogachev, Fiz. Tekh. Poluprovodn. (St. Petersburg) **30** (1), 17 (1996) [Semiconductors **30**, 9 (1996)].

Translated by D. Mashovets

Semiconductors, Vol. 36, No. 7, 2002, pp. 763–771. Translated from Fizika i Tekhnika Poluprovodnikov, Vol. 36, No. 7, 2002, pp. 817–825.

ELECTRONIC AND OPTICAL PROPERTIES OF SEMICONDUCTORS

The Effect of Composition on the Properties and Defect Structure of the $CdS–Ga_2S_3$ Solid Solution

E. F. Venger, I. B. Ermolovich*, V. V. Milenin, and V. P. Papusha

Institute of Semiconductor Physics, National Academy of Sciences of Ukraine, Kiev, 252028 Ukraine

**e-mail: irina_ermolovich@mail.ru*

Submitted December 17, 2001; accepted for publication December 19, 2001

Abstract—The effect of excess CdS in gallium thiogallate ($CdGa_2S_4$) on the spectrum of defect states in its band gap is investigated. Comparative investigations of Raman, photoluminescence, and cathodoluminescence spectra, as well as of the kinetics of photoconductivity in starting crystals (type *A*) and crystals obtained in conditions with excess CdS (type *B*), were carried out. It was found that the main types of defects in type *A* crystals are Cd and S vacancies, antisite Ga_{Cd} donor defects, as well as I_S defects, which are caused by the incorporation of carrier gas. In type *B* crystals, along with I_S, the main defects are antisite acceptor defects Cd_{Ga} as well as interstitial atoms Cd_i and S_i. It is demonstrated that the emission characteristics of the crystals investigated are determined by associations of the above defects. A luminescence band peaked at $h\nu_m = 0.971$ eV was observed for the first time. This band is related to intracenter transitions in the *d* shell of Cd of the Cd_{Ga} defect, which is split due to the effects of the crystalline field and spin–orbit interaction, in the presence of S_i. © *2002 MAIK "Nauka/Interperiodica".*

1. INTRODUCTION

Ternary $A^{II}B_2^{III}C_4^{VI}$ (A = Zn, Cd; B = Al, Ga, In; C = S, Se, Te) compounds, whose existence was first reported 45 years ago [1–3], have attracted considerable attention due to their properties. These are a wide band gap (up to 4 eV), high photosensitivity, and intense photoluminescence (PL) among others. To date, they have been much studied (see, for example, review [4]). The main fundamental characteristics of these compounds are determined: the type of crystal lattice and its parameters, the band gap E_g, and the types of band-to-band transitions. It was noted that these compounds could exist in the form of various structural polymorphs. The main structural polymorph is tetragonal, in which cations have a tetrahedral surrounding with the space group S_4^2. This is the β-polymorph, or so-called thiogallate polymorph, since it was originally found in $CdGa_2S_4$ (cadmium thiogallate). This polymorph has a chalcopyrite unit cell, in which one-quarter of the cation sites are unoccupied, and these sites (stoichiometric voids) are ordered.

Ternary compounds $A^{II}B_2^{III}C_4^{VI}$ are in fact solid solutions (alloys) of binary compounds II–VI and $B_2^{III}C_3^{VI}$ and have an extended homogeneity range. For example, for cadmium thiogallate ($CdS + Ga_2S_3$ alloy) it amounts to 3 mol % (from 47.5 to 50.5 mol % CdS) [5]. It should be noted that, in the literature, there is a considerable spread in the E_g values for the same compound. For example, for $CdGa_2S_4$ it ranges from 3.44 eV [6, 7] to 3.58 eV [8]. This also refers to the parameters of local states in the band gap, peak energies of luminescence bands, etc. In addition, the data on the role of background impurities and intrinsic defects in the formation of local states in the band gap of these compounds, including stoichiometric voids, are contradictory [4].

In this study, comparative investigations of the Raman, PL, and cathodoluminescence spectra at various temperatures and excitation levels were carried out. The kinetics of photoconductivity for crystals obtained in synthesis conditions $CdS + Ga_2S_3$ (type *A*) and for crystals obtained in synthesis conditions $2CdS + Ga_2S_3$ (type *B*) was also investigated. The purpose of the investigations was to ascertain the effect of excess CdS in $CdGa_2S_4$ on the spectrum of defect states in its band gap.

2. EXPERIMENTAL

Crystals were grown by the method of reverse gas-transport reactions, in which iodine was used as the carrier gas [3, 9–11]. Type *A* crystals were $5 \times 5 \times 3$ mm^3 in size. Type *B* crystals were no larger than $0.1 \times 2 \times 5$ mm^3. For the investigations of photoconductivity, In contacts were fused on smooth surfaces of the crystals. The fulfillment of the Ohm law for contacts was checked. The dark resistivity for both types of crystals was $\rho_d \gtrsim 10^{10}$ Ω cm.

Raman spectra were measured using a DFS-52 diffraction spectrometer and an Ar laser with the excitation wavelength $\lambda_{exc} = 514.5$ nm.

1063-7826/02/3607-0763$22.00 © 2002 MAIK "Nauka/Interperiodica"

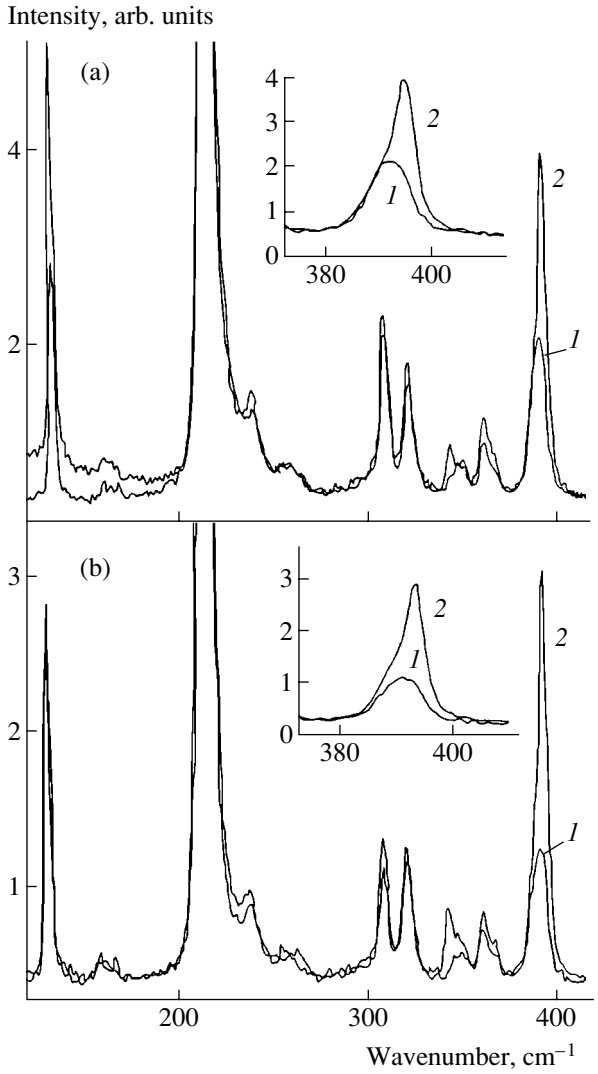

Fig. 1. Raman spectra for cadmium thiogallate crystals of (*1*) type *A* and (*2*) type *B* for polarization directions of exciting illumination (a) **E** ∥ **c** and (b) **E** ⊥ **c**. T = 300 K. The band at 397 cm^{-1} on the expanded scale along the abscissa is represented in the insets.

The PL spectra were measured on two installations. The short-wavelength spectral range with the photon energy $h\nu$ = 1.95–3.0 eV was measured on an installation based on an ISP-51 spectrograph. The long-wavelength spectral range of the PL spectrum with the photon energy $h\nu$ = 0.5–2.05 eV was measured using an IKS-12 monochromator. In both cases, PL was excited by the 365-nm line of the spectrum of a DRSh-250 Hg lamp. The amplitudes of both parts of the spectrum were joined in the overlapping spectral range ($h\nu$ = 1.95–2.05 eV). On both installations, the excitation intensity could be varied in a wide range.

Cathodoluminescence was excited in a vacuum chamber (10^{-5} Torr) using a focused electron beam with an energy of 50 keV and currents of 60, 80, and 160 μA in the scanning mode. A KSVU-23 spectral setup was used for the analysis of spectra.

The photocurrent kinetics was investigated with the use of optical pulses of an ISSh-500 lamp, with a duration of 10 μs, and corresponding filters, which provided the bulk absorption of light.

Measurements were carried out in the temperature range T = 77–450 K.

3. RESULTS

3.1. Raman Spectra

As noted above, $CdGa_2S_4$ crystallizes in the thiogallate structure with the space group S_4^2. Since its unit cell includes seven atoms, the vibration spectrum consists of 21 branches. The vibration spectrum for this case was decomposed in irreducible representations at various points of the Brillouin zone in study [12]. It was found that vibrations of all symmetries are allowed in Raman scattering. The activities of optical and acoustic vibrations in the infrared (IR) absorption spectrum and Raman spectrum were estimated. In Raman spectra, five modes of Γ_2 symmetry were demonstrated to be active for the orientation of the electric-field vector of the optical wave relative to the tetragonal axis **E** ∥ **c**. In addition, five modes of $\Gamma_3 + \Gamma_4$ symmetry are active for **E** ⊥ **c**. One mode of Γ_2 symmetry and one doubly degenerated mode of $\Gamma_2 + \Gamma_4$ symmetry are acoustic.

Figures 1a and 1b demonstrate Raman spectra for *A* crystal (curve *1*) and *B* crystal (curve *2*) for two directions of polarization of the electric vector of the excitation optical wave **E** relative to the long edge of crystals under investigation. It is assumed that the tetragonal axis **c** is directed along the edge. It can be seen that Raman spectra for both types of samples are isotropic. It seems likely that this is associated with the fact that the objects under investigation are not single crystals. More likely, they comprise polycrystals, which are formed by microcrystals oriented randomly (chaotically). It can also be seen that the Raman spectra for *A* and *B* crystals are identical. This points to the similarity of the character of chemical bonds and force constants for both types of crystals. The small width of Raman bands for *B* crystals compared with the bands in Raman spectra for *A* crystals has attracted attention. The phonon frequencies for the crystals investigated are determined and are equal to 234, 243, 265, 315, 326, and 397 cm^{-1}.

3.2. Investigations of Photoluminescence

The PL spectra for (a) *A* crystal and (b) *B* crystal are shown in Fig. 2. A substantial distinction between them can be seen, which points to the reconstruction of defect states in $CdGa_2S_4$ upon increasing the CdS content. At

T = 77 K, a broad band with a peak energy $h\nu_m$ = 1.17 eV and full width at half-maximum $H \approx 400$ meV and weaker broad bands with $h\nu_m$ = 1.79 and 2.05 meV are observed for *A* crystals. At room temperature, the crystals are not luminescent, since all three bands undergo thermal quenching.

For crystals of the *B* type, a very narrow line is observed at 77 K. The peak position of this line is $h\nu_m$ = 0.971 eV, and the width is $H \approx 90$ meV. Two bands with $h\nu_m$ = 1.91 and 2.65 eV are also observed. In general, the PL intensity is somewhat (by a factor of *2*) higher than for the *A* crystal, which points to a lower density of nonradiative centers in type *B* crystals. At room temperature, all bands become quenched, except for a narrow band whose peak shifts to longer wavelengths $h\nu_m$ = 0.960 eV and the width increases (H = 140 meV). The intensity of the band $h\nu_m$ = 0.96 eV at 300 K slightly increases compared with 77 K.

Temperature dependences of the most intense PL bands for the *B* crystal $h\nu_m$ = 1.91 and 0.971 eV are shown in Fig. 3. The analysis of intensity $W(T)$ using the Boltzmann formula $W(T) = W(0)\{1 + c\exp(-E_a/kT)\}^{-1}$ allowed us to determine the activation energies of the corresponding nonradiative transitions: 0.014 eV and 0.058 eV for the band $h\nu_m$ = 1.91 eV, and 0.12 and 0.56 eV for the band $h\nu_m$ = 0.971 eV. Dependences of the intensity of these bands on the excitation intensity at 77 K are also linear in the regions of their thermal quenching.

3.3. Investigations of Cathodoluminescence

Cathodoluminescence spectra at 77 K for the *A* crystal (curve *1*) and for the B crystal (curves *2*, 3) for low-intensity and high-intensity electron beams are shown in Figs. 4a–4c. In general, the cathodoluminescence intensity in type *B* crystals is higher than for type *A* crystals by approximately a factor of 4. The positions of the observed peaks (2.65 eV for the *B* crystal and 2.1 eV for the *A* crystal) are close to the positions of peaks of the shortest wavelength PL bands for these crystals. This means that the recombination of nonequilibrium charge carriers upon electron excitation occurs via the same local centers related to lattice defects, which operate under photoexcitation.

Even at the electron beams of the lowest intensity, it is possible to observe narrow emission lines against the background of broad bands for both types of crystals. Their amplitudes increase with increasing electron flux. We believe that these narrow lines are the lines of stimulated emission. Their considerable number is explained by the fact that the crystals investigated are not plane-parallel. On the contrary, they consist, as follows from the isotropy of Raman spectra, of several microcrystals of different thicknesses, which are most likely oriented randomly. Apparently, upon obtaining more or less perfect crystals and after the deposition of reflecting coatings on their faces, the attainment of solid-state lasers for the promising blue spectral range is possible. We failed to do this based on the material

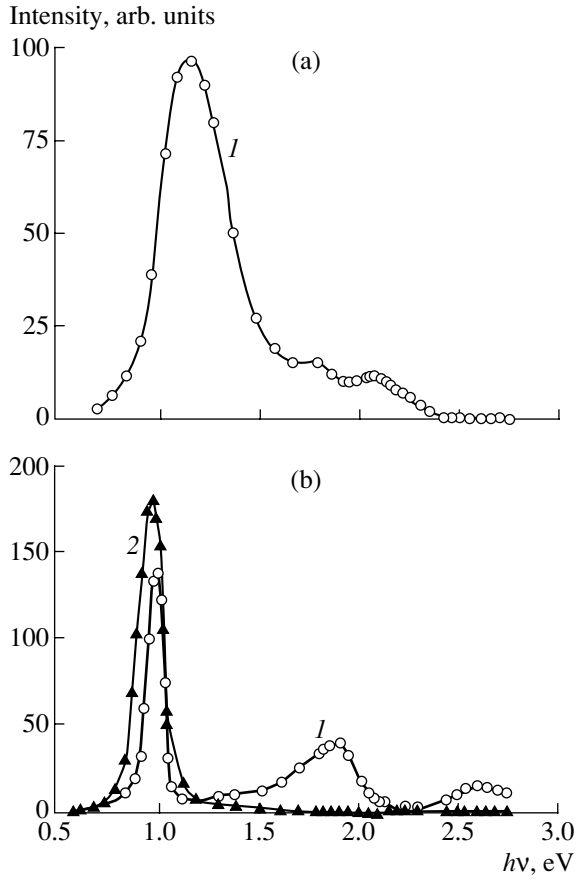

Fig. 2. Photoluminescence spectra for cadmium thiogallate crystals of (a) type *A* and (b) type *B* at T = 77 (*1*) and (*2*) 300 K.

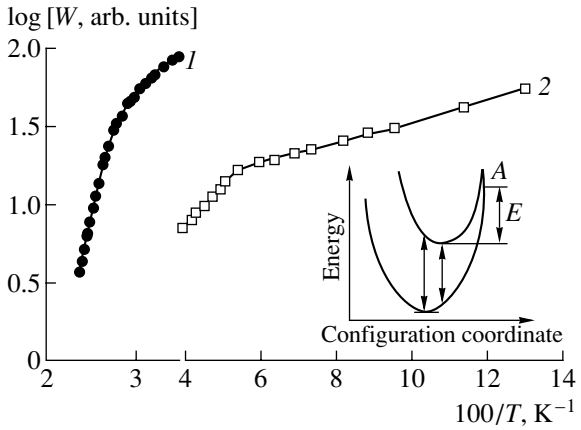

Fig. 3. Temperature dependences of intensities (W) of photoluminescence bands at (*1*) 0.971 and (*2*) 1.91 eV for the type *B* crystal. The energy model in configuration coordinates is shown in inset.

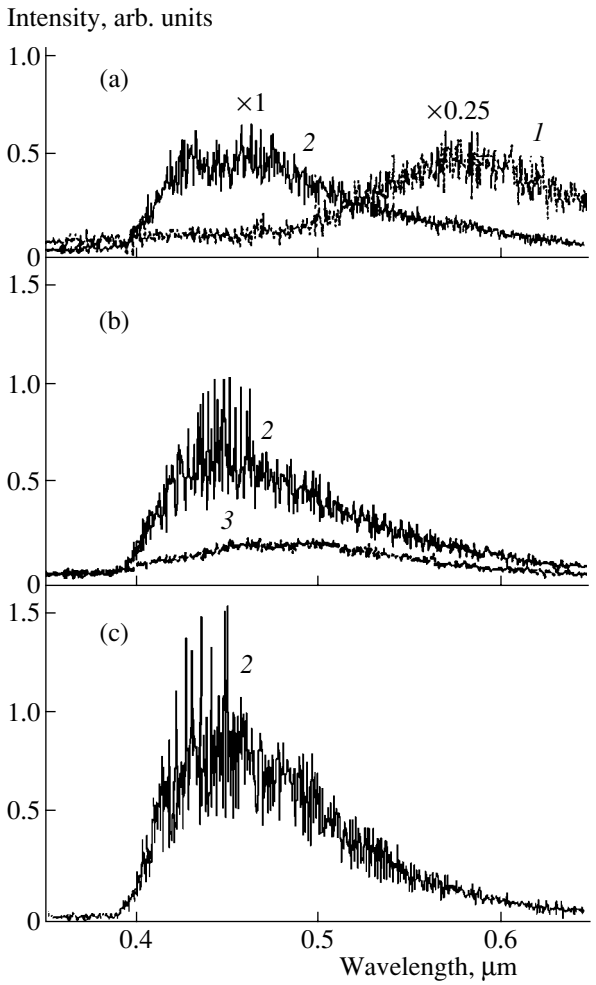

Fig. 4. Cathodoluminescence spectra for cadmium thiogallate crystals of (*1*) type *A* and (*2*, *3*) type *B* at (*1*, *2*) 77 and (*3*) 300 K. The excitation current is equal to (a) 60, (b) 80, and (c) 160 μA.

which was at our disposal. However, the basic possibility of such an application of $CdGa_2S_4$ crystals exists. It was reported upon obtaining the stimulated emission for $CdGa_2S_4$ at the energy $h\nu = 2.09$ eV [13].

3.4. Investigations of Photoconductivity

Based on the investigation of steady-state characteristics of the photocurrent, the possible presence of recombination centers of two types (centers of rapid and slow recombination) in crystals of $CdGa_2S_4$ [14, 15] was reported. We obtained direct evidence of this assumption by measuring the kinetics of photoconductivity decay for *A* and *B* crystals at 300 K with the bulk excitation of crystals in the optical shock mode. In this case, the density of carriers generated by light is higher than the density of attachment levels and photosensitivity centers, which constitute the centers of slow recombination [16, 17].

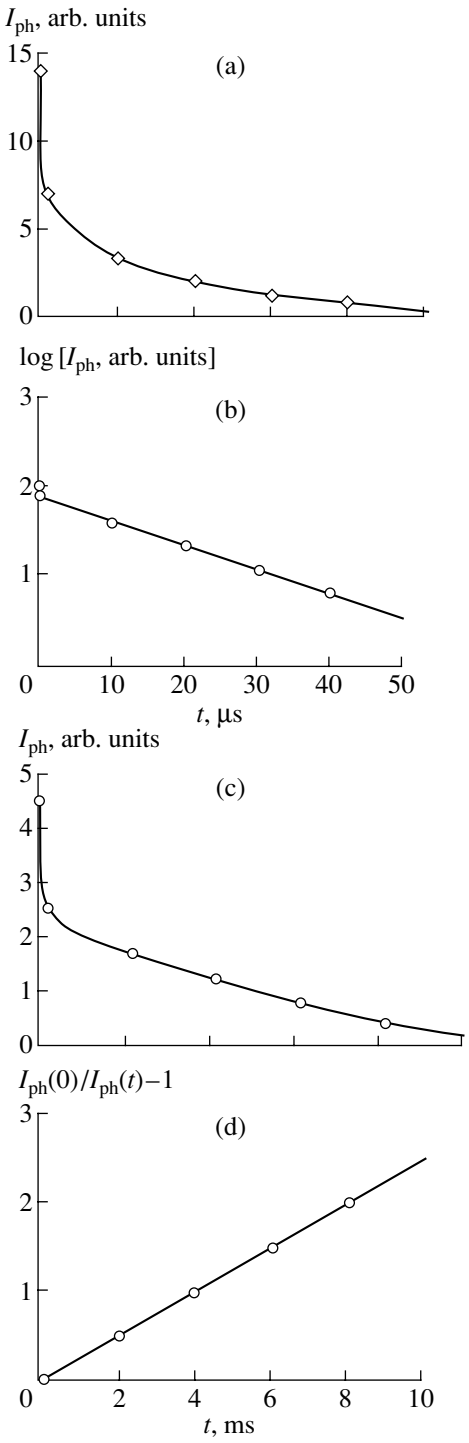

Fig. 5. Curves of photocurrent decay for crystals of (a, b) type *A* and (c, d) type *B*. $T = 300$ K.

It is found that the relaxation curves of the photocurrent (I_{ph}) in time (t) for both types of crystals consist of two portions, namely, short-time and long-time portions (Figs. 5a, 5c). This unambiguously points to the presence of two types of centers in the band gap of these crystals, namely, centers of slow (s) and rapid (r)

recombination. The short-time decay portion of the photocurrent for both types of crystals reproduces the shape of the exciting pulse. This means that the corresponding times of recombination via *s* centers are shorter than the duration of the optical pulse (10 μs).

The decay curve of the photocurrent in the long-time portion in the optical shock mode is described by the equation [16] $dn/dt = -C_{nr}n(P_r^0 + p_r)$, where n is the free-electron density; C_{nr} is the probability of free electron capture by r centers; $C_{nr} = S_{nr}\langle v\rangle$; S_{nr} is the cross-section of electron capture by the r center; $\langle v\rangle$ is the average thermal velocity of the electron, which is equal to ~10^7 cm/s at 300 K; P_r^0 is the dark hole density at r centers due to the occupation of quite deep attachment levels by electrons at room temperature; $P_r^0 \approx N_t$, with N_t being the electron density at the attachment levels; and p_r is the density of holes generated by illumination ($p_r = n$).

For an *A* crystal, the long-time decay portion of the photocurrent is described by an exponential function (Figs. 5a, 5b), which points to the monomolecular recombination mechanism: $n(t) = n_0\exp(-t/\tau_n)$, where the electron lifetime $\tau_n = (C_{nr}P_r^0)^{-1}$. This can take place if $P_r^0 \gg p_r$, i.e., if the density of occupied deep attachment centers for electrons N_t, which form P_r^0, is considerable.

For the type *B* crystals, the long-time decay portion of the photocurrent is a hyperbolic curve (Figs. 5c, 5d) and follows the law of variation in the concentration $n(t) = n_0[1 + C_{nr}n_0t]^{-1}$, where n_0 is the amplitude of the long-time portion. This means that the recombination via r centers with the excitation intensities used is bimolecular; i.e., we have $P_r^0 \ll p_r$, which corresponds to the low density of the attachment centers.

From the slope of the straight line plotted on the $[(n_0/n) - 1]$–t coordinates (Fig. 5d) for *B* crystals, the cross section of electron capture by r centers was determined assuming that the concentration of photosensitive r centers in *B* crystals is $N_r = n_0 \approx 10^{16}$ cm^{-3}. For example, such an r-center concentration is typical of CdS [15]. The values of the capture cross section obtained were equal to $S_{nr} \approx 10^{-18}$ cm^2, which is characteristic of radiative electron capture by the *m*-type complex recombination center, which comprises the associated donor–acceptor pair [18]. The large value of P_r^0 for *A* crystals compared with type *B* crystals points to a larger number of defects in A crystals and a higher density of deep attachment levels in them. In addition to the formation of P_r^0, these centers can act as *s* centers of rapid nonradiative recombination.

4. NATURE OF DEFECTS IN CADMIUM THIOGALLATE

As was noted above, during the period which had passed after the originally performed synthesis of ternary compounds $A^{II}B_2^{III}C_4^{VI}$, numerous studies were carried out which were devoted to the investigation of their properties. In addition to determining the fundamental characteristics of the material, considerable attention was given to an evaluation of the nature of local states in the band gap of these compounds. For this purpose, investigations of photoconductivity and photoluminescence, as well as thermally stimulated conductivity and luminescence, electroabsorption, etc., were used (see review [4] and references therein).

As for photoluminescence, the bands observed in the spectra of $CdGa_2S_4$ crystals were somewhat different by the peak position in publications of various authors. This was attributed to possible variations in technology and the conditions of their preparation, as well as with stoichiometric deviations of the crystals investigated. Various authors reported a somewhat different spectral range when measuring the PL spectra. Most often, this range spanned to the short-wavelength region of the spectrum ($h\nu$ = 2.0–4.0 eV). In our experiments, the measured range was extended to the IR side to 0.5 eV, which allowed us to observe the bands with $h\nu_m$ = 0.971 and 1.17 eV for cadmium thiogallate for the first time.

In study [19], the investigated crystals had a composition varying within the limits of the homogeneity range along the CdS–Ga_2S_3 section from 47.5 to 50.5 mol % CdS. PL bands at 2.76, 2.08, 1.73, and 1.38 eV were observed. An attempt was made to relate some of the PL bands observed to structure defects of cadmium thiogallate.

It should be noted that the $CdGa_2S_4$ compound belongs to diamond-like semiconductors with a tetragonal lattice, in which 1/4 of the cation sites are unoccupied. The tetragonal distortion of the unit cell is caused by the ordering of the vacant sites and a dimensional factor, which implies the presence of two types of cations with differing crystallochemical dimensions in the cation sublattice [2]. It was noted that with increasing relative content of Ga_2S_3 in $CdGa_2S_4$, its degree of ordering decreases [19]. This is also shown by a decrease in the parameter $\delta = 2 - c/a$ (c and a are the unit cell parameters) as the crystal composition deviates from stoichiometry to the Ga_2S_3 excess or the CdS deficiency (see Fig. 3 in study [19]). Thus, the defect density, which affects the degree of tetragonal distor-

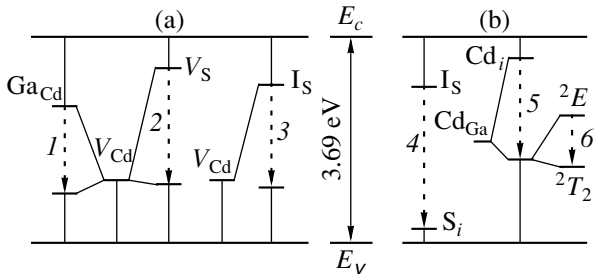

Fig. 6. Schematic energy diagram of defect levels in crystals of (a) type *A* and (b) type *B*. Radiative transitions, which correspond to photoluminescence bands with various $h\nu_m$, are shown: (*1*) 1.17, (*2*) 2.05, (*3*) 1.79, (*4*) 2.65, (*5*) 1.91, and (*6*) 0.971 eV. The following depths of levels of intrinsic defects are assumed (see the text): E_{cD} = 0.28 (Cd_i), 0.64 (V_S), 0.9 (I_S) [21], and 1.6 (Ga_{Cd}) [4] eV (for acceptors); and E_{vA} = 1.1 (V_{Cd}) [21], 0.14 (S_i), and 1.5 (Cd_{Ga}) eV (for acceptors).

tion of the lattice, is larger in the case of Ga_2S_3 excess in $CdGa_2S_4$ crystals.

It is believed that such a situation is realized in the type *A* crystals which we investigated. In this case, prevailing defects in the cation sublattice [19] are the acceptors V_{Cd} and donors Ga_{Cd}, which are charged oppositely and can form complexes, specifically, donor–acceptor pairs (V_{Cd} + Ga_{Cd}). We believe that these complexes are the centers responsible for the most intense PL bands (1.17 eV) in type *A* crystals.

In the PL spectra of $CdGa_2S_4$ crystals, which were grown from the melt in conditions of Cd depletion, an impurity photoconductivity band with $h\nu_m$ = 2.7 eV was observed [20]. This band was attributed by various authors to the presence of V_{Cd} defects in such crystals. Since cadmium thiogallate has the *n*-type conduction [11]; i.e., its photoconductivity is caused by free electrons, this means that the distance of the corresponding level from the valence band top E_{vA} is ~1.0 eV. The width of the band gap E_g for cadmium thiogallate, which was taken from [21], is 3.69 eV at 77 K. Note that the level formed by the isolated vacancy V_{Cd} in CdS, the so-called *r*-center of photosensitivity (of slowest recombination), is spaced by $E_{vA} \approx 1.1$ eV from the valence band [18, 22]. Moreover, in solid solutions with the cation substitution for II–VI compounds, for example, in $Zn_xCd_{1-x}S$, the distance of the cation vacancy level from the top of the valence band remains unchanged upon varying *x* from 0 to 1 [23]. It turns out that this rule is also valid for CdS–Ga_2S_3 solid solutions. Let us accept the purely ionic model of formation of a ternary compound. Thus, we assume that the electron states of the valence band are formed by S electron orbitals. In this case, dangling (unoccupied) S valence bonds, which are split from the valence band, form a defect level (cation vacancy). For this reason, this level is attached to the valence band.

The presence of donor antisite defects Ga_{Cd} in $CdGa_2S_4$ crystals was observed in investigations of electron spin resonance in $CdGa_2S_4$:Mn [24]. It should be noted that the considerable probability of the generation of antisite defects in $CdGa_2S_4$, namely, the donors Ga_{Cd} and acceptors Cd_{Ga}, follows from the closeness of the electronegativities for Cd and Ga atoms (1.7 and 1.6, respectively). The density of Ga_{Cd} centers increases due to annealing of volatile components, namely, Cd and S. This defect was found to form a deep donor level in the band gap. The level depth relative to the conduction band bottom is $E_{cD} \approx 1.6$ eV [4]. We may assume that it is this defect in the isolated state which is responsible for the formation of P_r^0 in the type *A* crystals which we investigated. At room temperature, this defect is an *s* center of the rapid nonradiative recombination.

Let us return to the PL band at 1.17 eV. It is our opinion that the complexes (V_{Cd} + Ga_{Cd}) are responsible for this band. The energy of the emission quantum of the donor–acceptor pair in the Coulomb approximation (neglecting the exchange interaction) is given by [25]

$$h\nu_m = E_g - (E_{vA} + E_{cD}) + \Delta. \quad (1)$$

Here, $\Delta = e^2/\varepsilon R_{AD}$ is the acceptor–donor Coulomb interaction energy, ε is the dielectric constant of the host, and R_{AD} is the acceptor–donor distance in the lattice. In the case under consideration, E_{vA} = 1.1 eV, E_{cD} = 1.6 eV, E_g = 3.69 eV, and $h\nu_m$ = 1.17 eV. Hence, it is easy to find, for a center related to the band at 1.17 eV, $\Delta \approx 180$ meV. Unfortunately, we failed to determine the value of ε for cadmium thiogallate. For this reason, it was impossible to determine the distance separating the above defects, whose combination gave rise to the emission center.

It was demonstrated that the properties of $CdGa_2S_4$ crystals depend on the I content in the charge during their growth by the gas-transport technique; i.e., it was demonstrated that I contributes to the formation of lattice defects [20]. Both donor (I substituting for S, I_S) and acceptor (interstitial I, I_i) centers can form in the band gap. The depth of the I donor level I_S was determined: E_{cD} = 0.9 eV. The presence of interstitial atoms I_i seems unlikely to be due to the large ionic radius of the I_i^{-1} ion (2.2 Å). We believe that the formation of complex centers (V_{Ga} + I_S) gives rise to the band at 1.79 eV, which we observed for type *A* crystals (Fig. 2a). The estimation from formula (1) demonstrates that, in this case, Δ = 100 meV; i.e., the distance between interacting defects is somewhat larger than in the case of complexes (V_{Cd} + Ga_{Cd}).

In addition, donor S vacancies (V_S) can be present in the *A* crystal under investigation, which was presumed by Georgobiani *et al.* [20]. Such vacancies are formed in crystals due to the self-compensation phenomenon, which is known for wide-gap binary compounds [26]. Thus, despite a high acceptor density, specifically Cd vacancies, attempts to obtain $CdGa_2S_4$ crystals with the *p*-type conduction have failed. These donors (V_S) can also interact with V_{Cd}, thus forming the complexes $V_{Cd} + V_S$. According to our assumption, these centers are responsible for the band of 2.05 eV. It is natural to expect that the distance between the components of this center is the same as in the case of complexes $V_{Cd} + I_S$, i.e., Δ also ~100 meV. In this case, the depth of the V_S level in the band gap of $CdGa_2S_4$ calculated from formula (1) will be equal to $E_{cD} \approx 0.6$ eV. The schematic energy diagram of corresponding levels and radiative electron transitions for $CdGa_2S_4$ crystals of type *A* is shown in Fig. 6a.

If the sample composition deviates from stoichiometry torwards an excess of CdS, as it happened for the type *B* crystals under investigation, the unit cell parameters and, consequently, the δ parameter remain unchanged [20]. According to the opinion of Georgobiani *et al.* [20], the reason for this is that the excess Cd atoms occupy preferentially interstitial sites (Cd_i) rather than unoccupied cation sites in the $CdGa_2S_4$ lattice. In addition, the presence of other acceptor-type defects, which are associated with the excess CdS content, is possible in such crystals, e.g., another antisite lattice defect Cd_{Ga} as well as the interstitial S atom S_i. In addition, similarly to the case of *A* crystals, atoms of the carrier gas can also be present in *B* crystals. Most likely, as was discussed above, these atoms are in the form of I_S.

Thus, in *B* crystals of $CdGa_2S_4$, which were obtained with excess CdS, acceptors of two types (S_i and Cd_{Ga}) and donors of two types (I_S and Cd_i) can be present. These donors and acceptors most likely also form complexes with each other. We believe that the band at 2.65 eV is caused by the complex $S_i + I_S$, whereas the band at 1.91 eV is related to the complex $Cd_{Ga} + Cd_i$. This conclusion is based on the following circumstances. As noted above, the depth of the donor level I_S is $E_{cD} \approx 0.9$ eV. In this case, according to formula (1), the depth of the acceptor level S_i with the Coulomb interaction energy disregarded is $E_{vA} \approx 0.14$ eV. It should be noted that, for a similar center in CdS, $E_{vA} \approx$ 0.12 eV [22, 27], which is close to the value obtained in this study. Note that for II–VI solid solutions with cation substitution (of the type $Zn_xCd_{1-x}S$), the depth of the level for such a defect, similarly to the case of V_{Cd}, does not vary with the composition [23].

As for the acceptor antisite defect Cd_{Ga}, the PL peak with $h\nu = 3.17$ eV is attributed to this defect [28]. With allowance made for the Stokes shift, we observed no PL band with an emission peak energy close to this value. For this reason, we believe that the band at 1.91 eV is related to this defect in the complex with Cd_i (Figs. 2b, 6b). The level of the isolated Cd_{Ga} defect is apparently close to the middle of the band gap. For example, let $E_{vA} = 1.5$ eV. In this case, according to expression (1), $E_{cD} - \Delta \approx 0.28$ eV; i.e., the depth of the donor level Cd_i $E_{cD} > 0.28$ eV. Note that in the case of CdS, the value of E_{cD} for a similar defect is considerably smaller (as in the case of V_S) [29]. An increase in the depth of attachment donor levels in ternary cation-substituted solid solutions based on CdS is their distinctive feature [30].

Finally, we believe that the most interesting result of this study is the band at 0.971 eV in $CdGa_2S_4$, which was observed for the first time; this band is very narrow and the most intense for type *B* crystals and, as mentioned above, undergoes thermal quenching at temperatures above 300 K with activation energies $E_a \approx 0.12$ and 0.56 eV. The unusual narrowness of this band for the PL of wide-gap imperfect semiconductors suggests that this luminescence is of the intracenter type. This means that the emission is caused by the radiative transition of the excited carrier from a higher energy state of a certain center to its lower energy level rather than the recombination of free nonequilibrium charge carriers at the defect center of a semiconductor. Such luminescence is observed for wide-gap semiconductors doped with transition metals, for example, an orange emission band for ZnS:Mn [31], a band at 1.62 μm for ZnS:Cu and CdS:Cu [32], etc. In these cases, luminescence is caused by radiative transitions between the states $G(^2E)$ and $E_{5/2}(^2T_2)$, which are split in the crystal field of unfilled *d* shells of transition metal atoms. The multiplicity of splitting is determined by the symmetry of the surroundings, and the magnitude is determined by the crystal-field strength [33].

It was noted that Cd belongs to the transition metals and completes their second row in the periodic table [34]. The configuration of its outer shells is $5s^24d^{10}$. It was also noted that the electrons of the *nd* shell have approximately the same energy as the electrons of the $(n + 1)s$ shell. Upon the formation of Cd compounds with a chalcogen (S, Se, Te), both $(n + 1)s$ electrons transfer from the Cd atom to the *p* orbitals of the chalcogenide atom. This should seemingly lead to the formation of ions with filled outer shells, i.e., to purely ionic bonding. However, there are numerous data [35] which point to the considerable fraction of covalent bonds in these compounds. This means that the mixing of the deeper electron states plays a considerable role in the formation of chemical bonds between Cd and a chalcogen. It was proved theoretically [36] and experimentally [37] that the *d* electrons of Cd contribute to chemical bonds in CdTe and CdS. Specifically, this contribution manifests itself in the luminescent properties of these compounds. If the latter contain interstitial

atoms with a high electron affinity (chalcogen, I, etc.), intracenter luminescence with the emission quantum energy $h\nu_m \sim 1$ eV is observed. This process is related to electron transitions between the terms of the split *d* shell of Cd.

In this study, type *B* crystals of $CdGa_2S_4$ enriched with CdS were investigated in which the conditions for the splitting of the *d* shell of a Cd ion, which occupies the Ga site, Cd_{Ga}, are satisfied. This is due to the presence of interstitial S atoms, which, as was noted above, have a high electron affinity.

The linear dependence of the intensity of the band of 0.971 eV on the excitation intensity at the temperature from the region of its thermal quenching also confirms its intracenter character. In this case [38], luminescence quenching occurs due to the tunneling of excited electrons and their passing through the point of intersection of adiabatic potentials (point A in Fig. 3, inset). These potentials describe the state of the center in the ground and excited states in configuration coordinates with a subsequent multiphonon transition to the minimum of the adiabatic curve, which describes the center in the ground state [39]. We measured the activation energy of thermal quenching of the band with $h\nu_m = 0.971$ eV and found that this energy is equal to 0.56 eV. Most likely, this is the energy coordinate of point A relative to the minimum of the adiabatic curve, which describes the center in the excited state (energy *E*). The activation energy, which is equal to 0.12 eV, characterizes the processes of tunneling through the potential barrier which separates these curves.

For recombination luminescence, the dependence of PL intensity on the excitation intensity at a temperature from the range of its thermal quenching should be superlinear [16, 38]. In this case, the activation energy measured is the depth of the corresponding acceptor level relative to the valence band top.

A schematic diagram of levels for lattice defects and radiative electron transitions between them for type *B* cadmium thiogallate crystals investigated is shown in Fig. 6b.

ACKNOWLEDGMENTS

We thank S.V. Belyaeva for placing at our disposal the type *A* and type *B* crystals of cadmium thiogallate, and S.A. Vasil'kovskii for measurements of Raman spectra.

This study was supported by the Foundation for Basic Research of the Ministry of Sciences of Ukraine, grant no. 2/840.

REFERENCES

1. H. Hahn, G. Frank, W. Klinger, *et al.*, Zh. Anorg. Allg. Chem. **279**, 241 (1955).
2. N. A. Goryunova, Dokl. Akad. Nauk SSSR **103**, 639 (1955).
3. N. A. Goryunova, *Compound Diamond-Like Semiconductors* (Sov. Radio, Moscow, 1968).
4. A. N. Georgobiani, S. I. Radautsan, and I. M. Tiginyanu, Fiz. Tekh. Poluprovodn. (Leningrad) **19**, 193 (1985) [Sov. Phys. Semicond. **19**, 121 (1985)].
5. C. I. Radautsan, Yu. O. Derid, V. F. Zhitar', *et al.*, Dokl. Akad. Nauk SSSR **267**, 673 (1982).
6. J. A. Beun, R. Nitsche, and M. Lichtensteiger, Physica (Amsterdam) **27**, 448 (1961).
7. V. B. Abdullaev, V. G. Agaev, V. B. Antonov, *et al.*, Fiz. Tekh. Poluprovodn. (Leningrad) **5**, 2132 (1971) [Sov. Phys. Semicond. **5**, 1854 (1971)].
8. D. V. Gitsu, V. F. Zhitar', V. Ya. Raĭyan, *et al.*, in *Proceedings of the VI International Conference on Amorphous and Liquid Semiconductors, Leningrad, 1976*, p. 287.
9. S. V. Belyaev, N. S. Khilimova, V. A. Khvostov, and Yu. G. Sinyuk, in *Proceedings of the 8th International Conference on Ternary and More Complicated Compounds* (Shtiintsa, Kishinev, 1990), p. 11.
10. L. I. Berger and V. D. Prochukhan, *Ternary Diamond-Like Semiconductors* (Metallurgiya, Moscow, 1968; Consultants Bureau, New York, 1969).
11. V. F. Zhitar', V. S. Donu, M. I. Val'kovskaya, and I. M. Markus, in *Physics and Chemistry of Compound Semiconductors* (Shtiintsa, Kishinev, 1975), p. 50.
12. T. G. Kerimova, R. Kh. Nani, V. K. Salaev, *et al.*, Fiz. Tverd. Tela (Leningrad) **21**, 1899 (1979) [Sov. Phys. Solid State **21**, 1093 (1979)].
13. V. F. Zhitar', A. I. Machuga, and S. I. Radautsan, Opt. Spektrosk. **51**, 948 (1981) [Opt. Spectrosc. **51**, 526 (1981)].
14. E. A. Sal'kov and M. K. Sheĭnkman, Fiz. Tverd. Tela (Leningrad) **5**, 397 (1963) [Sov. Phys. Solid State **5**, 289 (1963)].
15. I. B. Ermolovich and M. K. Sheĭnkman, Ukr. Fiz. Zh. **9**, 1153 (1964).
16. M. K. Sheĭnkman, I. B. Ermolovich, and G. L. Belen'kiĭ, Fiz. Tverd. Tela (Leningrad) **10**, 2628 (1968) [Sov. Phys. Solid State **10**, 2069 (1968)].
17. S. I. Radautsan, V. S. Donu, V. F. Zhitar, and E. E. Strumban, Phys. Status Solidi A **57**, K79 (1980).
18. A. N. Georgobiani, S. I. Radautsan, and I. M. Tiginyanu, Phys. Status Solidi A **69**, 513 (1982).
19. A. N. Georgobiani, Yu. O. Derid, S. I. Radautsan, and I. M. Tiginyanu, Kratk. Soobshch. Fiz., No. 8, 46 (1983).
20. A. N. Georgobiani, A. N. Gruzintsev, S. I. Radautsan, and I. M. Tiginyanu, Phys. Status Solidi A **80**, K45 (1983).
21. Yu. O. Ozerov, S. I. Radautsan, and I. M. Tiginyanu, Fiz. Tverd. Tela (Leningrad) **23**, 2094 (1981) [Sov. Phys. Solid State **23**, 1221 (1981)].
22. I. B. Ermolovich, G. I. Matvievskaya, G. S. Pekar', and M. K. Sheĭnkman, Ukr. Fiz. Zh. **18**, 729 (1973).
23. N. A. Vlasenko, I. B. Ermolovich, F. F. Kodzhespirov, *et al.*, Izv. Akad. Nauk SSSR, Ser. Fiz. **35**, 1433 (1971).
24. M. Shlaak and A. Weiss, Z. Naturforsch. A **27**, 1624 (1972).
25. F. E. Williams, Phys. Status Solidi **25**, 493 (1968).

26. F. A. Kröger, *The Chemistry of Imperfect Crystals* (Wiley, New York, 1964; Mir, Moscow, 1969).
27. I. B. Ermolovich, A. V. Lyubchenko, and M. K. Sheĭnkman, Fiz. Tekh. Poluprovodn. (Leningrad) **2**, 1639 (1968) [Sov. Phys. Semicond. **2**, 1364 (1969)].
28. A. N. Georgobiani, A. N. Gruzintsev, and S. I. Radautsan, Phys. Status Solidi A **80**, K45 (1983).
29. I. B. Ermolovich, V. V. Gorbunov, and I. D. Konozenko, Radiat. Eff. **17**, 161 (1978).
30. I. B. Ermolovich and N. K. Konovets, Ukr. Fiz. Zh. **18**, 803 (1973).
31. R. Parrot, C. Naud, D. Curie, *et al.*, J. Lumin. **31–32**, 293 (1984).
32. J. Broser, H. Maier, and H. Schulz, Phys. Rev. **140**, A2135 (1965).
33. O. N. Boksha and S. V. Grum-Grzhimaĭlo, *Optical Spectra Studies of Crystals with Ions from Iron Group under the Room and Low Temperatures* (Nauka, Moscow, 1972).
34. J. Murrel, S. Kettle, and J. Tedder, *The Chemical Bond* (Wiley, Chichester, 1978; Mir, Moscow, 1980).
35. *Physics and Chemistry of II–VI Compounds*, Ed. by M. Aven and J. S. Prener (North-Holland, Amsterdam, 1967; Mir, Moscow, 1970).
36. S. I. Kurganskiĭ, O. V. Farberovich, and É. P. Domanskaya, Fiz. Tekh. Poluprovodn. (Leningrad) **14**, 1412 (1980) [Sov. Phys. Semicond. **14**, 837 (1980)].
37. I. B. Ermolovich and I. I. Milenin, Zh. Prikl. Spektrosk. **47**, 829 (1987).
38. I. B. Ermolovich and V. V. Milenin, Phys. Status Solidi B **133**, 611 (1986).
39. D. Curie, *Luminescence cristalline* (Dunod, Paris, 1960; Nauka, Moscow, 1961).

Translated by N. Korovin

Semiconductors, Vol. 36, No. 7, 2002, pp. 772–781. Translated from Fizika i Tekhnika Poluprovodnikov, Vol. 36, No. 7, 2002, pp. 826–835.

ELECTRONIC AND OPTICAL PROPERTIES OF SEMICONDUCTORS

Microwave Magnetoresistance of Compensated *p*-Ge:Ga in the Region of the Insulator–Metal Phase Transition

A. I. Veĭnger*, A. G. Zabrodskiĭ, and T. V. Tisnek

Ioffe Physicotechnical Institute, Russian Academy of Sciences, Politekhnicheskaya ul. 26, St. Petersburg, 194021 Russia

**e-mail: anatoly.veinger@pop.ioffe.rssi.ru*

Submitted December 24, 2001; accepted for publication December 28, 2001

Abstract—The microwave magnetoresistance (MR) of neutron transmutation doped (moderately compensated) Ge:Ga in the insulator–metal transition region was studied using ESR technique. As the hole concentration increases, the MR mechanism changes in the insulator state near the phase transition point: the hopping conductivity that is characterized by the impurity wave-function contraction by the magnetic field is replaced by the state of weak localization. In the latter case, the temperature dependence of the diffusion coefficient is of great importance near the transition point (1.2×10^{17} cm^{-3}). This dependence decreases in the metallic state. In the metallic state, the diffusion coefficient is independent of temperature and the MR temperature dependence is described by the dephasing mechanism due to phonon scattering. The electron–electron interaction contribution to the dephasing time should be considered for heavier doping. © *2002 MAIK "Nauka/Interperiodica".*

1. INTRODUCTION

Magnetoresistance (MR) studies of heavily doped semiconductors at low temperatures, which have been conducted for more than 40 years, provide insight into the electronic properties of the solid state. Thus, inconsistent explanations of the negative MR within the context of classical theory stimulated the emergence and development of the quantum correction theory in conduction [1]. This theory, in turn, has caused further interest in the experimental study of different materials, in particular, semiconductors [2]. However, the primary attention of researchers has been concentrated, until now, on the study of *n*-type semiconductors in which corrections to conduction result in the occurrence of the negative MR effect. At the same time, negative MR has never been observed in *p*-type semiconductors. Due to this circumstance, these materials have aroused lesser interest, although, as the theory of quantum corrections show, MR in them has the same nature but opposite sign due to strong spin–orbit scattering. Since in *p*-type semiconductors the sign of MR coincides with the sign following from the classical theory, this effect was named "anomalous positive MR." This effect was observed for the first time in [3] before the development of the quantum correction theory.

The weak localization mechanism of the quantum correction theory gives a fundamental contribution to the MR of a metallic system. It is completely applicable to heavily doped semiconductors with metallic conduction. However, the conductivity of a semiconductor decreases as the impurity concentration decreases, and the metal–insulator phase transition occurs at the critical concentration N_C. Low-temperature conductivity of a semiconductor becomes of the hopping type for $N < N_C$, and, in this case, the mechanism mentioned above is irrelevant, although anomalous MR is observed in this case too, i.e., in *p*-Ge [4–7]. In this context, other mechanisms were developed for the description of positive MR in the hopping conduction region: deformation of the impurity center wave functions by the magnetic field [8]; quantum interference of the wave functions, which arises owing to scattering of tunneling carriers by intermediate centers, including spin-effects [9]; and narrowing of the impurity band in the magnetic field [10]. However, these mechanisms are applicable, strictly speaking, for the concentrations $N \ll N_C$.

As for the region in the immediate vicinity of the insulator–metal (IM) phase transition, there is no adequate description of the MR effect. At the same time, in this range of concentrations there is a special feature in the energy spectrum of the charge carriers (the Coulomb gap) [11], which was theoretically predicted by Efros and Shklovskii [8] for the conditions of strong localization. As shown in [12], collapse of the Coulomb gap defines the critical concentration for the IM phase transition. In this context, experimental investigation of the MR effect in the IM phase transition region has obvious interest from the point of view of the Coulomb gap concept of the insulator state. The results of such a study are reported in this paper.

1063-7826/02/3607-0772$22.00

2. SAMPLES

We measured the anomalous positive MR in *p*-Ge using a set of samples obtained by neutron transmutation doping of fairly pure *p*-Ge with an impurity concentration on the order of 10^{14} cm^{-3}. The advantage of this method of doping is that the arrangement of transmutation-introduced acceptors and donors is random. The doping level of such samples is defined by the neutron fluence, and the relative content of transmutation-introduced impurities is controlled by the isotopic composition of an initial material and by the spectrum of irradiating neutrons [13]. For the natural mixture of Ge isotopes in our samples, the shallow Ga acceptor is the basic transmutation impurity; the shallow As donor and deep, doubly charged Se donor are compensating impurities. The degree of compensation is about 0.35 for the spectrum of neutrons used in this study.

The concentration difference in the samples under study was equal to $N_A - N_D = (7.55–28.6) \times 10^{16}$ cm^{-3}. Since this concentration is much higher than the background concentration, the latter did not affect the experiments. As is well known [14], the transition from the insulator to metallic state occurs in *p*-Ge:Ga for a Ga concentration $N_{Ac} = 1.85 \times 10^{17}$ cm^{-3}, which corresponds to $p_c = 1.20 \times 10^{17}$ cm^{-3} for 35% compensation. Thus, the obtained set of samples includes both insulator (1–5) and metallic (7–15) samples. The parameters of the samples under study are listed in the table. Let us note that the concentration of the major Ga impurity was calculated from Hall effect measurements on the basis of calibrating curves at room temperature that take into account the concentration dependence of the Hall factor for a complex Ge valence band [15].

All samples had an identical rectangular shape with the dimensions of $10 \times 3 \times 1$ mm. The results of the resistivity temperature dependences in *p*-Ge were used to account for the skin effect in low-resistivity samples in the temperature range under consideration [16]. It is well known that the skin depth is approximately equal to 0.5 mm at the frequency of 10 GHz and for the resistivity $\rho \approx 1\ \Omega$ cm and varies proportionally to $\rho^{-1/2}$. The resistivity of the samples ranged from 2.8 Ω cm (in most lightly doped sample 1) to 0.2 Ω cm (in most heavily doped sample 15) at liquid helium temperature. The resistivity data at liquid helium temperature, listed in the table, show that it is necessary to make corrections for the skin depth only for the most heavily doped samples, beginning from sample 6.

Parameters of *p*-Ge samples

Sample no.	p, 10^{16} cm^{-3}	ρ_{He}, Ω cm
1	7.55	2.8
2	8.73	1.8
3	9.38	1.6
4	9.56	1.5
5	10.8	1.0
6	12.0	0.80
7	12.9	0.65
8	13.8	0.55
9	15.2	0.45
10	16.0	0.40
11	20.6	0.35
12	24.1	0.30
13	24.2	0.25
14	27.6	0.25
15	28.6	0.20

Note: p is the hole concentration at room temperature; ρ_{He} is the resistivity at $T = 4.2$ K.

3. EXPERIMENTAL TECHNIQUE

We studied the MR in the microwave (MW) range using an electron spin resonance (ESR) spectrometer. This technique was previously proposed in [17] for measurements of MR in *n*-Ge:As [18]. We used a Varian E-112 ESR spectrometer operating at a 10 GHz frequency with an Oxford Instruments ESR-9 flowing helium cryostat. MR measurements were performed in the temperature range from 3 to 300 K. The spectrometer detected a change in the energy P, which was absorbed by the cavity in which the sample was placed, as the magnetic field H was varied: dP/dH [19]. It is of fundamental importance that such an energy increment can occur not only because of a change in the energy absorption by spins, as in the ESR detection, but also for other reasons, in particular, due to variation of the sample resistivity in the magnetic field.

Let us consider in more detail the special features of the semiconductor MR measurements in the cavity in the MW range. Different dependences of the increment of the energy absorbed in the cavity on the sample resistance (R) variation are observed at various ratios between R and the wave impedance of the wave guide (generator) (R_g). In this case, $dP/dH \propto d\sigma/dH$ (σ is the conductivity of the sample) for high-resistivity samples and $dP/dH \propto dR/dH$ for low-resistivity samples. In fact, the energy absorbed by the sample is given by

$$P = \frac{E_g R}{(R_g n^2 + R)^2}, \tag{1}$$

where E_g is the emf of the generator, and n is the transformation ratio through the accumulation of energy in the cavity. According to the ratio (1), it is possible to write

$$\frac{dP}{dH} = \frac{dP}{dR}\frac{dR}{dH} = \frac{E_g^2}{(R_g n^2 + R)^2}\left[1 - \frac{2R}{(R_g n^2 + R)}\right]\frac{dR}{dH}, \tag{2}$$

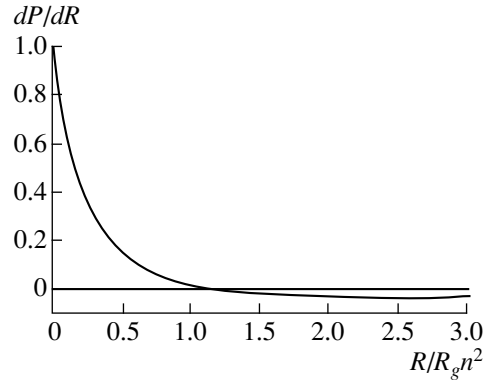

Fig. 1. The dependence of the *dP*/*dH* derivative of MW absorption with respect to the magnetic field on the ratio of the load resistance *R* to the resistance of generator R_g.

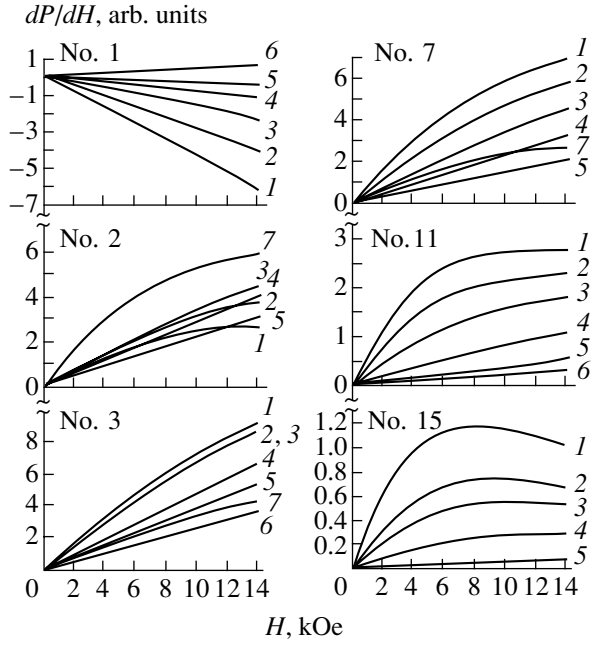

Fig. 2. The magnetic-field dependences of the derivative of MW absorption at temperatures *T* = (*1*) 3.2, (*2*) 4, (*3*) 6, (*4*) 10, (*5*) 20, (*6*) 30, and (*7*) 40 K. The numbers of the samples correspond to the numbers in the table.

whence follows that the factor in square brackets is negative for $R > R_g n^2$ and $dP/dH \propto -dR/dH \propto d\sigma/dH$; i.e., it is varied in the magnetic field in the same way as the conductivity. If $R < R_g n^2$, then $dP/dH \propto dR/dH$; that is, *dP*/*dH* is varied in the same manner as the resistance in the magnetic field.

Thus, the ratio between the resistances of the generator and the sample governs the sign of change in the derivative of MW absorption in the magnetic field. From here it follows that the derivative $dP/dH = 0$ if $R = R_g n^2$; i.e., the sensitivity of the method approaches zero. We do not consider other sources of losses in the cavity walls, so-called coupling losses, etc., since they are much smaller than losses in the sample and affect the experimental dependences insignificantly. It is necessary to note that the change of the sign of the absorption derivative with respect to the magnetic field does not manifest itself either in a classical insulator or classical metals because one of the inequalities, $R \gg R_g n^2$ or $R \ll R_g n^2$, holds within a wide margin.

The dependence of the derivative *dP*/*dR* on the ratio between the load resistance *R* and $n^2 R_g$, calculated according to (2), is shown in Fig. 1. One can see that the sensitivity of the method is almost constant for $R \gg n^2 R_g$ and varies appreciably when $R \simeq n^2 R_g$, thus changing its sign. Such sensitivity variation should not have an effect on the MR field dependences, because the sample resistance is insignificantly changed in the magnetic field (about 1%). This fact may be important when studying the MR temperature dependences.

Since, in the domain of the existence of anomalous positive MR, the resistance remains approximately constant in the metallic samples and decreases in the insulator ones, as temperature increases, the sensitivity of the method can only increase, and only moderately, with the temperature for $R < R_g n^2$. However, if $R > R_g n^2$, the sensitivity of the *dP*/*dR* detection decreases and it can become equal to zero as the temperature increases. Apparently, this effect manifests itself in most lightly doped sample 1 (Fig. 2), in which the derivative *dP*/*dH* is negative at low temperatures, i.e., $dP/dH \propto d\sigma/dH$. The sensitivity is equal to zero at $T \sim 25$ K; at higher temperatures, when conductivity becomes fairly high, $dP/dH \propto dR/dH$. Therefore, in this sample, the experimental dependence *dP*/*dH* changes its sign with temperature. In other samples, the resistance is always smaller than the generator resistance in the temperature range under study. This experimental effect manifests itself to a much lesser extent; as a result, as a first approximation it can be ignored. In addition, the resistance of metallic and insulator samples varies only slightly in the domain of existence of anomalous positive MR. [18]. Due to this fact, the temperature variations of the derivative of the MW absorption should be attributed mainly to variation in anomalous positive MR.

We will now focus our attention on other features of the technique we use. The advantage of this technique is that the use of recordings of the derivative of MW absorption with respect to the magnetic field drastically increases the sensitivity of measurements. The accuracy of fixing and measurements of the magnetic field, typical of ESR, increases the accuracy of the MR measurements. In addition, the method is contactless. However, for certain reasons, measurements in the MW fields do not give precise values of MR. First, the MW field only penetrates to skin depth in the low-resistivity samples. All experimental results concern this layer rather than the bulk. Second, MW absorption is measured in the cavity of the ESR spectrometer, and variation in the Q factor affects the magnitude of the effect.

Third, as mentioned above, variation in the sample resistivity causes variation in the sensitivity of the technique. In this context, additional correction factors were used for the evaluation of the derivative of MR with respect to the magnetic field for a more correct comparison of the field and temperature dependences in the samples (see below).

We should note an essential physical difference between the dc and MW measurements of MR. The point is that the basic contribution to total sample resistance is made by regions with the highest dc resistance. Absorption of energy at MW frequencies occurs in the regions where there are free charge carries, and the regions with lower resistance make the main contribution to absorption. This is not important until the potential fluctuations of the bottom of the conduction band are small, i.e., in uncompensated and weakly compensated samples. As compensation increases, this distinction also increases, and it may result in disagreement in the experimental results. In our case, these distinctions should not be large due to screening of fluctuations in the metallic samples. However, near the IM phase transition point, when insulator layers in the conducting clusters become important, the results of dc measurements significantly differ from the MW measurements at low temperatures.

In the course of experiment, the sample was placed into a cryostat, which was in the cavity of the ESR spectrometer, and it was cooled to the required temperature. The field dependences of the derivative of MW absorption were automatically recorded.

4. CONSIDERATION OF THE CAVITY Q FACTOR AND SKIN DEPTH VARIATION. EXPERIMENTAL RESULTS

The Q factor of the cavity varies when we change samples with different resistances and temperatures, which affects the sample resistance. To take into account all these variations of the Q factor, the MR and ESR signal from the calibrated Varian reference sample, the amplitude of which is proportional to the Q factor of the cavity, were measured simultaneously. This sample was in the same cavity but outside of the cryostat, so its temperature was always constant (room temperature). We used measurements of the temperature dependences of the resistivity in *p*-Ge [16] to take into account the skin effect in the low-resistivity samples. It should be noted that the skin effect only influences the derivative of absorption and does not affect the field and temperature dependences of the MR due to a small resistivity variation in the domain of existence of anomalous positive MR.

The recorded signal was reduced to commensurable values using correction factors κ_1 and κ_2 for comparison of the magnitude of the effect in different samples and at dissimilar temperatures. These factors account for the variations in the cavity Q factor and the skin depth of the sample. The first factor is defined by the ratio of the ESR signal amplitude of the testing-calibrated Varian (B_x) sample (the sample under study is in the same cavity) to the ESR signal amplitude of the same calibrated sample with investigated sample 15 (B_{15}) in the cavity:

$$\kappa_1 = B_x/B_{15}. \quad (3)$$

The factor κ_2 was taken to be equal to the reciprocal efficient absorbing volume, so that

$$\kappa_2^{-1} = V_{\text{eff}} = \begin{cases} S\delta, & \delta < W, \\ SW, & \delta > W, \end{cases} \quad (4)$$

where S is the area of the sample surface, δ is the skin depth, and W is the sample thickness.

In this case, the signal A_{15} from sample 15 was taken as unity in the magnetic field $H = 14$ kOe and at $T = 3.2$ K. To adjust the signal to the unified value A_{adj}, the signal amplitude at every point A_x was divided by the A_{15} amplitude and multiplied by the correction factors κ_1 and κ_2:

$$A_{\text{adj}} = (A_x/A_{15})\kappa_1\kappa_2. \quad (5)$$

It is these reduced field dependences for different temperatures that are shown in Fig. 2. The curve numbers increase with temperature.

One can see that the derivative of the MW absorption is negative for sample 1 at low temperatures, but in other samples it is positive for all temperatures. The MR effect diminishes, as a rule, with temperature. The character of the field dependences changes while crossing the metal–insulator phase transition point.

5. DISCUSSION

Let us consider in more detail the temperature and concentration dependences of MR on the magnetic field measured at MW frequencies.

5.1. The Magnetic Field Dependences

In this case, it is necessary to give special consideration to sample 1, in which the derivative of the MW absorption is negative at low temperatures. Probably, the sign reversal of the dP/dH derivative is caused by the sign reversal of the dP/dR derivative for $R = R_g n^2$ (Fig. 1). In fact, the sign of the dP/dH derivative is changed in the temperature range (several decades of K) where the sample resistance abruptly varies [16]. Comparison of R and $R_g n^2$ shows that they are only equal in the case of weak coupling of the sample with the cavity. In fact, the Q factor of the cavity with the sample is equal to $Q \approx 100$ (the Q factor of an empty cavity is about 1000; thus, the signal amplitude is 10 times smaller when the sample is placed into the cavity), $Q \approx n$, and $R_g = 250\ \Omega$ (the wave impedance of the cavity). In

the case of strong coupling, equality of the resistances should occur for $R \approx 2.5 \times 10^6$ Ω. However, sign inversion occurs in sample 1 for $\rho \approx 10$ Ω cm. This is only possible for weak coupling of the sample with the cavity. This conclusion is confirmed by the fact that the ESR signal phase of the reference sample does not change when the sign of the *dP*/*dH* function is reversed.

The derivative is linear in the low-field region. In this region, the MR dependence on the magnetic field is quadratic. Such a dependence holds for any MR mechanism. In this context, to clarify the effect of anomalous MR, we need to study the magnetic field dependences in higher magnetic fields as well as temperature dependences.

It can be seen from Fig. 2 that the field dependences are superlinear in the most lightly doped sample 1 at low temperatures. At the same time, these dependences are sublinear in other samples. The sublinearity increases with doping, and there is a peak in the dependence of the derivative of MW absorption in the metallic samples (sample 15) at low temperatures. The peak is shifted to higher magnetic fields with temperature, but the effect diminishes. The derivative of MW absorption decreases with temperature up to $T = 20$–30 K. At higher temperatures, it again increases, as one can see by the example of nonmetallic samples 2 and 3 and metallic sample 7.

In the insulator samples, far from the IM transition point, the theory which explains anomalous positive MR by deformation of the wave functions of localized carriers by the magnetic fields [8] is used for describing the experiments. This theory predicts a superlinear resistivity dependence on the magnetic field:

$$\rho(H)/\rho(0) = \exp(CH^2), \tag{6}$$

where C is a constant.

A comparison of (6) the experimental results for sample 1 shows that they can be satisfactorily explained on the basis of this theory. However, for other samples, the theory is irrelevant because the *dP*/*dH* dependences become sublinear.

The theory of quantum corrections is usually used for the MR description of the most heavily doped metallic samples [1, 2]. For semiconductors, as has been repeatedly shown, the weak localization conditions are dominant in the theory. In this case, the resistivity increases in the magnetic fields in *p*-type semiconductors. This is caused by the influence of the spin–orbit interaction on weak localization processes in relatively weak magnetic fields. If the spin relaxation time in a semiconductor $\tau_{so} \gg \tau_\varphi$ (the dephasing time), the spin–orbit interaction is not important in the effect. Then, the MR can be described by the relation [1, 2]

$$\Delta\sigma(H) = G_0\Phi(x)/(D\tau_\varphi)^{1/2}, \tag{7}$$

where $G_0 = e^2/(2\pi\hbar) = 1.233 \times 10^{-5}\ \Omega^{-1}$, $x = 4eD\tau_\varphi H/\hbar c$, $\Phi(x)$ is the function which cannot be analytically described in the general case, and its asymptotic expressions can be written as

$$\begin{cases} \Phi(x) = x^2/96 \quad \text{for} \quad x \ll 1, \quad H \longrightarrow 0; \\ \Phi(x) = 0.302x^{1/2} - 1 \quad \text{for} \quad x \gg 1, \quad H \longrightarrow \infty. \end{cases} \tag{8}$$

When the spin relaxation time τ_{so} is comparable with the dephasing time τ_φ, the relation for $\Phi(x)$ is changed and takes the form

$$\Phi^*(x) = 3\Phi(Cx)/2C^{1/2} - \Phi(x)/2, \tag{9}$$

where $C = (1 + 4\tau_\varphi/3\tau_{so})^{-1}$.

It can be seen that the first term in (9) is much smaller than the second as $\tau_{so} \ll \tau_\varphi$ in *p*-type semiconductors, and the entire MR effect is defined, as usual, by the dephasing time, but has the opposite sign. Thus, anomalous MR should be no less pronounced in *p*-type semiconductors than in *n*-semiconductors.

Let us compare experimental dependences with calculations according to this theory. As is well known, the function $\Phi(x)$ can be expressed either as an infinite series or as an improper integral which depends on the parameter and cannot be integrated analytically [20, 21]. For calculations, we used the integral derived in [22]:

$$\Phi(x) = \frac{\sqrt{x}}{4\pi}\int_0^\infty t^{-3/2}e^{-2t/x}(1 - t/\sinh t)dt = \frac{\sqrt{x}}{4\pi}f(x), \tag{10}$$

where x is defined as in (7).

Since the ESR spectrometer records the dependence of the derivative of the MW absorption on the magnetic field, it was necessary to find the derivative of relation (10) with respect to x for comparison of the theoretical and experimental dependences. It can be expressed as

$$\frac{d\Phi(x)}{dx} = \frac{f(x)}{4\sqrt{x}} + \frac{\sqrt{x}}{2}\frac{df(x)}{dx}, \tag{11}$$

where

$$\frac{df}{dx} = \int_0^\infty \frac{2}{\pi}\frac{e^{-2t/x}}{x^2\sqrt{t}}\left(1 - \frac{t}{\sinh(t)}\right)dt. \tag{12}$$

Numerical calculations of the derivative of $dP/dH \propto d\Phi/dH$ according to relations (11) and (12) and the experimental dependence for the most heavily doped sample (15) at $T = 3.2$ K are shown in Fig. 3.[1] It can be seen that in low fields up to the field corresponding to the maximum of the absorption derivative the experimental data are in good agreement with the theory. This shows that the weak localization conditions of the quantum correction theory can be applied to the "metallic" *p*-Ge in the vicinity of the IM transition point. At higher fields, in which the derivative of absorption

[1] The authors are grateful to S.O. Usov for performing the calculations.

decreases, the slope of the experimental curve is larger than that of the theoretical curve. Apparently, this occurs due to an increase in the contribution of two other mechanisms of quantum corrections: interaction of charge carriers in the diffusion or Cooper channels. For example, in *n*-Ge these mechanisms make a dominant contribution to the MR in high magnetic fields and, as a result, the MR changes from negative to positive [18]. Until now, the contribution of these effects was not experimentally investigated for the conditions of strong spin–orbit coupling in *p*-type materials.

As follows from the asymptotic values of $\Phi(x)$, the derivative of absorption has a maximum in weak localization conditions (8). In fact, $d\Phi/dx \propto x$ for $x \ll 1$; i.e., it increases with the field, and $d\Phi/dx \propto x^{-1/2}$ for $x \gg 1$; i.e., it decreases.

From the numerical calculations, it follows that the maximum of the derivative occurs in the field H_{max} which corresponds to $x = 5.1$. Thus, the dephasing length can be found:

$$L_\varphi = (D\tau_\varphi)^{1/2} = (x\hbar c/4eH_{max})^{1/2}. \quad (13)$$

Correspondingly, $L_\varphi = 1.8 \times 10^{-6}$ cm for sample 15 at $T = 3.2$ K and $H_{max} \approx 8000$ Oe.

A decrease in the concentration and an increase in temperature causes an abrupt decrease of the dephasing length. This manifests itself in the shift of the MR derivative maximum to higher fields. However, it is possible to fit, using scale variation, the calculated field dependences of the MR to the experimental curves for part of the samples and to obtain the temperature dependence of H_{max}. This dependence will be discussed below.

5.2. Temperature Dependences

The behavior of the proportionality coefficient β is important for understanding the mechanism of the MR quadratic dependence $\Delta\rho/\rho = \beta H^2$. In this context, the slopes of the initial linear portions of the *dP*/*dH* curves were determined:

$$d^2P/dH^2 = \frac{1}{H}dP/dH \quad \text{for} \quad H \longrightarrow 0. \quad (14)$$

The dependences of the absolute value of the second derivative of MW absorption, with respect to the magnetic field at $H \longrightarrow 0$, on temperature are displayed in Fig. 4 in a log–log scale for several samples. One can see that the signal amplitude decreases by the power law at $T > 3.2$ K. It can be expressed as

$$d^2P/dH^2 \propto T^{-\alpha}, \quad (15)$$

where $\alpha = 1.53$ for sample 1. This coefficient increases up to 0.39 in sample 2, and then it increases to 1.8 in the most heavily doped "metallic" sample 15.

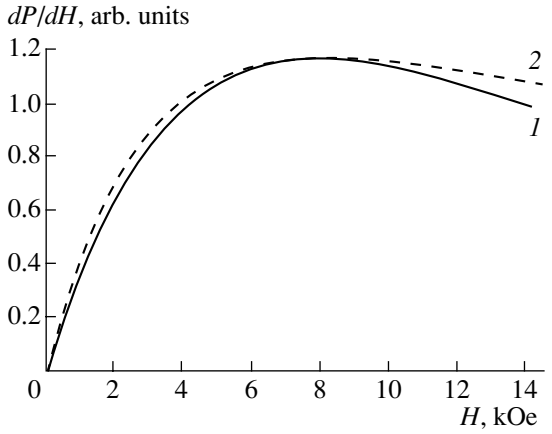

Fig. 3. Comparison of (curve *1*) the experimental dependence of the derivative of MW absorption on the magnetic field for sample 15 at T = 3.2 K with (curve *2*) calculations using relations (10) and (11).

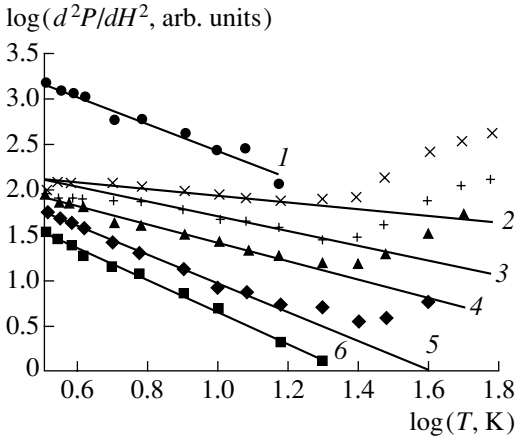

Fig. 4. Experimental and calculated temperature dependences of the second derivative of MW absorption at $H \longrightarrow 0$ for the samples with varied impurity concentration (the sample numbers correspond to the numbers in the table): (*1*) 1, (*2*) 2, (*3*) 3, (*4*) 7, (*5*) 10, and (*6*) 15. The curves are shifted relative to each other on an arbitrary value along the ordinate axis for clearer illustration.

Let us first analyze the temperature dependence of sample 1 using the theory of wave function contraction by a magnetic field. It was mentioned above that, in this case, the temperature dependence could be caused by the measurement effect. However, a decrease in the resistivity with temperature should be accompanied by variation in the cavity tuning. In this experiment, no variation of the cavity tuning occurs up to $T = 20$ K. This effect only develops at higher temperatures. Therefore, the variation in d^2P/dH^2 is completely predictable at lower temperatures, and this can be explained by a decrease in the β coefficient in the MR field dependence. Superlinear MR dependence on the magnetic field shows that conductivity has a hopping character in this sample. The conductivity with variable

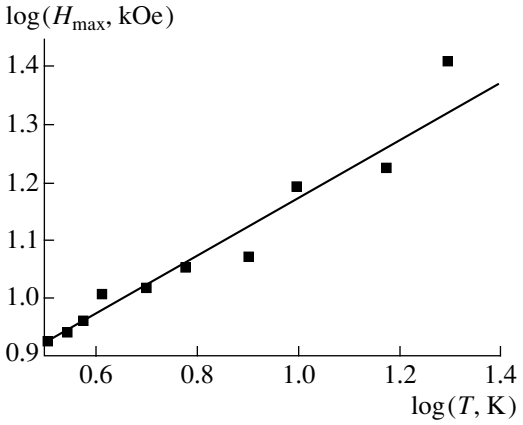

Fig. 5. The temperature dependence of the maximum position (H_{max}) of the derivative of MW absorption with respect to the magnetic field for sample 15.

range hopping (VRH) in low fields and in the presence of a Coulomb gap [23] can be described by the relation

$$\rho(H)/\rho(0) = AH^2T^{-3/2}, \quad (16)$$

where A is a constant.

It follows from (16) that the dependence of the derivative of MW absorption, as usual, should be a linear function of the magnetic field, and the signal amplitude should decrease proportionally to $T^{-3/2}$ with temperature. The exponent in the temperature dependence ($T^{-1.53}$) is close to this value in the temperature range of 3.2–15 K. It should be noted, however, that VRH conditions are realized in *p*-Ge:Ga at $T < 1$ K [16]. The origin of such a dependence of MR in sample 1 is obscure in the temperature range under study.

The exponent in the temperature dependence abruptly decreases from $\alpha = 1.53$ to $\alpha = 0.39$ as the doping level increases from 7.55×10^{16} cm^{-3} (sample 1) to 8.73×10^{16} cm^{-3} (sample 2). This is apparently related to a change in the MR mechanism. Additional features of the field dependences of MR in lightly doped samples 2 and 3 at low temperatures can be seen in Figs. 2 and 4. An increase of d^2P/dH^2 is observed in sample 2 in the temperature range of 3–5 K. There is no such increase in sample 3, but the second derivative remains constant in the temperature range of 3–6 K. Thus, the exponent α first abruptly decreases as the system approaches the IM phase transition and then it gradually increases up to 1.5 for the concentration $p \approx 1.5 \times 10^{17}$ cm^{-3}. This effect will be considered below when we analyze the concentration dependences.

As the impurity concentration increases, the slope of the temperature dependence is almost independent of the doping level in the metallic region near the IM phase transition. In the most heavily doped metallic samples, we have $\alpha = 1.8$. It is possible to compare this value with the prediction of the theory of quantum corrections under weak localization conditions. According to (5), the temperature dependence of MR is almost completely defined by the temperature dependence of τ_φ because other parameters are constant. In turn, the dephasing time is defined by inelastic scattering [1, 2].

If the dephasing is caused by interaction with phonons, then, for heavily doped semiconductors, $\tau_\varphi \sim T^{-1}$. Substituting this relation into (5), in the limit of $H \longrightarrow 0$ we have

$$d^2P/dH^2 \propto T^{-3/2}. \quad (17)$$

If dephasing is caused by electron–electron interaction, $\tau_\varphi \sim T^{-3/2}$ and, in the limit of $H \longrightarrow 0$, we have

$$d^2P/dH^2 \propto T^{-9/4}. \quad (18)$$

Therefore, for weak localization conditions in the quantum correction theory, the exponent α varies in the range of 1.5–2.25 as the scattering mechanism is varied from the phonon to the electron–electron one. In fact, according to the experiments, in the metallic state the slope gradually increases from 1.5, in the vicinity of the transition, to 1.8, in the most heavily doped samples 15 and 16. Thus, the temperature dependence of MR is completely defined by phonon scattering in the immediate vicinity of the transition. In the metallic region, electron–electron interaction also makes a contribution.

The slope of the second derivative of MW absorption increases for $H \longrightarrow 0$ at $T > 30$ K (Fig. 4). This fact shows that the MR is defined by other mechanisms of scattering

Using the results of numerical calculations, we can analyze the temperature variation of another characteristic parameter in the MR field dependence, specifically, the maximum of the MR derivative. According to calculations, this maximum corresponds to $x = 5.1$. Taking this into account and using (7), for the field H_{max} we have

$$H_{max} = 5.1\hbar c/4eD\tau_\varphi \propto T^\alpha, \quad (19)$$

where $\alpha = 1$ or 3/2 for the dephasing due to electron–phonon or electron–electron interactions.

By matching the calculated and experimental dependences for each temperature, we were able to determine the temperature dependence of H_{max} and plot the $H_{max}(T)$ dependence. For sample 15, this dependence is shown in Fig. 5 on the log–log scale. It can be seen that the dependence follows the power law with the exponent $\alpha = 0.5$, which is considerably smaller than the value that the quantum correction theory predicts for weak localization conditions.

Comparing the temperature dependences of the derivative slope (β) in the initial section of the curve and the position of the maximum (H_{max}), we notice significant disagreement between the results obtained from formulas (17), (18), and (19). There are reasons to believe that formula (19) is inapplicable. This is because the weak localization conditions do not

describe anomalous positive MR near the phase transition point where the dP/dH derivative has a maximum.

5.3. Concentration Dependences

First of all, we would like to draw attention to the change in the mechanism of anomalous positive MR in samples 1 and 2, which manifests itself in the variation of the field dependence of the derivative of MW absorption from superlinear to sublinear (Fig. 2) and in an abrupt change in the exponent α in the temperature dependence in (15) (Fig. 6). One can see the variation in the temperature dependences of d^2P/dH^2 in the limit $H \longrightarrow 0$ near the IM phase transition (samples 2 and 3) in the low-temperature region (Fig. 4). In more heavily doped samples, the temperature coefficient α remains constant up to T = 20–30 K. Simultaneously, the nonlinearity (sublinearity) of the field dependences increase in the low-temperature region. The magnitude of this effect varies only slightly (the slope of the magnetic field dependences remains constant) in low fields for these concentrations. However, the curves become more nonlinear in higher fields as the doping level increases, so that the amplitude of the absorption derivative decreases in this region as the impurity concentration increases.

The concentration dependence of α is shown in Fig. 6. It can be seen that after an abrupt decrease of α, which was mentioned above, on passing from sample 1 to sample 2 it begins to steadily increase with concentration. The concentration dependence of α has a kink, and the slope of this dependence decreases at $p \approx 1.5 \times 10^{17}$ cm^{-3} on the "metallic" side of the IM transition. At the inflection point, $\alpha \approx 1.5$. This is in agreement with relation (17) and shows that dephasing occurs owing to the scattering by phonons. The coefficient of α slowly increases up to $\alpha \approx 1.8$ with the impurity concentration in the metallic phase. This indicates that electron–electron scattering (18) also governs dephasing in heavily doped samples.

Therefore, there is a transition region in the vicinity of the IM phase-transition point where both MR theory for hopping conductivity and transport quantum theory of free carriers in a metal are irrelevant.

A change in the elastic scattering mechanism with increasing impurity concentration in the insulator phase near the IM phase transition, which manifests itself in the variation of the temperature and field MR characteristics of the samples, is apparently related to the change in character of the carrier transport near such a transition. Away from the phase transition point, holes are bound by the impurity centers, and the probability of hops from one impurity to another is low. The frequency of such hops is considerably lower than the electromagnetic field frequency applied to the sample. In this case, the constant magnetic field induces an effective contraction of the wave function of a localized carrier, and hops, during which the MW energy is absorbed, become less probable. This mechanism operates in the most lightly doped sample 1.

The frequency of a hop becomes higher than the frequency of the MW field as the impurity concentration increases and as the degree of localization near the IM phase transition decreases. This situation is similar to free carrier transport through the impurity band. The sublinear character of the field dependences shows that we can use the quantum correction theory for such doping levels. However, it is necessary to take into account additional factors for describing the small coefficient of α, which varies rapidly with concentration.

Variation of the diffusion coefficient in the vicinity of the IM phase transition point may be used as such an additional factor. In fact, the well known Einstein expression relates mobility μ to the diffusion coefficient D:

$$D = \frac{\mu kT}{e}\frac{F_{1/2}(\eta)}{F_{-1/2}(\eta)}, \tag{20}$$

where $F_{1/2}(\eta)$ and $F_{-1/2}(\eta)$ are the Fermi integrals with fractional indices, and η is the Fermi energy ε_F expressed in kT units and measured from the bottom of the conduction band (for electrons) or from the top of the valence band (for holes).

The integral ratio in (20) differs drastically for nondegenerate and degenerate semiconductors. In the former case, this ratio is independent of η; in the latter case, it linearly increases with η. The Einstein relation for degenerate semiconductors takes the form

$$D = \frac{\mu}{e}\varepsilon_F \propto \frac{\mu}{e}; \tag{21}$$

i.e., the temperature dependence of the diffusion coefficient D at low temperatures is controlled only by the mobility μ. At the same time, in a nondegenerate semiconductor in the insulator state, when the ratio $F_{1/2}(\eta)/F_{-1/2}(\eta) = 1$, the diffusion coefficient is proportional to temperature. Due to this fact, the temperature dependence of D becomes abruptly weaker near the IM phase transition. The product $D\tau_\varphi$, which is included in all formulas related to MR, defines temperature dependences of the MR. In this context, the exponent α should tend to zero in the insulator state when the diffusion coefficient is proportional to temperature and the dephasing time is defined, as usual, by the phonon scattering. The experimental minimum value of α is equal to 0.4 in sample 2. The mechanism of the MR is changed at lower concentrations.

As can be seen from Fig. 6, in the metallic state, with the diffusion coefficient being independent of temperature, the coefficient α is equal to 1.5, which is typical of dephasing due to phonon scattering. A further increase in the carrier concentration leads to a gradual increase in α, as was already mentioned. This can be caused by an increase in the contribution of charge-carrier interaction during the dephasing time.

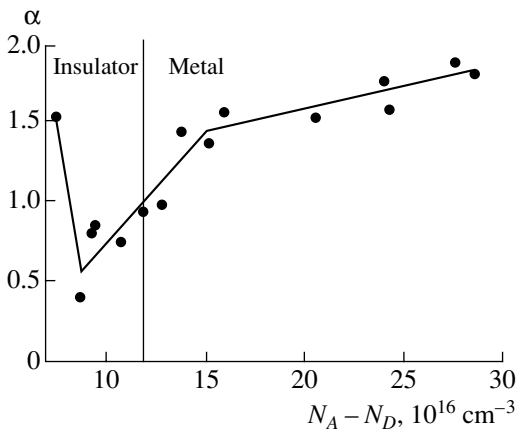

Fig. 6. The dependence of the exponent α in (15) on the difference between the acceptor and donor concentration in the insulator–metal transition region in *p*-Ge.

Thus, we observed a number of effects in the IM transition region as the impurity concentration increased. First of all, we observed a change in the MR mechanism from the contraction of the localized-carrier wave function, typical of hopping conductivity, to weak localization conditions, typical of free carriers. It is also necessary to take strong spin–orbit scattering into account. Apparently, this change occurs in the insulator state. The temperature dependence of the diffusion coefficient becomes weaker with doping. This effect begins to develop in the insulator state, but it completely vanishes in the metallic state as $\varepsilon_F \gg kT$. Free carrier (hole) scattering by acoustic phonons completely determines the dephasing time in this concentration region. Finally, electron–electron interactions begin to affect the dephasing time in the metallic state as the concentration of the shallow Ga impurity increases. This manifests itself in an increase in the exponent in the temperature dependence.

However, we did not observe any features of MR for the hole concentrations that correspond to the Coulomb gap collapse. This is quite understandable because the special features of conductivity in this material, which are related to the Coulomb gap, begin to manifest themselves only at $T < 1$ K [14]. Only in the vicinity of the phase transition [$(1.0–1.5) \times 10^{17}$ cm^{-3}] did we observe variation of the MR temperature dependence, which is related to the variation in the temperature dependence of the diffusion coefficient. It is still necessary to study the Coulomb gap effect on the MR at much lower temperatures or in other material with a wider Coulomb gap.

6. CONCLUSION

This study confirmed that MW investigations of MR, based on the ESR technique, increased the sensitivity and precision of measurements in comparison with dc measurements. At the same time, measurements in the MW cavity have certain special features that should be taken into account when explaining the experimental results. In particular, these features include change of sign of the effect and the dependence of the sensitivity of measurements on the resistivity of the semiconductor.

The main results are the following:

1. Approaching the IM phase transition point from the insulator state causes variation in the MR mechanism: in the insulator state, such a mechanism is related to the increase in the degree of localization due to contraction of the wave functions of localized holes by the magnetic field, whereas, in the vicinity of the phase transition and in the metallic state, the mechanism is related to weak localization but with the temperature-dependent diffusion coefficient in the IM region.

2. Transition to the metallic state is accompanied by the disappearance of the temperature dependence of the diffusion coefficient. In this case, the temperature dependence of MR is defined by the temperature dependence of the dephasing time, which, in turn, is determined by the phonon scattering. An increase in the impurity concentration in the metallic state makes the MR temperature dependence slightly heavier due to additional dephasing caused by electron–electron interaction.

ACKNOWLEDGMENTS

We thank V.A. Chekanov for the neutron irradiation of the material; M.V. Alekseenko, for measurements of the charge carrier concentration; participants in the workshop of the laboratory “Nonequilibrium Processes in Semiconductors,” for their participation in discussions and valuable comments; and the Russian Foundation for Basic Research, for support (project nos. 01-02-17813 and 00-15-96750).

REFERENCES

1. B. L. Altshuler and A. G. Aronov, in *Electron-Electron Interactions in Disordered Systems*, Ed. by A. L. Efros and M. Polak (North-Holland, Amsterdam, 1985), p. 1.
2. T. A. Polyanskaya and Yu. V. Shmartsev, Fiz. Tekh. Poluprovodn. (Leningrad) **23**, 3 (1989) [Sov. Phys. Semicond. **23**, 1 (1989)].
3. K. J. Sugiyama, J. Phys. Soc. Jpn. **19**, 1745 (1964).
4. W. W. Lee and R. J. Sladek, Phys. Rev. **158**, 794 (1967).
5. A. R. Gadzhiev and I. S. Shlimak, Fiz. Tekh. Poluprovodn. (Leningrad) **6**, 1582 (1972) [Sov. Phys. Semicond. **6**, 1829 (1972)].
6. J. Chroboczek, A. Klokocki, and K. Kopalko, J. Phys. C **7**, 3042 (1974).
7. A. N. Ionov, Pis’ma Zh. Éksp. Teor. Fiz. **29**, 76 (1979) [JETP Lett. **29**, 70 (1979)].
8. B. I. Shklovskiĭ and A. L. Efros, *Electronic Properties of Doped Semiconductors* (Nauka, Moscow, 1979; Springer-Verlag, New York, 1984).

9. B. I. Shklovskiĭ and B. Z. Spivak, in *Hopping Transport in Solids*, Ed. by M. Pollak and B. Shklovskii (Elsevier, Amsterdam, 1991), p. 271.
10. M. E. Raikh, J. Czingon, Qiu-yi Ye, *et al.*, Phys. Rev. B **45**, 6015 (1992).
11. A. G. Zabrodskiĭ, Fiz. Tekh. Poluprovodn. (Leningrad) **14**, 1324 (1980) [Sov. Phys. Semicond. **14**, 781 (1980)].
12. A. G. Zabrodskiĭ, Usp. Fiz. Nauk **168**, 804 (1998) [Phys. Usp. **41**, 722 (1998)].
13. A. G. Zabrodskiĭ and M. V. Alekseenko, Fiz. Tekh. Poluprovodn. (St. Petersburg) **28**, 168 (1994) [Semiconductors **28**, 101 (1994)].
14. A. G. Zabrodskiĭ, A. G. Andreev, and S. V. Egorov, Phys. Status Solidi B **205**, 61 (1998).
15. M. V. Alekseenko, A. G. Zabrodskiĭ, and L. M. Shterengas, Fiz. Tekh. Poluprovodn. (St. Petersburg) **32**, 811 (1998) [Semiconductors **32**, 720 (1998)].
16. A. G. Zabrodskiĭ, A. G. Andreev, and M. V. Alekseenko, Fiz. Tekh. Poluprovodn. (St. Petersburg) **26**, 431 (1992) [Sov. Phys. Semicond. **26**, 244 (1992)].
17. A. I. Veĭnger, A. G. Zabrodskiĭ, T. V. Tisnek, and G. Biskupski, Fiz. Tekh. Poluprovodn. (St. Petersburg) **32**, 557 (1998) [Semiconductors **32**, 497 (1998)].
18. A. I. Veĭnger, A. G. Zabrodskiĭ, and T. V. Tisnek, Fiz. Tekh. Poluprovodn. (St. Petersburg) **34**, 774 (2000) [Semiconductors **34**, 746 (2000)].
19. C. P. Poole, *Electron Spin Resonance. Comprehensive Treatise on Experimental Techniques* (Wiley, New York, 1967; Mir, Moscow, 1970).
20. B. L. Al'tshuler, A. G. Aronov, A. I. Larkin, and D. E. Khmel'nitskiĭ, Zh. Éksp. Teor. Fiz. **81**, 768 (1981) [Sov. Phys. JETP **54**, 411 (1981)].
21. A. G. Aronov, M. E. Gershenzon, and Yu. E. Zhuravlev, Zh. Éksp. Teor. Fiz. **87**, 971 (1984) [Sov. Phys. JETP **60**, 554 (1984)].
22. T. Yu. Bil'gil'deeva, A. M. Kreshchuk, T. A. Polyanskaya, and I. I. Saĭdashev, Preprint No. 999, Fiz.-Tekh. Inst. im. A. F. Ioffe (Ioffe Physicotechnical Institute, Academy of Sciences of USSR, Leningrad, 1986).
23. I. S. Shlimak, A. I. Ionov, and B. I. Shklovskiĭ, Fiz. Tekh. Poluprovodn. (Leningrad) **17**, 503 (1983) [Sov. Phys. Semicond. **17**, 314 (1983)].

Translated by I. Kucherenko

Semiconductors, Vol. 36, No. 7, 2002, pp. 782–783. Translated from Fizika i Tekhnika Poluprovodnikov, Vol. 36, No. 7, 2002, pp. 836–837.

ELECTRONIC AND OPTICAL PROPERTIES OF SEMICONDUCTORS

Thermally Stimulated Currents in $MnIn_2S_4$ Single Crystals

N. N. Niftiev

Azerbaidjan State Pedagogical University, Baku, Azerbaidjan

Submitted February 11, 2002; accepted for publication February 18, 2002

Abstract—Fast-attachment levels were detected in the band gap of $MnIn_2S_4$ single crystals by studying the thermally stimulated currents. The depth of the levels, the concentration of traps, and the cross sections for capture by these traps were determined. Based on the methods of thermally stimulated currents and the thermal reaction of clearing, it was found that there are exponentially distributed attachment levels (within 0.05–0.21 eV) and, against the background of these levels, discrete trapping levels located at 0.14 eV in the band gap of $MnIn_2S_4$ single crystals. © *2002 MAIK "Nauka/Interperiodica".*

Ternary compounds of the $A^{II}B_2^{III}X_4^{VI}$ type (where A = Mn, Fe, Co, Ni; B = Ga, In; and X = S, Se, Te) represent a class of magnetic semiconductors the interest in which has been progressively aroused over the last several years in connection with the possible widening of the functional range of semiconductor devices [1–4]. These compounds are promising as materials for lasers, optical modulators, photodetectors, and other devices controlled by a magnetic field.

The $MnIn_2S_4$ single crystals belong to the class of $A^{II}B_2^{III}X_4^{VI}$ compounds. In this paper, I report the results of studying the local attachment levels in the band gap of these single crystals using the methods of thermally stimulated conductivity (TSC) and the currents of thermally stimulated depolarization (TSD).

The $MnIn_2S_4$ single crystals were grown using the method of chemical transport reactions. Crystalline iodine (4 mg/cm^3) was used as a carrier. The temperatures of the hot and cold zones were chosen to be T_1 = 800°C and T_2 = 700°C, respectively. X-ray diffraction studies showed that the single crystals had a spinel structure with the crystal-lattice parameter a = 10.71 Å [2] and n-type conductivity. Contacts to the samples were formed by alloying indium to opposite surfaces (a sandwich structure). The distance between the electrodes varied from 50 to 300 μm.

Figure 1 shows the TSC (curves *1*, *2*) and TSD (curves *3*, *4*) spectra for the $MnIn_2S_4$ single crystals. It can be seen from curves *1* and *2* that the TSC peak becomes higher and shifts to higher temperatures as the heating rate increases. The large half-width of the TSC peak (45 K) indicates that the relatively shallow attachment levels in the band gap of $MnIn_2S_4$ single crystals are not discrete.

In order to determine more precisely the parameters of the trap levels, one should know the type of the attachment levels. An analysis of the TSC and TSD peaks shows [5] that the following condition is satisfied for all observed peaks:

$$\delta > e^{-1}\left(1 + \frac{2kT_m}{E_t}\right), \quad \delta = \frac{T_2 - T_m}{T_2 - T_1}.$$

Here, T_m is the temperature corresponding to the TSC (TSD) peak and T_1 and T_2 are the temperatures corresponding to the half-intensity of the TSC (TSD) peak on the low- and high-temperature sides, respectively. The fulfillment of this condition indicates that there are fast-attachment levels in the single-crystal band gap.

The depth of the trap levels in the band gap was determined by the method suggested by Bube [6], the method of differences in the heating rates [7], and by using the formulas that account for the shapes of the

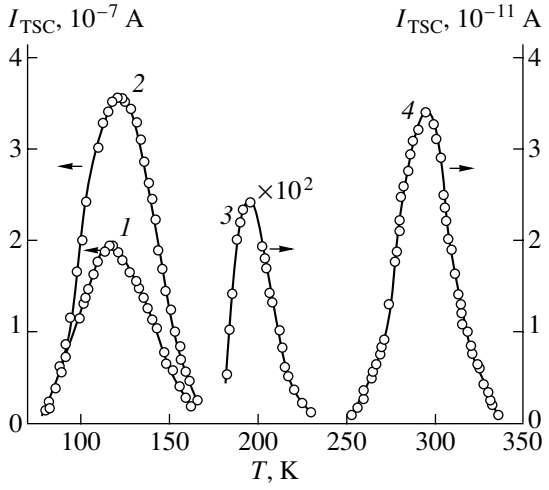

Fig. 1. The curves of (*1*, *2*) thermally stimulated conductance and (*3*, *4*) the currents of thermally stimulated depolarization in $MnIn_2S_4$ single crystals. The heating rates were (*1*) 0.25, (*2*) 0.60, and (*3*, *4*) 0.20 K/s. The polarizing-field strength was (*3*, *4*) 4.5×10^4 V/cm.

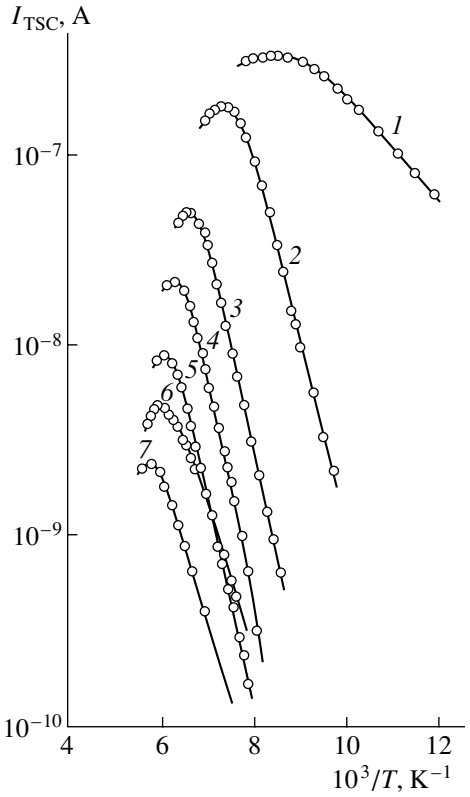

Fig. 2. The curves of thermally stimulated conductance in $MnIn_2S_4$; these curves were obtained using the successive (*1* ⟶ *7*) heating cycles.

TSC and TSD curves [8–10]. The concentrations and capture cross sections of the traps were determined in the same manner as in [10]. The average values of these quantities were found to be equal to

$$E_{t1} = 0.21 \pm 0.03 \text{ eV}; \quad E_{t2} = 0.38 \pm 0.02 \text{ eV};$$

$$E_{t3} = 0.59 \pm 0.02 \text{ eV};$$

$$N_{t1} = 2.2 \times 10^{15} \text{ cm}^{-3}; \quad N_{t2} = 2.6 \times 10^{13} \text{ cm}^{-3};$$

$$N_{t3} = 5.2 \times 10^{15} \text{ cm}^{-3};$$

$$S_{t1} = 4.4 \times 10^{-18} \text{ cm}^2; \quad S_{t2} = 1.7 \times 10^{-17} \text{ cm}^2;$$

$$S_{t3} = 2.3 \times 10^{-17} \text{ cm}^2.$$

Figure 2 shows the curves of thermal clearing in $MnIn_2S_4$ for the TSC peak with $T_m = 122$ K. It can be seen that the slope of the straight line corresponding to the initial rise in the TSC current increases (from 0.05 to 0.21 eV) as a result of successive heating cycles (curves *1–4*). As a result of succeeding cycles (curves *4–7*), the slope of the straight lines decreases and the corresponding activation energies also decrease (from 0.21 to 0.14 eV). According to the TSC theory, the attachment levels are quasi-continuously distributed in energy if the activation energy increases as a result of successive heating cycles, whereas the attachment levels are discrete if the activation energy decreases. Taking the above, into account as well as the results of studying the TSC, we may infer that there are two types of trapping levels in the band gap of $MnIn_2S_4$ single crystals: exponentially distributed (0.05–0.20 eV) attachment levels and, against the background of these levels, discrete trapping levels with an energy of 0.14 eV.

Thus, the presence of fast attachment levels was ascertained in the band gap of $MnIn_2S_4$ single crystals using the TSC and TSD methods. The depth of the levels and the concentration and capture cross section of the traps were determined. The method of thermal clearing of the TSC spectra was used to ascertain that there are exponentially distributed (0.05–0.21 eV) attachment levels in the band gap of $MnIn_2S_4$ single crystals; in addition, there are discrete trapping levels with an energy of 0.14 eV (against the background of the above attachment levels).

REFERENCES

1. S. Methfessel and D. C. Mattis, in *Nandbuch der Physik*, Ed. by H. P. J. Wijn (Springer-Verlag, Berlin, 1968), Vol. 18, Part 1, p. 389.
2. T. Kanomata, H. Ido, and T. Kaneko, J. Phys. Soc. Jpn. **34**, 554 (1973).
3. R. N. Bekembetov, Yu. V. Rud', and M. A. Tairov, Fiz. Tekh. Poluprovodn. (Leningrad) **21**, 1051 (1987) [Sov. Phys. Semicond. **21**, 642 (1987)].
4. S. Martsinkyavichyus, G. Ambrazyavichyus, R. N. Bekembetov, and G. A. Medvedkin, Fiz. Tekh. Poluprovodn. (Leningrad) **22**, 1919 (1988) [Sov. Phys. Semicond. **22**, 1216 (1988)].
5. P. G. Litovchenko and V. I. Ustianov, *Topical Problems in the Physics Semiconductor Devices* (Mokslas, Vilnius, 1960), p. 153.
6. R. H. Bube, *Photoconductivity of Solids* (Wiley, New York, 1960; Inostrannaya Literatura, Moscow, 1962).
7. G. F. Garlik and A. F. Gibson, Proc. Phys. Soc. London, Sect. A **60**, 574 (1948).
8. Ch. B. Lushchik, Dokl. Akad. Nauk SSSR **101** (4), 641 (1955).
9. Ya. A. Piasta, Mikroélektronika **3**, 178 (1974).
10. G. A. Bordovski, in *Photoconducting Lead Oxides: Collection of Scientific Works* (Leningr. Gos. Ped. Inst., Leningrad, 1976), p. 87.

Translated by A. Spitsyn

Semiconductors, Vol. 36, No. 7, 2002, pp. 784–788. Translated from Fizika i Tekhnika Poluprovodnikov, Vol. 36, No. 7, 2002, pp. 838–842.

ELECTRONIC AND OPTICAL PROPERTIES OF SEMICONDUCTORS

E_0 Photoreflectance Spectra of Semiconductor Structures with a High Density of Interface States

R. V. Kuz'menko* and É. P. Domashevskaya

Chair of Solid State Physics, Physics Department, Voronezh State University, Universitetskaya pl. 1, Voronezh, 394693 Russia

** e-mail: roman@ftt.vsu.ru*

Submitted October 15, 2001; accepted for publication December 18, 2001

Abstract—The results of a photoreflectance spectroscopy study of Ga_2Se_3/*n*-GaAs samples prepared by long-term annealing of GaAs wafers ($n \approx 10^{17}$ cm^{-3}) in a Se-vapor atmosphere are presented. It was established that no photovoltage appears in the interface region of these structures under illumination. Photogeneration of the charge carriers in the substrate does not lead to a change in the Fermi level position at the interface, with only the depth of the space-charge region being modulated. The quantitative analysis of the spectra also indicates that the growth of a thick (~1 μm) Ga_2Se_3 layer does not result in the expected shift of the Fermi level position in comparison to the natural oxide-covered surface. © *2002 MAIK "Nauka/Interperiodica".*

In the last several years, photoreflectance (PR) spectroscopy again became widely used as a tool for investigating the electrostatic field in the vicinity of surfaces and interfaces, the magnitude of band bending or the height of the surface barrier, and the photovoltaic effect in semiconductor wafers or in epitaxial structures whose layers are wide enough for analyzing their PR spectra in the context of three-dimensional models (see, e.g., [1–6]). When the measurements are carried out in the region of the fundamental transitions between the valence and conduction bands under intermediate-field conditions [7, 8], the PR spectrum exhibits gradually damping Franz–Keldysh oscillations in the energy region above the fundamental edge, with the oscillation period being determined by the electric-field strength in the surface (interface) region in the absence of external perturbation (e.g., photogeneration in the case of the PR arrangement). The main modulation mechanism that is fundamental for PR spectroscopy is the modulation of the surface electric-field strength occurring in a semiconductor periodically illuminated by radiation where the photon energy exceeds the band gap. Due to the Franz–Keldysh effect, the electric field modulation leads to a change in the semiconductor reflectivity, which is responsible for the appearance of electromodulation components in the PR spectra. Under depletion conditions in the space-charge region (SCR), the charge carriers generated there are separated by the field: the majority carriers are forced into the bulk of the semiconductor and the minority carriers move to the surface. Trapping of the minority carriers at the surface states leads to a decrease in the surface potential. However, as the surface potential is reduced, the restoring current (originating from the majority-carrier flow over the potential barrier) increases. It is the balance between the current of the photogenerated minority carriers and the restoring current that determines the photovoltage developing as a result of illumination of the semiconductor surface. It was found that, as a rule, at room temperature complete suppression of the surface electric field is not attained [9]. Thus, analyzing the PR data, one needs to assume that, in general, the surface electric field is partially modulated. If the behavior of the electric field in the surface region can be described in the context of the Schottky model, where a linear dependence of the field strength F on the depth z is assumed, then the partial modulation of the surface field amounts to a parallel shift with the gradient dF/dz remaining unchanged (see Fig. 1).

In this study, we use PR spectroscopy to examine the effect of long-term annealing of *n*-GaAs wafers in an Se-vapor atmosphere on the Fermi-level position in the region of the Ga_2Se_3/*n*-GaAs interface, which forms under such treatment. Pinning of the Fermi level at the surface or at the homo- or heterointerface near the midgap presents a considerable problem in GaAs-based opto- and microelectronic devices. The results of numerous studies indicate that this pinning is related to intrinsic GaAs states and, thus, in many cases, the Fermi level position at the interface does not depend on the type of film covering the surface and is not sensitive to various surface treatments [10–15]. However, it has been established that the formation of a thin (10 nm) passivating layer of Ga_2Se_3 upon the annealing of GaAs wafers in a Se-vapor atmosphere results in a decreased density of states at the Ga_2Se_3/*n*-GaAs interface as compared to the natural oxidized surface [16–19]. It was found that the magnitude of the variation of electric-field strength in the interface region depends on the thickness of the passivating layer [19]. Thus, in this

1063-7826/02/3607-0784$22.00 © 2002 MAIK "Nauka/Interperiodica"

work, we investigated samples with thick layers. Their PR spectra were measured at room temperature using a setup described previously [20]. The phase analysis of the spectra [21] was carried out using an SR850 dual-channel lock-in amplifier. Modulation of the sample reflectance was performed by excitation with a He–Ne laser operating at 632.8 nm (for GaAs, $1/\alpha = 250$ nm, where α is the absorption coefficient). The laser power density at the sample was $L \approx 1$ W/cm^2, and the modulation frequency was 500 Hz.

The five samples under study were prepared at the Technical University of Berlin. GaAs wafers with the charge-carrier density $n \approx 10^{17}$ cm^{-3} were annealed at 850 K for 2 h in a Se-vapor atmosphere under a Se pressure of ~100 Pa. According to the manufacturer's data, the thickness of the Ga_2Se_3 layer formed in this way varied from 700 to 1100 nm. The spread is related to variations in the technological parameters.

A typical PR spectrum of a naturally oxidized wafer in the vicinity of the E_0 transition recorded before annealing is shown in Fig. 2. The spectrum obtained by model calculation is also plotted here. The shape of the spectrum corresponds to the transition from intermediate-field to low-field conditions [7, 8]. However, a feature originating from the Franz–Keldysh oscillations is clearly seen, which makes it possible to estimate the electric-field strength with an error no larger than 5%. The theoretical curve was calculated in the context of the generalized multilayer model [22] assuming partial modulation of the electric field under illumination. The parameter of the partial modulation obtained is $\zeta = 0.5$; i.e., the electric-field strength is reduced by a factor of 2 under illumination; this value is typical for GaAs samples at room temperature [22]. The value of the fundamental transition energy E_0 obtained from calculations is indicative of the relatively high doping level in this sample.

A typical PR spectrum of a wafer annealed in a Se-vapor atmosphere (see Fig. 3) differs distinctly from the initial one (Fig. 2). First, pronounced Franz–Keldysh oscillations appear in the high-energy region of the spectrum. This indicates that the interface region now contains fewer defects and makes it possible to determine the electric-field strength more precisely (with an error as small as 1%). Second, the period of the Franz–Keldysh oscillations near the fundamental-transition energy is not constant, in contrast to the period of the high-energy oscillations. Third, the smooth behavior of the PR curve is disturbed in the high-energy wing of the first negative Franz–Keldysh oscillation. According to available publications, such spectral features have not been observed previously. We found it impossible to fit the experimental curve by a curve calculated in the context of the generalized multilayer model assuming partial modulation of the electric field in the interface region. One such typical inadequate multilayer-model fit is shown in Fig. 3.

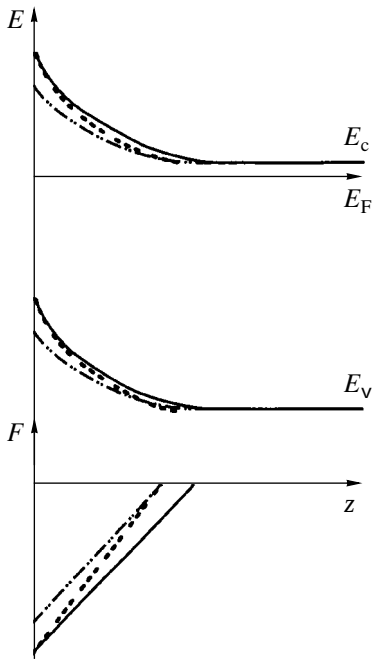

Fig. 1. A layout of the space-charge region for an *n*-type semiconductor in the case of the surface Fermi level E_F pinning at the midgap (the depletion conditions). Upper panel: energy diagram $E(z)$ of the band bending (E_c and E_v are the conduction and the valence bands, respectively). Lower panel: distribution of electric field $F(z)$ in the SCR. Solid lines correspond to the SCR in the dark; dash-and-dot lines, to the conditions of the photovoltaic effect under illumination; and dashed lines, to the case of the absence of the Fermi-level shift under illumination.

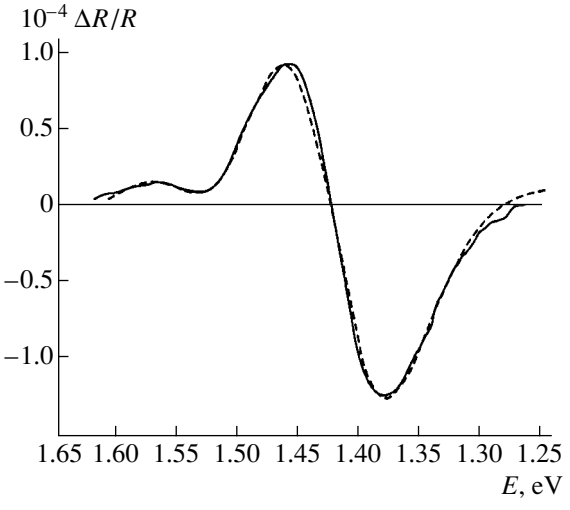

Fig. 2. The E_0 PR spectrum of an untreated wafer: dashed line, experiment; solid line, calculation in the context of the multilayer model assuming partial modulation of the surface electric field. The fitting parameters are $E_0 = 1.391$ eV, $F = 1.04 \times 10^7$ V/m, $\Gamma = 53$ meV, $d_F = 100$ nm, and $\xi = 0.5$.

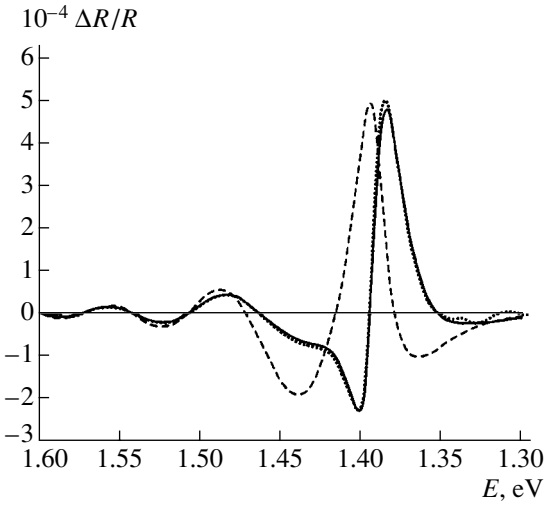

Fig. 3. The E_0 PR spectrum of a wafer annealed in Se-vapor atmosphere: dotted line, experiment; dashed line, calculation in the context of the multilayer model assuming partial modulation ($\xi = 0.5$) of the surface electric field; solid line, calculation in the context of a model assuming modulation of the SCR depth without variation of the Fermi level position. The fitting parameters are $E_0 = 1.393$ eV, $F = 9.5 \times 10^6$ V/m, $\Gamma = 5$ meV, and $d_F = 90$ nm in the dark and 85 nm under illumination.

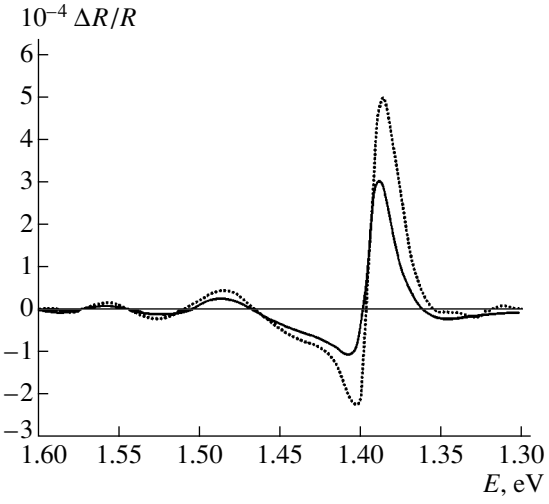

Fig. 4. The E_0-PR spectra of a wafer annealed in Se-vapor atmosphere: solid line, recorded under constant additional illumination with the laser power density of 10 W/cm^2; dotted line, recorded without additional illumination.

It is not infrequent for the PR spectra in the vicinity of the E_0 transition that the model curve deviates from the experimental one, which is related to the multiple-component nature of the spectra. However, the importance of the effects of overlapping is mostly limited to the region of the main peak [23–26]. In addition, phase analysis of the spectrum reveals that it contains only one electromodulation component appearing in the vicinity of the fundamental transition. It may be assumed that the observed changes in the spectra are related to the appearance of biaxial strain in the interface region of the wafer, which originates from lattice-constant mismatch (0.543 nm in Ga_2Se_3 and 0.5653 nm in GaAs) or from the difference in the thermal expansion coefficients of the two materials, and leads to the splitting of the degenerate subbands of the valence band. However, this is not the case. Due to the (100) orientation of the GaAs wafer, we cannot prove this experimentally using polarized monochromatic light. Nevertheless, the following are arguments in favor of the absence of the biaxial-stress effects. First, assuming that the position of the main spectral peak corresponds to the transition energy for the subband $|3/2; \pm 1/2\rangle$, we infer that the biaxial stress should be ~ 3.75 kbar, which is an unrealistically large value for this heterosystem. Second, in semiconductors possessing a cubic symmetry, the biaxial stress in the (100) plane results in a simultaneous upward or downward shift (depending on whether the stress is compressive or tensile, respectively) of the transition energies for both subbands. Meanwhile, the spectral feature in the high-energy wing of the first Franz–Keldysh oscillation that could be assigned to the main peak of the electromodulation component from the second subband appears at ~1.43 eV, and the main PR peak is at ~1.38 eV. Thus, we arrive at the conclusion that the observed structure in the PR spectra is caused by the electromodulation effect in the vicinity of the degenerate electron transition.

A quantitative estimation, performed in the context of the multilayer model, indicates that, within the accuracy of the analysis, the electric-field strength, which was determined from the period of the high-energy Franz–Keldysh oscillations, does not change upon annealing (cf. the fit parameters obtained for the spectra before and after annealing). Thus, we have to assume that either annealing does not change the distribution of electron states in the band gap of the samples under study or the interface formed is characterized by a very high density of states, so that the passivation effect becomes negligible. In the context of the second assumption, we calculated the spectra on the basis of a model describing the effects occurring under photogeneration in the surface region with a high concentration of defect materials [27] (see Fig. 1). It is assumed in this model that the density of states in the damaged, several-nanometer-thick surface layer is so high that the photogenerated charge carriers recombine without affecting the magnitude of the surface potential. Thus, the generation of nonequilibrium charge carriers leads only to the variation in the depth of the SCR. Calculations demonstrate that, even under large variations in the SCR depth, the strength of the surface electric field varies so insignificantly that it may be considered as virtually unchanged [27]. Although the experimentally observed PR spectrum was not fully reproduced in [27] in the context of this model, good qualitative agreement between the experimental and theoretical curves was achieved. Discrepancies between theory and experi-

ment were attributed to the high degree of amorphization of the surface region of the sample investigated.

Following [27], we tried to simulate the PR spectrum of the annealed sample assuming that the surface electric-field strength remains unmodulated. Since the concentration of defects in the samples under study is not high, better agreement between theory and experiment can be expected, provided that this model is adequate. The appropriateness of the model was checked in the following way. The values of the electric-field strength and the fundamental-transition energy were taken from a quantitative analysis of the spectrum of an untreated (naturally oxidized) sample (see Fig. 2). Calculating the spectrum of the sample after annealing, we varied these values by no more than several percent; only the energy broadening Γ and the SCR depth d_F were varied considerably. It was assumed that, both with and without illumination, the field strength decreases linearly in the SCR. It was found that the lineshape of all experimental spectra can be reproduced satisfactorily in the context of the adopted model. A typical result is shown in Fig. 3. One can see that an almost perfect fit to the experimental curve can be obtained by assuming that the depth of the SCR varies under illumination from 90 to 85 nm.

To verify experimentally the validity of the proposed model for the spectrum formation of the PR, we carried out the same PR measurements under constant additional illumination of the sample by a second He–Ne laser. For naturally oxidized GaAs wafers, constant additional illumination leads to a reduction in the electric-field strength of the surface even in the case of low laser-power density (~10 μW/cm^2); this should lead to a decrease both in the magnitude of the PR signal and in the period of the Franz–Keldysh oscillations [1, 4–6, 9]. At the same time, if we assume that the position of the Fermi level at the interface is not influenced by additional illumination, then the electric field either remains virtually unchanged or, in the case of a very high laser power density, increases due to a considerable decrease in the depth of the SCR. Varying the power density of the constant additional illumination in a wide range from 10 mW/cm^2 to 10 W/cm^2, we found that, although variations in the spectral lineshape do take place, the period of the high-energy Franz–Keldysh oscillations is not changed. As an illustration, Fig. 4 shows the spectra measured with and without illumination using an excitation-power density of 10 W/cm^2. Thus, the measurements corroborate the above assumption about the absence of the photovoltaic effect in the sample under study.

Two different explanations for the high density of states in the interface region of the samples under study may be proposed. On the one hand, the long-term annealing could lead to the formation of a relatively thick intermediate layer (rather than an abrupt interface) between GaAs and Ga_2Se_3 with protrusions of one material into another. The second possible reason, which seems to be more likely, is related to the following. It was shown previously [11, 13–15] that the states responsible for the Fermi level pinning are related to As atoms. The growth of the Ga_2Se_3 layer proceeds by an As/Se heterovalent exchange reaction. When a sufficiently thick layer of Ga_2Se_3 is formed in this way, accumulation of excess As in the interface region sets in. It is this process that leads to a sharp increase in the density of states. Auger analysis carried out under layer-by-layer etching of the sample confirmed the presence of excess As in the interface region. Nevertheless, additional studies are required to verify our assumptions about the mechanism leading to the formation of a high density of states.

Thus, we demonstrated that the absence of the photovoltaic effect upon the illumination of the samples under study can be revealed by PR spectroscopy. For the first time, we observed the specific shape of the intermediate-field PR spectra in the vicinity of the E_0 transition of semiconductor structures with a high density of interface states. These spectral curves were reproduced by calculations carried out in the context of a model assuming that a modulation of the SCR depth is not accompanied by a variation in the Fermi level position at the interface. Unlike previous publications reporting on the absence of photovoltage in the surface region of a highly imperfect structure with amorphous layers, we observed this effect in the interface region of a structure composed of crystalline material.

REFERENCES

1. R. Beaudry, S. P. Watkins, X. Xu, and P. Yeo, J. Appl. Phys. **87** (11), 7838 (2000).
2. U. Behn, A. Thamm, O. Brandt, and H. T. Grahn, J. Appl. Phys. **87** (9), 4315 (2000).
3. W.-H. Chang, T. M. Hsu, W. C. Lee, and R. S. Chuang, J. Appl. Phys. **83** (12), 7873 (1998).
4. M. E. Constantino, H. Navarro-Contreras, B. Salazar-Hernandez, *et al.*, J. Appl. Phys. **86** (1), 425 (1999).
5. H. Shen, W. Zhou, J. Pamulapati, and F. Ren, Appl. Phys. Lett. **74** (10), 1430 (1999).
6. D. F. Sousa, M. J. V. Bell, and L. A. O. Nunes, J. Appl. Phys. **83** (5), 2806 (1998).
7. D. E. Aspnes, Surf. Sci. **37**, 418 (1973).
8. D. E. Aspnes and A. A. Studna, Phys. Rev. B **7** (10), 4605 (1973).
9. H. Shen, M. Dutta, R. Lux, *et al.*, Appl. Phys. Lett. **59** (3), 321 (1991).
10. V. L. Alperovich, A. G. Paulish, and A. S. Terekhov, Surf. Sci. **331–333**, 1250 (1995).
11. G. Apostolopoulos, J. Herfort, W. Ulrici, *et al.*, Phys. Rev. B **60** (8), R5145 (1999).
12. W. Chen, M. Dumas, D. Mao, and A. Kahn, J. Vac. Sci. Technol. B **10** (4), 1886 (1992).
13. Y. H. Chen, Z. Yang, R. G. Li, *et al.*, Phys. Rev. B **55** (12), R7379 (1997).
14. O. J. Glembocki, J. A. Tuchman, K. K. Ko, *et al.*, Appl. Phys. Lett. **66** (22), 3054 (1995).

15. T. M. Hsu, W. C. Lee, J. R. Wu, and J. I. Chyi, Phys. Rev. B **51** (23), 17215 (1995).
16. B. I. Sysoev, V. V. Antyushin, V. D. Strygin, and V. N. Morgunov, Zh. Tekh. Fiz. **56** (5), 913 (1986) [Sov. Phys. Tech. Phys. **31**, 554 (1986)].
17. C. J. Sandroff, M. S. Hedge, L. A. Farrow, *et al.*, J. Appl. Phys. **67**, 586 (1989).
18. F. S. Turco, C. J. Sandroff, M. S. Hedge, and M. C. Tarmago, J. Vac. Sci. Technol. B **8**, 856 (1990).
19. S. Hildebrandt, J. Schreiber, W. Kircher, and R. Kusmenko, in *Proceedings of the Symposium D on Diagnostic Techniques for Semiconductor Materials Analysis and Fabrication Process Control of the 1992 E-MRS Spring Conference, Strasbourg, 1992*, Ed. by G. M. Crean, R. Stuck, and J. A. Woollam (North-Holland, Amsterdam, 1993).
20. S. Hildebrandt, M. Murtagh, R. Kusmenko, *et al.*, Phys. Status Solidi A **152**, 147 (1995).
21. A. V. Ganzha, W. Kircher, R. V. Kuz'menko, *et al.*, Fiz. Tekh. Poluprovodn. (St. Petersburg) **32** (3), 272 (1998) [Semiconductors **32**, 245 (1998)].
22. R. Kuz'menko, A. Ganzha, É. P. Domashevskaya, *et al.*, Fiz. Tekh. Poluprovodn. (St. Petersburg) **34** (9), 1086 (2000) [Semiconductors **34**, 1045 (2000)].
23. J. M. A. Gilman, A. Hamnett, and R. A. Batchelor, Phys. Rev. B **46**, 13363 (1992).
24. O. J. Glembocki, N. Bottka, and J. E. Furneaux, J. Appl. Phys. **57** (2), 432 (1985).
25. E. G. Seebauer, J. Appl. Phys. **66**, 4963 (1989).
26. R. Kuz'menko, A. Ganzha, J. Schreiber, and S. Hildebrandt, Fiz. Tverd. Tela (St. Petersburg) **39**, 2123 (1997) [Phys. Solid State **39**, 1900 (1997)].
27. A. Badakhshan, J. L. England, P. Thompson, *et al.*, J. Appl. Phys. **81** (2), 910 (1997).

Translated by M. Skorikov

Semiconductors, Vol. 36, No. 7, 2002, pp. 789–792. Translated from Fizika i Tekhnika Poluprovodnikov, Vol. 36, No. 7, 2002, pp. 843–846.

SEMICONDUCTOR STRUCTURES, INTERFACES, AND SURFACES

Switching Effect in Si–CdS Heterojunctions Synthesized in Highly Nonequilibrium Conditions

A. P. Belyaev* and V. P. Rubets

St. Petersburg State University of Technology, St. Petersburg, 198013 Russia

e-mail: Belyaev@tu.spb.ru

Submitted December 5, 2001; accepted for publication December 19, 2001

Abstract—The results of the investigation of electrical properties and processes of the formation of heterojunctions on crystalline Si substrate cooled to negative centigrade temperatures is reported. The data of technology, electron diffraction analysis, and electrical investigations are given. The effect of conductivity switching is revealed in heterojunctions based on two-phase CdS films, and conditions for the formation of amorphous CdS films and amorphous CdS films with crystalline inclusions are determined. It is demonstrated that the results are in agreement with the soliton model. © *2002 MAIK "Nauka/Interperiodica".*

1. INTRODUCTION

The development of electronics is causing researchers to search for new promising materials and to investigate possibilities for obtaining materials and systems of electronics in nontrivial conditions. In particular, highly nonequilibrium conditions are among such promising nontrivial conditions. Only in the last few years has the investigation of the mechanisms of the formation of film systems in highly nonequilibrium conditions resulted in the revealing of such processes as soliton epitaxy [1–4] and conductivity stimulated by temperature oscillations [5]. In this paper, we report new experimental data related to the processes of formation of the structure and properties of films in highly nonequilibrium conditions. In particular, we ascertained that it is possible to obtain a bistable system in highly nonequilibrium conditions, and this holds much promise for electronics.

2. EXPERIMENTAL

The samples were synthesized by the method of quasi-closed volume on the Si substrate cooled with liquid nitrogen [1, 2]. The film thickness for various samples was 0.8–1.2 μm. KDB-10 Si(100) wafers (B-doped *p*-Si(100) with a resistivity of 10 Ω cm) 0.3 mm thick were used as the substrates.

The film thickness was measured using an MII-4 microinterferometer. Electron diffraction analysis was carried out with an EMR-100 electron diffractometer. For electrical measurements, Au contacts 4×4 mm^2 in area were deposited on the samples using vacuum evaporation. All electrical measurements were carried out in vacuum at a residual pressure of ~10^{-3} Pa. The current–voltage (*I–V*) characteristics were measured using a U5-9 electrometer, and the capacitor–voltage (*C–V*) characteristics were measured using a BM-507 impedometer.

3. RESULTS

The processes of formation of CdS films on a crystalline Si substrate in highly nonequilibrium conditions, as well as the electrical characteristics of forming Si–CdS heterojunctions (HJs), were investigated. The investigation of the processes of formation was based on technological experiments and electron diffraction studies. The electrical characteristics were investigated by measuring the *I–V* and *C–V* characteristics.

We found that epitaxial crystalline CdS films grow on the substrate chilled to temperatures $T_r \approx 215$ and 150 K (Fig. 1a). At $T_r < 100$ K, the films were amorphous (Fig. 1b). In the temperature range of 100 K < T_r < 150 K, the films were two-phase; specifically, along with the amorphous phase, they contained crystalline inclusions (Fig. 1c).

Forward portions of *I–V* characteristics for all of the HJ types, specifically, with the oriented, amorphous, and two-phase films, were exponential. The shape of the reverse portions of the characteristics depended on the structure of the CdS film (Fig. 2). The *I–V* characteristic for the HJ with the epitaxial film had a shape characteristic of the rectifying contact (curve *1*). The reverse portion of the *I–V* characteristic for the HJ with the amorphous film was almost indistinguishable from the forward portion (curve *2*). Finally, the reverse portion of *I–V* characteristics for the HJ with the two-phase film had two stable states, which differed by several orders of magnitude in conductivity (curve *3*). Up to the instant of conductivity switching, the *I–V* characteristic for HJs with the two-phase and epitaxial films were qualitatively similar. The switching voltage depended on the CdS film thickness. Switching occurred at an

1063-7826/02/3607-0789$22.00

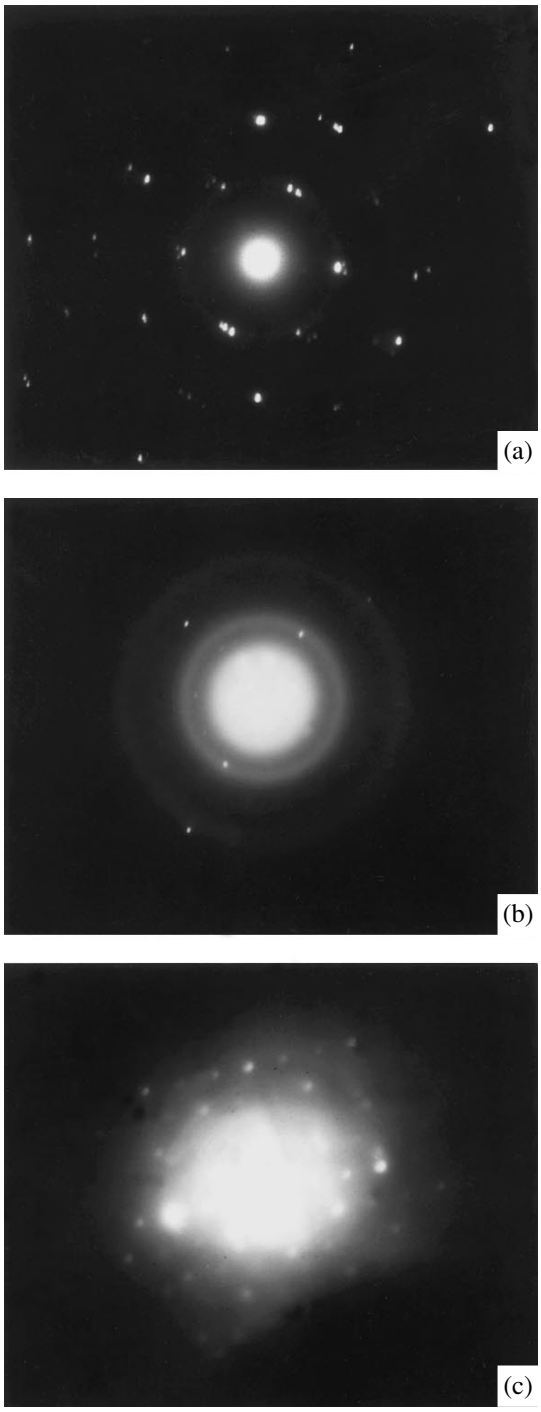

Fig. 1. Electron diffraction patterns of (a) epitaxial, (b) amorphous, and (c) two-phase CdS films, which were grown in highly nonequilibrium conditions on the Si crystalline substrate.

electric field strength $E \sim 10^5$ V/cm. The onset of conductivity switching was accompanied by current instabilities in the form of oscillations.

The dependence of capacitance on the voltage applied for the HJ with the epitaxial and two-phase films had a form characteristic of a highly nonuniform impurity distribution.

4. DISCUSSION

When film synthesis from the vapor phase is in highly nonequilibrium conditions, the film grows mainly from disperse particles, which are formed in the vapor phase due to first-order fluctuations [1, 2, 6]. The dissipation time for excess energy of disperse particles during their condensation on the substrate is finite. This depends on the size of a disperse particle [1, 2, 7]; i.e.,

$$\tau \propto r^2/\chi, \tag{1}$$

where τ is the characteristic dissipation time for excess energy, χ is the thermal diffusivity, and r is the radius of the disperse particle; the dissipation time depends also on the substrate temperature, or, more exactly, on the temperature difference between the disperse particle and the substrate.

For this reason, immediately after condensation, the temperature of a disperse particle is determined by its size. Depending on the temperature of a disperse particle, it will be subcritical or supercritical [4]. Subcritical disperse particles reevaporate, whereas supercritical disperse particles tend to accept the position correlated with the substrate, which is energetically most favorable. The most realistic mechanism of orientation of a disperse particle on a cooled substrate is the soliton mechanism [1–3, 6]. The soliton mechanism implies the motion of a disperse particle due to the motion of misfit dislocations between a disperse particle and the substrate. It is noteworthy that this motion is peculiar; specifically, it involves particle-like waves, i.e., so-called solitons. Through such motion, the sequential transfer of atoms in the plane including a disperse particle and a substrate occurs. At each instant of time, almost all atoms of a disperse particle remain at rest relative to the substrate and only a very small group of atoms moves. The atoms ahead of the wavefront are at rest, since the wave has not yet reached them. The atoms behind the front are at rest, since the wave has already passed through them. Only the atoms which constitute the wavefront at this instant participate in the motion. On the passage of such a wave (one soliton), a disperse particle shifts by one lattice constant. At low temperatures, when the atomic diffusivity is very small, the diffusion-free soliton mechanism is more favorable compared with other mechanisms of mass transfer by virtue of the fact that solitons can spread with low energy losses.

It was demonstrated [1, 2] that a certain relation between the lattice parameters of disperse particles $b(T_f)$ and a substrate $a(T_r)$ should hold for the origination of solitons; i.e.,

$$\frac{a(T_r) - b(T_f)}{b(T_f)} > (2/\pi)^{3/2}\sqrt{(f/\lambda)a(T_r)}. \tag{2}$$

If the values of $b(T_f)$ and $a(T_r)$ are almost the same, this relationship can be made valid by varying the substrate temperature T_r or the temperature of a disperse particle T_f. Here f and λ are the parameters which characterize the interaction forces between the atoms of a disperse particle and interaction forces between the atoms of the substrate, respectively.

Different temperatures of a disperse particle at the same substrate temperature lead to different conditions for the ordering of supercritical disperse particles of different sizes. Due to this, the arrangement of disperse particles of one size on the substrate is correlated and the positioning of particles of another size is uncorrelated.

The distribution function of disperse particles in the space of dimensions with film formation in highly nonequilibrium conditions is close to δ-like [1, 2]. This is caused, on the one hand, by the above-mentioned reevaporation of subcritical disperse particles and, on the other hand, by the fluctuation mechanism of their emergence, since the fluctuation probability decreases with increasing particle size. The character of distribution in the form of the δ function causes the films with a perfect crystallinity to be formed only in a limited temperature range. Out of this range, the conditions for the soliton origination are not met and, because of this, the films formed have a disordered structure.

However, the realistic distribution function has tails. For this reason, the dispersed particles, whose size falls within the tails, can have a correlated orientation on the substrate beyond the limits of the temperature range which corresponds to the formation of perfect films. Hence, we may expect that a mixed structure can form at the boundary of the temperature range of perfect growth. In this structure, along with the disordered phase, the phase with perfect crystallinity can also be present.

The notions described above correlate completely with the results of the experiment discussed. Amorphous films, which contain the crystalline phase, were formed only within a limited temperature range. At higher and at lower temperatures, epitaxial and amorphous films grew, respectively (Fig. 1).

Electrical properties of HJs are consistently explained in the context of the model considered above. Indeed, with the formation of amorphous films, the film–substrate interface contains numerous defects. As a consequence, the properties of the HJ formed will be determined mainly by these surface states [8]. The *I–V* characteristics expected in this case should be close to symmetric, and this was experimentally observed. With the formation of perfect layers on the substrate, the influence of the interface is less significant. Here, the HJ properties are determined by the characteristics of contacting materials. According to theory, the *I–V* characteristics of Si–CdS HJs should be asymmetric. We also observed this for HJs with epitaxial films grown in highly nonequilibrium conditions.

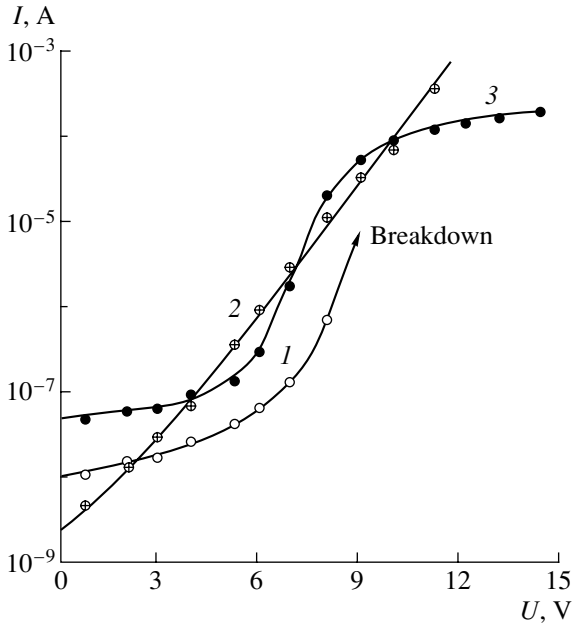

Fig. 2. Reverse portions of current–voltage characteristics for Si–CdS heterojunctions formed on the basis of (*1*) epitaxial, (*2*) amorphous, and (*3*) two-phase CdS films.

The mechanism for the formation of the *I–V* characteristics for the HJ with the two-phase film still requires detailed investigations. It is, however, possible to make some assumptions using our results.

The first assumption concerns the portion of the *I–V* characteristics up to the point of conductivity switching. Here, the *I–V* characteristics of HJs with the two-phase and epitaxial films are qualitatively similar. Consequently, we may assume that the *I–V* characteristic for this voltage region is formed by the contact of the Si substrate with crystalline inclusions of the two-phase film.

The second assumption concerns the switching mechanism. Let us take into account the presence of current instabilities and the electric field strength ($E \sim 10^5$ V/cm) at the instant the switching occurs. In this case, we may assume that switching is associated with the HJ avalanche breakdown between the substrate and crystalline phase. In these conditions, the second stable state of conductivity will apparently be associated with the amorphous phase. This phase acts as a ballast resistance that prevents the avalanche developing to the level which leads to irreversible variations in the HJ.

5. CONCLUSIONS

Based on the results presented, the following conclusions can be made:

(i) Highly nonequilibrium conditions of synthesis, depending on specific modes, allow for the formation on the crystalline substrate of both single-phase amor-

phous films and two-phase films, which contain crystalline inclusions along with an amorphous phase.

(ii) The heterojunction between the Si crystalline substrate and the two-phase CdS film grown in highly nonequilibrium conditions with the reverse switch-on involves two states which differ by several orders of magnitude in conductivity.

ACKNOWLEDGMENTS

This study was supported by the Russian Foundation for Basic Research, project no. 02-03-32405.

REFERENCES

1. A. P. Belyaev, V. P. Rubets, and I. P. Kalinkin, Fiz. Tverd. Tela (St. Petersburg) **39** (2), 382 (1997) [Phys. Solid State **39**, 333 (1997)].
2. A. P. Belyaev, V. P. Rubets, and I. P. Kalinkin, Neorg. Mater. **34** (3), 281 (1998).
3. A. P. Belyaev and V. P. Rubets, Fiz. Tekh. Poluprovodn. (St. Petersburg) **35** (3), 294 (2001) [Semiconductors **35**, 279 (2001)].
4. S. A. Kukushkin and A. V. Osipov, Usp. Fiz. Nauk **168** (10), 1083 (1998) [Phys. Usp. **41**, 983 (1998)].
5. A. P. Belyaev, V. P. Rubets, and I. P. Kalinkin, Fiz. Tekh. Poluprovodn. (St. Petersburg) **31** (8), 966 (1997) [Semiconductors **31**, 823 (1997)].
6. A. P. Belyaev, V. P. Rubets, and I. P. Kalinkin, Zh. Tekh. Fiz. **71** (4), 133 (2001) [Tech. Phys. **46**, 495 (2001)].
7. L. D. Landau and E. M. Lifshitz, *Course of Theoretical Physics*, Vol. 7: *Theory of Elasticity* (Nauka, Moscow, 1987; Pergamon, New York, 1986).
8. A. G. Milnes and D. L. Feucht, *Heterojunctions and Metal–Semiconductor Junctions* (Academic, New York, 1972; Mir, Moscow, 1975).

Translated by N. Korovin

Semiconductors, Vol. 36, No. 7, 2002, pp. 793–799. Translated from Fizika i Tekhnika Poluprovodnikov, Vol. 36, No. 7, 2002, pp. 847–852.

SEMICONDUCTOR STRUCTURES, INTERFACES, AND SURFACES

Special Features of the Magnetodiode Effect in Multivalley Semiconductors at Low Temperatures

A. A. Abramov* and I. N. Gorbatyĭ

Moscow State Institute of Electronic Engineering (Technical University), Zelenograd, Moscow, 103498 Russia

**e-mail: gpd@gf.miee.ru*

Submitted November 27, 2001; accepted for publication December 20, 2001

Abstract—The magnetodiode effect in a planar *p–i–n* structure was analyzed theoretically. This effect is accompanied by an intervalley redistribution of electrons in the vicinity of the structure's Hall surfaces at which the nonequilibrium charge carriers recombine. It is shown that consideration of the superposition of transverse charge-carrier fluxes caused by both the Lorentz force and the intervalley redistribution makes it possible to interpret the following special features of the current–voltage characteristics of Ge- and Si-based *p–i–n* structures at liquid-nitrogen and liquid-helium temperatures: (i) sublinear current–voltage characteristics observed at low temperatures both in the absence and in the presence of a magnetic field; and (ii) the emergence of a high polar magnetosensitivity at strong electric fields (at room temperature, the polar magnetosensitivity vanishes as a result of transition from weak to strong electric fields). © *2002 MAIK "Nauka/Interperiodica".*

The anisotropy (natural or induced) of conductivity gives rise to the large number of various anisotropic dimensional effects observed in thin semiconductor layers [1, 2]. Injection of nonequilibrium charge carriers into such layers is commonly accompanied by a number of additional special features in the manifestation of these effects. Thus, the Welker magnetoconcentration effect based on equilibrium charge carriers is clearly pronounced in pure semiconductors with almost intrinsic conductivity, whereas a similar effect can also be observed in heavily doped semiconductors under the conditions of high injection levels [3, 4]. Similarly, anisotropic dimensional effects caused by the intervalley redistribution of electrons [5, 6] can become appreciable at high injection levels in the *p*-Ge and *p*-Si samples, although these effects can only be observed in *n*-Si and *n*-Ge if there are equilibrium charge carriers.

At low temperatures (in which case, the intervalley-relaxation rate is not too high) and in sufficiently thin wafers (so that the intervalley redistribution of electrons in the vicinity of wafer sides can significantly affect the conductance of the entire sample), the concentration-related effects can superimpose on one another owing to magnetic deflection [3, 4] and the near-surface intervalley redistribution [5, 6]; as shown below, this may account for a wide variety of the current–voltage (*I–V*) characteristics in the *p–i–n* structures. These various *I–V* characteristics were, in fact, observed experimentally [7, 8].

Let us consider the injection of nonequilibrium charge carriers into a semiconductor wafer with dimensions $w2dl_z$ ($w \gg 2d$ and $l_z \gg 2d$). Electric current flows along the *x*-axis ($0 \le x \le w$) and the magnetic field with induction $\mathbf{B}(0, 0, B)$ oriented along the *z*-axis ($0 \le z \le l_z$). The surface recombination of nonequilibrium charge carriers with velocities S_p^+ and S_p^- and the surface intervalley relaxation with the rates S^+ and S^- occur at the Hall surfaces located at $y = \pm d$. Taking into account the shape of isoenergetic surfaces in Ge and Si, we will assume that only electron conductivity is anisotropic, with the current density of holes in the two-dimensional approximation $\mathbf{J}_p(J_{px}, J_{py}, 0)$ being given by the following expression using the generally accepted notation:

$$\begin{aligned} \mathbf{J}_p &= \mathbf{J}_p^0 - [\boldsymbol{\omega}_p, \mathbf{J}_p^0], \\ \boldsymbol{\omega}_p &= \mu_p^*\mathbf{B}, \quad \mathbf{J}_p^0 = e\mu_p(p\mathbf{E} - V_T\nabla_p), \quad V_T = kT/e. \end{aligned} \tag{1}$$

Here, μ_p^* is the Hall mobility of holes. It is assumed that the charge carriers are not heated, so the Einstein relations are presumably valid.

When determining the electron-current density $\mathbf{J}_n(J_{nx}, J_{ny}, 0)$ in the two-dimensional approximation, we restrict ourselves to the model of a two-valley semiconductor, with $\kappa = 1$ or 2 denoting the valley number; we note that the Ge and Si samples can be considered in terms of this model only if crystallographic axes are oriented specifically with respect to the vectors **B** and **J** [6]. In Fig. 1, we show the energy ellipsoids for both valleys and also the orientation of the axes of these ellipsoids $x_1^{(\kappa)}$, $x_2^{(\kappa)}$, and $x_3^{(\kappa)}$ in reference to the axes of the laboratory coordinate system *x*, *y*, *z*. The axes $x_3^{(1)}$ and $x_3^{(2)}$ are oriented along the *z*-axis, which is perpendicular to the plane of drawing in Fig. 1. In further calcula-

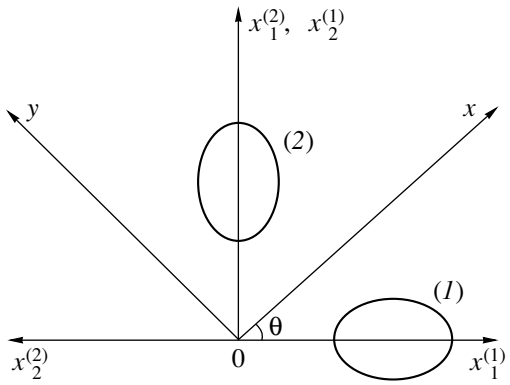

Fig. 1. Orientation of isoenergetic valleys in the conduction band of a multivalley semiconductor.

tions, the angle θ is assumed to be equal to π/4. Using the method for considering the kinetic phenomena in semiconductors with the tensor effective mass of charge carriers [9, 10], we first derive the expressions for $\mathbf{J}_n^{(\kappa)}$ in the intrinsic frame of reference $x_i^{(\kappa)}$ of the κth valley (i = 1, 2, 3). In the approximations of the scalar relaxation time, constant temperature, and linearity in **B**, we have

$$J_{ni}^{(\kappa)} = e\sum_{j=1}^{2}\mu_{ij}^{(\kappa)}\left(n^{(\kappa)}E_j + V_T\frac{\partial n^{(\kappa)}}{\partial x_j^{(\kappa)}}\right), \qquad (2)$$

where

$$\left\|\mu_{ij}^{(\kappa)}\right\| = \begin{pmatrix} \mu_\parallel & \mu_{x_1^{(\kappa)}x_2^{(\kappa)}z}B \\ \mu_{x_2^{(\kappa)}x_1^{(\kappa)}z}B & \mu_\perp \end{pmatrix},$$
$$\mu_{\parallel,\perp} = \frac{e\langle\tau\rangle}{m_{\parallel,\perp}}, \quad \mu_{x_2^{(\kappa)}x_1^{(\kappa)}z} = -\mu_{x_1^{(\kappa)}x_2^{(\kappa)}z} = \frac{e^2\langle\tau^2\rangle}{m_\perp m_\parallel}, \qquad (3)$$

the quantities $\langle\tau\rangle$ and $\langle\tau^2\rangle$ were defined in [10], and m_i^{-1} are the components of the tensor of the reciprocal charge-carrier effective masses ($m_i = m_\perp$ or $m_i = m_\parallel$ depending on the direction of the $x_i^{(\kappa)}$ axis relative to the principal axes of the energy ellipsoid for the valley under consideration).

Conversion to the common coordinate frame is accomplished by rotation of the system coordinates $x_i^{(1)}$ and $x_i^{(2)}$ around the z-axis by the angles θ = –π/4 and θ = π/4 for κ = 1 and κ = 2, respectively. As a result, we can use formula (2) to determine the electron-current densities $\mathbf{J}_n^{(1)}$ and $\mathbf{J}_n^{(2)}$ represented in the system of coordinates x, y, and z and expressed in terms of E_x, E_y, $\partial n^{(\kappa)}/\partial x$, and $\partial n^{(\kappa)}/\partial y$; at the same time, the transformed matrices (3) can be written as

$$\left\|\tilde{\mu}_{ij}^{(1)}\right\| = \mu_n\begin{pmatrix} 1 & a-\omega_n \\ a+\omega_n & 1 \end{pmatrix},$$
$$\left\|\tilde{\mu}_{ij}^{(2)}\right\| = \mu_n\begin{pmatrix} 1 & -a-\omega_n \\ -a+\omega_n & 1 \end{pmatrix}, \qquad (4)$$

where

$$\mu_n = \frac{\mu_\perp+\mu_\parallel}{2}, \quad a = \frac{\mu_\perp-\mu_\parallel}{\mu_\perp+\mu_\parallel}, \quad \omega_n = \frac{e^2\langle\tau^2\rangle\mathbf{B}}{\mu_n m_\parallel m_\perp}.$$

We now take into account the mobility matrices (4) and sum and subtract the contributions of both valleys $\mathbf{J}_n^{(1)}$ and $\mathbf{J}_n^{(2)}$; as a result, we find that the current-density components $\mathbf{J}_n = \mathbf{J}_n^{(1)} + \mathbf{J}_n^{(2)}$ and $\mathbf{J}_\nu = \mathbf{J}_n^{(1)} - \mathbf{J}_n^{(2)}$ are given by

$$J_{nx} = e\mu_n\left(nE_x + V_T\frac{\partial n}{\partial x} - \omega_n nE_y + a\nu E_y + aV_T\frac{\partial\nu}{\partial y} - \omega_n V_T\frac{\partial n}{\partial y}\right),$$
$$J_{ny} = e\mu_n\left(nE_y + V_T\frac{\partial n}{\partial y} - \omega_n nE_x + a\nu E_x + aV_T\frac{\partial\nu}{\partial x} - \omega_n V_T\frac{\partial n}{\partial x}\right), \qquad (5)$$
$$J_{\nu x} = e\mu_n\left(\nu E_x + V_T\frac{\partial\nu}{\partial x} + anE_y - \omega_n\nu E_y + aV_T\frac{\partial\nu}{\partial y} - \omega_n V_T\frac{\partial n}{\partial y}\right),$$
$$J_{\nu y} = e\mu_n\left(\nu E_y + V_T\frac{\partial\nu}{\partial y} + anE_x + \omega\nu E_x + aV_T\frac{\partial n}{\partial x} + \omega_n V_T\frac{\partial\nu}{\partial x}\right), \qquad (6)$$

where

$$n = n^{(1)} + n^{(2)}, \quad \nu = n^{(1)} - n^{(2)}.$$

In the problem under consideration, the parameters $\omega_{n,p}$ and a account for anisotropy introduced by the magnetic field and the intervalley redistribution, respectively. By varying the magnitude and direction of the applied magnetic field, we can control the transverse anisotropic fluxes of charge carriers to the Hall surfaces.

The input equations used to determine the functions $p(x, y)$ and $\nu(x, y)$ are derived by substituting the

expressions for the current densities (1), (5), and (6) into the continuity equations

$$\frac{1}{e}\nabla \mathbf{J}_n = -\frac{1}{e}\nabla \mathbf{J}_p = \frac{p - p_T}{\tau_p}, \quad (7)$$

$$\frac{1}{e}\nabla \mathbf{J}_\nu = \frac{\nu}{\tau}, \quad \frac{1}{\tau} = \frac{1}{\tau_p} + \frac{2}{\tau_{12}}, \quad (8)$$

where τ_p and $\tau_{12} = \tau_{21}$ are the bulk lifetime of nonequilibrium charge carriers and the intervalley-relaxation times, respectively; and p_T and n_T are the concentrations in the thermal equilibrium.

In this formulation, the problem is still cumbersome and can be solved only by numerical analysis. In order to clarify the main special features of interrelation between the magnetic field and the intervalley redistribution, we use a number of additional assumptions.

Taking into account the shortness of the time $\tau_{12}(\tau_{12} \ll \tau_p)$, the high rates of intervalley relaxation at the surface ($S^\pm \gg S_p^\pm$), and the fact that it is the surface effect which gives rise to the intervalley redistribution of charge carriers (a nonzero value of ν), we will assume that the values of ν and $\partial\nu/\partial y$ away from the surface (i.e., in the central part of the sample) are small; therefore, we disregard the quadratic terms proportional to $\propto\nu^2$, $\nu\omega_{p,n}$, and such in the relevant equations.

At the same time, we ignore both the deflection of charge carriers by the magnetic field and the bulk recombination in very thin surface layers with thicknesses $\varepsilon^\pm \ll d$, where the quantities ν and $\partial\nu/\partial y$ can be large. As a result, these layers can be analyzed similarly to [6, 11]. In this situation, the following expressions can be derived for the effective velocities of the surface recombination $S_1^\pm$ at the inner boundaries of these layers [11]:

$$\sigma_1^\pm = \frac{S_1^\pm \tau_p}{L_1} \approx \frac{\sigma_p^\pm (t + \sigma^\pm/\sqrt{2})}{1 + \sigma^\pm t/\sqrt{2}}. \quad (9)$$

Here,

$$\sigma_p^\pm = \frac{S_P^\pm \tau_p}{L_p}, \quad \sigma^\pm = \frac{S^\pm \tau}{L}, \quad L_1 = tL_p,$$

$$t = \sqrt{1 + \frac{\gamma^2}{2}}, \quad \gamma = \delta_w \bar{\gamma}, \quad \delta_w = \frac{aL}{w},$$

$$L = \sqrt{D_n \tau}, \quad L_p = \sqrt{D_a \tau_p}, \quad D_n = V_T \mu_n,$$

$$D_a = \frac{2V_T \mu_n \mu_p}{\mu_n + \mu_p}, \quad \bar{\gamma} = \frac{wE_x}{V_T}.$$

Expression (9) can also be written as

$$S_1^\pm = S_p^\pm \left(1 + \frac{\gamma^2}{2 + \sigma^\pm \sqrt{2 + \gamma^2}}\right),$$

which clearly shows that the surface-recombination velocities increase with increasing field strength E_x. If $\tau \longrightarrow 0$ ($L \longrightarrow 0$, $\delta_w \longrightarrow 0$), the effect of the charge-carrier intervalley redistribution is negligible.

When considering the central part of the sample, where $-d + \varepsilon^- \le y \le d - \varepsilon^+$, we use the drift approximation in the theory of double-injection currents, in which case the diffusion components of the charge-carrier fluxes along the x-axis are disregarded. We also use the approximations of quasi-neutrality and a high injection level (i.e., $p \approx n \gg p_T, n_T$). In addition, we assume that $E_y = E_y(y)$, which means that the transverse component of the electric field is independent of x.

Using the above assumptions and eliminating the transverse field E_y from expressions (1) and (5) using the condition $J_y = J_{ny} + J_{py} = 0$, we obtain the following expression for the current density J_{py}:

$$J_{py} = -J_{ny} \approx -eD_a\left[\left(1 + \frac{\gamma^2}{2}\right)\frac{\partial p}{\partial y} + \frac{(\omega_n + \omega_p)}{2V_T} E_x p\right]. \quad (10)$$

Retaining in the expressions for the current densities J_{nx} and J_{px} only the leading terms

$$J_{nx} \approx e\mu_n n E_x, \quad J_{px} \approx e\mu_p p E_x,$$

we can write the following approximate formulas for the average current density $J = \langle J_x \rangle = \langle J_{nx} + J_{px} \rangle$:

$$J \approx e(\mu_n + \mu_p)\langle p \rangle E_x. \quad (11)$$

Finally, using Eqs. (5), (6), and (8), performing a number of transformations, and using the assumptions that were already discussed in [11], we can derive the basic equation for the determination of $p(x, y)$ as

$$\frac{\partial^2 p}{\partial y^2} + \frac{1}{l_B}\frac{\partial p}{\partial y} = \frac{p - G\tau_p}{L_1^2}, \quad (12)$$

where

$$\frac{1}{l_B} = \frac{(\omega_p + \omega_n)E_x}{2V_T t^2}, \quad G = \frac{D_a(n_T - p_T)}{2V_T}\frac{dE_x}{dx}. \quad (13)$$

Equation (12) differs from the corresponding equation in [11] by the appearance of the term $\propto(\omega_p + \omega_n)E_x$ on the left-hand side of this equation; it is this term that accounts for the magnetodiode effect in the model under consideration. The boundary conditions for Eq. (12) are given by

$$\frac{1}{e} J_{py}\big|_{y = \pm d} = \pm S_1^\pm p(\pm d). \quad (14)$$

Using simple transformations of expressions (7), (10), and (14) and performing averaging over the diode

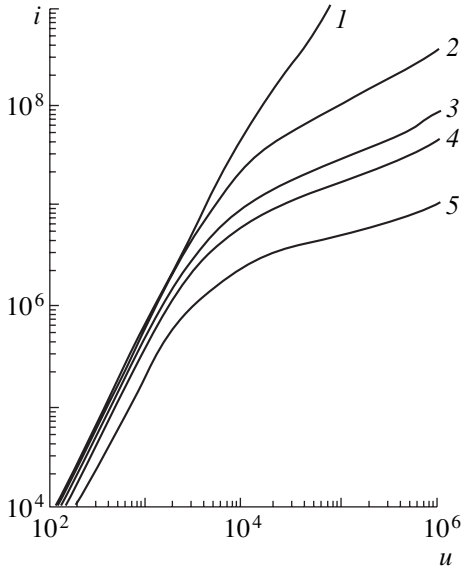

Fig. 2. Dimensionless *I–V* characteristics of a *p–i–n* structure with allowance made for the intervalley redistribution of electrons. The parameters used were $\beta_0 = 0$; $\delta_p = 0.5$; $\sigma^+ = 0.01$; $\sigma^- = 10$; $\delta_w = 0.001$; $\sigma_p^- = 1$; and $\sigma_p^+ = (1)$ 0, (*2*) 0.1, (*3*) 0.5, (*4*) 1, and (*5*) 10.

cross section, we can obtain the following expression for the mean concentration $\langle p \rangle$:

$$G = \frac{\langle p \rangle}{\tau_p} + \frac{S_1^+ p(+d) + S_1^- p(-d)}{2d} \equiv \frac{\langle p \rangle}{\tau_{\text{eff}}}. \qquad (15)$$

Equation (12) and expressions (11) and (13)–(15) appeared in the magnetodiode theory [12] (longitudinal diffusion was also taken into account in [4]). A special feature of the problem under consideration in this study consists in the allowance made for the intervalley electron redistribution, which results in the reduction of the effective wafer thickness (due to the replacement of L_p by $L_1 > L_p$) and in the increase in the effective surface-recombination velocities (due to the replacement of $S_p^\pm$ by $S_1^\pm > S_p^\pm$).

Solving Eq. (12) with boundary conditions (14) and substituting the obtained expressions for $p(\pm d)$ and $\langle p \rangle$ into (15), we obtain

$$\bar{\tau}(\bar{\gamma}) = \frac{\tau_{\text{eff}}}{\tau_p} = \frac{\langle p \rangle}{G\tau_p} = 1 + \frac{\Delta_1 + \Delta_2}{\Delta}, \qquad (16)$$

$$\Delta = Y \sinh X - (r^+ + r^-) X \cosh X,$$

$$\Delta_1 = \frac{\beta X}{2\alpha^2}\left[(r^+ - r^-)(\cosh\beta - \cosh X) + (r^+ + r^-)\left(\frac{\beta}{X}\sinh X - \sinh\beta\right)\right],$$

$$\Delta_2 = (r^+ + r^-)\sinh X - \frac{r^+ r^-}{\alpha^2} X(\cosh\beta - \cosh X),$$

$$X = \sqrt{\beta^2 + 4\alpha^2}, \quad Y = \beta(r^+ - r^-) - 2(\alpha^2 + r^+ r^-),$$

where

$$\alpha = \frac{\delta_p}{t}, \quad \delta_p = \frac{d}{L_p},$$

$$\beta = \frac{\beta_0 \bar{\gamma}}{t^2}, \quad \beta_0 = \frac{(\omega_p + \omega_n)}{2}\frac{d}{w}, \quad r^\pm = \frac{\delta_p \sigma_1^\pm}{t}.$$

Using formulas (13), (15), and (16), we can obtain the following expression for the *p–i–n*-structure *I–V* characteristic in the parametric form:

$$i = \frac{w^3 J}{e\mu_p \mu_n \tau_p (n_T - p_T) V_T^2} = \int_0^{\gamma_w} \bar{\tau}(\bar{\gamma})\bar{\gamma} d\bar{\gamma},$$
$$u = \frac{U}{V_T} = \frac{1}{i}\int_0^{\gamma_w} \bar{\tau}(\bar{\gamma})\bar{\gamma}^2 d\bar{\gamma}. \qquad (17)$$

The quantities *i* and *u* used in [11] differ from those introduced here in the multipliers δ_w^2 and δ_w, respectively. The dimensionless *I–V* characteristic obtained above is completely defined by specifying the following seven parameters: δ_p, β_0, δ_w, $\sigma_p^\pm$, and $\sigma^\pm$. If $\beta_0 = 0$ (there is no magnetic field), expressions (16) and (17) are transformed into the relationships derived in [11]. The results of calculating the low-temperature *I–V* characteristic of an asymmetric ($S_p^+ \neq S_p^-$ and $S^+ \neq S^-$) *p–i–n* structure with allowance made for the intervalley electron redistribution in this situation are shown in Fig. 2.

The sublinear portions of the *I–V* characteristics in Fig. 2 correspond to the situation where $\bar{\tau}(\bar{\gamma}) \sim \bar{\gamma}^{-2}$ in the region of strong fields (of large $\bar{\gamma}$). In the vicinity of the contact ($x = 0$), the field $\bar{\gamma}$ is weak and $\bar{\tau}$ = const. Then, if we approximate the dependence $\bar{\tau}(\bar{\gamma})$ using the expression $\bar{\tau} = (1 + A\bar{\gamma}^2)^{-1}$, the *p–i–n*-structure *I–V* characteristic defined by (17) turns out to be actually sublinear; i.e.,

$$u = \frac{[\exp(2Ai) - 1]^{1/2} - \arctan[\exp(2Ai) - 1]^{1/2}}{A^{3/2} i}. \qquad (18)$$

If, in addition, $\exp(2Ai) \gg 1$, we obtain

$$u \approx \frac{\exp(Ai)}{A^{3/2} i}. \qquad (19)$$

Here, we corrected the error in formulas (15) and (16) in publication [11].

It can be seen from Fig. 2 that, in the range of strong fields $\bar{\gamma}$, the *I–V* characteristic of a *p–i–n* structure depends heavily on $S_p^+(\sigma_p^+ \propto S_p^+)$, i.e., on the surface-recombination velocity at the surface where the value of S^+ (the rate of the surface intervalley relaxation) is small. Calculations show that the *I–V* characteristics of this *p–i–n* structure are slightly affected by S_p^-, i.e., by the recombination rate at the surface where the value of S^- is large and, consequently, the transverse flux of the charge carriers towards this surface is almost absent.

If $\delta_w = 0$ (there is no intervalley redistribution of electrons), expressions (16) and (17) are transformed into equations for a magnetodiode [12] whose typical *I–V* characteristics are shown in Fig. 3. Such *I–V* characteristics of magnetodiodes with polar magnetosensitivity ($S_p^+ \neq S_p^-$) were observed experimentally at room temperature [3, 13]. The theory of such a magnetodiode was considered first in [3] and then in a number of publications (in particular, in [12, 14]).

An analysis of the simultaneous effects of intervalley electron redistribution and magnetic deflection is hampered by a large number of parameters in the problem under consideration. For large values of β ($|\beta| \gg 1$, α, α^2), the following expression is found to be convenient:

$$\bar{\tau} = \frac{\alpha^2(1 + r^{\mp})}{\alpha^2 + r^+ r^- + r^{\mp}|\beta|}. \qquad (20)$$

Here, the upper and lower signs at $r^{\mp}$ correspond to $\beta > 0$ and $\beta < 0$, respectively.

Expressions (16) and (20) also appeared in [12]; however, in this study, the parameters α, β, and $r^{\pm}$ depend on the quantities δ_w, $\sigma^{\pm}$, and $\gamma = \delta_w\bar{\gamma}$, which control the effect of the intervalley electron redistribution.

For very high electric-field strengths ($\gamma \gg 1$), the parameters β, α, and X are proportional to $1/\gamma$. If $X \ll 1$, we have

$$\bar{\tau} = \frac{1}{6}\left\{\frac{YX^2 - 4\alpha^2[3 + 2(r^+ + r^-)]}{Y - (r^+ + r^-)}\right\}. \qquad (21)$$

The parameters r^+ and r^- are independent of γ ($r^{\pm} \approx \delta_p\sigma_p^{\pm}$) if $2/\sigma^{\pm} \gg \gamma \gg \sigma^{\pm}$ and decrease with increasing γ ($r^{\pm} \approx 2\delta_p\sigma_p^{\pm}/\sigma^{\pm}\gamma$) if $\gamma \gg \sigma^{\pm}$ and $2/\sigma^{\pm}$. Taking into account these circumstances, it is easy to show that $\bar{\tau}$ ceases to depend on β for very large values of γ; i.e.,

$$\bar{\tau} \approx \frac{2\alpha^2}{r^+ + r^-} \propto \frac{1}{\gamma}. \qquad (22)$$

Simultaneously, the magnetosensitivity decreases drastically and the *I–V* characteristic of the *p–i–n* structure becomes linear ($i \propto u$). This tendency towards the suppression of magnetosensitivity in strong fields can be clearly seen from the calculated *I–V* characteristics shown in Fig. 4, which demonstrate the influence of

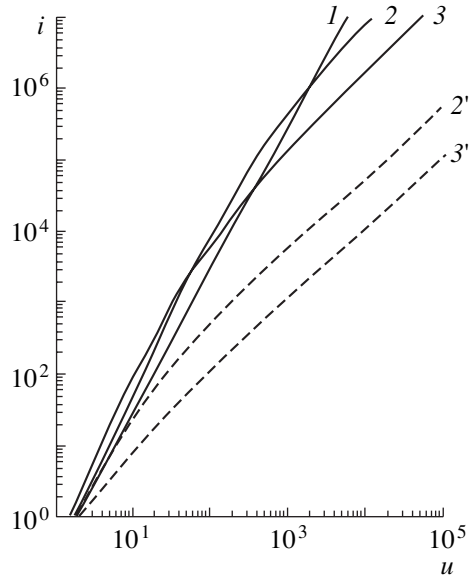

Fig. 3. Dimensionless *I–V* characteristics for the polar magnetodiode effect. The parameters used are $\delta_w = 0$; $\delta_p = 0.5$; $\sigma_p^+ = 0.01$; $\sigma_p^- = 10$; and $\beta_0 = (1)\ 0, (2)\ 0.1, (3)\ 0.5, (2')\ -0.1$, and $(3')\ -0.5$.

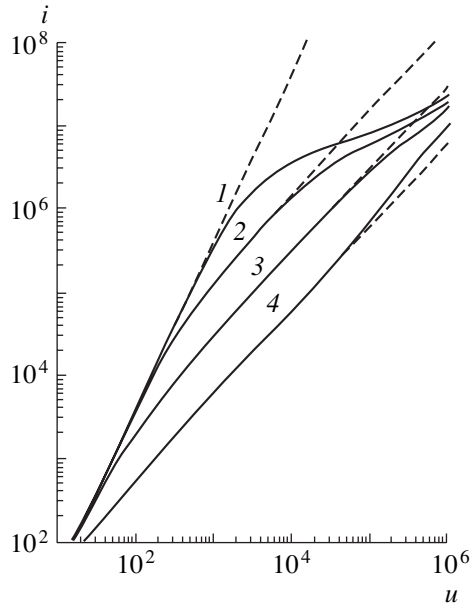

Fig. 4. Dimensionless *I–V* characteristics of a symmetric *p–i–n* structure under the conditions of the pure magnetodiode effect ($\delta_w = 0$, dashed lines) and in the case of simultaneous consideration of the intervalley electron redistribution and the magnetodiode effect ($\delta_w = 0.001$, the solid lines). The following values of the parameters were used: $\delta_p = 0.5$; $\sigma_p^+ = \sigma_p^- = 1$; $\sigma^+ = \sigma^- = 0.01$; and $\beta_0 = (1)\ 0, (2)\ 0.01, (3)\ 0.05$, and $(4)\ 0.25$.

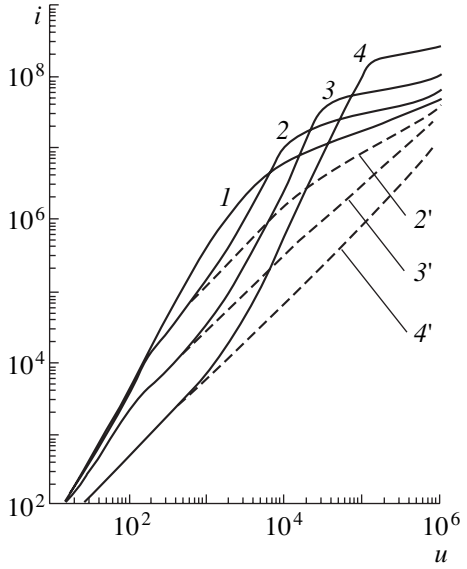

Fig. 5. Dimensionless *I–V* characteristics of an asymmetric *p–i–n* structure with simultaneous consideration of both the intervalley redistribution of electrons and the magnetodiode effect. The following values of the parameters were used: $\delta_p = 0.5$; $\delta_w = 0.001$; $\sigma_p^+ = \sigma_p^- = 1$; $\sigma^+ = 0.01$; $\sigma^- = 10$; and $\beta_0 =$ (*1*) 0, (*2*) 0.01, (*3*) 0.05, (*4*) 0.25, (*2'*) –0.01, (*3'*) –0.05, and (*4'*) –0.25.

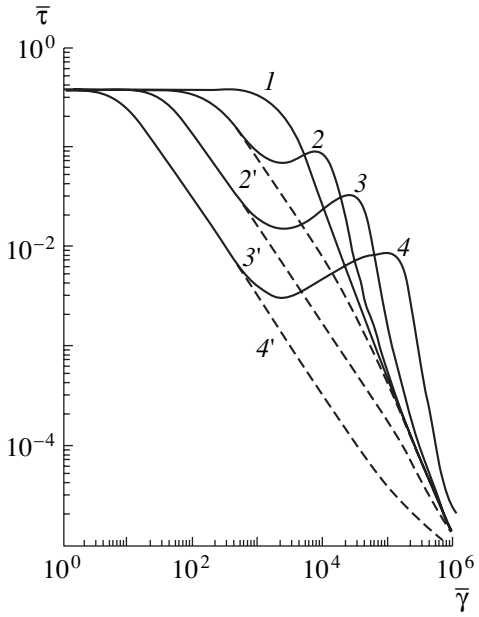

Fig. 6. Dependences of the effective charge-carrier lifetime on the electric field for the *p–i–n* structure whose *I–V* characteristics are shown in Fig. 5 (designations and parameters are the same as in Fig. 5).

electron intervalley redistribution in the vicinity of lateral areas of a symmetric *p–i–n* structure ($S_p^+ = S_p^-$, $S^+ = S^-$) on the magnetodiode effect. The decrease in the magnetosensitivity at strong fields gives rise, in particular, to a peak in the current dependence of magnetosensitivity of a *p–i–n* structure (in Fig. 4, this peak corresponds to $u \approx 3 \times 10^3$).

Especially interesting effects of intervalley electron redistribution are observed in asymmetric *p–i–n* structures. For one such structure with $S^+ \ll S^-$, Figs. 5 and 6 show the results of calculations of the *I–V* characteristics for various magnetic fields and the corresponding dependences of the effective charge-carrier lifetime on the electric field. For $B > 0$, the transverse charge-carrier flux caused by the Lorentz force is directed toward the surface $y = -d$, whereas the transverse charge-carrier flux caused by the intervalley redistribution of electrons is directed toward the surface $y = +d$ (since the rate of the surface intervalley relaxation is low at this surface). Therefore, for the *p–i–n* structure whose characteristics are represented in Figs. 5 and 6, the deflection of charge carriers by a magnetic field in a certain range of voltages at strong electric fields results in an increase in the effective lifetime of charge carriers $\tau|_{B>0}$ compared to $\tau|_{B=0}$ and, correspondingly, to positive current magnetosensitivity. For still higher electric fields (in which case, the parameter β begins to decrease appreciably), the lifetime starts to decrease again, whereas the magnetosensitivity passes first through a maximum, then decreases, and finally becomes negative again (this region of the *I–V* characteristic is not shown in Fig. 5). The effect of the emergence of polar magnetosensitivity in asymmetric Si *p–i–n* structures at the liquid-nitrogen and liquid-helium temperatures was observed by Gasanov [8]. At room temperature, as can be seen from Fig. 3 and reported in [13], the polar magnetosensitivity of *p–i–n* structures can be observed under weak electric fields; at strong electric fields, the current-related magnetosensitivity becomes negative for both directions of a magnetic field and the polarity dependence ceases to exist. Experimentally [8], maxima in the magnetosensitivity were also observed; a theoretical interpretation of these was given above. At the same time, the *I–V* characteristics measured in experiments [7, 8] with Ge and Si magnetodiodes featured, in certain cases, portions with a negative differential conductivity and hysteresis.

As has been shown previously [15, 16], the *I–V* characteristics of the *N* type can be observed in relatively short samples with contacts possessing high emissivity if the dependence $\tau(E)$ shows a sufficiently steep decline with decreasing efficiency of bipolar diffusion as the mechanism of transport of charge carriers from the contacts to the bulk of the semiconductor sample. In this case, the dependence of $\langle p \rangle$ on x becomes highly irregular; it includes a gently sloping central region and steep near-contact wings. In contrast, if the drift approximation and the idealized boundary condition $E_x = 0$ at the injecting junction ($x = 0$) are used, the *I–V* characteristics of the *p–i–n* structure are single-valued in voltage for an arbitrarily steep descending

dependence $\tau(E)$ [16]. Thus, if a more complete theory of the magnetodiode effect in multivalley semiconductors is assumed to also interpret such phenomena as negative differential conductance and hysteresis in the *I–V* characteristics, then it should account for longitudinal diffusion of charge carriers, which was not considered in this study. In addition, such a complete theory should account for the possibility of intervalley electron redistribution in heated electric fields (the Sasaki effect) and for the dependence of transport and recombination coefficients on the electric-field strength.

REFERENCES

1. É. I. Rashba, Z. S. Gribnikov, and V. Ya. Kravchenko, Usp. Fiz. Nauk **119**, 3 (1976) [Sov. Phys. Usp. **19**, 361 (1976)].
2. A. F. Kravchenko, V. V. Mitin, and É. M. Skok, *Transport Phenomena in Semiconductor Films* (Nauka, Novosibirsk, 1979).
3. Z. S. Gribnikov, G. I. Lomova, and V. A. Romanov, Phys. Status Solidi **28**, 815 (1968).
4. A. A. Abramov and I. N. Gorbatyĭ, Fiz. Tekh. Poluprovodn. (Leningrad) **18**, 2046 (1984) [Sov. Phys. Semicond. **18**, 1275 (1984)].
5. É. I. Rashba, Zh. Éksp. Teor. Fiz. **48**, 1427 (1965) [Sov. Phys. JETP **21**, 954 (1965)].
6. Z. S. Gribnikov, Fiz. Tekh. Poluprovodn. (Leningrad) **3**, 1821 (1969) [Sov. Phys. Semicond. **3**, 1543 (1970)].
7. K. Miyazaki and J. Yamaguchi, Jpn. J. Appl. Phys. **7**, 1210 (1968).
8. L. S. Gasanov, Fiz. Tekh. Poluprovodn. (Leningrad) **15**, 2416 (1981) [Sov. Phys. Semicond. **15**, 1404 (1981)].
9. P. S. Kireev, *Physics of Semiconductors* (Vysshaya Shkola, Moscow, 1975).
10. A. I. Anselm, *Introduction to Semiconductor Theory* (Nauka, Moscow, 1978; Prentice-Hall, Englewood Cliffs, 1981).
11. A. A. Abramov and I. N. Gorbatyĭ, Izv. Vyssh. Uchebn. Zaved., Élektron., No. 6, 41 (2000).
12. A. A. Abramov and A. U. Fattakhdinov, Fiz. Tekh. Poluprovodn. (Leningrad) **13**, 2144 (1979) [Sov. Phys. Semicond. **13**, 1254 (1979)].
13. T. Yamada, in *Proceedings of the IX International Conference on Physics of Semiconductors, 1968*, Vol. 2, p. 711.
14. H. Pfleiderer, Solid-State Electron. **15**, 335 (1972).
15. A. A. Akopyan and Z. S. Gribnikov, Fiz. Tekh. Poluprovodn. (Leningrad) **14**, 740 (1980) [Sov. Phys. Semicond. **14**, 435 (1980)].
16. A. A. Abramov and I. N. Gorbatyĭ, in *Abstracts of XII Conference on the Theory of Semiconductors, Tashkent, 1985*, Part 1, p. 9.

Translated by A. Spitsyn

Semiconductors, Vol. 36, No. 7, 2002, pp. 800–804. Translated from Fizika i Tekhnika Poluprovodnikov, Vol. 36, No. 7, 2002, pp. 853–857.

SEMICONDUCTOR STRUCTURES, INTERFACES, AND SURFACES

Behavior of Charge in a Buried Insulator of Silicon-on-Insulator Structures Subjected to Electric Fields

D. V. Nikolaev, I. V. Antonova*, O. V. Naumova, V. P. Popov, and S. A. Smagulova

Institute of Semiconductor Physics, Siberian Division, Russian Academy of Sciences, pr. Akademika Lavrent'eva 13, Novosibirsk, 630090 Russia

**e-mail: antonova@isp.nsc.ru*

Submitted November 5, 2001; accepted for publication November 21, 2001

Abstract—The behavior of charge in a buried oxide of the silicon-on-insulator structures obtained using the Dele-Cut technology was studied by keeping the structures under a voltage with an electric-field strength of 2–5.5 MV/cm. A mobile positive charge drifting under the effect of applied voltage was detected in the oxide. The expected charge accumulation in the oxide was not detected. It may be assumed that both of the observed effects are caused by the interaction of residual hydrogen, which is present in the oxide during the preparation of the structures, with traps in the thermal oxide. As a result, the traps become passivated in the buried insulator of the structure; in addition, the charge, which is mobile at room temperature, is introduced into the insulator.

1. INTRODUCTION

Charge in an insulator is an important parameter in such devices as those based on metal–oxide–semiconductor (MOS) and silicon-on-insulator (SOI) structures. A variation (accumulation) of charge in the gate insulator became one of the basic causes of the MOS-transistor instability of operation and of the failure of circuits, and it also became the main cause of dielectric breakdown in the oxide. For the SOI structures, the introduction of a charge into the buried insulator can result in an appreciable variation in the operational characteristics of the devices based on the SOI structures. Therefore, the study of the stability of buried oxide in a SOI structure is topical.

The generation of charge carriers and their capture in the oxide of metal–insulator–semiconductor (MIS) structures have been studied by many researchers over a period of several decades [1–5]. Mathematical models describing various mechanisms of the charge accumulation have been developed (see, for example, [3, 6, 7]). Recently, similar processes occurring in the buried insulator of SOI structures fabricated using SIMOX and Smart-Cut™ technologies have been studied [7–9]. The accumulation of positive charge, which was annealed out at temperatures of 200–400°C, was observed in the buried insulator of MIS structures held under a voltage [8].

In this paper, we report the results of studying the behavior of charge in the buried insulator of SOI structures fabricated using the Dele-Cut technology [10].

2. EXPERIMENTAL

In order to form the SOI structures, we used *n*-Si wafers grown by the Czochralski method. The method for the formation of SOI structures is based on the implantation of hydrogen into a silicon wafer, splitting off the wafer over the layer weakened by the hydrogen implantation, and transferring the thin silicon layer to the oxidized substrate. The dissimilarity of this method for fabricating SOI structures from Smart-Cut technology consists in the fact that hydrogen is implanted through the protective oxide layer; the latter is removed after implantation, and the ensuing buried oxide (BOX) is grown on the substrate with the film/oxide interface being bonded. The irradiated oxide is used as the ensuing buried insulator in the Smart-Cut technology.

The following SOI structures were used in our studies: *n*-type conductivity both in the film and in the substrate, with the concentrations of the charge carriers in the SOI film and the substrate being equal to 5×10^{15} and 1.5×10^{15} cm^{-3}, respectively. The thicknesses of the split-off silicon layer and the buried insulator were 0.48 and 0.4 μm, respectively. The SOI wafers were used to form capacitors, which consisted of a Al contact, a SOI layer, a buried-oxide layer, a substrate, and a bottom Al contact. The capacitors used in our studies had an area of 0.5 mm^2.

The simplest and most widely used method for measuring the charge in oxide is based on the determination of this charge from the voltage shift of the high-frequency capacitance–voltage (C–U) characteristic [11]. The operating frequency of our experimental setup was 1 MHz. In addition, we measured the current–voltage characteristics $I(U)$ and the time dependences of current $I(t)$. The charge was injected into the buried oxide by keeping the SOI mesastructures in a field with the strength of $E = \pm(2–5.5)$ MV/cm for a time interval of

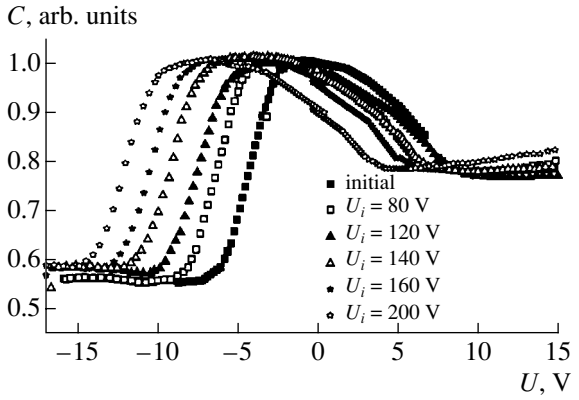

Fig. 1. The *C–U* characteristics of SOI structures subjected to the voltage U_i; the characteristics were measured immediately after the voltage was switched off. The structures were kept under voltage for t_i = 60 min.

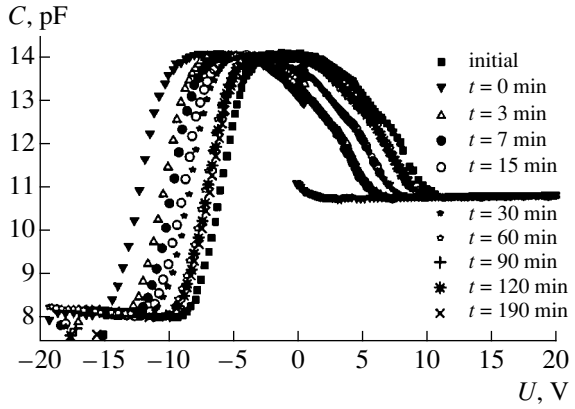

Fig. 2. The *C–U* characteristics before and after the SOI structures were kept with a positive voltage U_i = 160 V; the characteristics were measured within various times *t* after the voltage was switched off. The structures were exposed to voltage for t_i = 60 min.

120 min. Both positive and negative voltages were applied to the structure; this made it possible to inject the charge carriers through both boundaries of the buried oxide (from the Si film and from the substrate).

3. RESULTS

Typical *C–U* characteristics measured immediately after the structures ceased to be kept under the injection voltage of as high as U_i = 200 V for t_i = 60 min are shown in Fig. 1. Henceforth, the voltage polarity is determined by the sign of the potential applied to the split-off silicon layer. The *C–U* characteristics measured after a positive injection voltage U_i was applied are appreciably shifted to negative voltages. As can be seen, the *C–U* characteristics are subjected to a nearly parallel shift in reference to the initial characteristic. It follows from the calculations that the difference between the flat-band voltages at both interfaces remains virtually unchanged. In addition, the slope of the curves in the capacitance-modulation range remains also unchanged, which indicates that the density of surface states at the interfaces is unchanged.

In Fig. 2, we show the *C–U* characteristics for the injection voltage of U_i = 160 V in relation to the time *t* that elapsed from the charge injection. It can be seen that the shift of the *C–U* characteristic is not retained after the voltage U_i is switched off; at the same time, the structure relaxes to the initial state within several hours.

The values of the charge calculated from the *C–U* measurements and located at the oxide/substrate (Q_s) and the film/oxide (Q_f) interfaces, the total charge in the oxide ($Q_t = Q_s + Q_f$), and the position of the charge centroid (X) are shown in Fig. 3. All these quantities were calculated using conventional formulas based on the capacitances and the flat-band voltages [11, 12]. When a positive voltage U_i (t_i = 60 min, injection from substrate side) was applied, we observed an increase in the positive charge (reduced to the substrate/oxide interface) to the value of 7×10^{11} cm^{-2} at U_i = 200 V (the initial charge $Q_s^0 \approx 2.4 \times 10^{11}$ cm^{-2} at U_i = 0; the largest additional charge $\Delta Q_s^{\max} = 4.6 \times 10^{11}$ cm^{-2}). Correspondingly, a variation in the charge magnitude Q_f from 2×10^{11} to -2.3×10^{11} cm^{-2} (the largest additional charge $\Delta Q_f^{\max} = -4.3 \times 10^{11}$ cm^{-2}) is observed at the film/oxide interface. Since $|\Delta Q_s^{\max}| \approx |\Delta Q_f^{\max}|$, we have drift of the charge inside the oxide from one interface to the other rather than charge accumulation. The total charge $Q_t = Q_s + Q_f$ remains virtually unchanged. If a negative voltage U_i as high as –200 V is applied (injection of the charge carriers from the SOI-film side of the structure), the total charge in the oxide layer decreases somewhat ($\Delta Q_s^{\max} = -1.1 \times 10^{11}$ cm^{-2}, and $\Delta Q_f^{\max} = 2.5 \times 10^{10}$ cm^{-2}). The dependence of the charge centroid on the applied voltage is shown in the upper panel of Fig. 3. The position of the centroid is measured from the insulator–semiconductor interface, i.e., from the oxide/film interface. We note that, in the initial structures (before being kept under a voltage or for U_i = 0), this centroid is found, as a rule, at the midplane of the oxide or is a little closer to the upper film/oxide interface. In the range of negative voltages, the centroid is slightly shifted from the center part of the oxide to the upper-film/oxide interface. The value of the shift is small and amounts to ~0.5 μm. For positive voltages, the charge centroid shifts into the oxide bulk even for low electric-field strengths E; for E exceeding 3 MV/cm, the charge is localized near the boundary with the substrate.

A typical current–voltage characteristic $I(U)$ of a SOI structure is shown in Fig. 4. It can be seen that current in the structure depends somewhat on the voltage

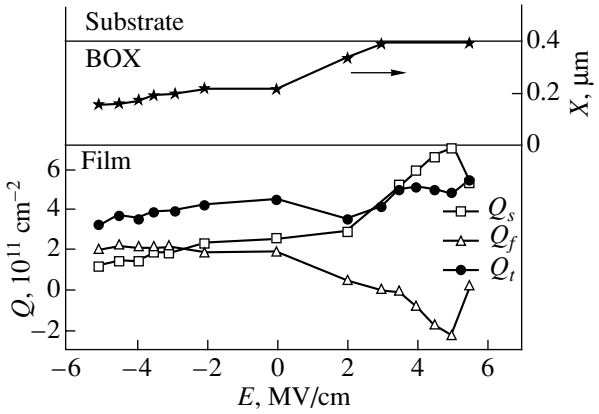

Fig. 3. Dependences of the magnitudes of charges at the interfaces with buried oxide (BOX) Q_s and Q_f, the total charge Q_t, and the position of the charge centroid in the oxide X on the applied voltage. The structures were kept under voltage for t_i = 60 min.

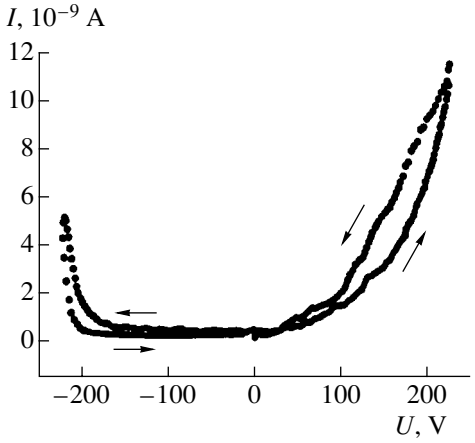

Fig. 4. A typical current–voltage characteristic of a SOI capacitor.

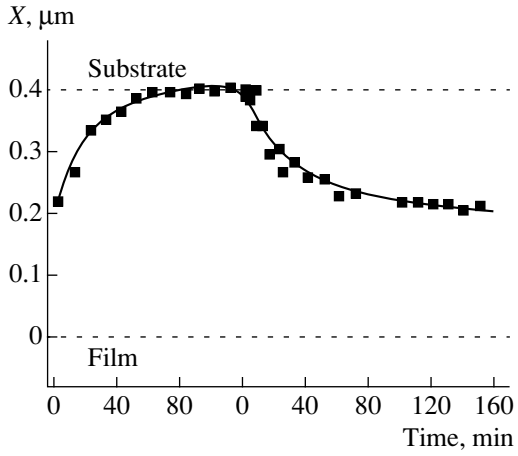

Fig. 5. Variations in the position of the charge centroid in relation to the duration of keeping the structure under voltage and the elapsed time from the instant the voltage was switched off.

polarity. A slightly pronounced current hysteresis is observed at both the positive and negative biases. The hysteresis features indicate that ion drift occurs under positive bias, whereas the traps are recharged if a negative bias is applied. Hysteresis in the *C–U* characteristics is also clearly seen in Fig. 2.

The dependence of the centroid position on the duration of keeping the structure under a postive voltage and on the time elapsed since the voltage was switched-off is shown in Fig. 5. It can be seen that, as a result of keeping the sample under the applied voltage, the main portion of the charge drifts in a relatively short time (~20 min), so that the charge centroid shifts from the oxide-layer midplane to the substrate and remains at this location as long as the voltage is still applied. After the voltage is switched off, the charge centroid reverts gradually to its original location in the oxide, so that, in about 140–150 min, the centroid resides again in the oxide-layer midplane. As was mentioned above, the total charge in the oxide remains almost unchanged. The voltage-induced shift of the charge and its return to the original location can be accomplished repeatedly.

For the sake of comparison, we measured the *C–V* characteristics of MIS structures that had a 0.28-μm-thick oxide and were kept for 1 h in an electric field of ±3 MV/cm. The oxide was grown under the same conditions as in the case of the oxide for the SOI structures. As might be expected, a positive charge ($Q_{acc} = 9 \times 10^{10}$ cm^{-2} at E = 3 MV/cm and $Q_{acc} = 4.31 \times 10^{11}$ cm^{-2} at E = –3 MV/cm) was accumulated in the MIS structures kept under voltage; this charge remained unchanged after the voltage was switched off.

4. DISCUSSION

The above results show that the behavior of the charge during and after exposure of the SOI structures (fabricated using the Dele-Cut technology) to voltage has certain specific features, which differentiate these structures from the MOS capacitors with thermal oxide and from the SOI structures obtained by the SIMOX and Smart-Cut methods. These differences consist in the following.

(1) The oxide charge does not increase during the exposure of the structure to voltage, despite the fact that electrons are injected into the oxide. Instead, the charge drifts in the oxide.

(2) As a rule, the application of external voltage of both polarities gives rise to similar effects in the oxides. However, in the Dele-Cut structures, a change in the voltage polarity brings about fundamentally different effects. Thus, the oxide charge is virtually unaffected by the negative bias applied to the structure, whereas positive bias causes the charge to drift.

Another important aspect is noteworthy. The amount of charge in the original oxide used in the fabrication of the SOI structures was equal to (1–4) × 10^{11} cm^{-2}. The

Comparison of injection and accumulation of charge in the buried oxide of SOI structures fabricated using the SIMOX [9] and Dele-Cut technologies

Dele-Cut (t_i = 60 min)				SIMOX (t_i = 2 min)			
U_i, V	E, MV/cm	Q_i, 10^{14} cm^{-2}	Q_t, 10^{11} cm^{-2}	U_i, V	E, MV/cm	Q_i, 10^{14} cm^{-2}	Q_t, 10^{11} cm^{-2}
Injection from the film							
–200	–5.0	23	3.32	–190	5.28	85	3.2
–180	–4.5	15	3.67	–170	4.72	48	2.9
–160	–4.0	9.5	3.56	–150	4.17	1.2	2.6
–140	–3.5	7.85	3.91	–130	3.61	0.1	2.5
0	0	0	4.33	0	0	0	2.2
Injection from the substrate							
140	3.5	7.85	5.0				
160	4.0	9.5	5.13	190	5.28	0.4	3.6
180	4.5	15	4.95	210	5.83	0.59	4.2
200	5.0	23	4.75	230	6.39	1.5	4.7
220	5.5	50.5	5.41	250	6.94	3.5	5.0

amount of charge increased to (3–5) $\times$ 10^{11} cm^{-2} after the SOI structure was formed.

For the sake of comparison, the table lists the results of electron injection into the SOI structures made using either the Dele-Cut or SIMOX technologies. In both cases, the injected charge is almost the same despite the fact that the injection in the Dele-Cut structures lasts 60 min, whereas it takes 2 min for the SIMOX structures. In the latter, accumulation of positive charge occurs for both polarities of applied voltage, whereas such an accumulation is not observed in the Dele-Cut structures.

The forward I–V characteristic (Fig. 4) is rectified in the Fowler–Nordheim coordinates for the electric-field strength $E \approx 5$ MV/cm. If $E > 5.5$ MV/cm, breakdown phenomena set in the structures investigated in this study. The flow of current through the oxide in the Dele-Cut structures is described by the conventional mechanism and is, in general, no different from that in the MIS or other SOI structures.

We should note once again that the accumulation of positive charge is observed in the initial thermal oxide exposed to voltage. As is typical of MIS structures, the accumulated charge is stable at room temperature.

A large number of publications (see, for example, [13, 14]) have been concerned with traps located in oxides and recharged during charge-carrier injection. By way of example, we will mention the following electron traps in the SIMOX structures: (i) the paramagnetic E' centers, which are related to excess silicon in the oxide host and have a capture cross section $\sigma = 10^{-14}$ cm^2; (ii) the traps that arise as a result of contamination during oxygen implantation and have $\sigma = 10^{-16}$ cm^2; and (iii) the traps that are related to water, are typically present in thermal oxides, and have $\sigma = 10^{-17}$ cm^2 [8]. The charge accumulation in the buried insulator is attributed to the presence of traps [8, 13, 14].

Let us consider in what respect the oxide in the Dele-Cut structures differs from the buried oxide in various types of SOI structures, during the fabrication of which implantation and annealing are used, and from the initial thermal oxide. In the course of the formation of SOI structures according to the SIMOX technology, the implantation of high doses of oxygen ions and subsequent annealing are used. After these treatments, a fairly large number of defects remain in the oxide; these defects are traps with deep levels, and they are responsible for the charge accumulation and storage. In the Smart-Cut structures, hydrogen is implanted through the oxide, which also gives rise to damage in the spatial structure of the oxide and to radiation defects. In the course of the formation of the Dele-Cut structures, the oxide remains undamaged, since it is not subjected to any external effects, except for the bonding of the wafers and subsequent high-temperature annealing. However, in the course of forming the Dele-Cut structures, hydrogen is present at a high concentration both at the interfaces and in the oxide itself [15]. Apparently, these data explain why the thermal oxide, which has conventional properties, acquires new characteristics in a SOI structure.

As is well known, the charge in a thermal oxide is mainly localized in the vicinity of the interface with Si; in the case under consideration, this is the oxide/substrate interface. As was already mentioned above, the charge in the oxide of a SOI structure increases appreciably, with the charge centroid residing mainly near the oxide-layer midplane. This suggests that the charge in the buried insulator also includes the charge of protons localized mostly at the defects near both interfaces.

If a positive bias is applied to the structure, the electric field causes protons to drift from the interface between the separated silicon layer and oxide to the oxide/substrate interface. Moreover, the emergence of negative charge at the former interface is probably related to the decomposition of neutral centers containing hydrogen and to the drift of protons to the other interface. When the voltage is switched off, an opposite-directed proton flux comes into existence owing to an internal electric field, so that protons return to their initial location at the interface between the separated silicon layer and the oxide.

An applied voltage of negative polarity should give rise to similar effects if there are protons at the oxide/substrate interface or in the oxide bulk. However, the absence of both a significant shift of the charge centroid and variations in the charges Q_s and Q_f indicates that there are no mobile protons either at the aforementioned interface or in the bulk. Apparently, the charge at this interface is related only to immobile centers. These can include alkali metals, hydrogen localized at defects, and other positively charged centers. It is most important that the charge under consideration is immobile at room temperature.

The absence of charge accumulation in the oxide is apparently caused by the interaction of hydrogen with traps, which are present in the oxide, and by the passivation of these traps. In other words, the defects in the oxide are transformed as a result of their interaction with hydrogen.

5. CONCLUSION

We studied the behavior of charge in the buried oxide of SOI structures fabricated by the Dele-Cut technology and subjected to external voltage with an electric-field strength of 2–5.5 MV/cm. We observed a drift of positive charge in the oxide and subsequent charge relaxation (i.e., return of the charge to its initial location) after the voltage was switched off. We did not detect the expected accumulation of charge in the oxide. We assume that the observed phenomena are caused by the effect of residual hydrogen; the latter is present at a high concentration in the oxide during the fabrication of SOI structures. As a result, the traps in the buried insulator become passivated; in addition, the charge, which is mobile at room temperature, is introduced.

ACKNOWLEDGMENTS

This study was supported by the Russian Foundation for Basic Research (project no. 01-02-16986) and, in part, by the International Science & Technology Center (grant no. 563).

REFERENCES

1. M. Lenzlinger and E. H. Snow, J. Appl. Phys. **40**, 278 (1969).
2. M. V. Fischetti, J. Appl. Phys. **57**, 2860 (1985).
3. Y. Lu and C.-T. Sah, J. Appl. Phys. **76**, 4724 (1994).
4. D. J. DiMaria, E. Cartier, and D. A. Buchanan, J. Appl. Phys. **80**, 304 (1996).
5. K. Kobayashi, A. Teramoto, and H. Miyoshi, IEEE Trans. Electron Devices **46**, 947 (1999).
6. M. V. Fisshetti, Phys. Rev. B **31**, 2099 (1985).
7. S. Mayo, J. S. Suehle, and P. Roitman, J. Appl. Phys. **74**, 4113 (1993).
8. C. S. Ngwa and S. Hall, Semicond. Sci. Technol. **9**, 1069 (1994).
9. A. N. Nazarov, V. I. Kilchytska, I. P. Barchuk, *et al.*, J. Vac. Sci. Technol. B **18**, 1254 (2000).
10. V. P. Popov, I. V. Antonova, V. F. Stus', and L. V. Mironova, RF Patent No. 2164719 (1999).
11. K. Nagai, T. Sekigawa, and Y. Hayashi, Solid-State Electron. **28**, 789 (1985).
12. F. T. Brady, S. S. Li, and D. E. Burk, Appl. Phys. Lett. **52**, 886 (1988).
13. A. A. Lebedev and W. Ecke, Fiz. Tekh. Poluprovodn. (Leningrad) **19**, 1087 (1985) [Sov. Phys. Semicond. **19**, 667 (1985)].
14. L. P. Reilly and T. Robertson, Phys. Rev. B **27**, 3780 (1983).
15. I. A. Antonova, V. P. Popov, V. F. Stas, *et al.*, Microelectron. Eng. **48**, 383 (1999).
16. E. H. Snow, A. S. Grove, B. E. Deal, and C. T. Sah, J. Appl. Phys. **36**, 1664 (1965).

Translated by A. Spitsyn

Semiconductors, Vol. 36, No. 7, 2002, pp. 805–807. Translated from Fizika i Tekhnika Poluprovodnikov, Vol. 36, No. 7, 2002, pp. 858–860.

SEMICONDUCTOR STRUCTURES, INTERFACES, AND SURFACES

Study of the Effect of Electron Irradiation on a GaSe–SiO_2 Structure by Spectroscopic Methods

T. D. Ibragimov*, E. A. Dzhafarova*, and Z. B. Safarov**

** Institute of Physics, Academy of Sciences of Azerbaĭjan, pr. Dzhavida 33, Baku, 370143 Azerbaĭjan*

e-mail: physic@lan.lab.az

*** Gyandzha State University, Gyandzha, 374700 Azerbaĭjan*

Submitted December 11, 2001; accepted for publication December 21, 2001

Abstract—Auger electron spectroscopy and Raman spectroscopy were used to study a GaSe–SiO_2 structure before and after irradiation with 4.0-MeV electrons at a dose of 3.0×10^{15} cm^{-2}. It was shown that after the irradiation the thickness of the transition region in the GaSe–SiO_2 structure decreases, while the oxide film becomes more homogenous. One of the possible causes of these changes may be radiation-stimulated gettering of Ga atoms by the GaSe–SiO_2 interface that serves as a sink. © *2002 MAIK "Nauka/Interperiodica".*

INTRODUCTION

As is known, radiation defects drastically change the electrical properties of crystalline semiconductors if the concentration of these defects is on the same order of magnitude or exceeds that of initial defects (generated in semiconductors during technological processes). Radiation defects not only accumulate, but also drift to sinks, which brings the irradiated crystal closer to equilibrium. In accordance with this, there may be some range of irradiation doses for which structural ordering of a crystal would occur. This ordering can manifest itself most drastically near the semiconductor-structure surfaces and interfaces, because they contain a large number of sinks and annihilation centers [1].

Heterostructures based on layered semiconductor crystals are of special interest in semiconductor physics. Since heterostructures have perfect surfaces (i.e., do not require any special treatment) and low densities of surface states, they can be considered as an ideal object for the investigation of barrier structures, including insulator–semiconductor structures. An example of such structures is GaSe–SiO_2, whose components do not chemically react. The electrical properties of GaSe–SiO_2 irradiated with 4.0-MeV electrons at different doses were studied previously in [2]. It was shown that the maximum change in the activation energy and minimum reverse current under Schottky emission can be attained at an irradiation dose of 3.0×10^{15} cm^{-2}. This indirectly indicates that irradiation with fast electrons at this dose makes the GaSe–SiO_2 interface more abrupt.

In this study, we used Auger electron spectroscopy and Raman spectroscopy to investigate GaSe–SiO_2 structures before and after irradiation with 4.0-MeV electrons at a dose of 3.0×10^{15} cm^{-2}.

Layered ε-GaSe crystals were grown by the Bridgman–Stockbarger method in evacuated quartz cells. Due to weak interlayer bonds, GaSe crystals can be easily split into plane-parallel wafers with thicknesses from 100 to 300 μm. Silicon dioxide films were deposited on GaSe wafers by the pyrolysis of tetraethylorthosilicate $Si(OC_2H_5)_4$ in Ar in an Izotron-6 commercial plant. The major part of this plant is a quartz reaction chamber heated in a three-zone furnace. A temperature control was used to stabilize the temperature in the chamber at the value of 467°C (the boiling temperature of $Si(OC_2H_5)_4$). A carrier gas (a mixture of O_2 and N_2) was used to transport the tetraethylorthosilicate vapors to the reaction zone, where it decomposed at T = 680–780°C to form oxide films on GaSe wafers. The deposition rate of SiO_2 and the film composition were controlled by choosing appropriate gas-flow rates and varying the wafer temperature in the range of 250–460°C. The deposition rate was 0.1 nm/s, and the film thickness ranged from 0.4 to 3 μm. The stoichiometry of the deposited films was checked by measuring the characteristic band with a peak at 1080 cm^{-1} (Si–O–Si stretching vibrations) ([3]) in the absorption spectra recorded using a Specord-75IR infrared spectrophotometer. A number of GaSe–SiO_2 structures were irradiated with 4.0-MeV electrons at a dose of 3.0×10^{15} cm^{-2}.

An IOS-09 two-chamber Auger spectrometer was used to record Auger spectra. The residual pressure of gases during the measurements was 10^{-10} Torr. The surfaces of the samples were cleaned in vacuum and sputtered by an Ar-ion beam in order to carry out AES profiling (down to a depth of 3.0 μm).

The Raman spectra of the GaSe structures before and after irradiation with fast electrons were recorded using a DFS-52 spectrometer. An Ar laser with a wavelength of 514.5 nm was used as the excitation source. The excitation light was incident on a SiO_2 film at a small angle. The scattered light was collected by a condenser and detected at the same side on which the excitation light was incident. Under these conditions, the

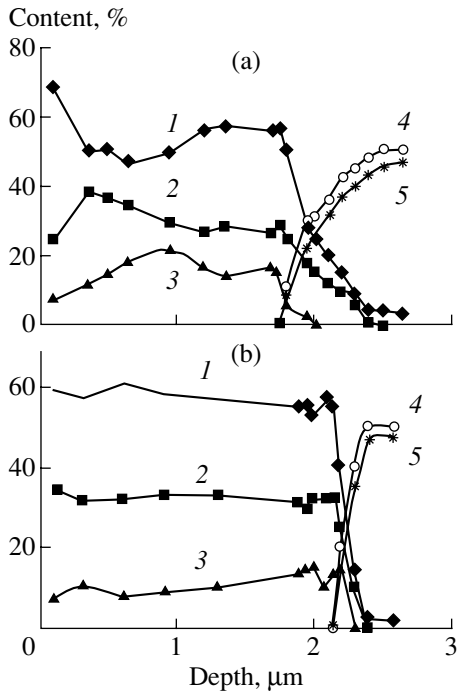

Fig. 1. Concentration profiles of (*1*) O, (*2*) free Si, (*3*) bound Si, (*4*) Ga, and (*5*) Se in a GaSe–SiO_2 structure (a) before and (b) after irradiation with 4.0-MeV electrons to a dose of 3.0×10^{15} cm^{-2}.

SiO_2 film virtually did not absorb the incident light, whereas the GaSe substrate readily absorbed it. Hence, the Raman spectra were actually recorded from the SiO_2 film, the thin surface layer of GaSe, and their interface [4]. For the purpose of comparison, Raman spectra were also recorded from the free surface of GaSe (with the same geometric layout of the experiment). The resolution and the accuracy of determination of the Raman line frequencies were no worse than 0.5 cm^{-1}.

Phonon frequencies in Raman spectra of a GaSe–SiO_2 structure (before and after irradiation with fast electrons) and GaSe substrate

Mode	GaSe, cm^{-1}	GaSe–SiO_2	
		before irradiation, cm^{-1}	after irradiation, cm^{-1}
E_1'	19.5	20.5	21.5
E_1''	60.0	60.0	60.0
A_1'	134.0	134.0	134.0
E_2''	211.0	211.0	211.0
$E_2'(LO)$	252.0	–	–
A_2'	306.0	306.0	306.0

Figure 1 shows the element-concentration profiles derived from Auger spectra. Analysis of these profiles shows that there is a transition region where O atoms are replaced by Se atoms, and Si atoms (mainly those that are in the free state) are replaced by Ga atoms penetrating into the amorphous SiO_2 film. After irradiation with fast electrons, radical changes were observed in the distribution of the elements. In particular, the irradiation of the structure coated with a 2.4-μm-thick SiO_2 film results in a decrease in the thickness of the transition region by nearly a factor of 3. The total thickness of the SiO_2 film and the transition region does not change after irradiation, which indicates that it is the amorphous SiO_2 film which is responsible for the formation of the transition region. After irradiation, the profiles of the elements in the SiO_2 film become smoother, which indicates that the Si and O atoms become more uniformly distributed in the oxide film.

The frequencies of the spectral lines in the Raman spectra of GaSe–SiO_2 structures before and after irradiation with fast electrons are listed in the table. For the purpose of comparison, the frequencies of spectral lines in the spectra of the unirradiated free surface of GaSe and a relevant, generally accepted classification of modes are also listed in the table. Spectral lines that correspond to modes E_1', E_1'', A_1', E_2'', and $E_1'(LO)$ are observed in the spectra of GaSe. The first of these modes corresponds to interlayer vibrations, while the others correspond to intralayer vibrations in GaSe. The presence of the SiO_2 film results in an increase in the intensity of the Rayleigh scattering. We attribute this to the presence of defects in the regions that contributed to the spectra. In addition to this, the intensity of the $E_1'(LO)$ mode becomes very low (on the verge of reliable measurements of the intensity and shape of the corresponding line). This fact indicates that longitudinal phonons are scattered at charged centers over the GaSe–SiO_2 interface, which is consistent with the results of the previous study [5]. In addition to this, the frequency of the interlayer mode slightly increases within experimental error. The shape of the relevant line becomes complex, which indicates that the boundary layer of GaSe is damaged and that there are other modifications of GaSe (Fig. 2).

After irradiation with fast electrons, the intensity of the Rayleigh scattering decreases, because the GaSe–SiO_2 interface becomes less damaged. The frequencies of the intralayer modes do not change, while the frequency of the interlayer mode increases even more. It is worth noting that the interlayer mode of GaSe is very sensitive to different factors. For example, the value of the Grüneisen parameter for this mode exceeds the relevant values for other modes by a factor of 20 [6]. A decrease in the thickness of a GaSe film results in a decrease in the frequency of the interlayer mode, because the electrostatic energy of the interlayer interaction decreases [7]. In our case, the increase in the frequency of the

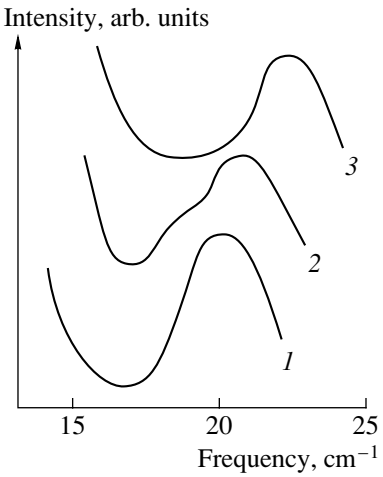

Fig. 2. Raman spectra of (*1*) GaSe, (*2*) GaSe–SiO_2 before irradiation, and (*3*) GaSe–SiO_2 after irradiation, in the vicinity of the interlayer mode.

interlayer mode indicates that the stress at the boundary between the SiO_2 film and GaSe substrate increases due to a decrease in the thickness of the transition region, which is confirmed by the results of the measurements of Auger spectra.

It is known that complex defects (complexes that consist of structural defects and impurity atoms from both components of the structure) and clusters of defects play a major role in the formation of a transition region. These complex defects, in their turn, can serve as annihilation centers for simpler defects. The thickness of the transition region may decrease due to the following mechanism. The high-energy electrons knock out Si atoms from the lattice sites. The knocked out Si atoms displace Ga atoms to interstices. Since the effective coefficient of radiation-stimulated heterodiffusion of Ga atoms is rather large [8], they diffuse to the interface that serves as a sink. The interaction of complex defects with simple defects gettered from the bulk (in particular, with interstitial Ga atoms) facilitates the reordering of complexes and annihilation of simple defects. On the whole, this results in the ordering of the structure.

REFERENCES

1. N. L. Dmitruk and V. G. Litovchenko, Optoélektron. Poluprovodn. Tekh., No. 3, 13 (1983).
2. Z. A. Safarov and M. G. Shakhtakhtinskiĭ, Dokl. Akad. Nauk Azerb., Ser. Fiz.-Mat. Tekh. Nauki **47** (12), 34 (1991).
3. A. L. Shabalov and M. S. Feldman, Thin Solid Films **151**, 317 (1987).
4. T. D. Ibragimov, G. G. Kurbanova, and V. S. Gorelik, Phys. Status Solidi B **155**, 113 (1989).
5. A. G. Abdullaev and T. D. Ibragimov, Fiz. Tverd. Tela (Leningrad) **28**, 2565 (1986) [Sov. Phys. Solid State **28**, 1439 (1986)].
6. J. M. Besson, Nuovo Cimento B **33**, 488 (1977).
7. V. S. Gorelik, A. G. Abdullaev, and T. D. Ibragimov, Poverkhnost, No. 4, 55 (1988).
8. O. Yu. Borkovskaya, N. L. Dmitruk, V. G. Litovchenko, and O. M. Minshchuk, Fiz. Tekh. Poluprovodn. (Leningrad) **23**, 207 (1989) [Sov. Phys. Semicond. **23**, 129 (1989)].

Translated by Yu. Sin'kov

Semiconductors, Vol. 36, No. 7, 2002, pp. 808–815. Translated from Fizika i Tekhnika Poluprovodnikov, Vol. 36, No. 7, 2002, pp. 861–868.

LOW-DIMENSIONAL SYSTEMS

Calculation of the Low-Field Mobility of Quasi-Two-Dimensional Electrons in a GaAs/$Al_{0.36}Ga_{0.64}As$ Superlattice at Temperatures in the Region of 77 K

S. I. Borisenko

Kuznetsov Siberian Physicotechnical Institute, pl. Revolyutsii 1, Tomsk, 634050 Russia
e-mail: sib@elefot.tsu.ru

Submitted November 30, 2001; accepted for publication December 4, 2001

Abstract—The longitudinal and transverse mobilities of quasi-two-dimensional electrons in a GaAs/$Al_{0.36}Ga_{0.64}As$ superlattice was calculated in the region of the liquid-nitrogen temperature and in the electron-concentration range from 10^{13} to 10^{15} cm^{-3}. Scattering of electrons by polar optical phonons, acoustic phonons, and impurity ions was taken into account. The Boltzmann equation in the linear approximation in the electric field with allowance made for inelasticity of scattering by polar optical phonons was solved by the sweep method. Analytical formulas for low-temperature longitudinal and transverse relaxation times with involvement of optical phonons were derived. The issue concerning the applicability of the Boltzmann equation to the analysis of longitudinal conductivity in the superlattices under consideration was studied. © *2002 MAIK "Nauka/Interperiodica".*

1. INTRODUCTION

As is well known, many specific properties of heterostructures with a quasi-two-dimensional (quasi-2D) electron gas manifest themselves at low temperatures [1–3]. One of the related important issues concerns the applicability of the Boltzmann equation to the analysis of kinetic phenomena under these conditions. In particular, this is related to calculation of longitudinal electron conductivity in superlattices (SLs) where the width of the main (lower) miniband is much smaller than the mean energy of charge carriers. For linear conductivity, according to general principles [4], the Boltzmann equation is applicable if the following conditions are met:

$$\hbar/\tau_{\parallel} < \Delta < k_0 T. \quad (1)$$

Here, $\tau_{\parallel}$ is the effective relaxation time, which corresponds to the motion of electrons along the SL axis; Δ is the width of the main miniband in the conduction band of an SL; and T is temperature. It is assumed that the electric-field strength E for an SL with the period d can always be chosen to be sufficiently small ($eEd < \hbar/\tau_{\parallel}$). The first of conditions (1) implies a weak scattering and large mean free path along the SL axis, which is necessary for the miniband to be formed. Fulfillment of the second condition ensures the 2D character of the electron gas.

In this study, the single-miniband approximation is used to investigate whether conditions (1) can be satisfied for the best understood GaAs/$Al_xGa_{1-x}As$ electron SLs with intersubband optical transitions in the region of infrared-radiation absorption [1, 5]. To this end, the Boltzmann equation was used to numerically analyze the effective relaxation time with allowance made for intraminiband scattering of electrons by polar optical (PO) and acoustic phonons of the bulk type and by the impurity ions. The influence of phonon confinement on electron scattering was ignored because the long-period SLs were considered [6]. The Boltzmann equation was solved with allowance made for the inelasticity of scattering by polar phonons using the sweep method instead of the method of iterations [6, 7]; the latter is unstable in the region of low temperatures. The linearized Boltzmann equation was reduced (as in the case of a bulk semiconductor [8]) to a functional equation for the transverse and longitudinal effective relaxation times. Numerical analysis of the longitudinal and transverse mobilities was performed for a GaAs/$Al_{0.36}Ga_{0.64}As$ SL with a quantum-well width $a = 8$ nm, an barrier width $b = 5$ nm, and an impurity-ion concentration in the range of 10^{13}–10^{15} cm^{-3} at a temperatures of 50–100 K.

2. SOLUTION OF THE BOLTZMANN EQUATION

As is well known, the Boltzmann equation has the following form for a small addition $g(\mathbf{k})$ to the nonequilibrium distribution function with allowance made for the inelasticity of electron scattering by polar optical phonons in a constant electric field E [6]:

$$g(\mathbf{k}) = \tau_0(\mathbf{k}) \times \left\{ \sum_{\mathbf{k}'} g(\mathbf{k}')[w_{\mathbf{k}'\mathbf{k}} + f_0(\varepsilon)(w_{\mathbf{k}\mathbf{k}'} - w_{\mathbf{k}'\mathbf{k}})] + e\frac{\partial f_0}{\partial \varepsilon} E\mathbf{v}(\mathbf{k}) \right\}. \quad (2)$$

1063-7826/02/3607-0808$22.00

Here,

$$\tau_0^{-1}(\mathbf{k}) = \sum_{\mathbf{k}'}[w_{\mathbf{k}\mathbf{k}'} + f_0(\varepsilon')(w_{\mathbf{k}'\mathbf{k}} - w_{\mathbf{k}\mathbf{k}'})],$$
$$f_0(\varepsilon) = \left(\exp\left(\frac{\varepsilon - \xi}{k_0 T}\right) + 1\right)^{-1} \quad (3)$$

is the nonequilibrium Fermi–Dirac distribution function; $\varepsilon = \varepsilon(\mathbf{k})$; $\varepsilon' = \varepsilon(\mathbf{k}')$ is the electron energy, which depends on the wave vector; ξ is the Fermi level measured from the bottom of the lower miniband; $w_{\mathbf{k}\mathbf{k}'}$ is the probability per unit time of transition from the state with the wave vector $\mathbf{k}$ to the state with the wave vector $\mathbf{k}'$; and $\mathbf{v}(\mathbf{k}) = \nabla_{\mathbf{k}}\varepsilon/\hbar$ is the electron velocity.

In the approximation which is linear in the electric-field strength, a nonequilibrium addition to the distribution function was sought in the conventional form; i.e.,

$$g(\mathbf{k}) = e\frac{\partial f_0}{\partial \varepsilon}\sum_i \tau_i(\mathbf{k})E_i v_i(\mathbf{k}), \quad (4)$$

where $\tau_i(\mathbf{k})$ are the functions which depend generally on the wave vector and will be called the effective relaxation times. This name is justified by the fact that, in the elastic-relaxation region, these functions transform into true relaxation times. Equations for these unknown functions are derived in the conventional manner by substituting expression (4) into Eq. (2); i.e.,

$$\tau_i(\mathbf{k}) = \tau_0(\mathbf{k})\left\{\sum_{\mathbf{k}'}[w_{\mathbf{k}'\mathbf{k}} + f_0(\varepsilon)(w_{\mathbf{k}\mathbf{k}'} - w_{\mathbf{k}'\mathbf{k}})] \times \frac{f_0'(\varepsilon')v_i(\mathbf{k}')}{f_0'(\varepsilon)v_i(\mathbf{k})}\tau_i(\mathbf{k}') + 1\right\}, \quad (5)$$

where $f_0'(\varepsilon)$ is the derivative of the equilibrium distribution function.

The energy spectrum of electrons in the main miniband of an SL with the z-axis directed along the SL symmetry axis is described, in the approximation of weakly interacting quantum wells (QWs), by the well-known formula

$$\varepsilon(\mathbf{k}) = \frac{\hbar^2 k_\perp^2}{2m_\perp} + \frac{\Delta}{2}[1 - \cos(k_z d)], \quad (6)$$

where $\mathbf{k}_\perp = (k_x, k_y, 0)$ is the wave vector perpendicular to the z-axis; and $m_\perp$ is the transverse effective mass, which is close to the effective electron mass m^* in the semiconductor comprising the QW. The following convenient formula for calculation of the miniband width was derived by solving the Kronig–Penney equation using the perturbation theory:

$$\Delta = \frac{16E_0}{\pi}\sqrt{\frac{m_b E_0}{m_a V}}\exp(-sb). \quad (7)$$

Here, $s = \sqrt{2m_b V}/\hbar$, a and b are the widths of the QW and the SL barrier with the lattice period $d = a + b$, m_a and m_b are the effective masses of electrons in the QW and in the barrier with the height V, and E_0 is the ground-level energy measured from the bottom of an isolated finite-depth QW. Formula (7) is valid if $V \gg E_0$.

In view of both the cylindrical symmetry of SL and the form of function (6) for a 2D electron gas ($\Delta < k_0 T$), Eqs. (5) can be rewritten as

$$\tau_\perp(\varepsilon) = \tau_0(\varepsilon)\left\{\sum_{\mathbf{k}'}[w_{\mathbf{k}'\mathbf{k}} + f_0(\varepsilon)(w_{\mathbf{k}\mathbf{k}'} - w_{\mathbf{k}'\mathbf{k}})] \times \frac{f_0'(\varepsilon')\mathbf{k}_\perp\mathbf{k}_\perp'}{f_0'(\varepsilon)k_\perp^2}\tau_\perp(\varepsilon') + 1\right\}, \quad (8)$$

$$\tau_\parallel(\varepsilon) = \tau_0(\varepsilon)\left\{\sum_{\mathbf{k}'}[w_{\mathbf{k}'\mathbf{k}} + f_0(\varepsilon)(w_{\mathbf{k}\mathbf{k}'} - w_{\mathbf{k}'\mathbf{k}})] \times \frac{f_0'(\varepsilon')\sin(k_z' d)}{f_0'(\varepsilon)\sin(k_z d)}\tau_\parallel(\varepsilon') + 1\right\}, \quad (9)$$

where $\tau_\perp(\varepsilon) = \tau_x(\varepsilon) = \tau_y(\varepsilon)$, $\tau_\parallel(\varepsilon) = \tau_z(\varepsilon)$, and $\varepsilon = \hbar^2 k_\perp^2/2m_\perp$. It is noteworthy that, in the 2D approximation, the functions of the effective relaxation time τ_i and the function τ_0 depend only on the energy of the electron transverse motion.

With allowance made for the transverse distribution of electrons in a QW, the probability of scattering of quasi-2D electrons by polar optical phonons in an SL can be represented as (see Appendix 1)

$$w_{\mathbf{k}\mathbf{k}'}(\mathbf{q}) = w^+_{\mathbf{k}\mathbf{k}'}(\mathbf{q}) + w^-_{\mathbf{k}\mathbf{k}'}(\mathbf{q}), \quad (10)$$

where

$$w^\pm_{\mathbf{k}\mathbf{k}'}(\mathbf{q}) = \frac{\pi e^2 P^2}{\varepsilon_0 \omega V}\left(N_q + \frac{1}{2} \pm \frac{1}{2}\right) \times \sum_n \left|S\left(k_z' - k_z + \frac{2\pi}{d}n\right)\right|^2 \left(\frac{q}{q^2 + \alpha_\infty^2}\right)^2 \delta[\varepsilon(\mathbf{k}') - \varepsilon(\mathbf{k}) \pm \hbar\omega]\delta_{k_\perp' - k_\perp, \mp q_\perp}\delta_{k_z' - k_z + \frac{2\pi n}{d}, \mp q_z}. \quad (11)$$

In the approximation of the quasi-2D electron gas with allowance made for (11), Eqs. (8) and (9) can be reduced to the following functional form after integration with respect to the phonon wave vector $\mathbf{q}$ and the longitudinal component of the electron wave vector k_z':

$$\tau_i(\varepsilon) = \tau_0(\varepsilon)\{G_i^+(\varepsilon)\tau_i(\varepsilon + \hbar\omega) + G_i^-(\varepsilon)\tau_i(\varepsilon - \hbar\omega) + 1\}. \quad (12)$$

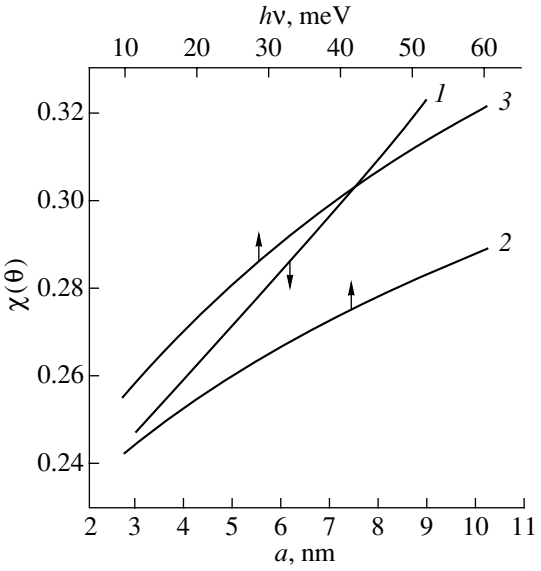

Fig. 1. Dependences of dimensionless function $\chi(\theta)$ on (*1*) the width of the quantum well in the superlattice and (*2*, *3*) the energy of the longitudinal optical phonon. In (*1*), $\hbar\omega = 0.037$ meV; $a =$ (*2*) 5 and (*3*) 7 nm.

Here, $\tau_0(\varepsilon)$ and $G_i^{\pm}(\varepsilon)$ are functions of transverse energy and are represented using single integrals (see Appendix 2), and subscript i = ⊥ or ||. The structure of functional Eqs. (12) is such that they can be solved numerically using the sweep method with the boundary condition for the sought-for function at high energies $\varepsilon \gg \hbar\omega$; for these energies, the effective relaxation time transforms into the conventional relaxation time:

$$\tau_i(\varepsilon) = \tau_0(\varepsilon)\{1 - \tau_0(\varepsilon)[G_i^+(\varepsilon) + G_i^-(\varepsilon)]\}^{-1}. \quad (13)$$

In the low-energy region $\varepsilon < \hbar\omega$, we have $\tau_i(\varepsilon + \hbar\omega) \ll \tau_i(\varepsilon)$ taking into account that there is no scattering with emission of phonons for $k_0T \ll \hbar\omega$ (see Appendix 2). Notably, the following expression for the transverse and longitudinal effective relaxation times at low temperatures ensues from Eqs. (12):

$$\tau_i(\varepsilon) \approx \tau_0(\varepsilon) = G_0^+(\varepsilon)^{-1}. \quad (14)$$

This formula can be rewritten in the following analytical form for a nondegenerate electron gas taking into account the approximate value of the function $G_0^+(\varepsilon)$ for $\varepsilon \longrightarrow 0$ and disregarding the screening of the long-range field of PO phonons:

$$\tau_0(\varepsilon) = \tau_0 = \chi(\theta)\tau. \quad (15)$$

Here,

$$\tau = \frac{6\sqrt{2}\pi\hbar^{3/2}\varepsilon_0\varepsilon^* e^{\hbar\omega/k_0T}}{e^2\sqrt{m^*\omega}}$$

is the time of low-temperature relaxation via the longitudinal polar optical phonons in the III–V semiconductors [9];

$$\chi(\theta) = \frac{\pi\theta^2(4+\theta^2)^2}{48} \times\left[\frac{\pi}{32}\theta(4+\theta^2)(8+3\theta^2) + \exp(-\pi\theta) - 1\right]^{-1}$$

is a dimensionless function, which depends on the dimensionless parameter $\theta = \sqrt{\hbar\omega/E_a}$; and $E_a = \pi^2\hbar^2/(2m_\perp a^2)$ is the energy of the lower level of an isolated, infinitely deep QW, with this energy depending on the QW width *a*. It follows from formula (15) that the low-temperature relaxation time is (like in the bulk III–V semiconductors) isotropic and independent of energy. Figure 1 displays the dependences of the function $\chi(\theta)$ on the QW width and on the PO-phonon energy; these dependences were calculated using the following values for the parameters of the electron and phonon spectra in GaAs: $m_\perp = 0.067m_0$ and $\hbar\omega = 0.037$ meV. It follows from Fig. 1 that $\chi(\theta) < 1$; i.e., according to the theory of scattering for a 2D electron gas [10], the intensity of scattering increases as a three-dimensional electron gas is replaced by a 2D electron gas. As the QW width and the PO-phonon energy increase, the difference in the scattering intensity between the bulk semiconductor and SL becomes less pronounced.

If there is mixed scattering by the PO phonons and by other elastic-scattering mechanisms described by the relaxation times $\tau_{j\perp}(\varepsilon)$ and $\tau_{j\|}(\varepsilon)$, the function $\tau_0(\varepsilon)$ in Eqs. (12) should be replaced by $\tau_{0i}(\varepsilon)$, where

$$\tau_{0i}^{-1}(\varepsilon) = \tau_0^{-1}(\varepsilon) + \sum_j \tau_{ji}^{-1}(\varepsilon). \quad (16)$$

If the elastic scattering of electrons by singly charged impurity ions is taken into account, the relaxation times will be calculated using the formulas derived conventionally [9] using the scattering probability presented in Appendix 1; i.e.,

$$\frac{1}{\tau_\perp(\varepsilon)} = C_I\int_0^\infty \frac{U^2(x)}{(x^2+\gamma_s^2)^{1/2}(4\varepsilon + x^2 + \gamma_s^2)^{3/2}}dx, \quad (17)$$

$$\frac{1}{\tau_\|(\varepsilon)} = C_I\int_0^\infty \frac{\sin^2(\eta x/2)U^2(x)(4\varepsilon + 2x^2 + 2\gamma_s^2)}{(x^2+\gamma_s^2)^{3/2}(4\varepsilon + x^2 + \gamma_s^2)^{3/2}}dx, \quad (18)$$

where

$$C_I = e^4N_I(2\pi\sqrt{2m^*}\varepsilon_0^2\varepsilon_s^2)^{-1}, \quad \gamma_s = \frac{\hbar}{\sqrt{2m^*}}\alpha_s$$

(see Appendix 2).

These formulas were derived in the approximation of chaotic phases for scattering potential and for uni-

form distribution of impurity ions throughout the volume of an SL or QW. If electrons are scattered elastically by acoustic phonons, calculation of the relaxation time in the approximation of a bulk phonon spectrum for the probability of scattering (see Appendix 1) yields a unified formula for both the transverse and the longitudinal relaxation:

$$\tau_\perp(\varepsilon) = \tau_\parallel(\varepsilon) = \tau = \frac{2}{3}\frac{ac_L\hbar^3}{m^* D_c^2 k_0 T} = 2\sqrt{\frac{\varepsilon}{E_a}}\tau_{AC}. \quad (19)$$

Here, τ_{AC} is the time of relaxation of electrons via the deformation potential of acoustic phonons in the approximation of elastic scattering in a bulk semiconductor [9]. According to formula (19) and in the context of the approximations used, the time of relaxation via acoustic phonons in an SL with a quasi-2D electron gas is isotropic, independent of energy, and directly proportional to the QW width, which is consistent with the data reported in previous publications [11].

3. AN ANALYSIS OF THE TEMPERATURE DEPENDENCE OF MOBILITY

The longitudinal and transverse mobilities of electrons in an SL were calculated with the following formulas used in estimating the current density in a quasi-2D electron gas with allowance made for a nonequilibrium addition to the distribution function given by (4):

$$\mu_\perp = e\langle\tau_\perp\rangle/m_\perp, \quad \mu_\parallel = e\langle\tau_\parallel\rangle/\langle m_\parallel\rangle. \quad (20)$$

Here, $\langle\tau_\perp\rangle$, $\langle\tau_\parallel\rangle$, and $\langle m_\parallel\rangle$ are the energy-averaged functions of the effective times for the transverse and longitudinal relaxation and also of the longitudinal effective mass for electrons in the main miniband; i.e.,

$$\langle\tau_\perp\rangle = \frac{\rho_c}{n}\int_0^\infty\left(-\frac{\partial f_0}{\partial\varepsilon}\right)\tau_\perp(\varepsilon)\varepsilon d\varepsilon,$$

$$\langle\tau_\parallel\rangle = [1-\exp(-n/N_c)]^{-1}\int_0^\infty\left(-\frac{\partial f_0}{\partial\varepsilon}\right)\tau_\parallel(\varepsilon)\varepsilon d\varepsilon, \quad (21)$$

$$\frac{1}{\langle m_\parallel\rangle} = \frac{\rho_c\Delta}{4m_\parallel n}[1-\exp(-n/N_c)], \quad (22)$$

where $\rho_c = m_\perp/(\pi d\hbar^2)$ is the 2D density of states in the lower conduction miniband, $N_c = k_0T\rho_c$ is the effective density of states, and $m_\parallel = 2\hbar^2/(\Delta d^2)$ is the longitudinal effective mass at the miniband bottom. According to formula (21), $\langle\tau_\parallel\rangle = \tau_\parallel$ if the longitudinal effective relaxation time is independent of energy. If the electron gas is nondegenerate ($n \ll N_c$), the expression for the energy-averaged longitudinal effective mass can be simplified and written as

$$\frac{1}{\langle m_\parallel\rangle} = \frac{\Delta}{k_0T}\frac{1}{m_\parallel}. \quad (23)$$

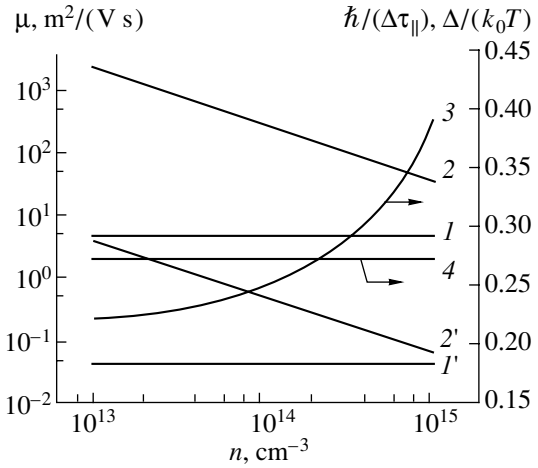

Fig. 2. Dependences of the longitudinal and transverse mobilities of electrons in a superlattice on the electron concentration for a = 8 nm, b = 5 nm, and T = 77 K: (*1*) corresponds to $\mu_\perp^{PO+AC}$; (*2*) is for $\mu_\perp^{ion}$; (*1'*), for $\mu_\parallel^{PO+AC}$; (*2'*), for $\mu_\parallel^{ion}$; (*3*), for $\hbar/(\Delta\tau_\parallel)$; and (*4*), for $\Delta/(k_0T)$.

In this study, dependences of the longitudinal and transverse mobilities on temperature and impurity-ion concentration were calculated for an SL with a quasi-2D electron gas. The mobility was calculated with allowance made for mixed scattering by the PO and acoustic phonons and by impurity ions, whose concentration was assumed to be equal to the electron concentration. The mobility was calculated using the above formulas for a compositional n-type GaAs/$Al_{0.36}Ga_{0.64}$Ad SL with the parameters a = 8 nm and b = 5 nm. The following values for GaAs parameters were used in calculations of the mobility and the probability of scattering [12]:

$$m_\perp = 0.067m_0, \quad \hbar\omega = 0.037 \text{ meV}, \quad \varepsilon_s = 12.7,$$

$$\varepsilon_\infty = 10.7, \quad c_L = 14.4\times10^{10} \text{ H/m}^2 \text{ and } D_c = 17.5 \text{ eV}.$$

The designations of the parameters are clarified in Appendix 1. According to the energy-spectrum calculations, which were performed by the method outlined elsewhere [13], the SL under consideration incorporates two conduction minibands in the QW at 77 K and can be used as a photodetector of infrared radiation with a wavelength of 9 μm. It was found that the width of the lower miniband Δ = 1.8 meV at 77 K, which is close to Δ obtained using formula (7) with the following values for the parameters:

$$m_a = 0.067m_0, \quad m_b = 0.097m_0,$$

$$V = 283 \text{ meV}, \quad E_0 = 43 \text{ meV}.$$

The calculated dependences of the longitudinal and transverse mobilities on the electron concentration at T = 77 K for the SL under consideration are shown in Fig. 2. The electron-concentration dependences of dimensionless quantities $\hbar/(\langle\tau_\parallel\rangle\Delta)$ and $\Delta/(k_0T)$ are also

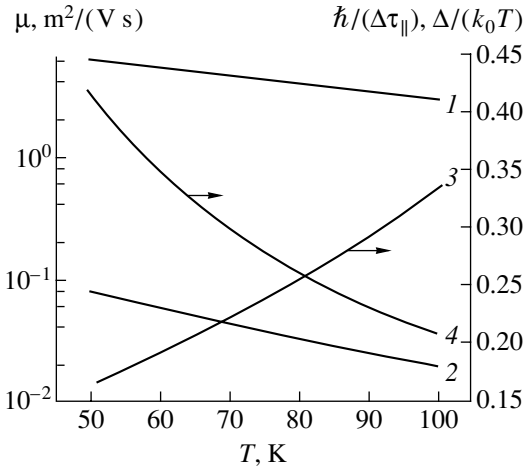

Fig. 3. Temperature dependences of electron mobilities in a superlattice for $a = 8$ nm, $b = 5$ nm, and $N_I = 10^{14}$ cm^{-3}: (*1*) is for $\mu_\perp$; (*2*), for $\mu_\parallel$; (*3*), for $\hbar/(\Delta\tau_\parallel)$; and (*4*), for $\Delta/(k_0T)$.

shown in Fig. 2; according to condition (1), the values of these quantities should be much smaller than unity. It follows from the plots that the condition for applicability of the Boltzmann equation (1) is approximately satisfied for the SL under consideration in the region of fields $E < 300$ V/cm if $n < 10^{15}$ cm^{-3}. The main mechanism of scattering in the specified range of electron concentrations is scattering by phonons. The value of mobility controlled by the lattice vibrations is almost independent of electron concentration in the range under consideration ($\mu_\perp \approx 4.4 \times 10^4$ cm^2/(V s) and $\mu_\parallel \approx 4.0 \times 10^2$ cm^2/(V s)) and is mainly governed by scattering by acoustic (AC) phonons: $\mu_\perp^{AC} \approx 4.7 \times 10^4$ cm^2/(V s) and $\mu_\parallel^{AC} \approx 4.2 \times 10^2$ cm^2/(V s). The partial values of mobilities controlled by scattering by the PO phonons are equal to $\mu_\perp^{PO} \approx 9.5 \times 10^5$ cm^2/(V s) and $\mu_\parallel^{PO} \approx 7.5 \times 10^3$ cm^2/(V s). The value of the transverse electron mobility governed by scattering by AC phonons in an SL is significantly different from the mobility μ_V calculated under the same conditions [8] for the bulk GaAs crystal: $\mu_V^{PO+AC} \approx 1.5 \times 10^5$, $\mu_V^{AC} \approx 1.9 \times 10^5$, and $\mu_V^{PO} \approx 1.0 \times 10^6$ cm^2/(V s). The low longitudinal mobility in the SL is caused by a large longitudinal effective mass ($\langle m_\parallel \rangle = 7.4 m_0$), whereas the mean values of the longitudinal and transverse effective relaxation times for scattering by lattice vibrations are close to each other ($\langle\tau_\perp\rangle \approx \langle\tau_\parallel\rangle = 1.7$ ps).

Figure 3 displays the temperature dependences of electron mobilities in an SL; the dependences were calculated for $N_I = 10^{14}$ cm^{-3}. It follows from the temperature dependences of quantities $\hbar(\langle\tau_\parallel\rangle\Delta)$ and $\Delta/(k_0T)$ also shown in Fig. 3 that condition (1) is approximately satisfied only within a small neighborhood of the liquid-nitrogen temperature. The temperature dependences of partial mobilities are shown in Fig. 4. As might be expected, in the specified temperature range where the condition $k_0T < \hbar\omega = 37$ meV is satisfied, the temperature dependence of the transverse and longitudinal mobilities controlled by scattering by the PO phonons is adequately described by the low-temperature relaxation time. For a nondegenerate electron gas, formulas (15) and (23) can be used to derive the following expressions for the low-temperature mobility in an SL if scattering by the PO phonons is dominant:

$$\mu_\perp^{PO} = \frac{6\sqrt{2}\pi\hbar^{3/2}\varepsilon_0\varepsilon^*\chi(\theta)e^{\hbar\omega/k_0T}}{em^*\sqrt{m^*\omega}},$$
$$\mu_\parallel^{PO} = \frac{3\pi\varepsilon_0\varepsilon^*\Delta^2 d^2\chi(\theta)e^{\hbar\omega/k_0T}}{2\sqrt{2}e\sqrt{m^*\hbar\omega}k_0T}. \quad (24)$$

In the temperature range under consideration, the mobility $\mu_\perp^{PO}$ is almost equal to the mobility calculated for the bulk GaAs crystal. If scattering by impurity ions is predominant, the transverse mobility in the SL (curve *3*') is close in its value and temperature dependence to the mobility in the bulk GaAs crystal (curve *3*), whereas the longitudinal mobility (curve *3*") in the SL differs significantly (in value and temperature dependence) from the corresponding mobility in the bulk GaAs crystal:

$$\mu_\perp^{ion} \propto \langle\tau_\perp\rangle \propto T^{1.4}, \quad \mu_\parallel^{ion} \propto \langle\tau_\parallel\rangle/T \propto T^{-0.5},$$
$$\mu_V^{ion} \propto \langle\tau\rangle \propto T^{1.3}. \quad (25)$$

The calculated values of the exponents in the temperature dependence of μ_i^{ion} differ appreciably from those predicted by the theory for a 2D electron gas ($\mu_\perp^{ion} \propto \langle\tau_\perp\rangle \propto T^2$, $\mu_\parallel^{ion} \propto \langle\tau_\parallel\rangle/T \propto T$ [10]), in which case the scattering-probability dispersion in respect to the wave longitudinal vector is disregarded.

In view of expressions (19) and (23), the mobility governed by the scattering by acoustic vibrations was calculated using the following formulas:

$$\mu_\perp^{AC} = \frac{2e\hbar^3 c_L a}{3(m^*D_c)^2 k_0T}, \quad \mu_\parallel^{AC} = \frac{e\hbar c_L a d^2\Delta^2}{12m^*(D_c k_0T)^2}. \quad (26)$$

It follows from Fig. 4 that, in contrast to the scattering by the PO phonons and impurity ions, the transverse component of mobility controlled by scattering by the AC phonons (curve *1*') is much smaller than its value in the bulk material (curve *1*). In view of (26) and the well known formula for the mobility μ_V^{AC} in a nondegenerate electron gas [9], we have

$$\frac{\mu_V^{AC}}{\mu_\perp^{AC}} = \sqrt{\frac{4E_a}{\pi k_0T}}. \quad (27)$$

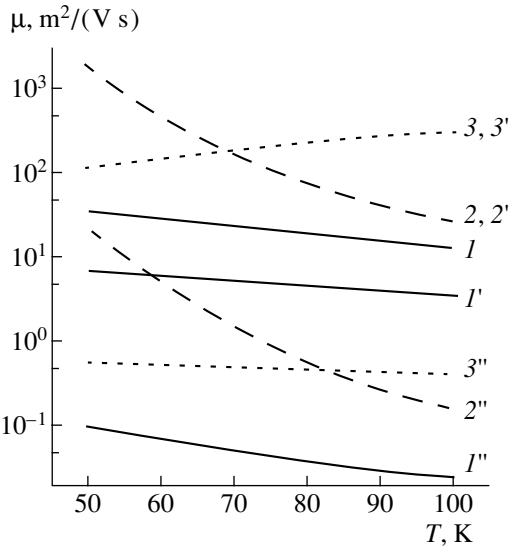

Fig. 4. Temperature dependences of partial electron mobilities in the bulk GaAs crystal (μ_V) and the superlattice under consideration ($\mu_\perp$, $\mu_\parallel$) for $N_I = 10^{14}$ cm^{-3}: (*1*) is for μ_V^{AC}; (*1*'), for $\mu_\perp^{AC}$; (*1*"), for $\mu_\parallel^{AC}$; (*2*), for μ_V^{PO}; (*2*'), for $\mu_\perp^{PO}$; (*2*"), for $\mu_\parallel^{PO}$; (*3*), for μ_V^{ion}; (*3*'), for $\mu_\perp^{ion}$; and (*3*"), for $\mu_\parallel^{ion}$.

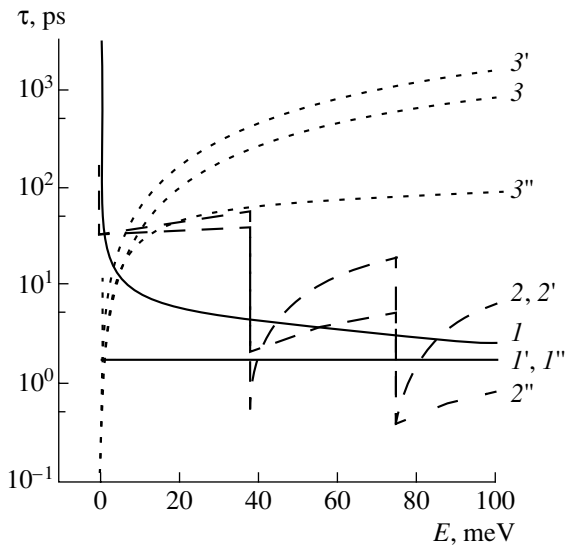

Fig. 5. Energy dependences of partial relaxation times of electrons in the superlattice under consideration and in the bulk GaAs crystal at $T = 77$ K and $N_I = 10^{14}$ cm^{-3}: (*1*) is for τ_V^{AC}; (*1*'), for $\tau_\perp^{AC}$; (*1*"), for $\tau_\parallel^{AC}$; (*2*), for τ_V^{PO}; (*2*'), for $\tau_\perp^{PO}$; (*2*"), for $\tau_\parallel^{PO}$; (*3*), for τ_V^{ion}; (*3*'), for $\tau_\perp^{ion}$; and (*3*"), for $\tau_\parallel^{ion}$.

According to this formula, the scattering of quasi-2D electrons by the AC phonons in an SL in the vicinity of the liquid-nitrogen temperature is approximately five times more intense than in the bulk material.

The energy dependences of the relaxation time for scattering by impurity ions and of the effective relaxation time for scattering by phonons at $T = 77$ K and $N_I = 10^{14}$ cm^{-3} are shown in Fig. 5. It can be seen that the effective time of electron relaxation via the PO phonons in an SL is, as in the bulk semiconductors [8], an oscillating function, with the oscillation period being equal to the energy of a longitudinal optical phonon. The transverse effective relaxation time (curve *2*') is close to the corresponding value in the bulk material (curve *2*), whereas this agreement is observed only for low energies in the case of longitudinal relaxation (curve *2*"). The energy dependence of the time of relaxation via the impurity ions in the temperature range under consideration almost obeys, as in the bulk semiconductors, the power law, which, according to (25), brings about a power-law dependence of mobility on temperature. The transverse relaxation time (curve *3*') at a given energy is somewhat longer than that in the bulk material (curve *3*), whereas the longitudinal relaxation time (curve *3*") is much shorter than in the bulk, which gives rise to a noticeable anisotropy of the relaxation time in an SL if electrons are scattered by the impurity ions ($\langle\tau_\perp^{ion}\rangle/\langle\tau_\parallel^{ion}\rangle \approx 5$). As might be expected, if electrons are scattered by the AC phonons, a significant distinction between the relaxation times in an SL and in the bulk material is observed in the low-energy region, where inelasticity of the scattering by the AC phonons should be taken into account [3].

4. CONCLUSION

The above numerical analysis shows that the Boltzmann equation can be used only in approximate calculations of the linear conductivity of quasi-2D electrons in the SL under consideration in the region of liquid-nitrogen temperature for electron concentrations lower than 10^{15} cm^{-3}, which is related to an increased role of scattering by acoustic phonons compared to what is observed in a bulk semiconductor. In the elastic-scattering approximation, the time of relaxation via acoustic phonons is energy-independent and isotropic. The scattering by the polar optical phonons in the region of liquid-nitrogen temperature can be described, as in the case of the bulk semiconductors, using the longitudinal and transverse relaxation times, which are independent of the electron energy. These relaxation times are close to those in the bulk semiconductor which composes the quantum well. For scattering by the impurity ions, the transverse times of electron relaxation in an SL and in the bulk material of the quantum well are almost the same, whereas the longitudinal relaxation time is much shorter than that in the bulk material.

APPENDIX 1

In the Born approximation, the probability of scattering of an electron, which resides in an SL with volume V, by the potential $V(\mathbf{r})e^{\pm i\omega t}$ from the state with the envelope function in the form of the Bloch function $\Psi_{\mathbf{k}}(\mathbf{r}) = (1/\sqrt{V})e^{i\mathbf{kr}}u_{k_z}(z)$ can be expressed as

$$w^{\pm}_{\mathbf{kk'}} = \frac{2\pi}{\hbar}|V_{\mathbf{k'k}}|^2\delta(\varepsilon(\mathbf{k'}) - \varepsilon(\mathbf{k}) \pm \hbar\omega), \qquad \text{(A1.1)}$$

where

$$V_{\mathbf{k'k}} = \frac{1}{V}\sum_n S_n(k'_z, k_z)V_n(\mathbf{k'} - \mathbf{k}), \qquad \text{(A1.2)}$$

$$S_n(k'_z, k_z) = \frac{1}{d}\int_{-d/2}^{d/2} e^{i2\pi nz/d}u^*_{k'_z}(z)u_{k_z}(z)dz, \qquad \text{(A1.3)}$$

$$V_n(\mathbf{q}) = \int_V V(\mathbf{r})e^{-i(\mathbf{qr} + 2\pi nz/d)}d\mathbf{r}. \qquad \text{(A1.4)}$$

The integral in (A1.3) for the envelope function of electrons in the lower miniband represented as the Bloch sum of the functions corresponding to the ground state of an isolated, infinitely deep QW has the following analytical representation:

$$S_n(k'_z, k_z) = S(q_{nz}) = \frac{\pi^2\sin(aq_{nz}/2)}{(aq_{nz}/2)[\pi^2 - (aq_{nz}/2)^2]}. \qquad \text{(A1.5)}$$

Here, $q_{nz} = k'_z - k_z + 2\pi n/d$.

For scattering of electrons by the screened long-range potential of the longitudinal polar optical lattice phonons, we obtain the following expression in the phonon-spectrum approximation for a homogeneous III–V semiconductor:

$$|V_n(\mathbf{q})| = \sqrt{\frac{\hbar\left(N_\omega + \frac{1}{2} \pm \frac{1}{2}\right)}{2\varepsilon_0\omega V}}\frac{eP\sqrt{q_\perp^2 + q_{nz}^2}}{(q_\perp^2 + q_{nz}^2 + \alpha_\infty^2)}. \qquad \text{(A1.6)}$$

Here, $\hbar\omega$ and P are the energy and strength for the oscillator corresponding to the longitudinal polar optical phonon; N_ω is the thermodynamically equilibrium number of phonons, which have the frequency ω and are described by the Bose–Einstein function; and α_∞ is the Debye screening coefficient for a high-frequency electric field. In view of (A1.6) and the law of conservation of quasi-momentum, formula (A1.1) is reduced to the expression given by (11).

According to the Lyddane–Sachs–Teller formula, we have the following expression in the case of a QW represented by the layer of a III–V semiconductor:

$$\left(\frac{P}{\omega}\right)^2 = \frac{1}{\varepsilon^*} = \frac{1}{\varepsilon_\infty} - \frac{1}{\varepsilon_s}. \qquad \text{(A1.7)}$$

Here, ε^*, ε_s, and ε_∞ are the reduced, static, and high-frequency dielectric constants. In the approximation of a quasi-2D electron gas with the electron concentration n, the Debye screening coefficient of a high-frequency electric field in an SL is equal to

$$\alpha_\infty^2 = \frac{e^2}{\varepsilon_0\varepsilon_\infty}\frac{\partial n}{\partial\xi} = \frac{e^2m^*}{\pi\varepsilon_0\varepsilon_\infty\hbar^2 d}[1 + \exp(-\xi/k_0T)]^{-1}, \qquad \text{(A1.8)}$$

where ξ is the chemical potential and ε_0 is the dielectric constant of free space. For a nondegenerate electron gas, α_∞ depends linearly on the electron concentration (as is also the case for bulk semiconductors) and is independent of the SL period; i.e.,

$$\alpha_\infty^2 = \frac{e^2n}{\varepsilon_0\varepsilon_\infty k_0T}. \qquad \text{(A1.9)}$$

In the case of scattering by impurity ions distributed uniformly over the entire SL or over the QW, the scattering probability is given by the following expression in the chaotic-phase approximation and in view of formulas (A1.1)–(A1.5):

$$w_{\mathbf{kk'}} = \frac{2\pi e^4Z^2N_I}{\hbar\varepsilon_0^2\varepsilon_s^2V} \times\sum_n\frac{S^2(q_{nz})}{(q_\perp^2 + q_{nz}^2 + \alpha_s^2)^2}\delta(\varepsilon(\mathbf{k'}) - \varepsilon(\mathbf{k})). \qquad \text{(A1.10)}$$

Here, N_I is the ion concentration, eZ is the ion charge, and $\alpha_s = \sqrt{\varepsilon_\infty/\varepsilon_s}\,\alpha_\infty$ is the Debye screening coefficient for a static electric field.

In the approximation of the phonon spectrum of the bulk material in the QW and in view of formulas (A1.1)–(A1.5), the probability of elastic scattering of electrons

by the deformation potential of acoustic phonons in an SL is given by

$$w_{\mathbf{kk}'} = \frac{2\pi k_0 T D_c^2}{\hbar c_L V}\sum_n S^2(q_{nz})\delta(\varepsilon(\mathbf{k}') - \varepsilon(\mathbf{k})), \quad \text{(A1.11)}$$

where $c_L = c_{11} + \frac{2}{5}(c_{12} + 2c_{44} - c_{11})$ is the mean value of the modulus of elasticity for longitudinal acoustic vibrations, and D_c is the deformation-potential constant at the conduction-band edge. This formula was derived taking into account the integration over the phonon wave vector.

APPENDIX 2

The notation used in the Appendix is the same as in the main text of this paper; i.e.,

$$\tau_0^{-1}(\varepsilon) = G_0^+(\varepsilon) + G_0^-(\varepsilon), \quad \text{(A2.1)}$$

$$G_0^\pm(\varepsilon) = C\left[N_\omega + \frac{1}{2} \mp \frac{1}{2} \pm f_0(\varepsilon \pm \hbar\omega)\right]S_0^\pm(\varepsilon),$$
$$S_0^\pm(\varepsilon) = \int_0^\infty U^2(x)\varphi_0(a_\pm, b_\pm, x)dx, \quad \text{(A2.2)}$$

$$G_i^\pm(\varepsilon) = C\left[N_\omega + \frac{1}{2} \pm \frac{1}{2} \mp f_0(\varepsilon)\right]\frac{f_0'(\varepsilon \pm \hbar\omega)}{f_0'(\varepsilon)}S_i^\pm(\varepsilon), \quad \text{(A2.3)}$$

$$S_\perp^\pm(\varepsilon) = \int_0^\infty U^2(x) \times\left[\left(1 \pm \frac{\hbar\omega}{2\varepsilon}\right)\varphi_0(a_\pm, b_\pm, x) - \frac{\varphi(a_\pm, b_\pm, x)}{2\varepsilon}\right]dx, \quad \text{(A2.4)}$$

$$S_\parallel^\pm(\varepsilon) = \int_0^\infty U^2(x)\varphi_0(a_\pm, b_\pm, x)\cos(\eta x)dx, \quad \text{(A2.5)}$$

$$U(x) = \frac{\pi^2\sin(\beta x/2)}{(\beta x/2)[\pi^2 - (\beta x/2)^2]}, \quad \text{(A2.6)}$$

$$\varphi_0(a, b, x) = \frac{\pi}{\sqrt{AB}}\left[1 - \frac{\gamma^2(A+B)}{2AB}\right],$$
$$\varphi(a, b, x) = \pi\left[1 - \frac{x^2 + 2\gamma^2}{\sqrt{AB}} + \frac{\gamma^2(x^2+\gamma^2)(A+B)}{2AB\sqrt{AB}}\right], \quad \text{(A2.7)}$$

where

$$A = a^2 + x^2 + \gamma^2, \quad B = b^2 + x^2 + \gamma^2,$$

$$\gamma = \frac{\hbar}{\sqrt{2m^*}}\alpha_\infty, \quad \beta = \frac{\sqrt{2m^*}}{\hbar}a, \quad \eta = \frac{\sqrt{2m^*}}{\hbar}d,$$

$$C = \frac{\sqrt{m^*}e^2\omega}{2\sqrt{2}\pi^2\varepsilon_0\varepsilon^*\hbar},$$

$$b_\pm = \sqrt{\varepsilon} + \sqrt{\varepsilon \pm \hbar\omega}, \quad a_\pm = \sqrt{\varepsilon} - \sqrt{\varepsilon \pm \hbar\omega}.$$

The functions with the index (+) are related to the photon absorption and, therefore, are defined for $\varepsilon \geq 0$, whereas the functions with the index (–) are related to the photon emission and, therefore, vanish for $\varepsilon < \hbar\omega$.

REFERENCES

1. A. A. Dremin, V. B. Timofeev, D. Birkedal, and J. M. Hvam, Phys. Status Solidi A **164**, 557 (1997).
2. T. P. Pearsall, A. DiVergilio, G. Pierre, *et al.*, Appl. Phys. Lett. **72**, 76 (1998).
3. Yu. V. Ivanov, M. V. Vedernikov, and Yu. I. Ravich, Pis'ma Zh. Éksp. Teor. Fiz. **69**, 290 (1999) [JETP Lett. **69**, 317 (1999)].
4. A. Ya. Shik, Fiz. Tekh. Poluprovodn. (Leningrad) **8**, 1841 (1974) [Sov. Phys. Semicond. **8**, 1195 (1974)].
5. B. F. Levin, K. K. Choi, C. G. Bethea, *et al.*, Appl. Phys. Lett. **50**, 1092 (1987); Appl. Phys. Lett. **50**, 1814 (1987).
6. I. Dharssi and P. N. Butcher, J. Phys.: Condens. Matter **2**, 119 (1990).
7. G. J. Warren and P. N. Butcher, Semicond. Sci. Technol. **1**, 133 (1986).
8. S. I. Borisenko, Fiz. Tekh. Poluprovodn. (St. Petersburg) **35**, 313 (2001) [Semiconductors **35**, 298 (2001)].
9. A. I. Anselm, *Introduction to Semiconductor Theory* (Nauka, Moscow, 1978; Prentice-Hall, Englewood Cliffs, 1981).
10. A. Ya. Shik, *Two-Dimensional Electron Systems: Textbook* (Sankt-Peterb. Gos. Tekh. Univ., St. Petersburg, 1993), Chap. 5, p. 33.
11. B. K. Ridley, J. Phys. C **15**, 5899 (1982).
12. *Landolt-Börnstein: Numerical Data and Functional Relationships in Science and Technology, New Series* (Springer-Verlag, Berlin, 1987), Group III, Vol. 22a.
13. S. I. Borisenko and G. F. Karavaev, Fiz. Tekh. Poluprovodn. (St. Petersburg) **32**, 607 (1998) [Semiconductors **32**, 544 (1998)].

Translated by A. Spitsyn

Semiconductors, Vol. 36, No. 7, 2002, pp. 816–820. Translated from Fizika i Tekhnika Poluprovodnikov, Vol. 36, No. 7, 2002, pp. 869–873.

LOW-DIMENSIONAL SYSTEMS

GaAs in GaSb: Strained Nanostructures for Mid-Infrared Optoelectronics

V. A. Solov'ev*^, A. A. Toropov*, B. Ya. Meltser*, Ya. A. Terent'ev*, R. N. Kyutt*, A. A. Sitnikova*, A. N. Semenov, S. V. Ivanov*, Motlan***, E. M. Goldys***, and P. S. Kop'ev***

** Ioffe Physicotechnical Institute, Russian Academy of Sciences, Politekhnicheskaya ul. 26, St. Petersburg, 194021 Russia*

^ e-mail: vasol@beam.ioffe.rssi.ru

*** St. Petersburg State Electrotechnical University, St. Petersburg, 197376 Russia*

**** Division of Information and Communication Sciences, Macquarie University, North Ryde, NSW 2109, Australia*

Submitted December 11, 2001; accepted for publication December 18, 2001

Abstract—Molecular beam epitaxy was used for the first time to grow novel GaAs/GaSb heterostructures with ultrathin (0.8–3 monolayers) GaAs layers embedded in GaSb. These structures were studied by X-ray diffraction, transmission electron microscopy, and photoluminescence. By contrast to known structures with self-assembled quantum dots, GaAs layers in GaAs/GaSb structures are subject to elastic tensile stresses due to 7% lattice mismatch. The structures exhibit intense photoluminescence in the 2 μm region at low temperatures. Quantum-dimensional islands are formed in the structure at a nominal GaAs layer thickness exceeding 1.5 monolayers. The band alignment of the structures is of type II. © *2002 MAIK "Nauka/Interperiodica"*.

1. INTRODUCTION

The considerable interest in quantum dot (QD) heterostructures is motivated, on the one hand, by their unique fundamental properties and, on the other, by the possibility of their application in optoelectronics, in particular, in the design of low-threshold semiconductor lasers [1]. The processes of QD self-organization have been fairly well studied for many semiconductor heterocouples with a large (up to 7%) lattice mismatch, such as InAs/GaAs [2], (Ga,In,Al)Sb/GaAs [3, 4], InAs/InP [5], and InP/InGaP [6]. In different systems, the band structure alignment in heterojunctions can either be type I [2, 5, 6] or type II [3, 4]. The common feature of the listed heterostructures is a thin layer of a narrow-gap semiconductor embedded in the matrix of a relatively wide-gap material with a smaller lattice parameter and subjected to compressive stress. The lasing wavelength of lasers based on such materials cannot exceed the wavelength corresponding to the absorption edge of the wide-gap host (GaAs or InGaP), and it is always below 1.55 μm. Therefore, the extension of the lasing wavelength of QD heterostructures to the region of 2 μm seems to be a further challenge. It is worth noting that considerable suppression of the Auger recombination channels in type II QD heterostructures offers good prospects for their application in lasers of the mid-IR (2–5 μm) range, where the Auger processes impose substantial limitations on conventional heterolasers [7]. Here, we present a pioneering report on the fabrication of a novel type of lattice-mismatched GaAs/GaSb type-II heterostructures characterized by intense photoluminescence (PL) in the 1.7–2.3 μm spectral range.

2. SAMPLES

Ultrathin GaAs layers were grown in a GaSb host by molecular beam epitaxy (MBE) in the pseudomorphic mode. The thickness of the GaAs layers varied from 1 to 3 monolayers (ML); i.e., it was in the range of thicknesses typical of the self-assembled QD formation related to a 7% mismatch between the GaAs and GaSb lattice parameters [3]. In contrast with the QD systems studied previously, in our case the layer of a relatively wide-gap semiconductor (GaAs, the lattice constant a = 5.6532 Å, the band gap E_g = 1.52 eV) is embedded in the host of a narrow-gap semiconductor (GaSb, a = 6.0959 Å, E_g = 0.81 eV) and it is subject to tensile stress. Therefore, the proposed structures can be used as model structures for experimental investigations of the MBE growth of thin layers with tensile stresses, the more so as the formation of self-assembled QDs in the inverted system (a thin GaSb layer in the GaAs matrix) has been thoroughly studied [3, 4]. We should also note that we know of only one recent study where the luminescent properties of similar structures were discussed and where intense luminescence from monolayer-thick AlAs layers in AlSb was observed [8].

1063-7826/02/3607-0816$22.00

Samples containing a single GaAs layer in GaSb or GaAs/GaSb superlattices (SLs) were grown on (001) GaSb substrates at a temperature of 520°C. A Riber-32 MBE system was equipped with conventional effusion cells providing Ga, Al, and As_4 molecular beams, while the Sb_2 flux was produced by an RB-075-Sb cracking source. The structures included a 0.5-μm-thick buffer layer and a 0.3-μm GaSb layer which were confined on both sides by thin (30 nm) $Al_{0.5}Ga_{0.5}Sb$ barriers. Either a GaAs single layer (of varied thickness) or an SL was embedded in the center of the GaSb layer. During all the stages of growth, the state of the sample surface was monitored using a reflection high-energy electron diffraction (RHEED) system. During the growth of ultrathin GaAs layers, the RHEED demonstrated a (2×4) surface reconstruction pattern corresponding to an As-stabilized surface. To exclude the intermixture of As and Sb fluxes, 10-sec interruptions were introduced before and after the growing of GaAs layers. The time intervals of GaAs growth varied from 2 to 5 s for different structures, which corresponded to layer thicknesses of 1.2–3 ML. Several structures were grown without the rotation of the substrate holder, which provided a smooth variation of the GaAs layer thickness over the structure area. A ten-period SL containing 1.2-ML-thick GaAs and 4-nm-thick GaSb layers was grown in the same conditions as the structures with single GaAs layers.

3. STRUCTURAL AND OPTICAL STUDIES

The structure with the SL was studied by high-resolution X-ray diffraction (XRD). Figure 1 presents a (θ–2θ)-rocking curve measured with (004) reflection. Zero-order reflection from the SL, as well as higher order satellites, are discernible. The SL period and the nominal thickness of GaAs layers evaluated from the position of the peaks were 4.3 nm and 1.2 ML, respectively, which coincides with the values stipulated by the technology. Moreover, the fitting of the calculated rocking curve to the experimental one (Fig. 1) allows for the evaluation of the average increase in the layer thickness along the growth direction, which arises from the interdiffusion or segregation of Sb in the course of MBE [9]. The theoretical modeling of the rocking curves for their fitting was done in terms of the semikinematic approximation described previously [10]. Thus, the average broadening of the GaAs layer in the structure under study was determined as 4–5 ML. The obtained results allow us to exclude the formation of quantum wells with ideal abrupt boundaries, as well as an array of three-dimensional (3D) QDs. Rather, the X-ray diffraction data imply that the SL contains layers of ternary GaAsSb solid solution, which is virtually nonuniform over the area, owing to nanometer fluctuations in the composition or thickness of these layers.

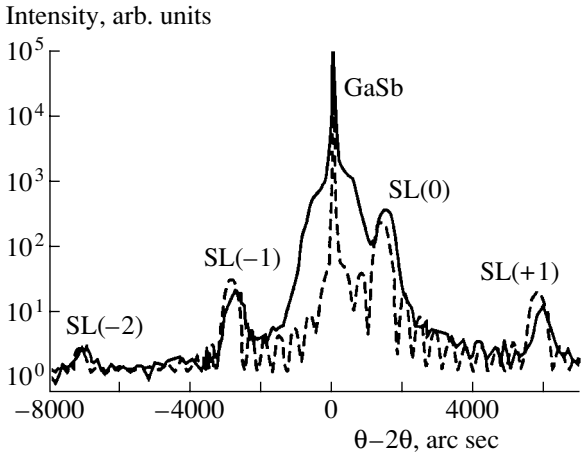

Fig. 1. Double-crystal (θ–2θ) rocking curves near the GaSb (004) reflection for a structure with a 10-period GaAs(1.2 ML)/GaSb(4 nm) superlattice: (solid line) experimental, (dashed line) calculated. The calculations were performed assuming the Gaussian distribution of As atoms in the growth direction with the distribution half-width of 4.5 ML.

Several structures with single GaAs layers were studied by cross-sectional transmission electron microscopy (TEM) using a Philips EM-420 system with 100 kV accelerating voltage. It is known that the diffraction reflections (200) are sensitive to variation of the chemical composition in the materials with an fcc lattice and they can be efficiently used to visualize the spatial fluctuations of the composition [11]. Figure 2 shows dark-field TEM images of samples containing GaAs layers of various thicknesses in the GaSb host. All the images were obtained in similar conditions. GaAs layers are represented in all the images by dark lines. The transformation of the morphology of the GaAs insertion with increasing thickness is clearly seen in Fig. 2. The image of an insertion less than 0.8 ML thick looks like a dark line without any noticeable traces of clusterization (Fig. 2a). With the nominal thickness of the GaAs layer increasing, two-dimensional (2D) islands surrounded by fields with rather strong stresses appear in the TEM image (Fig. 2b). With a further increase in the GaAs-insertion thickness, the size of these islands increases markedly in the growth direction (this is shown by the increase of a dark halo near the islands), which indicates the onset of the formation of 3D QDs when the insertion thickness ~1.5 ML (Fig. 2c). Finally, extended defects are seen near some of the islands (Fig. 2d); this indicates the onset of relaxation of elastic stresses in the structure with an ~2-ML-thick GaAs layer.

An intensive PL of the structures under study was observed at low temperatures. The PL was studied in the temperature range of 8–300 K in a closed-cycle

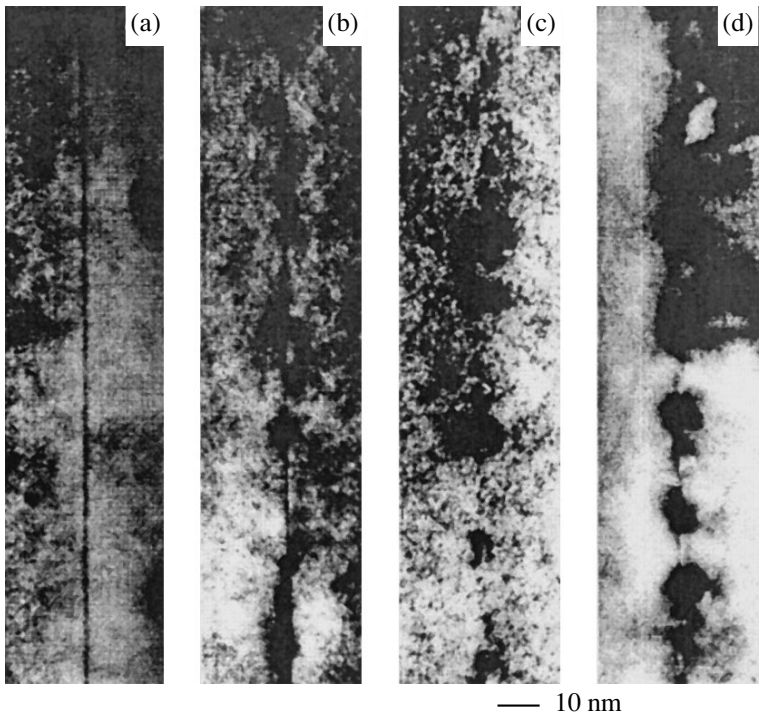

Fig. 2. Cross-sectional TEM images of structures with a single GaAs layer. Nominal thickness: (a) 0.8, (b) 1.2, (c) 1.5, and (d) 2 ML.

helium or liquid-nitrogen cryostat. PL was excited using CW injection lasers with a radiation wavelength of 0.8 and 1.3 μm.

Figure 3 presents PL spectra for structures with single GaAs layers of various thicknesses recorded at 80 K at a relatively low excitation level of ~ 1 W cm^{-2}. Two relatively narrow short-wavelength peaks observed in all the spectra represent the PL from the GaSb buffer layer. One of these, with a photon energy of ~ 0.8 eV, is related to interband radiative transitions, and the peak with the photon energy of 0.775 eV corresponds to

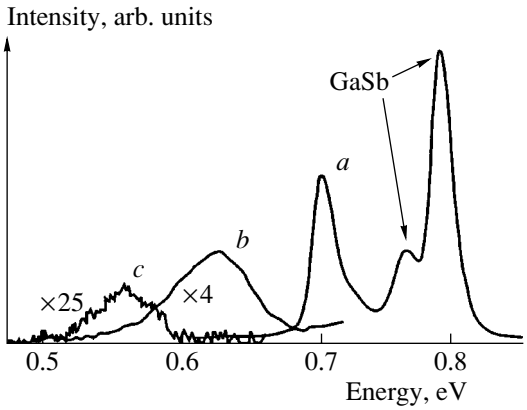

Fig. 3. PL spectra of structures with a single GaAs layer. Nominal thickness: (*a*) 1.2, (*b*) 1.8, and (*c*) 3 ML. Temperature 80 K, low excitation level.

transitions between a donor and a deep intrinsic acceptor in GaSb. One more peak is observed in the spectra, with its position correlating with the thickness of the GaAs insertion. The good agreement between the PL and TEM data should be noted. When the thickness of an insertion increases from 1.2 to 3.5 ML, the peak shifts to longer wavelengths, from 1.7 to 2.3 μm. Simultaneously, the peak broadens and its maximal intensity decreases drastically. We attribute the observed broadening of the PL peak to fluctuations in QD size, which are observed in TEM for the samples with a GaAs thickness larger than 1.5 ML (Fig. 2c). The integrated intensity of the PL peak varies only slightly when the nominal thickness of the GaAs insertion is below ~2 ML and then sharply decreases with a further increase in the thickness. This is probably due to the increasing density of dislocations (see Fig. 2d), which are the effective centers of nonradiative recombination.

It is necessary to note that, in all the structures studied, the energy of the emitted photon is significantly lower than the GaSb band gap, which indicates that GaAs/GaSb heterojunctions are of type II. We estimated the band offsets at the interface using the van der Walle model [12], which made it possible to consider the effect of elastic stresses on the band structure. Figure 4 presents the calculated results for the case of pseudomorphic 2D growth and possible optical transitions in the structure under study. Strong tensile stresses induced by a 7% mismatch between the GaAs and GaSb lattices reduce the GaAs band gap to ~0.4 eV,

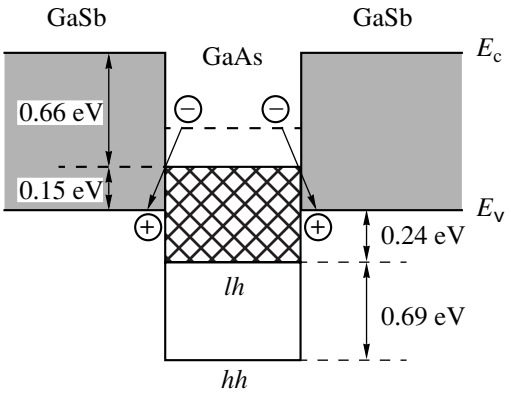

Fig. 4. Energy-band diagram of a GaAs/GaSb QW structure and possible optical transitions. *lh*, *hh*: light and heavy holes.

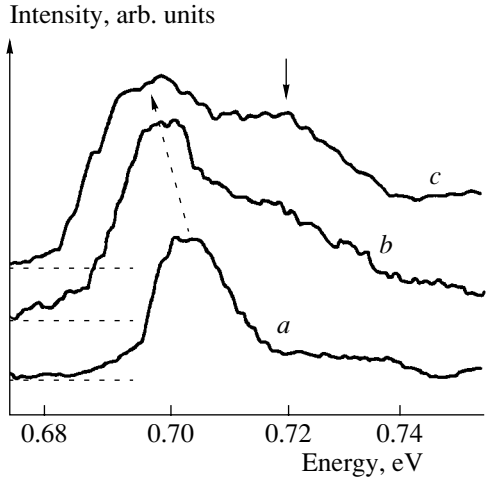

Fig. 5. PL spectra of a structure with 1.2-ML-thick GaAs layer. The excitation power and the temperature of the sample heated by radiation (evaluated from the shift of GaSb-related lines) were (*a*) 70 W/cm^2, 20 K; (*b*) 300 W/cm^2, 80 K; (*c*) 400 W/cm^2, 90 K. Arrows indicate the features of the spectra.

which is significantly narrower than the band gap of the GaSb surroundings. Nevertheless, the band diagram is of type II and, in the equilibrium state, electrons are located in GaAs, and holes, in GaSb.

Despite the general similarity of the QD formation mechanisms in the system under study and in those studied previously, several distinctions are evident. The conventional PL spectra of structures with self-assembled QDs exhibit, along with a peak attributed to the QD array, an additional peak related to the emission from the so-called wetting layer. This peak was absent in the PL spectra of our structures at a low excitation level. However, the PL spectrum is modified as the excitation power increases. Figure 5 shows the relevant PL spectra of a sample with a single 1.5-ML-thick insertion. An obvious effect is the long-wavelength shift of the PL spectrum due to sample heating, which is confirmed by a similar shift of peaks corresponding to bulk GaSb. Moreover, at a sufficiently high excitation level, an additional peak appears at an energy of 25–30 meV higher than the main peak and overlaps with the latter. A similar behavior of the PL spectrum was also observed in the sample with an SL, but the difference between the peak energies was smaller (~15 meV). It is noteworthy that the excitation of the second PL band is associated with an increase in the excitation power, rather than with the accompanying rise of the sample temperature; this becomes evident if we compare the upper PL curve in Fig. 5 with the corresponding spectrum in Fig. 3, which was recorded from the same sample at nearly the same temperature but at a low excitation level. We attribute the presence of two luminescence bands in the PL spectra to a spatial inhomogeneity in the plane of growth of the GaAsSb layer. The low-energy PL peak results from the recombination of carriers localized in As-enriched quantum-dimensional islands, while the higher energy PL stems from the recombination of nonequilibrium carriers in the layer surrounding these islands. In several aspects, this layer resembles the wetting layer observed in the majority of self-assembled QD systems studied to date. However, in contrast to these, in our case, the transport of carriers from the wetting layer to the sites of carrier localization is sufficiently rapid, which does not allow for the observation of steady-state PL from the wetting layer under relatively weak excitation.

4. CONCLUSION

Structural and optical studies were performed in a new type of heterostructure containing ultrathin stressed GaAs layers in a GaSb host. The proposed structures are characterized by a type-II band offset at GaAs/GaSb heterojunctions and intense PL in the 1.7- to 2.3-μm spectral range, depending on the nominal thickness of the GaAs insertion. In the course of epitaxial growth, the GaAs layer in these structures is transformed into a layer of the ternary compound GaAsSb with the formation of QDs when the nominal thickness of the GaAs layer ~1.5 ML or greater.

ACKNOWLEDGMENT

This study was supported by the Russian Foundation for Basic Research (project no. 01-02-17933a), the Ministry of Science program “Physics of Solid-State Nanostructures” (project nos. 1035 and 2014), and by the CRDF (grant no. RPI-2265).

REFERENCES

1. Y. Arakawa and H. Sakaki, Appl. Phys. Lett. **40**, 939 (1982).
2. A. Madhukar, Q. Xie, P. Chen, and A. Konkar, Appl. Phys. Lett. **64**, 2727 (1994).
3. F. Hatami, N. N. Ledentsov, M. Grundmann, *et al.*, Appl. Phys. Lett. **67**, 656 (1995).
4. E. R. Glaser, B. R. Bennett, B. V. Shanabrook, and R. Magno, Appl. Phys. Lett. **68**, 3614 (1996).
5. H. Marchand, P. Desjardins, S. Guillon, *et al.*, Appl. Phys. Lett. **71**, 527 (1997).
6. N. Carlsson, W. Seifert, A. Petersson, *et al.*, Appl. Phys. Lett. **65**, 3093 (1994).
7. G. G. Zegrya and A. D. Andreev, Appl. Phys. Lett. **67**, 2681 (1995).
8. E. R. Glaser, T. A. Kennedy, B. R. Bennett, and B. V. Shanabrook, Phys. Rev. B **59**, 2240 (1999).
9. R. N. Kyutt, A. A. Toropov, S. V. Sorokin, *et al.*, Appl. Phys. Lett. **75**, 373 (1999).
10. R. N. Kyutt, A. A. Toropov, T. V. Shubina, *et al.*, Appl. Surf. Sci. **166**, 278 (2000).
11. E. Bithnel and W. Stobbs, Philos. Mag. A **60**, 39 (1989).
12. C. G. van der Walle, Phys. Rev. B **39**, 1871 (1989).

Translated by D. Mashovets

Semiconductors, Vol. 36, No. 7, 2002, pp. 821–827. Translated from Fizika i Tekhnika Poluprovodnikov, Vol. 36, No. 7, 2002, pp. 874–880.

LOW-DIMENSIONAL SYSTEMS

Inhomogeneous Broadening of the Ground Electron Level in a Quantum Dot Array

V. I. Belyavskiĭ and S. V. Shevtsov

Voronezh State Pedagogical University, Voronezh, 394611 Russia

e-mail: vib@vspu.ac.ru

Submitted December 17, 2001; accepted for publication December 23, 2001

Abstract—The connection between the size and shape distribution of quantum dots (QDs) and the density of electron states is analyzed. It is shown that, in an array of nonidentical QDs, the density of states in the vicinity of the ground level takes the form of an asymmetric peak whose shape and position are determined by the statistical parameters of the array (equilibrium radius, as well as variance and asymmetry of the size distribution of the QDs). General relationships between these parameters and the shape of the peak are determined. © *2002 MAIK "Nauka/Interperiodica".*

1. In recent years, much interest has been attracted to the experimental and theoretical studies of a new class of low-dimensional solid-state systems, referred to as quantum dots (QDs), where the motion of charge carriers is confined in all three dimensions. Progress in the fabrication of such quasi-zero-dimensional objects made it possible to grow both individual QDs and arrays of coherently strained QDs [1, 2], which possess a number of unique properties used in new optoelectronic devices. For example, QD lasers that exhibit characteristics superior to those of quantum-well lasers have already been created. Their advantages originate primarily from the δ-like shape of the density of the charge-carrier states in quasi-zero-dimensional systems and from the effective overlap of electron and hole wave functions due to their spatial confinement. In particular, the electronic spectrum of an individual QD represents a set of discrete quantum-confinement levels. In this respect, it resembles the electronic spectrum of an individual atom. Thus, QDs may be considered as giant artificial atoms whose parameters, such as the depth and profile of the quantizing potential and the QD size and shape, can be varied in a controllable way by varying the technological conditions of their growth.

The latest advances in the technique of submonolayer migration-enhanced epitaxy make it possible to grow QD arrays that are fairly uniform in their dot size and shape [1–4]. Such arrays are formed as a result of the spontaneous islanding of a thin layer of a semiconductor deposited on the surface of another semiconductor with a different lattice constant. This process is related to the relaxation of elastic stresses that appear in a heteroepitaxial system under the conditions of lattice mismatch and is accompanied by a gain in the free energy of the system. This gain is at a maximum when the three-dimensional islands thus formed have a certain (equilibrium) shape and size. In actual structures, the size and shape of individual QDs differ from the equilibrium ones. This has an impact on the optical properties of the QD systems [5–8] and affects the feasibility of the implementation of optoelectronic devices based on them [7, 9, 10].

Thus, it is clear that the scatter in geometric parameters of individual dots has to be systematically accounted for in the analysis of the physical properties of QD systems. In particular, due to such a scatter, the electron spectra of individual QDs grown under given technological conditions are not identical. This results in the transformation of δ-like singularities in the density of the charge-carrier states into finite-width peaks whose profile is determined by the statistical scatter in the geometric parameters of the QD. Thus, one can state that there is inhomogeneous broadening of the energy levels in the systems of QDs. In this paper, under rather general assumptions on the characteristics of this scatter, we consider the issue of ground level broadening and investigate the shape of the corresponding peak in the density of states.

To study electron states in QDs, we employ the effective-mass method using the envelope-function approximation [11], which is commonly used to describe the properties of quantum wells and quantum wires. In this method, the profile of the conduction-band bottom in the heterostructure is considered as the potential-energy profile, which determines the energy spectrum and the quantum states of electrons. In the case of QDs, the profile is shaped as a three-dimensional potential well. It is formed due to the existence of a conduction-band offset at the heterointerface between a QD and the host, which is related to the difference in the band gaps of the two materials. For the sake of simplicity, let us suppose that the position of the conduction-band edge is constant everywhere, except for the offset at the heterointerface; in general, this

assumption is incorrect in the case of coherently strained QD systems, due to the presence of elastic-stress fields around the dots [7, 12]. However, we believe that this choice of the quantum-confinement potential is acceptable, given the limitations of the method itself; in any case, one can expect only qualitative agreement with experiment from the theory based on the application of the effective-mass approximation to nanometer-size semiconductor structures. In this context, we note that similar difficulties arise with any other choice for the confinement potential, e.g., in the frequently used parabolic-potential model [13, 14] or in the hard-wall model. However, it may be reasoned that the data on the broadening of electron levels due to the scatter in the geometric parameters of the QDs are sufficiently reliable not only qualitatively, but quantitatively as well, since only relative shifts of electron levels, rather than absolute level positions, are of significance for this problem. Next, neglecting the anisotropy effects, which are observed in the QDs obtained in actual heteroepitaxial systems, we assume that the equilibrium shape of the QDs is spherical and deviations from this shape are equiprobable in all directions. Note that, due to anisotropy, the equilibrium QD shape can differ from the spherical one; in particular, pyramidal dots are observed [7, 15]. We also disregard the anisotropy of the dispersion law of the charge carriers and the difference in effective masses in the conduction bands of the QDs and the host.

2. In the single-band approximation, the quantum states of an electron in an isolated QD are described by the following equation:

$$-\frac{\hbar^2}{2m^*}\nabla^2\psi(\mathbf{r}) + V(\mathbf{r})\psi(\mathbf{r}) = E\psi(\mathbf{r}), \qquad (1)$$

where E is the energy, $\psi(\mathbf{r})$ is the envelope wave function, m^* is the effective mass, and $V(\mathbf{r})$ is the confining potential: $V(\mathbf{r}) = 0$ inside the QD and $V(\mathbf{r}) = U_0$ outside the QD (U_0 is the conduction-band offset at the heterointerface). Using conventional boundary conditions for the envelope wave function, we can, in principle, determine the energy spectrum and the wave functions of the quantum-confined electron states in a single QD. The spectrum consists of a series of discrete levels of quantum confinement; one can roughly estimate the characteristic spacing between them by evaluating the position of the levels in a spherical potential well with a size typical for the QDs under study. For example, in the GaAs–InAs heterosystem, it is possible to grow almost structurally perfect QDs, whose typical size R_0 is 10–15 nm with the relative spread mostly being below 10%. Taking into account that typical values of the conduction-band offset and electron effective mass are, respectively, $U_0 \approx 300$ meV and $m^* \approx 0.1m_0$ (where m_0 is the free-electron mass), one can easily find that the spacing between the lowest energy levels in such QDs is on the order of $\hbar^2\pi^2/8m^*R_0^2 \cong 60$ meV.

Let us describe the QD surface by the equation $r = R(\vartheta, \varphi)$ in the spherical coordinate system with the origin being at the center of the QD (determined similarly to the center of mass of a homogeneous body). Then, the surface of the corresponding spherical QD is described by the equation $r = R_0$, where R_0 is the equilibrium QD radius. If we consider a statistical ensemble of independent QDs, $R(\vartheta, \varphi)$ should be treated as a random function of its arguments. We make only very general assumptions about the statistical properties of this function, which are largely determined by the form of the one-dimensional and two-dimensional distribution laws $w(R|\vartheta, \varphi)$ and $w(R_1, R_2|\vartheta_1, \varphi_1, \vartheta_2, \varphi_2)$ for the values of the function under consideration. First of all, since we neglected the anisotropy effects, it can be stated that R is a stationary random function in the sense that its properties do not depend on the angles ϑ and φ. This enables us to write the above distribution laws in a simpler form as $w(R)$ and $w(R_1, R_2|\Omega)$, respectively (here, Ω is the angle between the directions determined by the angles ϑ_1, φ_1 and ϑ_2, φ_2).

The function $w(R)$, which has the meaning of one-dimensional probability density, describes the size distribution of QDs and is characterized by the two main parameters of the QD array, the expectation $\bar{R}$ and the variance D_R:

$$R_0 = \bar{R} = \int_0^\infty Rw(R)dR, \qquad (2)$$

$$D_R = \int_0^\infty (R - R_0)^2 w(R)dR. \qquad (3)$$

The first of these represents the average (equilibrium) QD radius; the second one determines the spread of QDs in their size and can be estimated by the rms deviation $\sigma_R = \sqrt{D_R}$. With the currently achieved level of perfection in the fabrication of QDs, σ_R can be about $\approx 0.1R_0$; thus, the "broadening" of the distribution $w(R)$ is characterized by a small parameter $\sigma_R/R_0 \approx 0.1$.

The two-dimensional probability density $w(R_1, R_2|\Omega)$ characterizes the correlation between the values of the function R in any two given directions spaced by an angle Ω ($0 \le \Omega \le 2\pi$) and, thus, determines the typical scale of the surface roughness of the QD. The highest degree of correlation corresponds to the situation where the values of the function R are the same for all angles ϑ and φ; i.e., all QDs have the same strictly spherical shape, while the statistical scatter in the dot radius is preserved. Thus, this limiting case of absolute (complete) angular correlation describes an array of geometrically similar QDs. The two-dimensional distribution function will be given by

$$w(R_1, R_2|\Omega) = w(R_1)\delta(R_1 - R_2), \qquad (4)$$

where $\delta(R_1 - R_2)$ is the Dirac delta function. In the opposite limiting case, there is no correlation between the values of the function R in different directions. This means that the QD surface becomes irregular (stochastic); i.e., it consists of chaotically alternating protrusions and depressions whose heights and depths are absolutely uncorrelated to each other and are distributed randomly according to the law given by $w(R)$. Thus, we have an array of "hedgehog" QDs whose surface is totally irregular. The two-dimensional distribution function is given in this situation by

$$w(R_1, R_2|\Omega) = w(R_1)w(R_2). \quad (5)$$

Obviously, this case should be considered as a mathematical abstraction only, but it is important for the analysis of the influence of angular correlations on the shape of the peak in the density of states. The growth process of an actual QD array gives rise to a certain finite degree of correlation; thus, the parameters characterizing the statistical broadening of the energy levels in a QD, such as the variance and other high-order central moments, always lie between the values corresponding to the two limiting cases considered above. The one-dimensional and the two-dimensional distribution functions are related by the following identity, which is valid for any Ω:

$$\int_0^\infty w(R_1, R_2|\Omega)dR_2 = w(R_1). \quad (6)$$

3. Because of the fluctuations in the shape of the heterointerface, the QD potential $V(r, \vartheta, \varphi)$ in (1) is also a random function that can assume one of its two possible values, 0 or U_0, at each point. Thus, one can state that there is a mean potential (i.e., the potential averaged over the statistical ensemble) given by

$$U(r) \equiv \bar{V} = \int_0^\infty U_0\Theta(r - R)w(R)dR = U_0\int_0^r w(R)dR. \quad (7)$$

Here, $\Theta(r - R)$ is the Heaviside unit-step function, and the bar over the symbol denotes (here and below) statistical averaging. Due to the isotropy, the mean potential (7) is independent of the angles ϑ and φ and is only a function of the variable r. In contrast to the steplike potential of an individual QD, the function $U(r)$ varies smoothly in a narrow range of r (of width on the order of σ_R) around R_0 between the minimum value $U(0) = 0$ and the maximum value $U(\infty) = U_0$ (see figure). We refer to $U(r)$ as the statistical-average QD potential. Note that the introduction of such a single statistical-average potential is justified if all QDs in the array can be described by a single characteristic mean size R_0. In the situations where, because of changing growth conditions (e.g., in the case of the layer-by-layer growth of the QD array) or due to some other reasons, the characteristic QD size varies across the bulk of the array, it makes sense to introduce several typical values of R_0 and the corresponding distribution functions and to consider the statistical-average potentials associated with each of them.

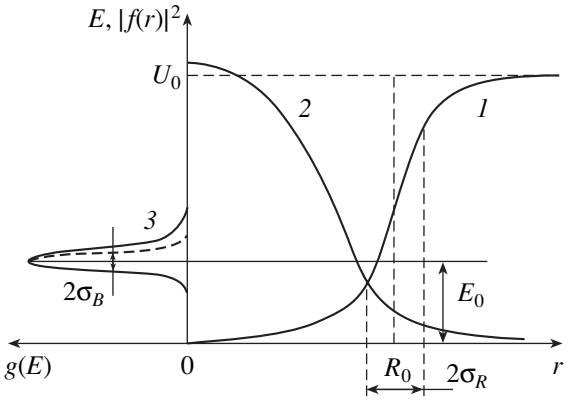

(*1*) Statistical-average potential well for an electron in a quantum-dot array, (*2*) squared envelope wave function of the electron ground state, and (*3*) density of states in the vicinity of the ground level. The dashed line represents the symmetric part of the peak in the density of states.

Since the surface of an actual QD lacks spherical symmetry, it is impossible to obtain an analytical solution to Eq. (1). However, if the QDs in an array deviate from the equilibrium spherical shape only by a small amount (in comparison to R_0) on the order of σ_R, the solution can be found using the perturbation theory. As a zeroth approximation, let us choose the energy-level positions and the wave functions of an electron in a statistical-average potential well (7). These are determined from the Schrödinger equation for a particle of mass m^* in the potential field $U(r)$:

$$-\frac{\hbar^2}{2m^*}\nabla^2\chi + U(r)\chi = E\chi. \quad (8)$$

The states of a particle in a spherically symmetric field can be represented as

$$\chi_{nlm}(r, \vartheta, \varphi) = f_{nl}(r)Y_{lm}(\vartheta, \varphi), \quad (9)$$

where $Y_{lm}(\vartheta, \varphi)$ are the spherical harmonics and $f_{nl}(r)$ are the normalized radial wave functions. The normalized wave function of the ground state can be written as

$$|\chi\rangle \equiv \chi_{100}(r) = \frac{1}{\sqrt{4\pi}}f(r). \quad (10)$$

Designating the ground-state electron energy in the statistical-average potential by E_0, we obtain the following first-order perturbation-theory expression for the ground-state energy E of an electron in a QD characterized by the potential $V(r, \vartheta, \varphi)$:

$$E = E_0 + \langle\chi|V - U|\chi\rangle. \quad (11)$$

Here, $\langle\chi|V-U|\chi\rangle$ is, as usual, the matrix element of the perturbation $V(r, \vartheta, \varphi) - U(r)$ calculated using the zeroth-approximation wave functions:

$$\langle\chi|V-U|\chi\rangle = \frac{1}{\sqrt{4\pi}}\int_0^{2\pi} d\varphi \int_0^{\pi} \sin\vartheta d\vartheta \times \int_0^{\infty} f^2(r) r^2 [U_0\Theta(r - R(\vartheta, \varphi)) - U(r)] dr. \quad (12)$$

The difference in the square brackets in this formula does not vanish only in a narrow range of r (of width $\approx\sigma_R$) around R_0, where its sign is changed. This makes it possible to limit our treatment to the situation where the matrix element (12) is small compared to the energy spacing between the lowest quantum-confinement levels in the QD. Indeed, even if the QD surface deviates from the equilibrium one by the highest possible amount $\approx\sigma_R$ (which has low statistical probability), the magnitude of expression (12) does not exceed $U_0\int_{R_0-\sigma_R}^{R_0+\sigma_R} f^2(r)r^2dr$. This value is small since the electron in the ground state has a low probability of appearing in a narrow layer of width $\sim\sigma_R$ near the boundary of the potential well. Similar reasoning is also valid for the nondiagonal matrix elements. Thus, considering the statistical broadening of the ground level, we can limit ourselves to the first order of the perturbation theory.

4. On account of the random character of the QD potential, the energy E in (11) is also a random quantity, and its distribution law $g(E)$ determines the shape of the peak in the density of electron states originating from the inhomogeneous broadening of the δ-like feature related to the ground electron level. This distribution law can be found provided all central moments $\mu_E^{(k)}$ of the random quantity E are known. They can be easily calculated using (11). Performing averaging in (11) and taking into account that $\bar{V} = U$ and the function χ is not random, we obtain $\bar{E} = E_0$. This means that the position of the peak in $g(E)$ coincides with the energy of the ground electron level in the statistical-average potential well. Thus, for the central moment of order k of the quantity E, we obtain

$$\mu_E^{(k)} = \overline{(E-\bar{E})^k} = \overline{\langle\chi|V-U|\chi\rangle^k}, \quad (13)$$

where the bar on the right-hand side of the formula designates statistical averaging over the multidimensional distribution law of order k of the function R.

For the sake of convenience, it will be useful to transform (13) by introducing an auxiliary random function F related to R by

$$F(R) = \int_0^R f^2(r)r^2dr. \quad (14)$$

It follows from (14) that F determines the probability of finding an electron inside a sphere of radius R with the center at the coordinate origin and which is a monotonic function of R. Transforming the inner integral in (12) via integration by parts, we obtain (taking into account that integrated terms vanish)

$$\mu_E^{(k)} = (-1)^k U_0^k \overline{\langle F - \bar{F}\rangle_{\vartheta,\varphi}^k}. \quad (15)$$

Here, $\bar{F}$ is the value of F averaged over the distribution of R,

$$\bar{F} = \int_0^{\infty} F(R)w(R)dR, \quad (16)$$

and the symbol $\langle\ldots\rangle_{\vartheta,\varphi}$ denotes integration (in other words, averaging) over the angle variables.

In the case where there are no angular correlations between the values of the function R, its multidimensional distribution laws expand into the product of independent one-dimensional distributions $w(R)$ [similarly to (5)]. This means that the statistical averaging in (15) can be performed for each of the k factors separately, which results in the vanishing of all of the central moments of the quantity E. One can see that it is a general conclusion valid for all orders of the perturbation theory, because the calculation in any order is reduced to averaging the products of the factors of the form $\langle\chi_{nlm}|V - U|\chi_{n'l'm'}\rangle$, where χ_{nlm} are nonrandom wave functions of an electron in the statistical-average potential. Owing to the statistical independence of the values of the function V appearing in different factors, averaging can be performed independently for each of them, which results in the vanishing of all central moments because of the condition $\bar{V} = U$. The result obtained implies that, in the case of such a completely stochastic character of the QD surface, the quantum-confinement levels in such a dot coincide exactly with those in the statistical-average potential. This means that the peak in the density of states associated with the ground electron level has the form $g(E) = \delta(E - E_0)$; i.e., it represents a δ-like feature at $E = E_0$ without any broadening.

This conclusion is quite reasonable. We note once again that, in the case considered, all QDs are identical to each other and, since the QD surface exhibits completely irregular fluctuations, the quantum-confinement levels in the dots coincide with the levels in the statistical-average potential.

In the limiting case of absolute angular correlation between the values of the function R, the latter becomes independent of the angles ϑ and φ, which enables one to perform integration over these variables in (12). The remaining integral over r can be taken by parts, and we obtain the relationship

$$E = E_0 - U_0(F(R) - \bar{F}), \quad (17)$$

which establishes a one-to-one functional dependence between random quantities R and E. Then, for the function $g(E)$, we obtain the following expression:

$$g(E) = \frac{1}{U_0}\frac{w(R)}{f^2(R)R^2}\bigg|_{R=R(E)}, \quad (18)$$

where R on the right-hand side should be treated as a function of E determined from (17).

Evaluating the numerical characteristics of distribution (18), we take into account that the existing moderate scatter in the values of R is limited to a narrow interval around R_0 and, consequently, only a narrow range of variation in the function F is important for the transformation from R to E performed by (17). Within this range, F may be approximated by a linear function. Substituting for F in (17) the first two terms of its Taylor expansion in the vicinity of R_0, we obtain a linearized form of this equation, from which it can be immediately found that

$$\mu_E^{(k)} = (-1)^k U_0^k (f^2(R_0)R_0^2)^k \mu_R^{(k)}, \quad (19)$$

where $\mu_R^{(k)}$ is the central moment of order k of the function R:

$$\mu_R^{(k)} = \int_0^\infty (R - R_0)^k w(R)dR. \quad (20)$$

Thus, in the case of absolute angular correlation, the central moments of the energy distribution are proportional to the corresponding moments of the radial size distribution of the QDs. The density of states is given by (18); it exhibits a peak of finite width whose shape, under the approximations adopted, coincides with the shape of the distribution $w(R)$. It should be noted that a similar result for the gain spectrum of QD lasers was obtained in [16], where the effect of QD size fluctuations on laser performance was analyzed. The single-parameter statistical averaging over the relative deviation of the QD size from its mean (equilibrium) value, which was carried out in [16], corresponds exactly to the case of absolute angular correlation just considered. The width of the peak in the density of states is characterized by the variance, which can be determined from (19):

$$\sigma_E = \sqrt{D_E} = U_0 f^2(R_0)R_0^2\sigma_R. \quad (21)$$

In the case of a sufficiently deep, several-nanometer-wide potential well $U(r)$, the probability density $f^2(R_0)R_0^2$ of finding an electron in the neighborhood of the well boundary is low. The calculation carried out below demonstrates that it does not exceed $\approx 0.1R_0^{-1}$; thus, $\sigma_E/U_0 \le 0.1\sigma_R/R_0$ and the distribution $g(E)$ represents a narrow peak whose width, determined by the relative scatter in the QD size, is much smaller than the spacing between the quantum-confinement levels. The third-order moments $\mu_R^{(3)}$ and $\mu_E^{(3)}$, which characterize the asymmetry of the corresponding distributions, have opposite signs [see (19)]; this is related to the fact that the quantum-confinement levels shift downwards with an increase in the QD size.

5. According to (13), in order to determine the numerical characteristics of the distribution $g(E)$ in the case of arbitrary angular correlation, one needs to know the multidimensional distribution laws for the function R. The values of the central moments will be intermediate between those obtained in the limiting cases considered above:

$$|\mu_E^{(k)}| \le U_0^k (f^2(R_0)R_0^2)^k |\mu_R^{(k)}|. \quad (22)$$

Correspondingly, the peak in the distribution $g(E)$ is higher and narrower than it would be in the case of complete angular correlation.

To estimate the variance, we use formula (15) for $k = 2$, substituting for F the first two terms of its Taylor expansion in the vicinity of R_0, and obtain

$$D_E = U_0^2 \frac{[f^2(R_0)R_0^2]^2}{(4\pi)^2} \times \oiint \overline{(R(\vartheta_1, \varphi_1) - R_0)(R(\vartheta_2, \varphi_2) - R_0)} do_1 do_2, \quad (23)$$

where $do_i = \sin\vartheta_i d\vartheta_i d\varphi_i$ ($i = 1, 2$) and the integration is performed over the full solid angle. The mean in (23) is the correlation function of the stationary random function F, which depends only on the angle Ω between the directions set by the angles ϑ_1, φ_1 and ϑ_2, φ_2. Let us introduce the dimensionless normalized correlation function $k(\Omega)$,

$$k(\Omega) = \frac{1}{D_R}\int_0^\infty\int_0^\infty (R_1 - R_0)(R_2 - R_0)w(R_1, R_2|\Omega)dR_1 dR_2, \quad (24)$$

which satisfies the condition $|k(\Omega)| \le 1$. Performing partial integration over the angle variables in (23), we obtain

$$D_E = U_0^2 (f^2(R_0)R_0^2)^2 D_R \frac{1}{2}\int_0^\pi k(\Omega)\sin\Omega d\Omega. \quad (25)$$

Since $|k(\Omega)| \le 1$, the variance of the distribution $g(E)$ satisfies general condition (22). In the case of total angular correlation, when $k(\Omega) \equiv 1$, we return to (21). In the case of the total absence of angular correlations, $D_E = 0$, because $k(\Omega) \equiv 0$. Thus, for a given scatter in the QD size, enhancement of angular correlations leads to an increase in the width of the peak in the density of states.

To determine the function $g(E)$, we expand it into a series over Hermitean polynomials [17]:

$$g(E) = \frac{1}{\sqrt{2\pi}\sigma_E}\exp(-\xi^2)\left(1 + \sum_3^\infty b_k H_k(\xi)\right), \quad (26)$$

where $\xi = (E - \bar{E})/\sqrt{2}\,\sigma_E$, $H_k(\xi)$ is the Hermitean polynomial of degree k, and the coefficients b_k can be expressed in terms of the central moments $\mu_E^{(k)}$ based on the relationship

$$b_k = \frac{1}{2^k k!}\int_{-\infty}^{\infty} g(E)H_k\left(\frac{E-\bar{E}}{\sqrt{2}\sigma_E}\right)dE; \quad (27)$$

here, integration is performed over the entire number axis, because $g(E)$ equals zero almost everywhere except for the narrow interval (of width $\approx\sigma_E$) around $\bar{E}$. If the distribution law $g(E)$ only slightly deviates from the normal distribution law, it is sufficient to retain just the first three terms in expansion (26) (see [17]):

$$g(E) = \frac{1}{\sqrt{2\pi}\sigma_E}\exp(-\xi^2) \times\left\{1 + \frac{1}{12\sqrt{2}}\frac{\mu_E^{(3)}}{\sigma_E^3}H_3(\xi) + \frac{1}{96}\left(\frac{\mu_E^{(4)}}{\sigma_E^4} - 3\right)H_4(\xi)\right\}. \quad (28)$$

The second and third terms in the braces account for the skewness and the kurtosis, respectively.

It should be stressed that, due to the nonlinear character of the relationship between R and E, a certain degree of asymmetry can be present in the energy spectrum even in the case when the initial distribution $w(R)$ is sufficiently symmetric and $\mu_R^{(3)} = 0$. For instance, choosing a Gaussian shape for $w(R)$ and considering the case of total Gaussian correlation, we find from (15) that, in the quadratic approximation in $(R - R_0)$,

$$\mu_E^{(3)} = -U_0^3\frac{d}{dR_0}[(f^2(R_0)R_0^2)^3]D_R^2. \quad (29)$$

It was already noted above that the nonlinearity of the relationship between R and E is rather weak; thus, in all cases where $w(R)$ is close to the Gaussian law, the distribution $g(E)$ is also nearly Gaussian and can be described quite accurately by expression (28).

6. The approximate value of the energy E_0 and the wave function $f(r)$ of the electron ground state in the statistical-average potential can be found by a method based on the perturbation theory [18]. It consists in finding a spherical rectangular potential well of depth U_0 with a radius that gives the best approximation to $U(r)$ in the following sense. Let us denote the energy of the ground state and the corresponding wave function for an electron in a rectangular potential well of radius R_s by $E_0(R_s)$ and $f_s(r)$, respectively. Then, in the first order of the perturbation theory, we obtain

$$E_0 = E_0(R_s) + \int_0^\infty f_s^2(r)r^2[U(r) - U_0\Theta(r - R_s)]dr. \quad (30)$$

Now, we choose R_s on the condition that the first-order correction (represented by an integral in this expression) vanishes. This will mean that the rectangular potential well $U_0\Theta(r - R_s)$ approximates the shape of the potential $U(r)$ in the best way, since the second- and higher-order corrections can be neglected, as was mentioned above. With R_s chosen in this way, $E_0 = E_0(R_s)$ and the zeroth-approximation wave function $f_s(r)$ can be used for $f(r)$. In order to determine R_s from the above condition, we transform the integral in (30) by parts. Taking into account the small width of the distribution $w(R)$, we find in the first approximation that $R_s \cong R_0$. The smaller the variance D_R, the more accurate is this relationship.

Thus, the problem of finding the ground-state energy and wave function of an electron in the statistical-average potential is reduced to finding these for an electron in a spherical square well of depth U_0 and radius R_0. To obtain numerical estimates, we use the parameters typical of the QDs in a InAs–GaAs system; then, for $f^2(R_0)R_0^2$ (the probability density for the electron to appear near $r = R_0$) we obtain a value on the order of $0.1R_0^{-1}$, which was already given above.

7. The scatter of QDs in their size and shape considerably affects the character of the density of electron states in a system of nonidentical QDs and leads to the transformation of the δ-like singularities into peaks, whose shape and position depend on the statistical properties of the QD array. In particular, the density of states in the vicinity of the ground electron level has the form of an asymmetric peak centered at the energy of the ground state of an electron in the statistical-average potential, the peak profile being determined by the radial-size distribution of the QDs. The width of the peak depends both on the radial distribution and the degree of correlation in the shape of the QD surface along different directions; it increases from zero (in the absence of correlations) to a maximum value corresponding to the case of highest correlation, when all the QDs are geometrically similar. The asymmetry of the peak in the density of states is related both to the high-order moments in the radial-size distribution of the QDs and to the character of the dependence of the energy-level shift on the magnitude and sign of the deviation of the QD size from the equilibrium one.

ACKNOWLEDGMENTS

This study was supported by the Russian interdisciplinary program "Physics of Solid-State Nanostructures."

REFERENCES

1. S. S. Ruvimov, P. Werner, K. Scheerschmidt, *et al.*, Phys. Rev. B **51**, 14766 (1995).
2. N. N. Ledentsov, V. M. Ustinov, S. V. Ivanov, *et al.*, Usp. Fiz. Nauk **166**, 423 (1996) [Phys. Usp. **39**, 393 (1996)].
3. D. Leonard, M. Krischnamurthy, C. M. Reaves, *et al.*, Appl. Phys. Lett. **63**, 3203 (1993).
4. J. M. Moison, F. Houzay, F. Barthe, *et al.*, Appl. Phys. Lett. **64**, 196 (1994).
5. N. N. Ledentsov, M. Grundmann, N. Kirstaedter, *et al.*, Solid-State Electron. **40**, 785 (1996).
6. G. É. Tsyrlin, V. N. Petrov, M. V. Maksimov, and N. N. Ledentsov, Fiz. Tekh. Poluprovodn. (St. Petersburg) **31**, 912 (1997) [Semiconductors **31**, 777 (1997)].
7. N. N. Ledentsov, V. M. Ustinov, V. A. Shchukin, *et al.*, Fiz. Tekh. Poluprovodn. (St. Petersburg) **32**, 385 (1998) [Semiconductors **32**, 343 (1998)].
8. V. G. Talalaev, B. V. Novikov, S. Yu. Verbin, *et al.*, Fiz. Tekh. Poluprovodn. (St. Petersburg) **34**, 467 (2000) [Semiconductors **34**, 453 (2000)].
9. H. Sakaki, G. Yusa, T. Someya, *et al.*, Appl. Phys. Lett. **67**, 3444 (1995).
10. A. E. Zhukov, A. R. Kovsh, and V. M. Ustinov, Fiz. Tekh. Poluprovodn. (St. Petersburg) **33**, 1395 (1999) [Semiconductors **33**, 1260 (1999)].
11. M. Altarelli, Springer Proc. Phys. **15**, 170 (1988).
12. V. A. Shchukin, A. I. Borovkov, N. N. Ledentsov, *et al.*, Phys. Low-Dimens. Struct. **12**, 43 (1995).
13. U. E. H. Laheld, F. B. Pedersen, and P. S. Hemmer, Phys. Rev. B **52**, 2697 (1995).
14. N. E. Kaputkina and Yu. E. Lozovik, Fiz. Tverd. Tela (St. Petersburg) **40**, 2127 (1998) [Phys. Solid State **40**, 1929 (1998)].
15. N. N. Ledentsov, M. V. Maximov, P. S. Kop'ev, *et al.*, Microelectron. J. **26**, 871 (1995).
16. L. V. Asryan and R. A. Suris, Semicond. Sci. Technol. **11**, 554 (1996).
17. A. A. Sveshnikov, *Applied Methods in the Theory of Random Functions* (Nauka, Moscow, 1968, 2nd ed.; Pergamon, Oxford, 1966).
18. Y. C. Lee, W. N. Mei, and K. C. Lin, J. Phys. C **15**, L469 (1982).

Translated by M. Skorikov

Semiconductors, Vol. 36, No. 7, 2002, pp. 828–831. Translated from Fizika i Tekhnika Poluprovodnikov, Vol. 36, No. 7, 2002, pp. 881–884.

PHYSICS OF SEMICONDUCTOR DEVICES

Optically Pumped "Immersion-Lens" Infrared Light Emitting Diodes Based on Narrow-Gap III–V Semiconductors

M. Aĭdaraliev, N. V. Zotova, S. A. Karandashev, B. A. Matveev*, M. A. Remennyĭ, N. M. Stus', and G. N. Talalakin

Ioffe Physicotechnical Institute, Russian Academy of Sciences, Politekhnicheskaya ul. 26, St. Petersburg, 19402, Russia

**e-mail: bmat@iropt3.ioffe.rssi.ru*

Submitted October 2, 2001; accepted for publication October 9, 2001

Abstract—Spectral and power characteristics of light emitting diodes (LEDs) for the 3.3- to 7-μm range with GaAs LED pumping are presented. The LEDs consist of narrow-gap In(Ga)As, InAsSb(P), or InAs layers on a n^+–InAs substrate (band width $\sim\lambda_{max}/10$) or on InSb (band width ~1 μm). The LEDs equipped with an immersion lens exhibit a conversion efficiency as high as 0.08–3 mW/A, which is comparable to or exceeds the highest reported data for the injection LEDs. © *2002 MAIK "Nauka/Interperiodica".*

1. INTRODUCTION

To obtain the highest efficiency for light emitters and detectors of the mid-IR range, the lowest density of current carriers in the active region is preferential. For example, intrinsic InSb was employed as an active layer in the "long-wavelength" (6 μm) LED [1]; in the 3- to 5-μm LEDs based on solid solutions, the efficiency was improved by the inclusion of rare-earth elements as getters in the fabrication process [2, 3]. At the same time, it is noteworthy that the growth of the *p*–*n* junction and active region in the same process does not necessarily provide the desired result because of the diffusion of dopants. The production of mid-IR light emitters is significantly simplified when two separate processes are used in the formation of the active region and injector. This separation can be easily accomplished for a system with an active region (or phosphor) excited with an external source [4, 5], where the narrow-gap (active) and wide-gap (injector) sections of the device are optically coupled with an optically transparent "glue", do not comprise a single-crystal unit, and thus can be fabricated independently. A wide-gap pumping source, e.g., a GaAs LED, can be coupled with a narrow-gap phosphor by a chalcogenide glass with a high refractive index (n = 2.6) [6]; in this case, an output power close to that of the best III–V LEDs was achieved in structures with an In(Ga)As(Sb) narrow-gap section in the "transmission" configuration [5].

One of the most important advantages of optically pumped (OP) LEDs is an emission surface free of contacts, which favors optical coupling with immersion lenses; thus, the reflection losses are significantly reduced and the emission directional pattern is narrowed; however, these "immersion" LEDs have not yet been studied.

In this paper, we present data on λ = 3–7 μm OP LEDs coupled with CdSb immersion lenses; the narrow-gap section of a LED is made of *n*-type InAs, In(Ga)As, or InAsSb(P) solid solutions close to InAs or InSb in composition.

2. EXPERIMENTAL

Active layers (phosphors) of OP LEDs emitting at λ = 4.3–5.5 μm were 30- to 50-μm thick undoped *n*-InAsSbP epitaxial layers with an electron density $n \approx 10^{17}$ cm^{-3} and a band-gap gradient ∇E_g = 1–2 meV μm^{-1}. These layers were LPE-grown at 650–720°C on (111) *n*-InAs substrates with $n = (2–4) \times 10^{16}$ cm^{-3}. The basic structural properties of similar samples, with the band gap decreasing in the growth direction, were described previously [7, 8]. In shorter wavelength (λ = 3.1–3.6 μm) OP LEDs, the phosphors were single or double *p*-InAsSbP/n-InGaAs/n-InAsSbP, *p*-InAsSbP/n-InGaAs, or *p*-InAsSbP/n-InAs heterostructures grown at the same temperatures but on heavily doped (100) n^+-InAs substrates with an electron density $n = (3–6) \times 10^{18}$ cm^{-3}. Heavy doping led to the pronounced degeneracy of electrons in the conduction band (the Moss–Burstein effect) and provided low output losses of the emission in the "transmission" mode [5]. The thickness of In(Ga)As or InAs phosphors was ~1 μm, and wide-gap ($E_g \approx$ 430 meV) InAsSbP confinement layers were 3–5 μm thick. In most cases, the growth was performed from a Gd-doped melt, as described in [2].

In the case of the gradient InAsSbP/n-InAs structures, the substrate was removed by selective chemical etching; for heterostructures grown on n^+-InAs, it was thinned to ~70 μm. An *n*-InSb wafer (~7 μm thick, $n = (1–3) \times 10^{16}$ cm^{-3}) was used as a long-wavelength (λ < 6 μm) phosphor.

The emission of OP LEDs (or, in other words, the photoluminescence in the transmission mode) was measured at room temperature under excitation by a GaAs LED (emission wavelength $\lambda \approx 0.87$ μm, external quantum efficiency $\eta_{ext} = 8\%$, 1×0.9 mm^2 in size, the mesa diameter was 0.3 mm) mounted on a silicon holder ($1.1 \times 1.6 \times 0.4$ mm^3). The chip had a *U*-shaped contact to the *n*-region (cathode) and a circular *p*-contact (anode) lying in the same plane, which is typical of flip-chip bonded or episide-bonded structures (see also Fig. 1 in [9]). The absence of contacts on the external surface of the pumping GaAs diode allowed for the easy fixation of a narrow-gap luminescent structure onto this surface. In this case, the narrow-gap layer and the pumping diode were optically coupled by a chalcogenide glass (refractive index $\bar{n} = 2.6$), which was coupled with InSb, with the narrow-gap section of an InAsSb(P) gradient layer or with the *p*-type layers of corresponding heterostructures.

In all spectral measurements, a signal from the cooled CdHgTe photodiode (with the sensitivity peak at 9.4 μm) was detected using a lock-in amplifier (pulse repetition rate 500 Hz, pulse duration 5–30 μs). In the power measurements, the specific features of the spectra and the directional pattern of the OP LEDs were taken into account.

The CdSb ($\bar{n} \approx 5$) immersion lens ~ 3.5 mm in diameter and in height was also coupled with the emitting surface by a chalcogenide glass and fixed with an epoxy resin, as shown in the left-hand part of Fig. 1. The right-hand part of Fig. 1 presents the far-field directional pattern of the emission; as can be seen, the directional pattern of the OP LED with an immersion lens is substantially narrowed, so that the full width at half maximum (FWHM) becomes as small as about 50°.

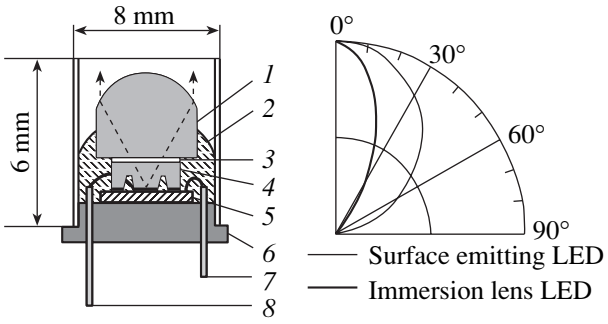

Fig. 1. On the left: design of an "immersion" LED. On the right: the emission directional pattern for (thin line) surface-emitting, and (thick line) "immersion" LEDs. (*1*) CdSb lens, (*2*) epoxy resin, (*3*) narrow-gap active element produced of III–V semiconductor or heterostructure, (*4*) pumping source (LED), (*5*) silicon holder, (*6*) TO-39 package, (*7*) cathode, and (*8*) anode connected to the central part (mesa).

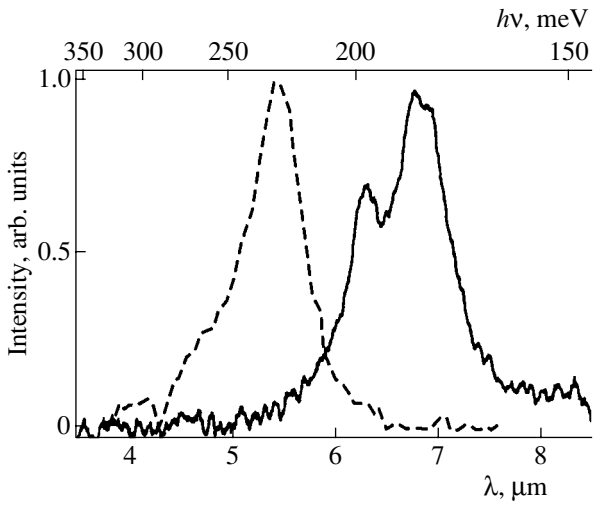

Fig. 2. Room-temperature emission spectrum of an OP LED with the active region of an (dashed line) InAsSb gradient layer and (solid line) InSb.

3. RESULTS AND DISCUSSION

The emission spectra of OP LEDs are similar to those of conventional LEDs; i.e., they exhibit a single band with the peak corresponding to interband transitions, a peak energy $h\nu_{max}$ close to E_g, and a FWHM of 30–50 meV. Figure 2 shows typical spectra of InSb and InAsSb(P) OP LEDs. In contrast to similar LEDs, for example, an InSb/InAlSb LED with $\lambda_{max} \approx 5.5$ μm produced by MBE [1], our LEDs do not exhibit the dynamical Moss–Burstein effect at a comparable output power. Consequently, the emission peak ($\lambda_{max} \approx 7$ μm) appears at a longer wavelength than in [1] and its spectral width is ~1 μm, which is twice as narrow as in [1].

Another specific feature of an InSb OP LED is its small size, which allows effective optical coupling with fibers or lenses. It is necessary to note that, due to a sharp drop of the conversion efficiency at high currents, the authors of [1] were forced to use LEDs 3×3 mm^2 in size for practical applications.

The effect of the immersion lens manifested itself not only in the narrowing of the directional pattern (see Fig. 1), but also in the substantial (nearly 10-fold) rise of the emission power, as compared with similar surface-emitting LEDs free of any coating. Figure 3 shows the output emission power vs. the wavelength for current $I = 1$ A. As can be seen in Fig. 3, the spectral dependence of the power coincides with a similar dependence of the conversion efficiency of the injection LEDs taken from [10]. We may conclude that the main contribution to the power decrease at longer wavelengths is made by the variation in quantum efficiency, rather than by the decrease in the *p–n* junction emission efficiency.

Variations in the emission efficiency of semiconductor layers with band gap variation is commonly attributed to a modulated rate of the nonradiative recombination [11, 12]. We can also correlate the dependences presented in Fig. 3 with the parameters defining the

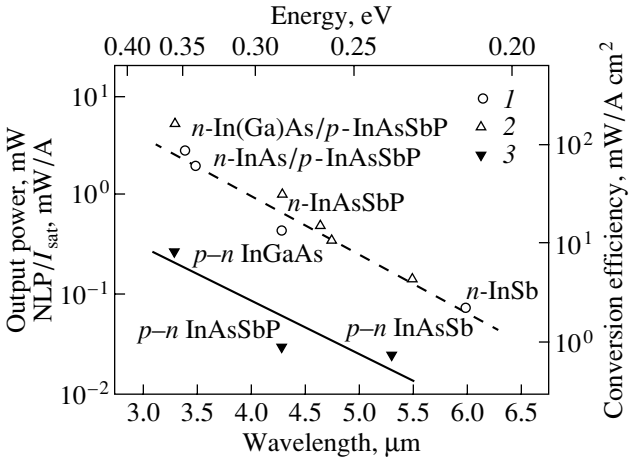

Fig. 3. Spectral dependences: (*1* and the dashed line, left-hand scale) emission power of OP LEDs at current $I = 1$ A, this study; (*2*, right-hand scale) conversion efficiency at $I = 0.2$ A for a unit area [10]; (*3* and the solid line, left-hand scale) maximal power of negative luminescence of a *p*–*n* homojunction divided by the saturation current, this study.

state of a semiconductor (or p–*n* junction) at thermodynamic equilibrium for different values of the energy gap E_g in a way similar to that derived by Stepanov for a two-level system [13]. As parameters, we use the power of the negative photoluminescence of a *p*–*n* junction (NPL), that is, the excess absorption of a semiconductor under the extraction of carriers from the active region (see, e.g., [14]), and the saturation current (I_{sat}). With these parameters, we can determine the maximal conversion coefficient as the ratio NPL/I_{sat}. This approach is justified by the presence of a linear portion of the output power dependence on current (reverse and/or forward current at their comparable values); the linearity of this dependence follows from numerous experimental observations of positive and negative luminescence [14–16] and from the most general considerations.[1] The NPL/I_{sat} values presented in Fig. 3 were obtained by calculating the area of overlap of the black-body spectrum with the emission spectrum of *p*–*n* homostructure LEDs described in [10] (their composition and configuration were close to those discussed here), with further division of the overlap integral by the experimental values of the saturation current (38, 5, and 0.1 mA for the emission wavelengths of 5.3, 4.3, and 3.3 μm, respectively). As can be seen from Fig. 3, the values of NPL/I_{sat} are by an order of magnitude smaller than the power of "immersion" OP LEDs, which is consistent with the obtained decrease in the coefficient of Brewster losses when "immersion" is introduced. The value of NPL/I_{sat} also offers a fairly reliable prediction for the spectral variation in the emission efficiency of a semiconductor, which can be used in evaluations of the quality of injection LEDs.

We believe that OP LEDs are the best emitters in the long-wave length range, since their output power is the same as that obtained from InAs-based ($\lambda = 3.3$ μm) [17] LEDs and several times higher than that from InSb/InAlSb-based ($\lambda = 6$ μm) devices [1].

4. CONCLUSION

We produced optically excited LEDs for the mid-IR spectral range ($\lambda = 3.3$–7 μm) based on III–V semiconductor structures coupled with an immersion optical system; their power matches or exceeds the highest values obtained in conventional LEDs. The high voltage and related high power consumption of these LEDs is compensated for by the simplicity of their fabrication: the narrow-gap active layer can be produced without photolithography and *p*–*n* junction formation. It is noteworthy that the proposed design of OP LEDs is applicable to fiber-optic sensors, because the coupling of these LEDs with fibers presents no technological problems.

ACKNOWLEDGMENTS

We are grateful to O.N. Sarayev for providing the GaAs LED chips.

This study was supported by the Ministry of Science and Technology of the Russian Federation program "Fundamental and Technological Problems in the Design of New Nanostructures for Electronics and Optoelectronics", and by Schlumberger Oilfield Services Co., with the administrative support of the US Civilian Research and Development Foundation for CIS countries (CRDF).

REFERENCES

1. J. G. Crowder, T. Ashley, C. T. Eliott, *et al.*, Electron. Lett. **36**, 1867 (2000).
2. N. V. Zotova, S. A. Karandashev, B. A. Matveev, *et al.*, Fiz. Tekh. Poluprovodn. (St. Petersburg) **33** (8), 1010 (1999) [Semiconductors **33**, 920 (1999)].
3. A. Krier, H. H. Gao, and V. V. Sherstnev, J. Appl. Phys. **85** (12), 8419 (1999).
4. C. Roux, E. Hadji, and J.-L. Pautrat, Appl. Phys. Lett. **75** (24), 3763 (1999).
5. N. V. Zotova, S. A. Karandashev, B. A. Matveev, *et al.*, Fiz. Tekh. Poluprovodn. (St. Petersburg) **35** (3), 371 (2001) [Semiconductors **35**, 357 (2001)].
6. B. A. Matveev, N. V. Zotova, N. D. Il'inskaya, *et al.*, Patent PCT/WO 00/65665 (2000).
7. B. A. Matveev, N. M. Stus', and G. N. Talalakin, Kristallografiya **32** (1), 216 (1988) [Sov. Phys. Crystallogr. **32**, 124 (1988)].
8. B. A. Matveev, N. V. Zotova, S. A. Karandashov, *et al.*, Proc. SPIE **4278**, 189 (2001).

[1] $\Delta P = P_0(np - n_0p_0)/n_i^2$, where P_0, P is the power of equilibrium (thermal) and nonequilibrium emission from a semiconductor; n_0, p_0, n, p are the carrier densities at equilibrium and under bias, respectively; and n_1^i is the intrinsic carrier density.

9. M. Aĭdaraliev, N. V. Zotova, S. A. Karandashev, *et al.*, Fiz. Tekh. Poluprovodn. (St. Petersburg) **34** (1), 99 (2000) [Semiconductors **34**, 104 (2000)].

10. M. Aĭdaraliev, N. V. Zotova, S. A. Karandashev, *et al.*, Fiz. Tekh. Poluprovodn. (St. Petersburg) **35** (5), 619 (2001) [Semiconductors **35**, 598 (2001)].

11. M. E. Flatte, C. H. Grein. T. C. Hasenberg, *et al.*, Phys. Rev. B **59** (8), 5745 (1999).

12. G. G. Zegrya and A. D. Andreev, Appl. Phys. Lett. **67** (18), 2681 (1995).

13. B. I. Stepanov, *Foundations of Spectroscopy of Negative Luminous Fluxes* (Minsk, 1961).

14. W. W. Bewley, M. J. Jurkovic, C. L. Felix, *et al.*, Appl. Phys. Lett. **78** (20), 3082 (2001).

15. L. J. Olafsen, I. Vurgaftman, W. W. Bewley, *et al.*, Appl. Phys. Lett. **74** (18), 2681 (1999).

16. B. A. Matveev, N. V. Zotova, S. A. Karandashev, *et al.*, IEE Proc.: Optoelectron. **149**, 33 (2002).

17. A. Krier and V. V. Sherstnev, J. Phys. D **33**, 101 (2000).

Translated by D. Mashovets

Semiconductors, Vol. 36, No. 7, 2002, pp. 832–836. Translated from Fizika i Tekhnika Poluprovodnikov, Vol. 36, No. 7, 2002, pp. 885–889.

PHYSICS OF SEMICONDUCTOR DEVICES

Amorphization of the Surface Region in Epitaxial *n*-GaAs Treated with Atomic Hydrogen

N. A. Torkhov*, I. V. Ivonin, and E. V. Chernikov

Kuznetsov Physicotechnical Institute, Tomsk State University, pl. Revolyutsii 1, Tomsk, 634050 Russia

** e-mail: tna@ic.tsu.ru*

Submitted November 27, 2001; accepted for publication December 18, 2001

Abstract—It was found that the atomic-hydrogen treatment of *n*-GaAs epitaxial samples having initially high-quality surfaces both with a SiO_2 protective film on the *n*-layer surface and without it can lead to the amorphization of these surfaces and a thin (≈7 nm) surface layer, which is accompanied by the formation of a hydride phase. The lack of a hydrogen sublattice in the near-surface layer can imply that the main driving forces in the amorphization of epitaxial *n*-GaAs are short-range chemical interactions between hydrogen atoms and also between hydrogen atoms and atoms of the basic matrix of the crystal. *© 2002 MAIK "Nauka/Interperiodica".*

1. INTRODUCTION

It was previously shown [1–7] that the treatment (hydrogenation) of GaAS samples in atomic hydrogen affected the electrical properties of the material, which was accompanied by the modification of static device characteristics of Au-*n*–n^+-GaAs structures with a Schottky barrier, an increase in the reverse voltage V_r, and a decrease in the ideality index *n* [5, 6, 8–11]. In [5, 6, 12], a suggestion was made that such a modification in the device characteristics and also in the electrochemical properties of the surface (a decrease in the etching rate of a material and in the rate of electrochemical deposition of gold [13, 14]) can be induced by the formation of a thin amorphized GaAs surface layer with a low conductivity and with different physical and chemical properties compared with those in the bulk.

In this study, we experimentally prove that treatment in atomic hydrogen both through a SiO_2 protective film and without it can lead to the amorphization of the surface region of epitaxial *n*-GaAs. It was found that the amorphization of epitaxial *n*-GaAs can be accompanied by the formation of a gallium-hydride phase.

2. EXPERIMENTAL

In the experiments, we used *n*–n^+-GaAs:Sn (100) epistructures. The electron concentration amounted to $\approx 3.5 \times 10^{16}$ cm^{-3} in the *n* epilayer and 2×10^{18} cm^{-3} in the n^+ layer. From the side of the n^+ substrate, an ohmic contact was formed on the basis of GeNi + Au. The ohmic contact was necessary for providing a good electric connection during the investigation using a scanning tunneling microscope (STM) and also for preventing charge accumulation on the *n*-layer surface during the electron-diffraction investigations.

After forming the ohmic contact on the n-layer surface, we deposited a SiO_2 protective film which was 5 nm thick and permeable to atomic hydrogen (*P*-type samples). Before the deposition of the SiO_2 film, the structures were treated in the ammonium etchant $NH_4OH : H_2O = 1 : 5$ to remove native oxide from the *n*-layer surface [13]. Immediately before the atomic hydrogen treatment, the SiO_2 protective film was removed from some of the samples (*U*-type samples) in the buffer etchant $HF : H_2O = 1 : 10$.

The structures prepared by this method were simultaneously treated in an atomic-hydrogen flow generated in the source based on low-voltage arc gas discharge [15]. The hydrogen pressure in the treatment zone amounted to 1.3×10^{-2} Pa, the treatment temperature T_{tr} was chosen to be equal to 150°C, and the treatment duration was 5 min. The construction of the source ruled out the possibility of the appearance of radiation defects on the sample surface during hydrogenation [11].

The STM investigations of the *P*- and *U*-type samples were carried out using an SMM-2000TA commercial scanning multimicroscope. From the surface of the *P*-type samples, the SiO_2 protective film was removed in the buffer etchant. Immediately before the STM measurements, the *n*-layer surface of both types of samples was treated in an ammonium etchant. The STM measurements were performed using a platinum tip (Pt 99.99) in the dc mode. The voltage between the tip and the semiconductor surface was chosen to be equal to 1.5 V. The measurements were carried out under atmospheric conditions and at room temperature.

The structure of the near-surface layers of both types of samples was investigated in an ÉMR-102 electron diffractometer using the reflection high-energy electron diffraction from an ≈7-nm-deep layer at an electron energy of 75 keV. Before the measurements, we removed the SiO_2 protective film from the surface of

1063-7826/02/3607-0832$22.00

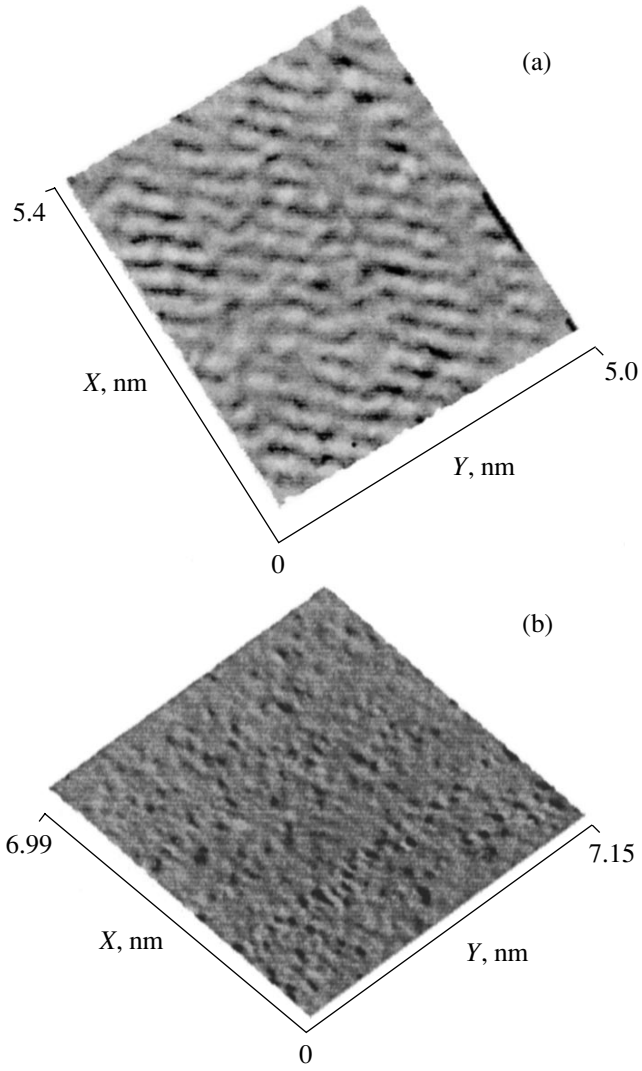

Fig. 1. STEM image of the n–n^+-GaAs surface treated in the ammonium etchant: (a) original, (b) treated in atomic hydrogen.

the *P*-type samples in the buffer etchant. Immediately before loading into the vacuum chamber of the electron diffractometer, the samples of both types treated in atomic hydrogen were repeatedly treated in the ammonium etchant together with the original samples.

The structure of the deeper layers was investigated using a transmission electron microscope (TEM) in the diffraction mode. For this purpose, we prepared a one-sided wedge tapered down to the *n*-layer surface using the chemical etching of the sample. The thickness of the transmitted region was no larger than 100 nm.

For improving the image contrast, the electron-diffraction patterns were processed using the graphic editor CorelDraw (version 9) with the 3D "relief" effect.

An elemental analysis of the surface region of the GaAs *n*-layer was carried out using an MS-7201M secondary-ion mass spectrometer (SIMS). We measured the overall mass spectrum in the range from 60 to 85 amu and also the currents for Si^+, Ga^+, and H^+ ions as functions of the time of sputtering.

3. RESULTS AND DISCUSSION

Scanning Tunneling Microscopy

In Fig. 1, we display the STM image of the original sample and that after the treatment in atomic hydrogen. For the original sample, the presence of a periodic structure (Fig. 1a) is a characteristic which, according to [13], is indicative of a single-crystalline structure and the high quality of the *n*-GaAs surface. For the samples treated by atomic hydrogen through SiO_2 (*P*-samples) or directly (*U*-samples), no periodic structure was observed (Fig. 1b). This fact can be interpreted as the transition to the amorphous state of the surface.

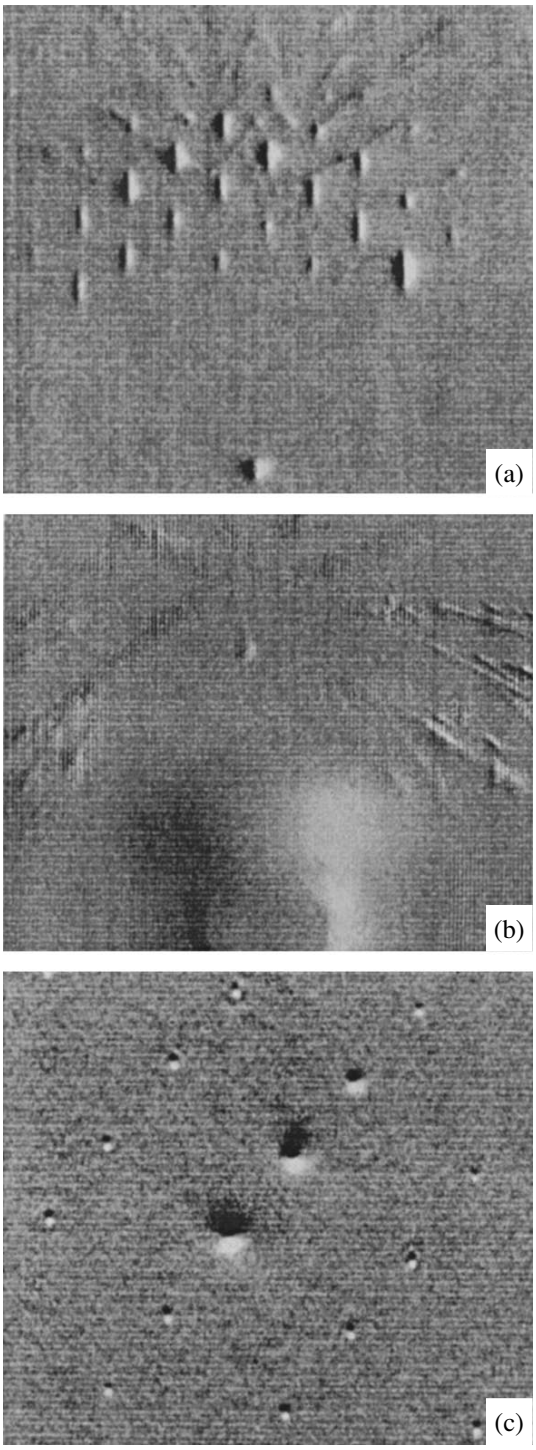

Fig. 2. Reflection electron-diffraction patterns from the surface (≈7-nm) region of the *n*-GaAs sample: (a) original, (b) treated in atomic hydrogen, (c) transmission electron-diffraction pattern from the near-surface (≈100-nm) region of the *n*-GaAs sample treated in atomic hydrogen.

Electron Diffraction

The results of the electron-diffraction investigations show that treatment in atomic hydrogen also affects the surface-region structure. The electron-diffraction pattern of the *n*-GaAs surface region of the original sample is shown in Fig. 2a. The reflection spots characterizing the periodic structure of the surface layer, which is ≈7 nm thick, can be clearly seen. A weak manifestation of the Kikuchi lines is indicative of the existence of inelastic electron scattering induced by the specific morphology of the surface previously described in [5, 6]. The electron-diffraction pattern from the surface region of the atomic-hydrogen-treated *P*-type sample is shown in Fig. 2b (the electron-diffraction patterns from the *U*-type samples after the atomic-hydrogen treatment are similar and, thus, are not shown). It can be seen that the diffraction pattern of the surface region is substantially modified as a result of the atomic-hydrogen treatment. Near the central spot, a wide diffuse halo appears, which directly points to the amorphization of the surface region. The TEM diffraction studies of deeper (≈100-nm) surface layers of the hydrogenated *n*-GaAs (Fig. 2c) showed that the diffraction pattern corresponded to a GaAs single crystal. No traces of the amorphous phase were observed in this case. Thus, the amorphization of *n*-GaAs is localized in a thin surface layer for the atomic-hydrogen-treatment conditions used.

The absence of additional reflections on the electron-diffraction pattern in Fig. 2b implies that an interstitial solid solution of hydrogen is not formed in the 7-nm-thick *n*-GaAs near-surface layer. Such a solution is also not formed in the sample bulk (Fig. 2c). Therefore, in spite of a high concentration of hydrogen in the surface region [7, 18, 19], a hydrogen sublattice is not formed in *n*-GaAs and the observed reflections correspond to GaAs atomic planes. Therefore, we can conclude that the changes in the physical and chemical properties of the material near the surface are not associated with the forming of the hydrogen interstitial solid solution.

We may assume that the driving forces in the process of the amorphization of epitaxial *n*-GaAs are not long-range chemical interactions; rather, they are short-range chemical interactions between hydrogen atoms and also between hydrogen atoms and the atoms of the basic matrix of the crystal. The results of study [6] partially support this assumption. In that study, we suggested that treatment in atomic hydrogen can lead to the formation of hydrogen-involving dimers on the *n*-GaAs surface. A similar situation was also previously observed on the Si surface by the authors of [20]. The assumption proposed is corroborated by the results of SIMS investigations. We found that hydrogen is actually present in the *n*-GaAs surface layer in the form of compounds with gallium. In the mass spectrum from the surface region of the hydrogenated sample (Fig. 3a, curve *1*), along with known peaks corresponding to ions of the isotopes $^{69}Ga^+$ ($\mathbf{M}_1$) and $^{71}Ga^+$ ($\mathbf{M}_2$), we observed additional peaks corresponding to the ions $(^{69}Ga^1H)^+$ ($\mathbf{M}_3$) and $(^{71}Ga^1H)^+$ ($\mathbf{M}_4$).

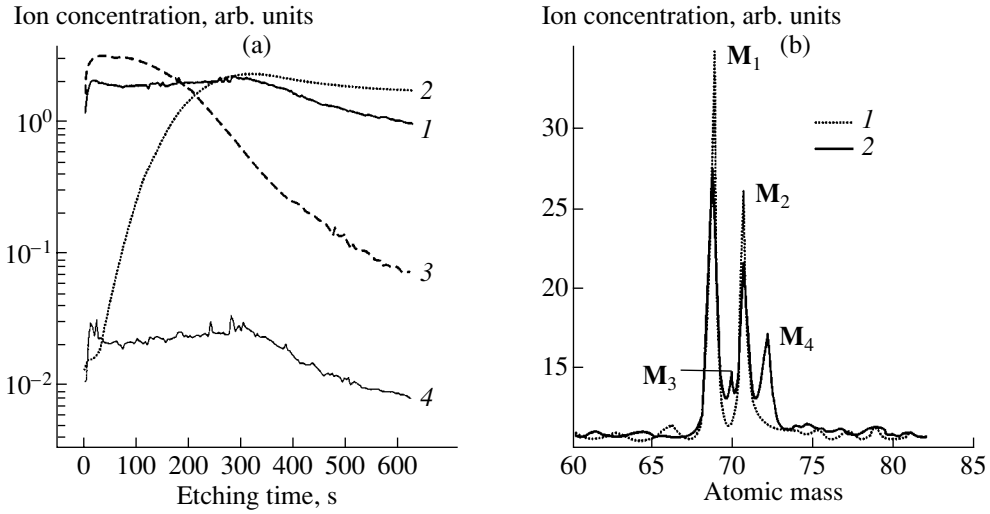

Fig. 3. (a) Profiles of concentrations of positive ions (*1*) H^+, (*2*) Ga^+, (*3*) Si^+, and (*4*) GaH^+ in the SiO_2/n–n^+-GaAs structure with the SiO_2 film 5 nm thick; (b) the overall mass spectrum in the range from 60 to 85 amu, $\mathbf{M}_1$—$^{69}Ga^+$, $\mathbf{M}_2$—$^{71}Ga^+$, $\mathbf{M}_3$—$(^{69}Ga^1H)^+$, and $\mathbf{M}_4$—$(^{71}Ga^1H)^+$. (*1*) Is the mass spectrum of the original sample; (*2*) is the mass spectrum from the sample treated in atomic hydrogen.

As the secondary ions are detected from deeper layers of the SiO_2 film, the intensity of the ion currents for $^{69}Ga^+$ and $^{71}Ga^+$ abruptly increases, which indicates that the *n*-GaAs layer is approached (Fig. 3b). The intensity of the $(^{69}Ga^1H)^+$ and $(^{71}Ga^1H)^+$ ion currents (as well as that of the $^1H^+$ ion current) remains virtually unchanged. If we assume that Ga hydrides are formed in the secondary beam, an increase in the Ga^+-ion yield must also be accompanied by an increase in the GaH^+ yield, which contradicts the results obtained. This circumstance enables us to state that the gallium hydrides are actually contained in the surface layer and are not formed in the secondary beam after sputtering.

Because the Ga hydrides were observed only in the samples treated in atomic hydrogen, we may assume that the amorphization of the surface region and the formation of the hydride phase are related. Until now, we failed to determine whether the formation of the hydride phase during the atomic-hydrogen treatment initiates the decomposition of the periodic structure in the near-surface region of epitaxial *n*-GaAs and, thus, promotes its amorphization, or whether the hydride phase is formed later in the layer, which is already amorphized.

4. CONCLUSION

Using scanning tunneling microscopy and electron diffraction, we ascertained that the treatment of samples of epitaxial *n*-GaAs in atomic hydrogen both with and without a SiO_2 protective film on the surface of the *n*-layer can lead to the amorphization of the surface and a thin (≈7-nm) surface layer.

In spite of the high concentration of hydrogen dissolved in the *n*-GaAs near-surface epilayer, a hydrogen sublattice is not formed; i.e., the amorphous phase in *n*-GaAs is formed via an intermediate phase based on the interstitial solid solution of hydrogen.

The driving forces in the amorphization of epitaxial *n*-GaAs are assumed to be chemical short-range interactions between hydrogen atoms and also between hydrogen atoms and the atoms of the basic matrix of the crystal. This assumption was corroborated by the SIMS results, in which it was established that the amorphization of epitaxial *n*-GaAs was accompanied by the formation of a gallium-hydride phase near the surface of epitaxial *n*-GaAs.

REFERENCES

1. S. J. Pearton, J. Electron. Mater. **14**, 737 (1985).
2. S. J. Pearton, E. E. Haller, and A. G. Elliot, Appl. Phys. Lett. **44**, 684 (1984).
3. É. M. Omel'yanovskiĭ, A. V. Pakhomov, and A. Ya. Polyakov, Fiz. Tekh. Poluprovodn. (Leningrad) **21**, 842 (1987) [Sov. Phys. Semicond. **21**, 514 (1987)].
4. É. M. Omel'yanovskiĭ, A. V. Pakhomov, A. Ya. Polyakov, *et al.*, Fiz. Tekh. Poluprovodn. (Leningrad) **22**, 1203 (1988) [Sov. Phys. Semicond. **22**, 763 (1988)].
5. N. A. Torkhov and S. V. Eremeev, Fiz. Tekh. Poluprovodn. (St. Petersburg) **34**, 186 (2000) [Semiconductors **34**, 181 (2000)].
6. N. A. Torkhov and S. V. Eremeev, Fiz. Tekh. Poluprovodn. (St. Petersburg) **33**, 1209 (1999) [Semiconductors **33**, 1100 (1999)].
7. A. V. Panin and N. A. Torkhov, Fiz. Tekh. Poluprovodn. (St. Petersburg) **34**, 698 (2000) [Semiconductors **34**, 671 (2000)].

8. A. Paccagnella, A. Callegari, E. Latta, and M. Gasser, Appl. Phys. Lett. **55**, 259 (1989).
9. U. K. Chakrabarti, S. J. Pearton, W. S. Hobson, *et al.*, Appl. Phys. Lett. **57**, 887 (1990).
10. Y. G. Wang and S. Ashok, J. Appl. Phys. **75**, 2447 (1994).
11. V. G. Bozhkov, V. A. Kagadeĭ, and N. A. Torkhov, Fiz. Tekh. Poluprovodn. (St. Petersburg) **32**, 1343 (1998) [Semiconductors **32**, 1196 (1998)].
12. Y. G. Wang and S. Ashok, J. Appl. Phys. **75**, 2447 (1994).
13. N. A. Torkhov and V. G. Bozhkov, Poverkhnost, No. 8, 100 (2001).
14. N. A. Torkhov, V. G. Bozhkov, V. A. Kagadeĭ, and I. V. Ivonin, in *Proceedings of the II International Conference "Radiation-Thermal Effects and Processes in Inorganic Materials", Maksimikha, Russia, 2000*, p. 86.
15. V. A. Kagadeĭ, D. I. Proskurovskiĭ, and O. E. Troyan, RF Patent No. 2088056.
16. N. Watanabe, T. Nittono, H. Ito, *et al.*, J. Appl. Phys. **73**, 8146 (1993).
17. V. A. Kagadeĭ, D. I. Proskurovskiĭ, S. D. Reger, and L. M. Romas', Mikroélektronika **27**, 10 (1998).
18. U. K. Chakrabarti, S. J. Pearton, W. S. Hobson, *et al.*, Appl. Phys. Lett. **57**, 887 (1990).
19. A. V. Pakhomov, A. Ya. Polyakov, É. M. Omel'yanovskiĭ, *et al.*, Fiz. Tekh. Poluprovodn. (Leningrad) **22**, 1203 (1988) [Sov. Phys. Semicond. **22**, 763 (1988)].
20. A. Watanabe, M. Unno, F. Hojo, and T. Miwa, Jpn. J. Appl. Phys., Part 2 **39** (10), L961 (2000).

Translated by V. Bukhanov